Spatio-Angularly Multiplexed (SAM) Holographic Storage in Photorefractive Crystals

Thesis by

Shiquan TAO

Submitted to the University of London
for the Degree of Doctor of Philosophy

Department of Electronic and Electrical Engineering
University College London
Torrington Place, London WC1E 7JE
United Kingdom

June 1993

ACKNOWLEDGEMENTS

First of all I wish to express my heartfelt thanks to my supervisor, Dr. D. R. Selviah, and to the Head of Department, Professor J. E. Midwinter, for their kind encouragement and strong support throughout this work. It was Dr. Selviah who originally suggested the spatio-angular multiplexing, which has become the topic of this thesis. Also, I would like to thank Professor C. Pitt of this department for his helpful discussions on photorefractive crystal properties, Professor L. Solymar of Oxford University and Dr. Z. Q. Mao of Loughborough University for stimulating the particular research direction, Dr. D. Godwin for his kind help in checking the English for this thesis, and P. C. H. Poon for help with computing, and discussions regarding the selection of suitable materials.

I am indebted to many of my colleagues in this department, especially, A. Overbury, C. Carey, B. Glover, P. Mackie, Mrs. P. Karia, and M. F. Gillett and his colleagues in the workshop, for their help in setting up the holographic laboratory, which was essential for the experiments in this work.

This work was financially supported by the Science and Engineering Research Council, U. K., through the Optoelectronic Interdisciplinary Research Centre. I am also grateful to the Chinese Government, without whose financial support I would not have had the opportunity to study in England. Thorn-EMI, CRL, Smectic Technology (who supplied the ferroelectric liquid crystal SLM), Photox Optical Systems, U. K., the Shanghai Institute of Ceramics, at the Chinese Academy of Sciences (who supplied the $Fe:LiNbO_3$ crystals), and Micro-Controle (who supplied the motorised motion system) are warmly acknowledged.

Finally, I wish to express my deep appreciation to my husband, not only for his specific help with equipment and programming which enabled the experiments in this thesis to be complete in time, but also for his patient encouragement whilst I was writing up this thesis.

To my family

ABSTRACT

In this thesis a novel multiplexing scheme for dense holographic storage in photorefractive crystals, Spatio-Angular Multiplexing (or SAM), is described in detail. In SAM Fourier transform holograms are formed in spatially overlapping regions of a crystal and are distinguished from one another by using variously angled reference beams. SAM takes advantage of both the high storage density possible using angularly multiplexed volume holograms and also the low crosstalk possible using spatially multiplexed Fourier transform holograms. Compared to pure spatial multiplexing, SAM increases the storage capacity by fully utilising the volume of the storage medium. On the other hand, SAM reduces the number of holograms overlapping any one hologram in a given volume, and so increases the diffraction efficiency achievable as compared to pure angular multiplexing. SAM offers the possibility of incorporating the recorded crystal into a content addressable memory (CAM) system for parallel access of all stored patterns.

In order to obtain the maximum diffraction efficiency and signal to noise ratio, the hologram must be replayed by a readout beam incident at the correct angle of readout beam. The optimum angle may be shifted away from the angle used in recording by a "Bragg-shift", caused (under certain conditions) by phase coupling between the two writing beams during recording. Although this Bragg shift is small, a large diffraction efficiency enhancement is obtained when the grating is read out at the optimum angle. We have calculated the Bragg shift, using a numerical calculation based on an earlier theory, and have obtained good agreement with experiment.

Using the novel SAM scheme, we have succeeded in storing 756 high resolution binary patterns in an Fe:LiNbO$_3$ crystal of volume 1cm^3, with an average diffraction efficiency of 0.5%. This large database is designed for practical use in a novel associative memory system, called a high order feedback neural network (HOFNET). We also present the readout scheme required for parallel access of the information stored within the crystal. This is essential for operation of the HOFNET.

CONTENTS

DEFINITIONS AND ABBREVIATIONS

DEFINITIONS:

d: Hologram thickness

$\mathrm{d_H}$: Hologram dimension

$\mathrm{d_I}$: Pixel size (pitch) in the detection plane

$\mathrm{d_s}$: Pixel size (pitch) in the object plane

$\mathrm{D_H}$: Dimension of the recording material

$\mathrm{D_I}$: Dimension of the detection plane

$\mathrm{D_s}$: Dimension of the object plane

$\mathrm{D_r}$: Dimension of the reference plane

$\mathrm{E_r}$: Complex amplitude distribution of reference wave on recording plane

E_r: Amplitude distribution of reference wave on recording plane

$\mathrm{E_S}$: Complex amplitude distribution of object wave on recording plane

E_s: Amplitude distribution of object wave on recording plane

E_η: Diffraction efficiency enhancement factor

f: Focal length of Fourier transform lens

F: Hologram filling factor

Γ: Coupling strength of photorefractive gratings

K: Length of grating vector

$\mathbf{K}$: Grating vector

k: Propagation constant of light

$\mathbf{k}$: Wave vector of light

m: Fringe modulation depth responsible for the hologram formation

$\mathrm{m_O}$: Initial ratio of reference beam intensity to object beam intensity

$\mathrm{M_{ang}}$: Degree of angular multiplexing, number of holograms superimposed in the same volume

$\mathrm{M_{BOHS}}$: Total number of holograms stored using BOHS

$\mathrm{M_O}$: Number of holograms limited by the number of available reference angles

$\mathrm{M_P}$: Number of pixels stored in each hologram (page)

$\mathrm{M_S}$: Degree of spatial multiplexing, number of holograms stored using pure spatial multiplexing

M_{SAM}: Total number of holograms stored using SAM
n: Average refractive index
Δn: Modulation depth of the refractive index
δ: Phase mismatch during grating readout
$\Delta\lambda$: Wavelength deviation from recording wavelength
$\Delta\theta$: Readout angle deviation from recording angle
$\Delta\Theta$: Selective angle of volume grating in the horizontal plane
$\Delta\Phi$: Selective angle of volume grating in the vertical plane
ϕ: Grating slant angle
Φ_g: Phase shift between writing intensity pattern and resultant grating fringes
η: Diffraction efficiency
λ: Wavelength of light in crystal
Λ: Grating spacing
μ: Spatial overlapping factor of SAM
σ: Bragg angle shift from the recording angle for intermodal diffraction
ξ: Spatial frequency coordinate, $\xi=x/\lambda f$
ξ: Phase mismatch parameter of volume grating
ζ: Spatial frequency coordinate, $\zeta = z/\lambda f$
*: Complex conjugation sign

ABBREVIATIONS

BOHS: block oriented holographic storage
F.T. :Fourier transform (transformation)
HOFNET: High order feedback neural network
MAWBG: multiple angled weighted beam generator
SAM: spatio-angular multiplexing
SBP: space-bandwidth-product
SLM: spatial light modulator
SNR: signal-to-noise ratio
UV: ultraviolet

CHAPTER ONE

INTRODUCTION

The rapid development of today's advanced computing systems requires high performance (in particular, high access speeds), and high capacity storage. Since the mid-eighties, speed advances in dynamic random access memory chips (that make up the main memory in personal computers and workstations) have not kept pace with advances in processor clock speeds. In a typical computing system there are usually four or five types of storage ranging from register storage (which feeds the processor's functional units) to magnetic tape storage (which backs up the magnetic hard disk). This hierarchical storage system is designed to keep the processor as busy as possible, by supplying it with the required information in a timely manner [Rya92]. This memory hierarchy can be viewed as a pyramid, and a typical pyramid applying at the present time [Zec92] can be seen in Fig. 1.1. There is always a compromise to be made between the storage capacity, cost per megabyte, and the access time of the present memory technologies (as can be seen from Fig. 1.1). Also all of the storage technologies shown in Fig. 1.1 store information in a planar surface. Due to this two dimensional (2-D) nature, the storage densities are limited.

The impetus of optical storage as a solution to the above problems came from the understanding that the potential storage density in a three dimensional (3-D) optical storage material could be as high as $1/\lambda^3$ (λ is the light wavelength used for recording). This was estimated by van Heerden in 1963 [vHe63]. Today, CD-ROM (compact disk - read only memory), with a capacity of over half a gigabyte, is best used as an information-distribution medium; and optical read/write storage that uses MO (magneto-optical) technology will take an important place in direct-access storage over the next few years [Rya92]. Although both MO and CD-ROM technologies are based on 2-D recording, their optical nature promises a storage density of $1/\lambda^2$ (4×10^6 bits/mm^2 for λ=0.5μ), which is still higher than that achieved by the current non-optical technologies. (A typical high capacity magnetic disk, for example, might have a storage density of 2×10^5 bits/mm^2.) Unfortunately, the access time achieved by the current optical storage technologies is quite low, as can be seen in Fig. 1.1. Recently, a three dimensional optical memory, based on the two-photon effect, was proposed. This promises a high access speed and the potential of parallel access [Hun90, Str91]. It is claimed that the highest densities have been realised using this technology (>10^{12} bits/cm^3, almost reaching the upper limit for 3-D optical storage) [Str91].

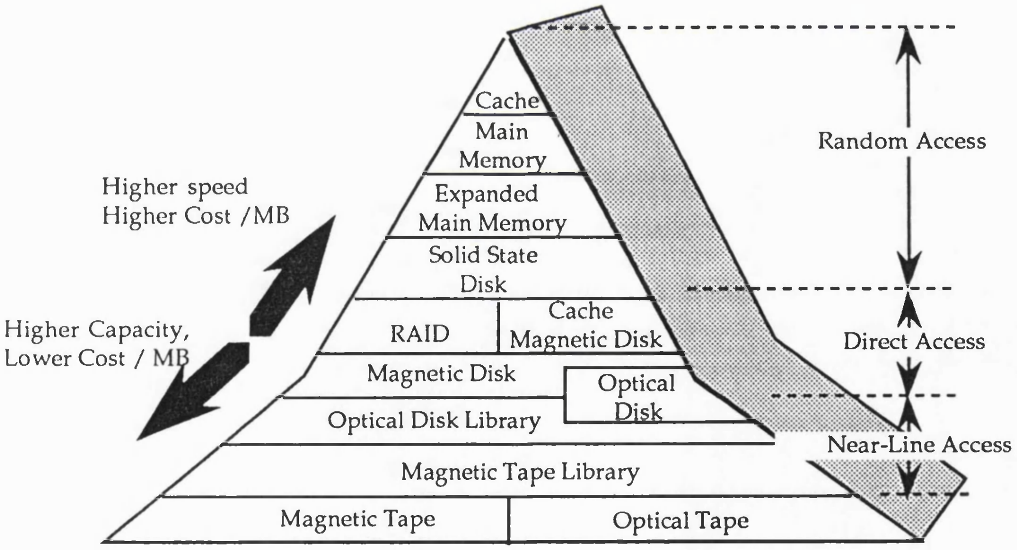

Fig. 1.1 A pyramid diagram showing the 1990's memory hierarchy. The base of each segment represents its relative capacity in comparison to the other storage types, whilst its height represents the relative speed (higher means faster) and cost (higher means more expensive). RAID: redundant arrays of inexpensive disks.

Holograms have been considered as potential optical storage devices since holography was established in the early sixties. In fact, the seminal paper of van Heerden ([vHe63]), which discussed theoretical limits on storage capacity for optical 3-D storage, was based on 3-D holographic storage. Attempts in the 70s to store a large number of data pages holographically, in an erasable material (such as a photorefractive crystal), such that any bit on a page could be independently erasable, were deemed impractical [Sol89a]. However, during the period from about 1963 to 1975, designs and implementations of high performance, high capacity storage systems, based on volume holography, were presented [d'Au74], and the challenge to realise higher capacity systems remain today.

The challenge for holographic storage was stimulated in recent years by the increasing research into optical neural networks [Psa90], optical interconnections [And87, Wu90, Goo90], and applications for pattern recognition [Mok92] and parallel correlation [Mao92b]. These applications can be referred to collectively as optical computing. The advantages of using holographic storage for these applications accrue from the following properties of holography:

1) High redundancy. The information stored in the form of a hologram is distributed throughout the whole surface (or volume) of the hologram, so that local defects or damage in the recording material do not cause loss of information.

2) Very high data transfer rates and fast access time. Volume holographic memories can write and read information pages, in a bit-parallel format, as opposed to the bit-serial format used in disk or tape drivers. Also, holographic databases may accessed by means of inertia-free beam deflection or wavelength selection, instead of the electro-mechanical read/write heads used to record and access data on disks or tapes. Therefore, very high data transfer rates and fast access times are potentially available from holographic memories.

3) The possibility of fully parallel readout. It is possible to read all the information stored in the whole holographic memory at once, and all

of the reconstructed information can be processed in an optical neural network system (such as a high order feedback neural network, or HOFNET, for example, [Mao92b]).

4) High capacity. The upper limit on the storage capacity for 3-D optical storage, $1/\lambda^3$, also applies to holographic storage. The storage capacity of volume holography can be potentially further enhanced, by using so-called four dimensional (4-D) storage. This can be implemented in certain kinds of material, using the technique of persistent spectral hole burning (PSHB). This enables a large number of holograms to be stored in a given volume, by using more than one wavelength [Wev91, Oll93, Wil93] in addition to the named 3-D holographic storage schemes. (The technique of PSHB is beyond the topic of this thesis, and in the following chapters, the term "wavelength multiplexing" is regarded as simply another form of three dimensional storage, which takes advantage of the high angular and wavelength sensitivities of volume holograms.)

Several recording schemes have been investigated in the past two decades, as well as various storage materials, to take full advantage of holographic storage. Most holographic storage materials are static, non-erasable and non-recyclable. Memories recorded in such materials are read-only memories. The most promising materials, at present, for 3-D holographic storage, are photorefractive crystals. The phase type of hologram stored in a photorefractive crystal can give high diffraction efficiencies, and therefore, high storage capacities. The possibility of selective erasure of parts of the stored information may be added into the advantages of general holographic storage, by using photorefractive materials, so that the photorefractive holographic memory can be a write/read type, hence, random access memory. However, the dynamic and self-diffraction nature of photorefractive holograms causes complexities in the recording and readout processes [Kuk79, Hea84]. As a result, the performance of holograms stored in photorefractive materials needs to be investigated in-depth.

The high capacity of 3-D holographic storage has so far been demonstrated using a technique called block oriented holographic storage (BOHS), in which there is an array of spatially well separated hologram storage blocks. Within each block many holograms, containing many pages of high information content, are incoherently superimposed, each page being recorded as a Fourier transform (F. T.) hologram. The use of an array of hologram storage block sites is referred to as spatial multiplexing, whilst the incoherent superposition of many holograms in a given volume (block) is referred to as angular multiplexing. The total storage capacity of BOHS is simply the product of the number of hologram sites, the number of incoherent superimposed holograms in each site, and the number of bits per hologram. Both conventional BOHS memories and purely angularly multiplexed memories have given good results in terms of storage capacity [Red88, Mok93], although have given rather low efficiencies in the latter case. However, incorporating such a memory into a parallel correlation system, like HOFNET, needs complicated hardware, so that it is difficult to implement in a compact and efficient manner.

In this thesis, a new multiplexing scheme, "Spatio-Angular Multiplexing" (abbreviated to SAM) is proposed. Like BOHS, SAM is a 3-D multiplexing scheme which uses the entire volume of the recording medium. However, in contrast to the conventional BOHS scheme, SAM combines spatial multiplexing and angular multiplexing in a novel way, such that each hologram is partially overlapped in space by the adjacent ones, and can be distinguished from the others by a distinctly angled reference beam. There are no individual blocks in a SAM memory. The storage capacity of SAM is of the same order as that of BOHS, and is much higher than that for pure spatial or pure angular multiplexing. By reducing the degree of angular multiplexing, while increasing the degree of spatial multiplexing, the diffraction efficiency of SAM can be much higher than that obtained by pure angular multiplexing. As crystal growth technology advances, thick crystals with a large entrance size will be grown (4 cm x 4 cm x 1 cm are already possible for Fe:$LiNbO_3$), and SAM will benefit from this advance more than angular multiplexing. The most important aspect of SAM is the possibility that a 3-D memory could be straightforwardly incorporated into a system, such as a HOFNET, for parallel recall and correlation of all stored images with an arbitrary input image.

This thesis is mainly concerned with investigating the spatio-angular multiplexing (SAM) technique, and its implementation in photorefractive crystals. Although SAM is suitable for a specific neural network, HOFNET, a discussion of the theory and implementation of neural networks in depth is outside the topic of this thesis. The thesis concentrates on the evaluation of the storage capacity of photorefractive crystals using different multiplexing schemes, including SAM. The thesis also discusses the performance of photorefractive holograms and, in particular, the optimum readout angle for maximum diffraction efficiency, which we investigated through extensive numerical calculation and experiment.

This thesis is organised as follows. The background work is reviewed in Chapters Two and Three to aid the development of our new work in the subsequent chapters. In Chapter Two we describe the fundamentals of optical holography as related to page oriented holographic storage. This includes the main types of hologram referred to in this thesis, and also the various hologram multiplexing schemes. The physical mechanism of hologram formation and diffraction in photorefractive materials is then briefly introduced in Chapter Three. The properties required of photorefractive materials for holographic storage are also discussed in this chapter. The remaining chapters introduce our new research. Chapter Four describes our new experimental and numerical work, and gives some background to the performance of holographic gratings in photorefractive crystals. The "Bragg shift" (the difference between the optimum readout angle and the recording angle) is observed experimentally (and to our knowledge, for the first time), and a good agreement between experimental measurement and numerical calculation (based on well-established theory) is shown. In Chapter Five, we turn our attention to the limitations on the storage capacity for angularly multiplexed recording in photorefractives which is the main holographic competitor to SAM. The emphasis is on the crosstalk limitation which, through our own investigation, seems more serious if the reference points are arranged in two dimensions. The noise limit is also described, and in such a way that it is related to the finite index modulation range of the photorefractive material. The following chapters are devoted to our novel spatio-angular multiplexing scheme (SAM). In Chapter Six we propose the new SAM holographic storage scheme for use in a high order feedback neural network (HOFNET). The storage capacity and diffraction efficiency of SAM are investigated theoretically, and are compared with those obtained for other multiplexing schemes, illustrating the benefits of SAM. A preliminary calibration experiment on the storage of 756 high resolution patterns in a single Fe:$LiNbO_3$ crystal using SAM is described in detail in Chapter Seven. The experimental results are presented, and are critically analysed to assess our exposure model for SAM. Finally, in Chapter Eight, conclusions are given and possible future work is proposed.

CHAPTER TWO

OPTICAL HOLOGRAPHY

2.1 Introduction

Holography is a method of recording the complete wave field of an object (including both its intensity and phase information). In conventional photography a two-dimensional image of the object is formed, and its intensity distribution on the image plane is recorded in a photographic plate or film. In holography the amplitude (or its square, intensity) as well as the relative phase of the object wave are recorded as a hologram. No detectors or recording materials are sensitive to the relative phase distribution of a light wave. To record the phase information, the phase variation of the wave-field must be encoded appropriately into an intensity variation. Once the hologram is recorded it can be decoded, so as to reconstruct the complete wave field. In optical holography, both encoding (interference) and decoding (diffraction) techniques are optical.

With the aim of improving the resolution in images obtained with an electron microscope, Gabor solved the major problem in the invention of holography by encoding the relative phase into the interference fringe pattern (Gab48, Gab49, Gab51). Gabor's method required a subject with a large transparent area and small opaque areas. When the transparency was illuminated by an electron wave a strong transmitted background wave passed through to the recording plate. This background wave was coherent with the waves, scattered from the edges of the opaque areas, so that the interference pattern of the background wave with the scattered waves was recorded as a hologram (Fig. 2.1a). Although this attempt to improve the resolution of electron microscopy was unsuccessful, Gabor and other earlier holographers made progress in optical holography [Rog52, Loh56]: optical decoding (diffraction) of an optically recorded hologram reconstructed the exact wavefronts of the object wave. This early holographic work was referred to as "in-line holography" since the source and subject wave were placed on an optical axis which was normal to the photographic plate.

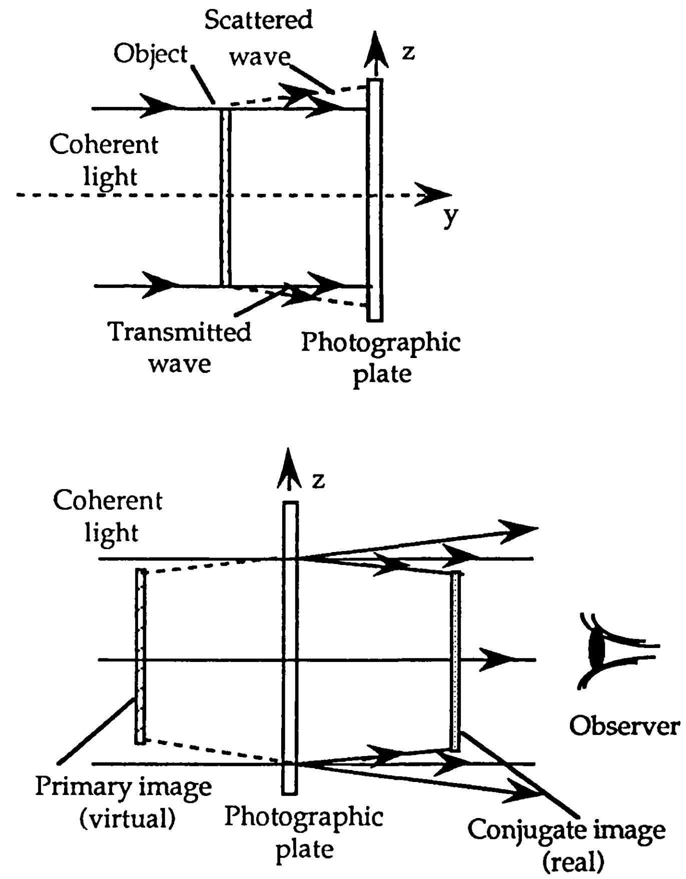

a Recording an in-line (Gabor) hologram

b Reconstruction of an image from an in-line (Gabor) hologram, showing the formation of twin images

Fig. 2.1 In-line (Gabor) holography

An "in-line" hologram looks like and behaves like a zone plate. The reconstructed image from an in-line hologram is always accompanied by an unwanted "twin image", or conjugate image, which comes from the other primary diffraction order of this type of hologram. There is also a strong zero order due to the directly transmitted replay beam (Fig. 2.1**b**). This twin-image problem hampered applications of optical holography until the mid-sixties when Leith and Upatnieks introduced the concept of a "spatial carrier frequency" into holography. They used a separate coherent background wave called the "reference beam". The reference wave impinged on the recording plate at some non-zero angle with respect to the object wave. The resultant hologram looked like and behaved like a diffraction grating so that the reconstructed image was separated from the unwanted twin image and the background wave by the grating diffraction [Lei62, Lei63, Lei64]. With the help of lasers (high power coherent light sources invented almost at the same time), they experimented with holograms of diffusing objects and 3-D objects using their "off-axis" geometry.

Meanwhile Denisyuk invented reflection holography using reference and object waves propagating in opposite directions (Den62, Den63, Den65). The resulting fine interference fringes created inside the emulsion were almost parallel to the plate surface with a spacing of the order of a half wavelength of light. Photographic emulsions with a 15μm thickness therefore contained about 30 such fringe planes. Since the third, or depth, dimension of the recording material as well as the lateral dimension contributed to the holographic operation, Denisyuk's holograms were also called "volume holograms". The progress in off-axis holography and volume, reflection holography during the sixties greatly stimulated interdisciplinary interest in optical holography. Since then holography has been receiving significant attention in the fields of display, interferometry, image processing, holographic optical elements, optical interconnection, and data storage.

There are different ways to classify holograms. They are divided into: i) amplitude or phase types by their effect on an incident light wave, i.e. providing amplitude or phase change or both; ii) plane (thin) or volume (thick) types by their thickness; iii) transmission or reflection types by the relative direction of the incident beam and the diffracted imaging beam; iv) Fresnel, Fourier transform or image type by the convergence of object and reference beams with respect to the hologram medium, etc.

We first discuss in Section 2.2 the basic concepts of holography and describe the main hologram types which are concerned with this work. In Section 2.3 the well known coupled-wave theory for analysis of volume holographic gratings is described. Holographic storage is introduced and a brief discussion of the storage capacity is given in Section 2.4. Finally, the most common recording materials are presented in Section 2.5.

2.2 Principles of Holography

In this section three types of hologram will be described. We have chosen off-axis Fresnel holography (with a plane reference wave) to explain the basic holographic process in Section 2.2.1, and we shall also discuss Fourier transform holography (Section 2.2.2) and volume holography (Section 2.2.3). These last two types of hologram are those most useful for holographic storage.

2.2.1 The off-axis Fresnel hologram with a plane reference wave

In off-axis Fresnel holography with a plane reference wave (Fig. 2.2), the object is a finite distance away from the hologram plate, so that the object wave distribution at the plate can be regarded as the Fresnel (or near-field) diffraction pattern of the object. Without loss of generality, we can choose the object to be on the system axis, y, and to have the incident plane as the x-y plane. Let $\mathcal{E}_s(x, z)$ and $\mathcal{E}_r$ be the amplitudes of the object (signal) and reference wave fields on the recording plane (x-z) respectively. The spatially varying components of the complex electric field, $E_s(x, z)$ and $E_r(x, z)$, may be written as

$$E_s(x, z) = \mathcal{E}_s(x,z)\exp(j\phi_s) \tag{2.1a}$$

$$E_r(x, z) = \mathcal{E}_r\exp(jkz\sin\theta_r) \tag{2.1b}$$

where *j* is the square root of -1, ϕ_s is the phase of the object wave (which is a function of x and z coordinates), θ_r is the offset angle of the reference wave with respect to the system axis, y, and k is the propagation constant of the light wave. Coherent superposition of the two wave fields yields an intensity distribution I(x, z):

$$\begin{aligned} I(x, z) &= (E_s+E_r)(E_s+E_r)^* \\ &= E_rE_r^*+E_sE_s^*+E_sE_r^*+E_rE_s^* \end{aligned} \tag{2.2}$$

where * indicates complex conjugation. Eq. 2.2 can be rewritten as

$$I(x,\ z) = E_r^2+E_s^2+2E_r\, E_s(x,\ z)\cos(\phi_s\text{-}kz\sin\theta_r) \tag{2.3}$$

or

$$I(x, z) = I_0[1+m\cos(\phi_s\text{-}kz\sin\theta_r)] \tag{2.4}$$

where $I_0= E_r^2+E_s^2$ is the total exposure intensity and $m=2E_rE_s/I_0$ is the visibility or modulation of the interference fringes. From Eq.(2.3) one can see both amplitude and phase of the object wave are encoded into the resultant intensity pattern.

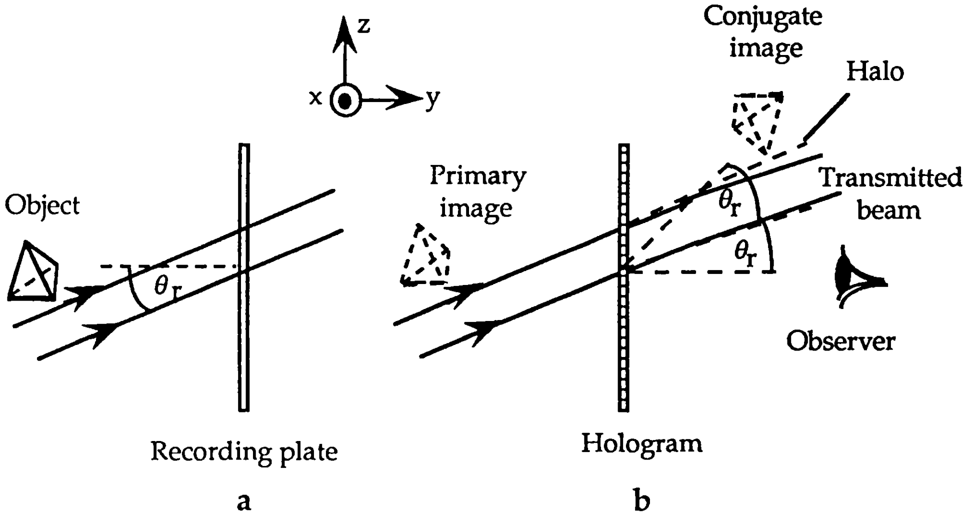

Fig. 2.2 Fresnel hologram: a recording and b reconstruction

In static holography the recording and readout are separated in time. A development process is usually necessary to make the "latent recording" readable. For thin holograms the development process normally yields an amplitude transmission function for the resultant hologram,T(x,z):

$$T(x,z) = \mathbf{F}\{I(x, z)\}$$

Depending on the material type the function $\mathbf{F}\{I(x, z)\}$ may be real (amplitude holograms) or imaginary (phase holograms) or complex. Also $\mathbf{F}\{I(x, z)\}$ may be a rather complicated function of the light intensity distribution. In any case, as long as the modulation depth m and the intensity I_0 in Eq.(2.4) are small enough, a linear approximation (for example, a Taylor expansion to the first two terms) is valid, and this leads to the following transmission function (for an amplitude hologram):

$$\begin{aligned} T(x, z) &= T_0 + \beta I(x, z) \\ &= T_0 + \beta (E_r E_r^* + E_s E_s^* + E_s E_r^* + E_r E_s^*) \end{aligned} \tag{2.5}$$

here T_0 is a constant background and β is the proportionality factor related to the material's parameters and the exposure time.

On readout, the common practice is to illuminate the hologram using a readout beam identical to the reference beam. The field distribution behind the hologram, E_i, can then be expressed as

$$\begin{aligned} E_i(x, z) &= E_r(x, z)T(x, z) \\ &= u_1 + u_2 + u_3 + u_4 \end{aligned} \tag{2.6}$$

where

$$\begin{aligned} u_1 &= (T_0+\beta E_r E_r^*)E_r = (T_0+\beta E_r^2)E_r \\ u_2 &= \beta E_s E_s^* E_r = \beta[E_s(x, z)]^2 E_r \\ u_3 &= \beta E_s E_r^* E_r = \beta E_r^2 E_s \\ u_4 &= \beta E_r E_s^* E_r = \beta E_r^2 E_s^* \, exp(2jkz\sin\theta_r) \end{aligned}$$

u_1 represents the directly transmitted readout beam, and u_2 represents a spatially varying halo around u_1 (since $E_s(x, z)$ is not spatially constant).

u_1 and u_2 are together termed the zero-order waves. u_3 is proportional to the original object wave, E_s, and is called the "primary image" beam. u_4 is proportional to the conjugate of the object beam and has a direction of propagation offset from the system axis by $2\theta_r$, and is called the "conjugate image" beam. These two beams, u_3 and u_4, are two first-order waves. It is clear from Fig. 2.2b that, by giving the reference beam an offset angle, θ_r, with respect to the object beam, the unwanted conjugate image and the zero-order background wave are spatially separated from the desired primary image, by angles of $2\theta_r$ and θ_r respectively.

2.2.2 The Fourier transform hologram

If the object is a two-dimensional pattern placed in the front focal plane of a converging lens and is illuminated by a plane wave, the field distribution in the recording plane which is located in the back focal plane of the lens, is the Fourier transform of the object [Goo68]:

$$\begin{aligned} E_s &= \text{F.T.}\{s(x_i, z_i)\} \\ &= S(\xi, \zeta) \end{aligned} \tag{2.7}$$

where F.T. indicates Fourier transformation, $s(x_i, z_i)$ is the object field distribution in the input plane (x_i, z_i), $S(\xi, \zeta)$ is its Fourier spectrum on the hologram plane. The spatial frequency coordinates ξ and ζ are related to the spatial coordinates x and z, in the back focal plane, by the following formula:

$$\xi = x/\lambda f, \quad \zeta = z/\lambda f \tag{2.8}$$

where λ is the wavelength of the light used and f is the focal length of the Fourier transform lens. Using an angled plane reference beam E_r to record $S(\xi, \zeta)$ (Fig.2.3a) we obtain a Fourier transform (F.T.) hologram. On replay using a readout beam identical to the reference beam E_r (Fig. 2.3b), the third term in Eq.(2.6) is proportional to $S(\xi, \zeta)$, which is further transformed by another F.T. lens into a spatially reversed image of the object [Goo68]:

$$U(x_o, z_o)=\text{F.T.}\ \{S\ (\xi, \zeta)\} = s\ (-x_i, -z_i)$$

where x_o, z_o are coordinates in the output plane. It is worth noting that the same arguments (ξ, ζ) can be used to specify the spatial frequency components of the object and its image (angular spectrum) [Goo68]. From Eq.(2.8) we can see that, in a practical optical system, an object with reasonably high resolution (ten line pairs per millimetre for example) will occupy a small area of only a few millimetres in the F.T. hologram plane. This feature is particularly useful for holographic storage.

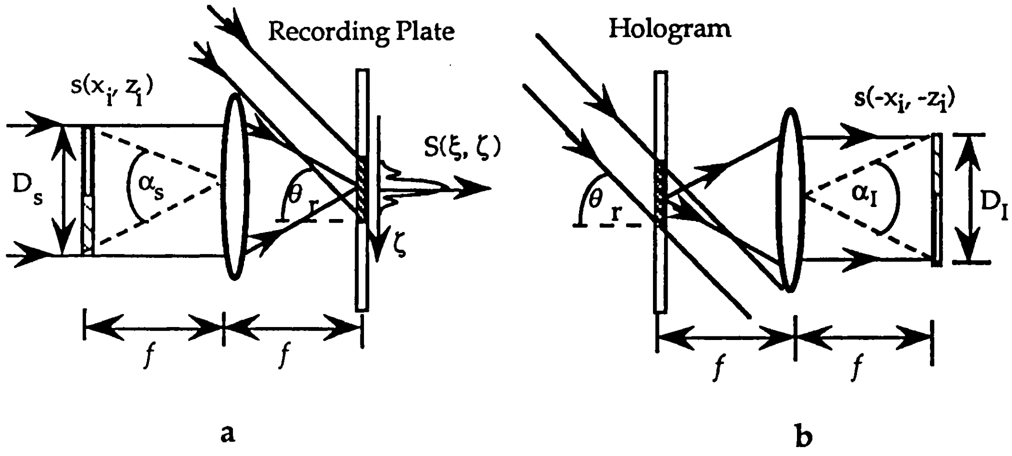

Fig. 2.3 Fourier transform hologram **a** recording, and **b** reconstruction

We have so far discussed only plane or thin holograms, which can be treated as infinitely thin layers, altering the amplitude (and/or phase) of an incident readout beam (through the two-dimensional amplitude transmission function, T(x, z)), to give reconstructed images. Even under a linear approximation, the reconstructed wave field consists of a zero-order beam and a conjugate image in addition to the desired primary image. The diffraction efficiency, which is defined as the ratio of the power diffracted into the reconstructed (primary) image beam to the power of the incident readout beam, cannot be very high. The theoretical upper limit to the diffraction efficiency of linear plane holograms is 6.25% (for amplitude types) and 33.8% (for phase types) [Ram72]. Volume holograms overcome this problem and significantly extend the applications of holography.

2.2.3 Volume Holograms

When the recording material becomes thick, the interference between the two waves creates a series of interference surfaces inside the material instead of fringes on the material surface. Provided the hologram media is not exclusively for the manufacture of surface-relief holograms (e. g. some photoresists, photoplastics, etc.), a volume hologram may result which can be regarded as a three dimensional grating (see Fig. 2.4). As is well known from x-ray diffraction by crystals, diffraction by a three-dimensional grating is subject to the Bragg condition,

$$2\Lambda \sin\theta = \lambda \tag{2.9}$$

here θ is the incident Bragg angle with respect to the grating plane and Λ is the spacing between grating planes.

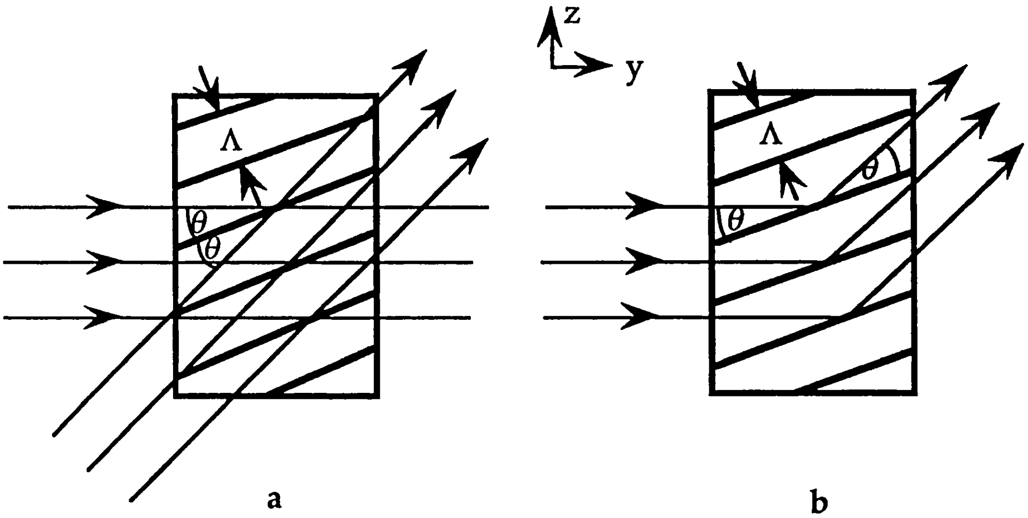

Fig. 2.4 **a**: Formation of a volume hologram, **b** diffraction by a volume hologram

One advantage of volume holograms is their ability to suppress unwanted diffraction orders. This ability depends not only on the recording material's thickness, but also upon the grating spacing and Bragg angle. Klein [Kle66] introduced a parameter, Q, given by

$$Q = 2\pi\lambda_a d / n\Lambda^2 \tag{2.10}$$

which is used as a criterion for distinguishing between thin and volume holograms. Here λ_a is the wavelength in air, d is the hologram thickness, and n is the refractive index of the material. Using Eq. (2.9), Eq. (2.10) can be rewritten:

$$Q = 4\pi\, d \sin\theta / \Lambda$$

which means that, if the Bragg angle, θ, is too small, the hologram may not act as a volume grating, even though the ratio d/Λ is fairly large. It has been noted by Klein, that if a hologram has $Q>7$ it acts as a true volume hologram, being capable of over 95% holographic efficiency (for a phase type). If $Q<3$ the reconstructed twin (conjugate) image is at least half as bright as the desired image, and the hologram is regarded as a thin hologram [Ram72].

In most practical cases of volume holography, $Q>>10$ and the replay is at or near the Bragg angle, so that there is only one significant diffraction order (which obeys, or only slightly violates, the Bragg condition). The k-vector diagram is useful for the analysis of these cases, as shown in Fig. 2.5, in which the k's are wave vectors inside the medium (all with length k, equal to the propagation constant, $2\pi/\lambda$, if the medium is homogeneous and isotropic), and K is the grating vector, which is in the direction of the normal to the grating planes and has a length, K, given by

$$K = 2\pi/\Lambda. \tag{2.11}$$

From Fig.2.5a the grating vector, K, can be expressed as:

$$K = k_1 - k_2$$

and the length of K can be easily calculated (see Fig.2.5a) to be:

$$K = 2k\sin[(\theta_1+\theta_2)/2] \tag{2.12}$$

The Bragg condition for replay, by a readout beam with wave vector k_r, may be written

$$k_s = k_r - K$$

where k_s is the wave vector of the diffracted beam. If the readout wavelength is the same as that used for recording (see Fig. 2.5**b**), this condition requires that either $k_r=k_1$, or $k_r=k_2$. Any angular deviation of the readout beam angle from the Bragg angle, $\Delta\theta$, will cause a phase mismatch, δ (not shown in the figure).

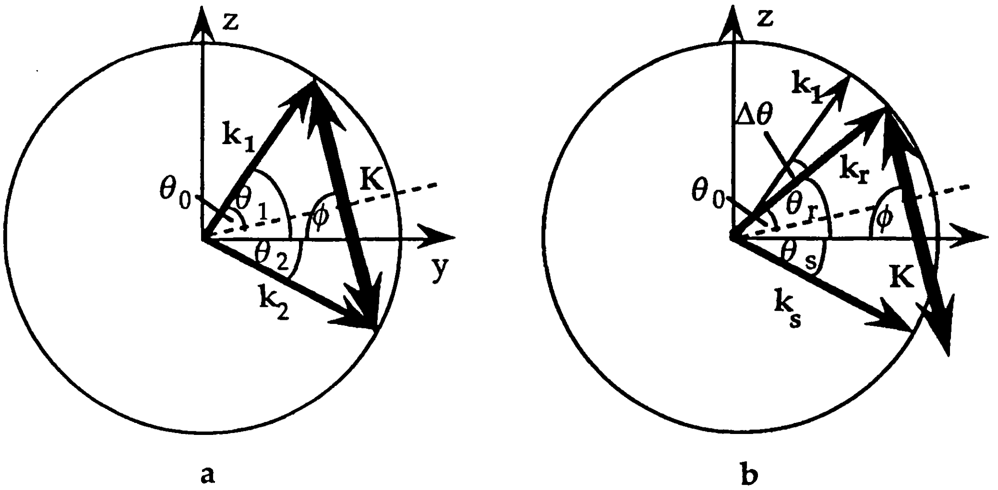

Fig. 2.5 The k-vector diagram for a volume grating a: formation, and b: replay. A grating, K, is written by two beams with wave vectors k_1 and k_2 (incident at angles of θ_1 and θ_2 with respect to the y-axis, which is the normal to the recording medium). $\theta_0=(\theta_1+\theta_2)/2$ is the Bragg angle, and ϕ is the grating slant angle. The Bragg condition for readout of the recorded grating, is that $k_s=k_r-K$. An off-Bragg readout is shown in **b** above.

Any angular and/or wavelength variation which breaks the Bragg condition will lead to a sharp decrease in diffraction efficiency. Therefore, volume holograms feature high angular and wavelength selectivity, and this makes it difficult to obtain the maximum diffraction efficiency. On the other hand, high angular (and wavelength) selectivity allows many holograms to be multiplexed within the same volume, by using reference beams incident at different angles (or by using light at different wavelengths). This is particularly favourable for holographic storage. In the next section we shall discuss the diffraction efficiency and angular selectivity of volume holograms using the coupled-wave theory.

2.3 Coupled-wave theory

The coupled-wave theory for volume gratings, which was first introduced to holography by Kogelnik, is a versatile model in the analysis of the diffraction behavior of volume holographic gratings. It has been widely adopted for the prediction of diffraction efficiencies and angular selectivity in various volume gratings. Here we shall give only a brief description of this analysis, the discussion being based on the well-known paper of Kogelnik [Kog69]. The main assumptions of this analysis are that:

1. Gratings are formed with plane waves of uniform amplitude, and are replayed by plane waves.
2. The spatial modulation of the refractive index and the absorption constant is sinusoidal.
3. Light is incident at or near the Bragg angle, so that only two significant beams (the incident beam and one diffracted beam) are present in the medium. All other diffraction orders are neglected.
4. The complex amplitude variation of the waves is small on a scale comparable to the wavelength of light, so that the second derivatives of the wave amplitudes can also be neglected.

Using the same coordinate system as that used in Section 2.2, the incident plane is (y-z) and the fringe planes are perpendicular to the (y-z) plane. On the above assumptions a set of coupled-wave equations, derived from Maxwell's wave equations, are given by Kogelnik [Kog69] as follows (in our notation):

$$\frac{dE_r}{dy} + \frac{\alpha}{\cos\theta_r} E_r = -j\frac{\kappa}{\cos\theta_r} E_s \tag{2.13a}$$

$$\frac{dE_s}{dy} + \frac{\alpha + j\delta}{\cos\theta_s} E_s = -j\frac{\kappa}{\cos\theta_s} E_r \tag{2.13b}$$

where E_r and E_s are the field amplitudes of the incident beam and the diffracted beam respectively, α is the absorption constant, θ_r is the incident angle, θ_s is the angle of the diffracted beam, and κ is the coupling constant given as

$$\kappa = \pi\Delta n/\lambda - j\Delta\alpha/2 \tag{2.14}$$

where Δn and $\Delta\alpha$ are the spatial modulations of the refractive index and absorption respectively. The phase mismatch, δ, in Eq.(2.13) due to any small angular deviation, $\Delta\theta$, from the Bragg angle, θ_0, and any wavelength deviation, $\Delta\lambda$, from the correct wavelength, λ_0, is defined as:

$$\delta = \Delta\theta\, K \sin(\phi - \theta_0) - \Delta\lambda\, K^2/4\pi n \tag{2.15}$$

where n is the refractive index of the material and ϕ is the grating slant angle (see Fig. 2.5b). Under the boundary conditions determined by the hologram type (either transmissive or reflective), Eq.(2.13) can be solved analytically, for various volume gratings, to give the value of the diffracted wave amplitude E_s. Then the diffraction efficiency can be calculated using the formula

$$\eta = (\cos\theta_s/\cos\theta_r)\, E_s E_s^* \tag{2.16}$$

where an incident wave with unit amplitude is assumed. The simplest case, and that most commonly used, corresponds to lossless transmission volume phase gratings, for which the diffraction efficiency can be written as:

$$\eta = \frac{\sin^2\left(v^2+\xi^2\right)^{\frac{1}{2}}}{1+\left(\frac{\xi}{v}\right)^2} \tag{2.17}$$

where the parameter ξ, (indicating the phase mismatch for angular deviation only) is:

$$\xi = \Delta\theta \ \mathrm{K\,d}\sin(\phi - \theta_0) \ / 2\cos\theta_s \tag{2.18}$$

v, indicating grating strength, is given by:

$$v = \pi \Delta \mathrm{n\,d} / \lambda \, (\cos\theta_r \cos\theta_s)^{\frac{1}{2}} \tag{2.19}$$

The diffraction efficiency obtained when read out at the Bragg angle (ξ=0) is

$$\eta_0 = \sin^2 v \tag{2.20}$$

Typical curves for η (plotted as a function of ξ, with a parameter v) are shown in Fig. 2.6, and were calculated using Eq.(2.17). From Fig. 2.6 it can be seen that, as v increases, η_0 oscillates, and the selective angle (usually specified by the full angular width of the main lobe), is slightly narrowed, whilst the side lobe intensity increases significantly. Equations (2.17)-(2.20), and the angular response curve, are widely used to assess the diffraction efficiency and angular selectivity of volume gratings.

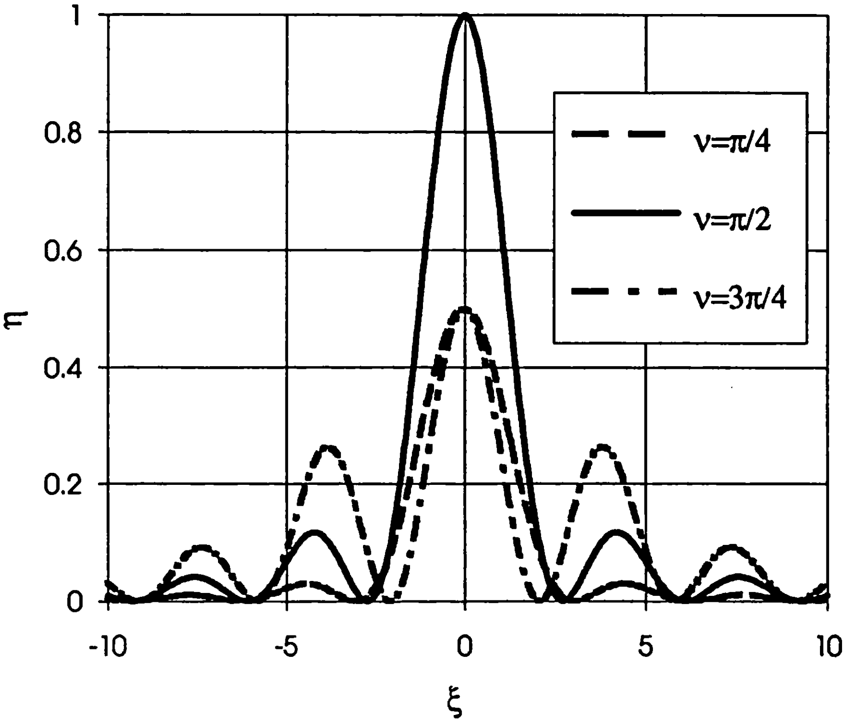

Fig. 2.6 The diffraction efficiency, η, of a lossless transmission grating (as a function of the off-Bragg parameter, ξ), for three values of v.

2.4 Holographic Storage

2.4.1 Basic concepts of holographic storage

The holographic storage of information in compact media has been an exciting prospect from the earliest days of holography. This is due mostly to a predicted theoretical storage capacity of $\sim V/\lambda^3$ bits in a volume V [vdH63], or 8×10^{12} bits in a 1 cm^3 volume at λ=0.5 μm, which applies to all types of optical storage as an upper limit of storage capacity.

Page oriented holographic storage

Although a hologram is capable of storing and retrieving three-dimensional information, the most commonly considered form of information is two-dimensional, such as a geometric array of dots, i.e. an information page. Information in this form with a bright dot at a location representing a logical 1 and its absence in the same location representing logical 0, is well suited for computer applications and for a quantitative comparison of the storage capacity of different holographic media [Ram72].

Channel capacity

From an information theory perspective, a hologram is a communication channel. Its storage capacity, C (channel capacity), can be described, based on the Shannon Limit [Ram72], by:

$$\mathrm{C} = \mathrm{N}\log_2\sqrt{1+\left(\frac{S}{N}\right)^2} \qquad (2.21)$$

where N is the number of independent samples (pixels) stored in the hologram and S/N[1] is the detected signal to noise ratio (SNR). The logarithmic term in equation (2.21) quantizes the number of grey levels that can be distinguished for each stored pixel [Jon61, Yu73]. The channel capacity increases with the number of stored pixels and the SNR obtained.

---

[1] Note italic *N* is use to denote noise as opposite to N for number of pixels

Alternatively, if the channel capacity is fixed, the number of stored pixels must be reduced if an increase in SNR is desired. The channel capacity of a holographic storage medium can be referred to as its space-bandwidth-product (SBP) [Smi69]. For materials having a very high spatial resolution, C has an upper-limit of V/λ^3 (A/λ^2 for 2-D materials with material area A), as mentioned above.

It has been proved by Ramberg that to record a pattern (of prescribed information content) on a plane hologram requires approximately eight times the surface area as that required for direct photographic recording. (This assumes that the storage materials for these two approaches have the same SBP, and that this SBP is fully utilised.) [Ram72]. This is because, in the holographic case, the spatial carrier frequency must be recorded, and this takes up some of the available SBP [DeV79]. Thus, holographic storage in plane holograms has no advantage over direct photography, in terms of the storage capacity. However, holographic storage (and, in particular F.T. holography) offers a high information redundancy [Fir72], due to the non-local distribution of information. This has the result that local defects in the system will not cause information loss, only loss of SNR. Furthermore, a F.T. hologram array offers the possibility of all the array elements being recalled and processed in parallel [Mao91]. These two factors give even 2-D holographic storage great potential. For page-oriented dense holographic storage, a 2-D Fourier transform hologram array (which stores information pages at different locations in the hologram), has been investigated for mass storage of the book information library in China [Yua91]. 3-D volume holograms have even higher storage capabilities, since many pages can be multiplexed at a single location. In the following subsections we briefly discuss the holographic storage capacity and its limitations for different multiplexing schemes.

2.4.2. Multiple storage: Spatial multiplexing

Fourier transform holography, as already mentioned in Section 2.2, is widely accepted as an information storage method since a large storage density can be achieved. The main part of the Fourier transform of a relatively large information page occupies a relatively small area in the F.T. plane (hologram plane). For a given F.T. lens, the minimum size of a F.T. hologram depends on the minimum pixel size to be resolved on reconstruction no matter how many pixels are contained in the page. This allows different pages to be stored in well-separated locations of the recording material without aliasing between them. This is referred to as spatial multiplexing. A schematic diagram of spatially multiplexed F.T. holograms is shown in Fig. 2.7.

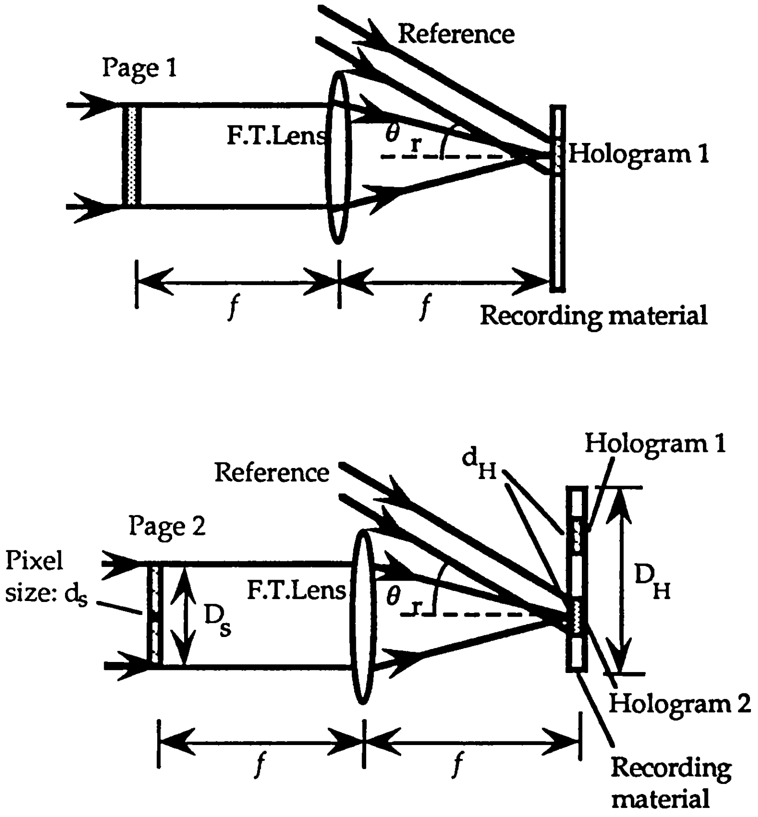

Fig. 2.7 Spatial multiplexing of F. T. holograms

In spatial multiplexing the storage density, S_D, is determined by the product of the number of array elements (i.e. information pages to be stored) and the number of pixels on every page. For example, Solymar and Cooke [Sol81] estimated the storage density based on the pixel size in the image output plane. If the maximum pixel size in the image is d_I (given by the detector resolution), the minimum hologram size, d_H, acting as a diffraction aperture, is determined by [Sol81]:

$$d_I = 2D\lambda / d_H$$

here the factor 2 is rather arbitrary, and depends upon the definition of resolution. D is the distance between the memory plane and the image plane. (In the case of F. T. holograms, D is replaced by the focal length of the F. T. lens.) A "memory filling factor", F, is defined as [Sol81]:

$$F = \sqrt{M_s}\frac{d_H}{D_H} \tag{2.22}$$

where M_s is the number of spatially multiplexed holograms and D_H is the dimension of the whole recording material. Thus, the total number of pixels which can be stored in the image is:

$$C_H = M_s\left(\frac{D_I}{d_I}\right)^2 = F^2\frac{D_H{}^2 D_I{}^2}{4\lambda^2 D^2}$$

where D_I is the image dimension. The storage density can be written

$$S_D = \frac{F^2}{4}\frac{\alpha_I{}^2}{\lambda^2} \tag{2.23}$$

where $\alpha_I = D_I / D$ is the angle of the imaging beam from a point on the memory plane, see Fig. 2.3b.

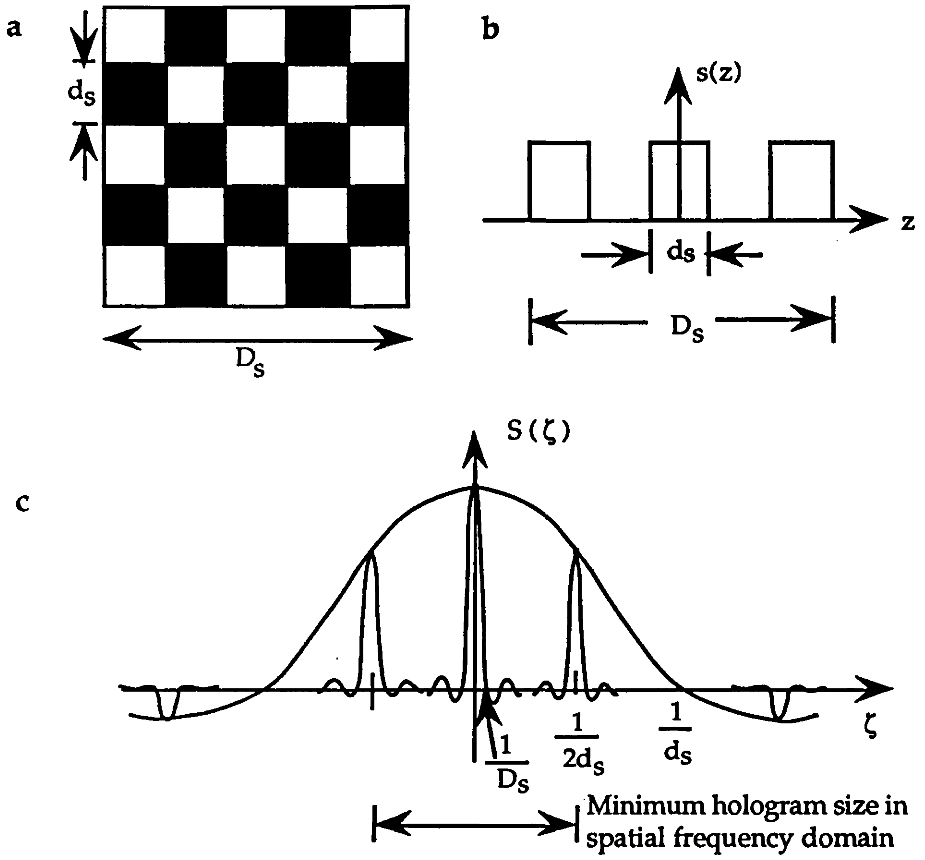

Fig. 2.8 Schematic diagram showing **a** a binary data page, **b** its amplitude transmission function, and **c** its Fourier spectrum on the hologram plane (one-dimensional).

Alternatively, we can start with the minimum hologram size required to record a page with a given resolution. Referring to Fig. 2.8, if the object page dimension is D_s with the pixel dimension d_s, the number of pixels in one page, M_p, is then $(D_s/d_s)^2$ and the fundamental spatial frequency of the object is $1/2d_s$. To record this frequency component, the hologram size, d_H, must be not smaller than $2\lambda f(1/2d_s)$. Using the definition of the filling factor F given above by Eq.(2.22), the total number of pixels that can be stored, $C_H=M_sM_p$, is

$$C_H = F^2 \frac{D_H^2}{\lambda^2}\left(\frac{D_s}{f}\right)^2 \tag{2.24}$$

and the storage density can be written

$$S_D = F^2 \frac{\alpha_s^2}{\lambda^2} \tag{2.25}$$

here $\alpha_s=D_s/f$ is the angle of the object from a point on the lens plane. For a system with unit magnification (shown in Fig. 2.3) α_s and α_I are identical, thus expression (2.25) differs from (2.23) by only a constant factor. This is because of different resolution criteria chosen for the derivation. At the storage density determined by (2.25) only the fundamental spatial frequency can be recorded, and the resultant image definition will be very poor. Because of the limitations of optical components, the finite numerical aperture of optics in particular, it is not possible to increase the storage density by simply increasing the number of pixels in the object plane, i.e. increasing α_s. $F=\alpha_s=1$ specifies the condition under which the theoretical upper limit for 2-D storage, A/λ^2, will be obtained. For a realistic system the storage density is about 10^7 bits/cm^2 with parameters $F=0.8$, $\lambda=514.5$nm and $\alpha_s=0.2$. Conventional spatial multiplexing ($M_s>1$, $F\leq1$) does not increase the maximum storage density (since the maximum value of F is unity), although near full capacity may be realised when $d_H \ll D_H$, i.e. the material size is relatively large while the pixel size in each page is not very small. All real materials have a finite thickness, and when we consider also the thickness of the substrate, a total storage capacity of 10^{10} bits requires the material to have a thickness of 10μm, and a total area of 0.1m^2, this is about three orders of magnitude lower than the upper limit given by V/λ^3.

2.4.3 Multiple storage: Angular multiplexing

The high angular selectivity of volume holograms allows different pages to be stored in a common volume of the recording material and these can be distinguished by altering the reference beam angle for each of the holograms. This is referred to as angular multiplexing (Fig.2.9).

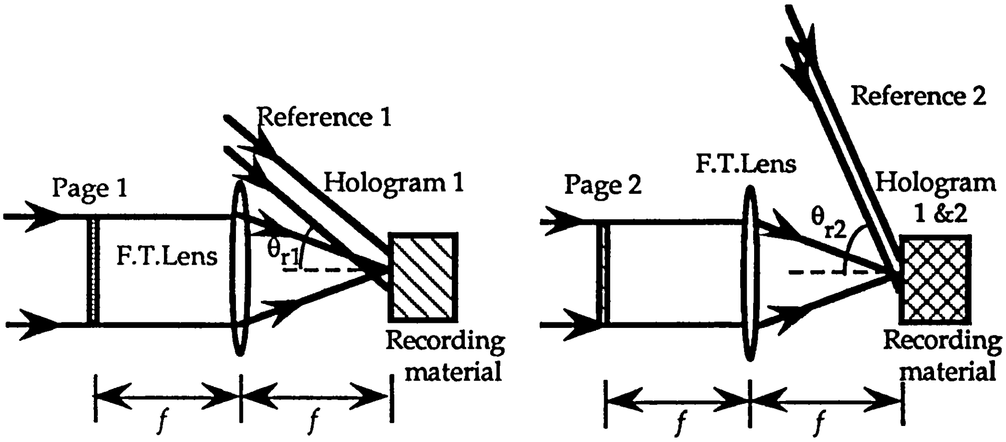

Fig. 2.9 Angular multiplexing of F. T. holograms

The storage capacity for angular multiplexing, given in terms of bits, can be expressed as the product of the number of pixels stored in each hologram (page), M_p, times the number of holograms superimposed in a given volume using angular multiplexing, M_{ang}. We refer to M_{ang} as the degree of angular multiplexing. The maximum degree of angular multiplexing for a recording medium with thickness, d, depends on the material type, the recording configuration and the required SNR. Crosstalk is a major source of noise in angular multiplexing. With careful adjustment in the angular separation between reference beam angles for different holograms, the crosstalk noise can be minimised as a result of the angular selectivity of volume holograms. The coupled-wave theory, described in Section 2.3, can be used to calculate the angular selectivity, and, therefore, the maximum degree of angular multiplexing. We can now calculate the degree of angular multiplexing, M_{ang}, for an unslanted, lossless, transmission grating. According to the theory, the normalised diffraction efficiency, η/η_o, is given by (see Eq. 2.17):

$$\frac{\eta}{\eta_o} = \frac{1}{\eta_o} \cdot \frac{\sin^2\left(\nu^2 + \xi^2\right)^{\frac{1}{2}}}{1 + \left(\frac{\xi}{\nu}\right)^2} \tag{2.26}$$

where η_o is the diffraction efficiency at the Bragg angle. The parameter ξ in Eq. (2.26) can be rewritten as

$$\xi = \Delta\theta \cdot \frac{\pi \, n \sin 2\Phi}{\lambda \cos\theta_s} \cdot d \tag{2.27}$$

where $2\Phi = \theta_r - \theta_S$ is the recording interbeam angle, n and d are the refractive index and the thickness of the material respectively. The expression for the parameter, ν, remains that given in Eq. (2.19).

The acceptable level of cross-talk determines the selective angle (the minimum angular separation of the reference beams between adjacent recordings), and this level varies with different applications. The experimental 10dB angular width of the η/η_o vs $\Delta\theta$ curve is good enough to be accepted for a small number of angularly multiplexed holograms [Tao91]. However, for simplicity, we define $\Delta\Theta$, the full width of the main lobe of the η/η_o vs $\Delta\theta$ curve, as the selective angle in estimating the storage capacity. For $\nu \ll \pi$, $\Delta\Theta$ is given as (through $\xi = \pm\pi$ in equation 2.27)

$$\Delta\Theta = \frac{2\,\lambda \cos\theta_s}{n \, d \sin 2\Phi} \tag{2.28}$$

For a symmetrical recording geometry, $\theta_S=-\theta_r$, so that $\Delta\Theta$ can be further simplified to be:

$$\Delta\Theta = \frac{\lambda}{\mathrm{n\,d}\sin\theta_r} \tag{2.29}$$

where θ_r indicates the reference beam angle inside the material. For every θ_r within the range of 0 to $\pi/2$, there is an object beam angle, θ_S ($\theta_S=-\theta_r$) within the range 0 to $-\pi/2$. Integrating $\frac{d\theta_r}{d\Theta}$ over the range 0 to $\pi/2$ gives the total number of the reference beam angles possible, each angle corresponding to one unslanted grating. Therefore we have:

$$M_{a,u} = \int_0^{\frac{\pi}{2}} \frac{\mathrm{n\,d}\sin\theta_r}{\lambda} d\theta_r$$

$$= \frac{\mathrm{n\,d}}{\lambda} \tag{2.30}$$

This result (2.30) is similar to the number of independent wavelengths (quoted by van Heerden [vHe63]) that can be stored in a material with thickness d. The similarity arises from the fact that a set of unslanted gratings can be formed by fixing the symmetrical geometry, and changing the recording wavelengths between gratings, see Fig. 2.10.

Note that the above result (Eq. 2.30) is based on the assumption that $\nu<<\pi$, and so Eq. (2.28) is valid. However, when this condition applies, crosstalk cannot be neglected. We will discuss this, and other limitations on the storage capacity of angular multiplexing, in detail, in Chapter Five. The storage capacity, in terms of the number of holograms that can be stored, as given by Eq. (2.30), can be regarded as a diffraction limited value, as no other limitations have been considered.

In the rest of this subsection we briefly describe some variations of angular multiplexing for volume holographic storage.

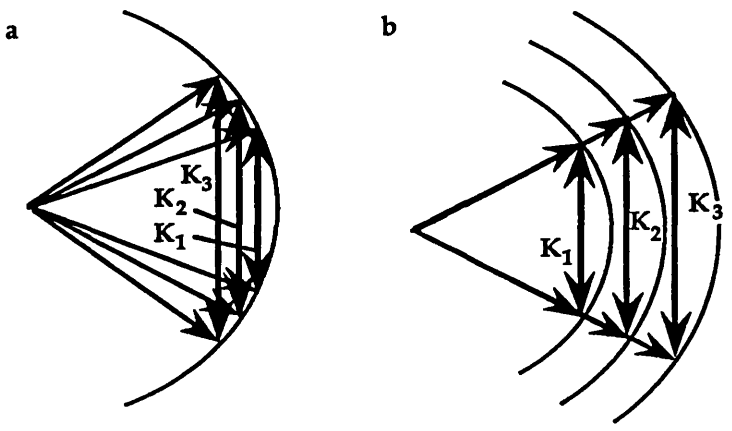

Fig. 2.10 A set of gratings, K_1, K_2 and K_3, formed by a angular multiplexing, and **b** wavelength multiplexing.

Deterministic binary phase encoding multiplexing technology

Traditional angular multiplexing is a kind of linear phase encoding in which the phase of the *n*th reference wave is encoded as $kz\sin\theta_n$ with θ_n being the *n*th reference beam angle. Sequentially changing the reference beam angles requires either mechanical equipment with high reliability and repeatability [d'A74, Ste75, Kur77, Tao91] or some other energy consuming methods (such as an intensity spatial light modulator [Man90]) to define the various incident directions. To overcome these problems several phase encoding techniques have been proposed [And87; Tak91; Den92]. Among them deterministic phase encoding seems to be promising. In this method each image is stored with N pure and deterministic binary reference beams, each beam is phase-modulated through a pixel of a binary spatial phase modulator. Each set of adjustable phases for these reference beams represents the address of one of the N stored images and is orthogonal to all other addresses. This orthogonality provides discrimination between the desired image and all other images because the reconstructions of the undesired images interfere destructively to produce zero intensity. It is claimed that this phase-encoding technique permits noiseless reconstruction, lower energy consumption and easy, and fast image retrieval with a high storage capacity. The theoretical capacity of the phase-encoding technique is claimed to be the same as for other angular multiplexing technique. In practice, the capacity is limited by the imperfections of available optical components [Den92].

Multiple storage: wavelength multiplexing

Van Heerden stated in his well known paper of 1963 [vHe63] that the information storage in a volume could be regarded as a number of independent wavelengths stored in a solid of thickness d. Since the number of separately resolved wavelengths is given by $\sim d/\lambda_0$, where λ_0 is the average wavelength, he arrived for the first time at the conclusion that the holographic storage capacity is $\sim V/\lambda^3$. From Kogelnik's theory [Kog69] the phase mismatch caused by the readout angular deviation from the Bragg angle, can be compensated by the phase mismatch caused by the readout wavelength deviation from that used for recording, according to Eq. (2.15). This means that simultaneous changes in angle and in wavelength of the readout beam may address the same grating. Angular multiplexing uses the whole of the available K-space (the volume of the material) by altering the directions of **k** whilst remaining k constant (see Fig. 2.10a). From this point of view wavelength multiplexing uses K-space by altering the lengths of k whilst keeping the direction of **k** unchanged (see Fig.2.10b), so that both angular and wavelength multiplexing should give approximately the same storage capacity.

Recently, Rakuijic et al [Rak92] reported an orthogonal wavelength multiplexing scheme, based on the recording of holograms by interference between counterpropagating reference and object waves with a single propagation axis. Successive pages were recorded and reconstructed using wavelength multiplexing. The term "orthogonal" means that the wave vectors of the readout beams are perpendicular to the loci of the end points of the grating vectors (K, see Fig. 2.11). Rakuijic et al claimed that, using this scheme, the crosstalk between holograms did not increase with added spatial information (unlike the case of angular multiplexing), and so a higher storage capacity in bits could be achieved.

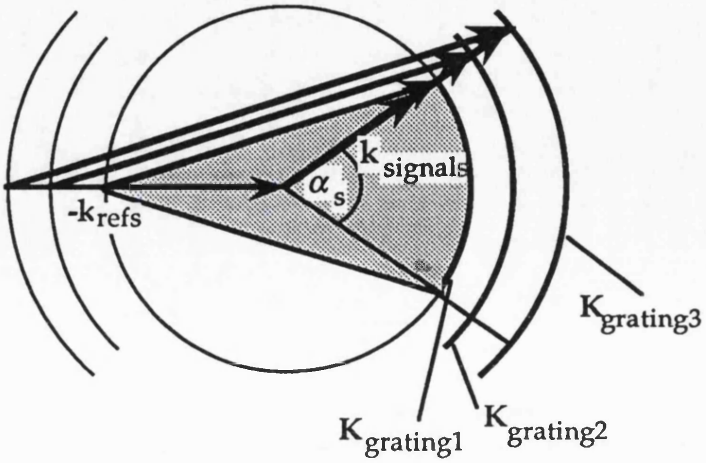

Fig. 2.11 Orthogonal wavelength multiplexing. $\mathbf{k}_{refs}$ and $\mathbf{k}_{signals}$ indicate wave vectors for all reference waves (which have the same direction, but different lengths) and signal waves (again, with similar directions, and different lengths). The $\mathbf{K}_{grating}$s indicate the loci of the end points of the resulting grating vectors.

2.4.4 Three-dimensional storage: block oriented holographic storage (BOHS)

Three-dimensional (3-D) holographic storage was proposed in the early seventies to take full advantage of the high capacity of volume holographic materials and the high information content and low cross-talk of F.T. holograms [d'A74]. The data pages are superimposed in well-spaced blocks using angular multiplexing, so we call this multiplexing block oriented holographic storage (BOHS). The memory contains M_s spatially separated block locations, each with M_{ang} angularly multiplexed holograms. If each hologram stores a page containing M_p pixels, the storage capacity is $M_s \cdot M_{ang} \cdot M_p$.

An experimental holographic read-write memory system using BOHS, which consisted of a well-spaced 5x5 array of photorefractive $LiNbO_3$

crystals with 10 information pages superimposed holographically within each crystal, was demonstrated by d'Auria et al in 1974 [d'A74]. Further designs of BOHS systems have been presented by Gaylord [Gay79]. Moreover, Redfield and Hesselink [Red88] reported a working device, called Bobcat, which had a measured total capacity of 1 G bits (1000 blocks with 10 pages per block and 99K bits per page were stored in a photorefractive strontium barium niobate (SBN) crystal). Recently, Hesselink and Wilde [Hes91] reported a novel optical architecture, involving an array of SBN fibers, which allowed access times 2-3 orders of magnitude less than those for conventional magnetic data storage devices.

2.5 Storage materials

The development of holography depends on holographic recording materials. One limitation to the applications of holography is the lack of perfect recording materials. Every advance made in the development of recording materials has aroused interest in and enthusiasm for the research and development of holography. In Table 2.1 the main types of available materials for volume recording are listed. Materials whose recording mechanism involves latent image formation during recording, so that the high diffraction efficiency only appears after development, are used for static holography. For the past years the most important and widely used are silver halide photographic emulsions. Holograms recorded in bleached silver halide can be regarded as volume phase holograms giving high efficiency and fidelity. Hardened dichromated gelatin (DCG) can also produce the same (even better) features, but its short persistence and "preparation before use" limits its applications. Although high density 2-D storage (F.T. hologram arrays) have been implemented in silver halide, both silver halide and DCG have a typical thickness of tens of micrometres. It is difficult to obtain the large degree of angular multiplexing required for dense volume holographic storage in such thin layers.

The most promising materials for dense 3-D holographic storage are the much thicker materials listed in Table 2.1, especially the photorefractive crystals. They have typical thicknesses of several millimetres in which a grating formed may have an angular width of a few hundredths of a degree, so that a large number of holograms can be formed in it (without observable cross-talk) by angularly multiplexing. Some of them, iron doped lithium niobate (Fe:$LiNbO_3$) and bismuth silicon oxide (BSO) for example, can be grown to a large size with a good optical quality, so that many locations in it can be used for spatial multiplexing. They are recyclable, the data-base stored in them can be easily erased and refreshed. This offers the possibility of dynamic read-write-erase memories and real-time data processing. Due to their dynamic nature the holographic process in photorefractive materials is more complicated than in static materials. In the next chapter we discuss the principle photorefractive effects.

Table 2.1 Outline characteristics of volume recording materials [Sol81]

	Processing	Latent image formation	Form of stored grating	Recyclable	Exposure requirement (J/cm^{-2})	Typical thickness	Recording wavelength range available	Resolution line mm^{-1} (nominal)
Silver halide emulsions	Wet chemical	Yes	Amplitude/ phase	No	10^{-6}-10^{-3}	6-16μm	UV. visible	>4000 (>5000 in USSR)
Hardened dichromated gelatin	Wet chemical	Yes	Phase	No	$3x10^{-3}$-$4x10^{-1}$ at 441-514nm	1-15μm	UV to green, but can be sensitized for red	>5000
Photopolymers	None/ post-exposure/ post-heating	No	Phase	No	10^{-3}-10^{2}	5μm-2mm	Mostly UV to blue/ green	3000-5000
Photochromics and photodichroics	None	No	Amplitude/ phase/mixed	Yes	$3x10^{-3}$-1(low efficiency)	0.1-2mm	UV, visible	>2000
Photorefractive crystals	None (fixing by heating)	No	Phase	Yes	10^{-3}-1 (for 1% efficiency)	10μm-1cm	UV, visible	>1500

CHAPTER THREE

THE PHYSICS OF HOLOGRAPHIC RECORDING IN PHOTOREFRACTIVE CRYSTALS

3.1 Introduction

In this chapter we describe the basic physics of holographic grating formation in photorefractive crystals, and look at some of the properties of the recorded gratings.

The photorefractive effect can be defined as a change in the refractive index of a material that is proportional to the intensity pattern of the light incident upon it [Yar89]. In 1966 it was discovered that an intense blue or green laser beam could cause a change in the refractive index of $LiNbO_3$ or $LiTaO_3$ crystals [Ash66]. Later it was found that this "laser damage effect", (unlike the catastrophic damage caused by a much higher light intensity,) could be reversed by heat or uniform illumination of the crystal. The origin of these reversible light-induced refractive index changes, was found to be in a combination of photosensitivity and the electro-optic effect. The overall process is now referred to as the *photorefractive effect* by analogy with the *photochromic effect* which describes light induced absorption changes.

Two years after the discovery of the photorefractive effect Chen et al performed the first holographic experiment with $LiNbO_3$ crystals, proposing the possibility of using photorefractive materials for holographic storage [Che68]. The information stored in photorefractive materials may be erased by exposure to a uniform light of appropriate wavelength, or may be fixed by several methods [Her86, Ari89]. This flexibility is the prime advantage of photorefractive materials, and offers potential applications in read-only or read-write memories. In addition, high diffraction efficiency (owing to the volume phase type of holograms stored in them), high storage capacity (owing to their thicknesses), high resolution and high holographic sensitivity (depending on different materials) are all possible.

Photorefractive effects have been observed in a variety of electrooptic materials including ferroelectrics ($LiNbO_3$, $BaTiO_3$, KTN and SBN etc.), sillenite ($Bi_{12}SiO_{20}$, $Bi_{12}GeO_{20}$ etc.), semiconductors (GaAs, InP etc.), PLZT ceramics and even in some organic crystals. The photorefractive effects in these materials are widely used for coherent light amplification, phase conjugation, real-time information processing and holographic storage. For our purposes (using photorefractive crystals as multiple memory storage media), we lay the foundations for our work in this chapter by discussing the main theoretical aspects concerning holographic recording and replay. We consider a simple configuration with the following features: 1) single gratings written by two plane waves (an arbitrary, complicated grating may be decomposed into a sum of plane gratings); 2) gratings written with symmetrical geometries (grating vectors parallel to the crystal C-axis are recommended); 3) transmission gratings; and 4) readout using the reference beam, not a conjugate reference beam. The principle physical mechanisms of grating formation in photorefractive crystals are described in Section 3.2; The beam coupling occurring during grating formation is discussed in Section 3.3; The diffraction properties of photorefractive gratings are discussed in Section 3.4; the writing and erasure time constants are introduced in Section 3.5; finally a summary of the properties of various crystal for multiple holographic storage is given in Section 3.6.

3.2 Formation of a Holographic Grating in a Photorefractive Crystal

The creation of a holographic grating in a photorefractive crystal involves three processes:

1. Charge carrier excitation under spatially non-uniform light illumination, generated by an interference fringe pattern of coherent beams.

2. Transport of photo-induced charge carriers.

3. Modulation of the refractive index by the space-charge field, through the linear electrooptic effect.

There are two separate models for describing the charge transport process: the hopping model and the band transport model. The hopping model assumes that carrier transport occurs via hopping from a filled donor site to a neighbouring empty trap [Fei80]. The band transport model assumes that the electrons (or holes) are optically excited from filled donor (or acceptor) sites to the conduction (or valence) band, where they migrate to dark region in the crystal before recombining into an empty trap [Kuk77, Kuk79a,b]. The latter has been developed to a great degree, and enables most of the experimental phenomena to be explained. The band transport model is widely used in the literature, and is the model used in this thesis.

First we must describe the field and intensity of the driving light which excites the charge carrier from donor atoms into the conduction band.

3.2.1 Driving light and its intensity distribution

We use the coordinate system and notation of Chapter 2, in particular, the subscripts r and s are used to specify the reference beam and the signal (object) beam respectively. For the simple configuration described in Section 3.1 (shown in Fig. 3.1), the crystal entrance is in the x-z plane. We use the following crystal orientation: In the case of $LiNbO_3$, the C-axis of the crystal parallel to the z axis, whereas for BSO, an external electric field along the z axis is applied to the pair of $1\underline{1}0$ faces. The two writing beams are plane waves, each with scalar complex amplitude E, phase ϕ, unit polarisation vector $\mathbf{e}$, and wave vector $\mathbf{k}$. Frequency detuning between the two writing beams, resulting in a moving grating, is often introduced to certain kinds of crystals to enhance the energy transfer [Hui81, Ma91]. It may be possible to prove that this increases the diffraction efficiency of the written grating [Ma91, For92]. However, throughout our work no moving grating has been involved, and so we can write the same time variation term, ωt, in the field expressions for each beam. The two beams are incident at angles, θ_r and θ_s, respectively, with respect to the crystal normal. Note that in Fig. 3.1 θ_r and θ_s have opposite senses. Both beams are extraordinarily polarized, i.e. $\mathbf{e}_r$ and $\mathbf{e}_s$ lie in the incident plane which is parallel to the C-axis of the crystal. The vectorial amplitudes, E_r and E_s, of the two coherent light beams which form the interference pattern can then be expressed as

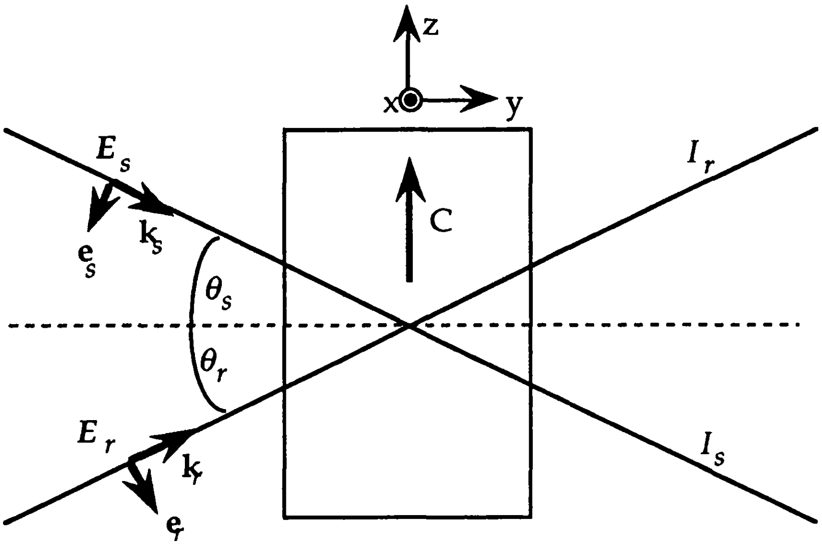

Fig. 3.1 Recording geometry for transmission gratings

$$E_r = E_r e^{-j(\mathbf{k}_r \cdot \mathbf{r} - \omega t)} \mathbf{e}_r \tag{3.1a}$$

$$E_s = E_s e^{-j(\mathbf{k}_s \cdot \mathbf{r} - \omega t)} \mathbf{e}_s \tag{3.1b}$$

where the complex amplitudes, E_r and E_s, are

$$E_r = E_r(y) e^{-j\phi_r(y)} \text{ and } E_s = E_s(y) e^{-j\phi_s(y)} \tag{3.1c}$$

and the scalar real amplitude $E(y)$ and the phase $\phi(y)$ are allowed to vary slowly along the crystal depth, y. The coherent superposition of the two waves, described by Eqs. (3.1a,b), yields an intensity pattern:

$$\begin{aligned} I &= (\boldsymbol{E}_r + \boldsymbol{E}_s)\cdot(\boldsymbol{E}_r + \boldsymbol{E}_s)^* \\ &= |E_r|^2 + |E_s|^2 + E_r E_s^* \mathbf{e}_r \cdot \mathbf{e}_s \, e^{-j(\mathbf{k}_r - \mathbf{k}_s)\cdot\mathbf{r}} + c.c. \end{aligned} \qquad (3.2)$$

where c.c. means complex conjugation. Introducing the grating vector **K**:

$$\mathbf{K} = \mathbf{k}_r - \mathbf{k}_s \qquad (3.3)$$

where, for symmetrical geometries, $\theta_r = -\theta_s = \theta$, so **K**=K**z** (K= | **K** |); and the longitudinal component of the electric field vector in photorefractive crystals vanishes [Rin91], so that $\mathbf{e}_r \cdot \mathbf{e}_s = \cos 2\theta$. Eq.(3.2) can be rewritten

$$I = |E_r|^2 + |E_s|^2 + E_r E_s^* \cos 2\theta \, e^{-jKz} + c.c. \qquad (3.4)$$

We ignore, for simplicity, the light loss caused by reflection, absorption and scattering, so that the total intensity remains constant: $|E_r^2| + |E_s^2| \equiv I_0$ and Eq.(3.4) can be further rewritten

$$I = I_0(1 + \mathrm{m}\, e^{-jKz} + c.c.) \qquad (3.5)$$

where m is the modulation of the fringe pattern given by

$$\mathrm{m} = \frac{E_r E_s^*}{I_0} \cos 2\theta \qquad (3.6)$$

Note that m may not be constant with respect to y, since E_r and E_s are functions of y. It is the non-uniform illumination expressed by Eq.(3.5) that excites the charge carriers (electrons in most cases) inside the crystal, and we will discuss this in the next subsection.

3.2.2 Generation and transport of charge carriers

The band transport model is schematically shown in Fig. 3.2 (using iron doped lithium niobate as an example). According to this model, the electrons in bright regions are optically excited from filled donor sites into the conduction band, where they migrate to dark regions in the crystal before recombining into an empty trap. This migration may occur through drift (due to any internal or external electric fields), diffusion (due to the non-uniform distribution of the electron density) and the bulk photovoltaic effect. These processes are described by a set of material equations (Eqs. 3.7 - 3.10).

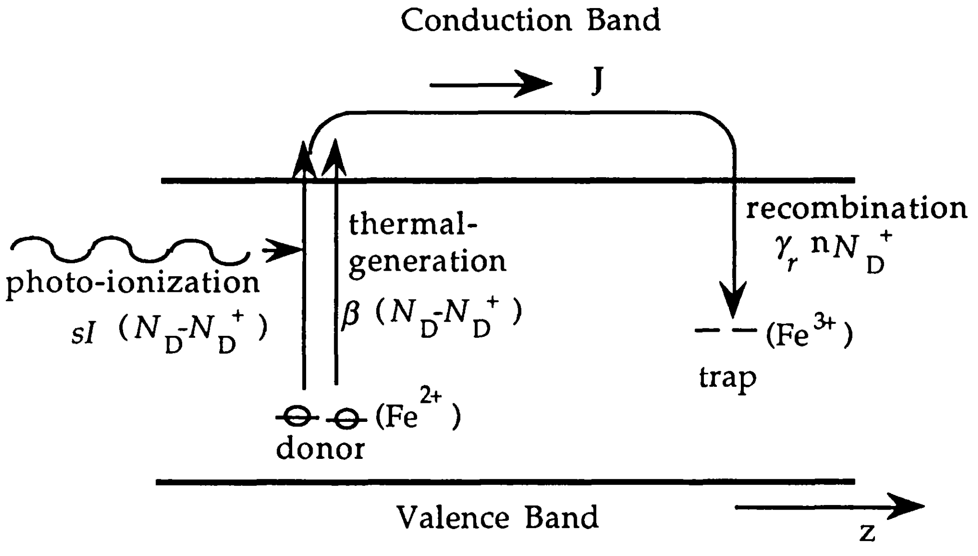

Fig. 3.2 Band transport model

The first equation describes the time rate of change of the ionized donor density, N_D^+:

$$\frac{\partial N_D^+}{\partial t} = (sI + \beta)(N_D - N_D^+) - \gamma_r n N_D^+ \qquad (3.7)$$

The terms in this equation, and for the next three equations, will be defined immediately after Eq. (3.10).

The second equation relates this ionization rate to the rate of change of the mobile charge density, *n*, and the current density, *J*, through the continuity equation:

$$\frac{\partial n}{\partial t} = \frac{\partial N_D^+}{\partial t} - \frac{1}{e}\nabla \cdot J \qquad (3.8)$$

The third material equation describes three charge transport processes which form the spatially modulated current, and the terms representing these processes appear on the right of the equation below. The terms correspond, in order, to drift, the photovoltaic effect and diffusion:

$$J = \mu e n E_{sc} + p\, I(N_D - N_D^+) - \mu k_B T\ \nabla n \qquad (3.9)$$

Finally the redistribution of the spatial charges is balanced by a periodic space charge electric field, E_{sc}, in accordance with Poisson's equation:

$$\nabla \cdot E_{sc} = \frac{e}{\varepsilon_s}(N_A + n - N_D^+) \qquad (3.10)$$

where in equations 3.7-3.10

n	is the electron number density,
N_D	is the constant, total density of dopants (Fe in $LiNbO_3$ crystal, for example),
N_D^+	is the number density of ionized donors (Fe^{3+} in $LiNbO_3$ crystal, for example),
N_A	is a constant of the crystal, the number density of negative charges that compensate for the charge of N_D^+ under dark conditions,
N_D-N_D^+	is the number density of filled donors (Fe^{2+} in $LiNbO_3$ crystal, for example),
J	is the current density,
s	is the photoionization cross section,
I	is the driving light intensity (Eq.3.5)
β	is the thermal generation coefficient,
γ_r	is the recombination coefficient,
μ	is the mobility,
E_{SC}	is the space charge electric field,

k_B is the Boltzmann constant,
T is the absolute temperature,
e is the charge on the electron,
ε_S is the static dielectric constant, and
p is the vectorial photovoltaic coefficient.

It is worth noting that although the photovoltaic current (in $LiNbO_3$ crystal) is generally described by a third rank tensor [Fes82], it has been claimed that it only has components parallel to the C-axis [Kan87]. We have chosen the latter in Eq.(3.9). Since the driving light intensity is modulated along the direction of the C-axis, all physical quantities in the crystal are expected to be modulated in the same direction, and so the vectors in Eqs.(3.8-3.10) can be simplified to scalars. The next stage is to solve for the steady-state ($\frac{\partial}{\partial t}=0$) space charge field, E_{sc}, from the set of the material equations.

3.2.3 Photo-induced space charge field

Eqs. 3.7-3.10 are non-linear partial differential equations with respect to the one temporal and the three spatial dimensions. Generally speaking, they can only be solved numerically. To obtain an analytical solution of the steady-state space charge field, a series of treatments are needed under certain simplifying assumptions, in addition to the scalar approximation already mentioned in the last subsection. These treatments include:

1. Approximate treatment for material parameters. There are many free parameters (such as the various particle number densities) whose values differ by orders of magnitude, so that it is reasonable to neglect some of them compared with some others. Thermal generation (β) is also negligible compared to the photo-ionization.

2. One-dimensional treatment. This is the direct extension of the scalar treatment, i.e. all vectors (E_{sc}, J and ∇n) in the crystal have non-zero z-components only, and their z-dependence is stronger than their y-dependence, so that the vectorial differential operator, ∇, can be reduced to $\frac{\partial}{\partial z}\mathbf{z}$.

3. First order approximation and linearisation. Grating formation in

photorefractive materials at high modulation and illumination is non-linear and has been solved numerically by Au and Solymar [Au88, Au89], and Bledowski and coworkers [Ble91]. However, most of the experimental results, even at a large modulation, can be explained with a linearised theory except those involving moving gratings [Au88]. As long as the total driving intensity, I, is not extremely large, and the fringe modulation, m, is much less than unity, every physical quantity which responds to the driving light intensity is assumed to have the same functional form as the driving pattern, given by Eq. (3.5). This allows the non-linear term, $\gamma_r n N_D^+$, to be linearised, and this also means that the higher orders of the Fourier expansion of every physical quantity are neglected. In particular, the space charge field can be expressed as

$$E_{SC}=E_{SC}\mathbf{z} \tag{3.11}$$

where

$$E_{sc} = E_{sc0} + E_{sc1}e^{-jKz} + c.c. \tag{3.12}$$

where E_{sc0} is the electric field due to any applied voltage and E_{sc1} is the amplitude of the fundamental Fourier component of the modulated space charge field.

With the above assumptions Kukhtarev et al [Kuk79a] provided a formula for the fundamental Fourier component of the space charge field, but did not give a derivation. Solymar et al presented a detailed method for deriving the results [Sol84, Erb88]. A step-by-step derivation of the results obtained by the Oxford group can also be found in Ref. [Lo92]. The results are given as

$$E_{sc1} = -\mathrm{m}E_\omega \tag{3.13}$$

where

$$E_\omega = \frac{E_{sc0} + E_p - jE_t}{1 + \frac{E_t}{E_q} + j\frac{E_{s0}}{E_q}} \tag{3.14}$$

where E_p, E_t and E_q are characteristic fields defined as :

$$E_p = \frac{p\gamma_r N_A}{\mu e s}, \quad E_t = \frac{k_B T K}{e}, \quad \text{and } E_q = \frac{e N_A}{\varepsilon_s K}.$$

E_p is the photovoltaic field, E_t is the diffusion field and E_q is proportional to the maximum value that the space charge field can have. These fields depend on both the material parameters and the grating spacing. A general complex value (Eq. 3.14) means that the space charge field is generally not in phase with the incident light pattern. The phase shift between the space charge field and the light intensity pattern, Φ_g, is then given by:

$$\Phi_g = \arg(E_{sc1}) \tag{3.15}$$

We can estimate Φ_g for special cases of Eqs. (3.13) and (3.14). The case when $(E_{sc0}+E_p) << E_t$, $\Phi_g \sim \pi/2$, is called diffusion dominant, and when $E_t << (E_{sc0}+E_p) << E_q$ (large grating spacing), $\Phi_g \sim 0$, the case is called drift dominant.

By substituting Eqs (3.13) and (3.15) into Eq. (3.12), the space charge field can be expressed as

$$E_{sc} = E_{sc0} + \mathrm{m}\ |E_\omega| e^{j\Phi_g} e^{-jKz} + c.c. \tag{3.16}$$

This space charge field modulates the refractive index of the crystal via the linear electrooptic effect, resulting in a refractive index grating.

3.2.4 Refractive index grating

For anisotropic media an electric field, E, modifies the optical impermeability tensor, $\underline{\underline{\eta}}$, such that [Yar84]

$$\underline{\underline{\eta}}(\mathrm{E}) = \underline{\underline{\eta}}(0) + \underline{\underline{\underline{r}}}\,\mathrm{E} \tag{3.17}$$

where $\underline{\underline{\eta}}(\mathrm{E})$ and $\underline{\underline{\eta}}(0)$ are the impermeability tensors (second rank) with and without the electric field applied respectively, and $\underline{\underline{\underline{r}}}$ is the third rank electrooptic tensor. Eq. (3.17) describes the linear electrooptic effect (Pockels effect). The dielectric tensor, $\underline{\underline{\varepsilon}}$, is related to the impermeability tensor by

$$\underline{\underline{\varepsilon}} = \varepsilon_0 \underline{\underline{\eta}}^{-1} \qquad (3.18)$$

where ε_0 is the permittivity of vacuum. We can write the change in the dielectric tensor, $\Delta\underline{\underline{\varepsilon}}$, caused by the field, E, in the form below [Rin91]:

$$\Delta\underline{\underline{\varepsilon}} = -\frac{1}{\varepsilon_0}\underline{\underline{\varepsilon}}(0)\underline{\underline{\underline{r}}}\,\mathrm{E}\,\underline{\underline{\varepsilon}}(0) \qquad (3.19)$$

where $\underline{\underline{\varepsilon}}(0)$ is the dielectric tensor without the field. The light waves, E_s and E_r (expressed by Eq. 3.1a and 3.1b), form the space charge field, E_{sc} (expressed by Eqs. 3.11-3.16), which in turn causes a scalar modulation in the dielectric constant, $\Delta\varepsilon_r$, as seen by the two waves, and given by:

$$\Delta\varepsilon_r = -\frac{1}{\varepsilon_0} e_r{}^{*}\underline{\underline{\varepsilon}}(0)\underline{\underline{\underline{r}}}\,\mathrm{z}\,\underline{\underline{\varepsilon}}(0) e_s E_{sc1} \qquad (3.20)$$

An effective electrooptic coefficient, r_{eff}, which is the appropriate electrooptic tensor component or combination of components, is often used to simplify the expression:

$$\Delta\varepsilon_r = \varepsilon_{r0}{}^2 r_{eff}\, E_{sc1} \qquad (3.21)$$

where ε_{r0} is the bulk relative dielectric constant including any change caused by an average electric field. The modulated dielectric constant can then be expressed as

$$\varepsilon_r = \varepsilon_{r0} + \Delta\varepsilon_r e^{jKz} + c.c. \qquad (3.22)$$

The modulated refractive index, Δn, is related to the change in the dielectric constant by $\Delta n = \Delta\varepsilon_r / 2n$, so that there is an index grating formed by the two waves, E_s and E_r. These waves are, in turn, affected by this grating which they have formed, and so the grating is a dynamic one. During grating formation the two writing beams are coupled to each other by the grating written by themselves in a self-consistent manner (self-diffraction). In the next section we deal with the beam coupling in a two-wave mixing situation by deriving and solving the coupled wave equations taking into account the index grating formed by the two waves.

3.3 Beam Coupling

Consider the wave expressions in Eqs. 3.1 and 3.2. If we neglect any vectorial complications such as optical activity or birefringence, and assume that the polarizations of the two beams are parallel (this is valid if the incident angle, θ, is small for extraordinarily polarized beams), the total scalar complex amplitude, E, is given by the superposition of the two waves:

$$E = E_r e^{-j(\mathbf{k}_r \cdot \mathbf{r} - \omega t)} + E_s e^{-j(\mathbf{k}_s \cdot \mathbf{r} - \omega t)} \tag{3.23}$$

The scalar wave equation that E must satisfy is given by:

$$\nabla^2 E + \omega^2 \mu_0 \varepsilon_r \varepsilon_0 E = 0 \tag{3.24}$$

where ω is the angular frequency of the two waves, μ_0 is the permeability of free space, ε_0 is the permittivity of vacuum, and ε_r is the relative dielectric constant of the medium given by Eq.(3.24).

Substituting Eqs. 3.22 and 3.23 into 3.24, we can make the usual approximation of slowly varying amplitudes with respect to y, and neglect second derivatives and higher diffraction orders. Assuming further $\mathbf{k}_r \cdot \mathbf{r} \approx \mathbf{k}_s \cdot \mathbf{r} \approx \mathrm{k}y$, we obtain two coupled wave equations:

$$\frac{dE_r}{dy} = -j \frac{\Delta\varepsilon_r^{*} \mathrm{k}}{2\varepsilon_{r0}} E_s \tag{3.25}$$

$$\frac{dE_s}{dy} = -j \frac{\Delta\varepsilon_r \mathrm{k}}{2\varepsilon_{r0}} E_r \tag{3.26}$$

where $\mathrm{k} = |\mathbf{k}_r| = |\mathbf{k}_s|$ and $\mathrm{k}^2 = \omega^2 \mu_0 \varepsilon_{r0} \varepsilon_0$.

Using expression (3.1c), and considering Eqs. 3.21 and 3.16, we can decompose the complex equation pair (3.25) and (3.26) into terms involving the intensity and phase of each wave, yielding four real equations:

$$\frac{dI_r}{dy} = 2\frac{I_r I_s}{I_0}\Gamma\sin\Phi_g \tag{3.27}$$

$$\frac{dI_s}{dy} = -2\frac{I_r I_s}{I_0}\Gamma\sin\Phi_g \tag{3.28}$$

$$\frac{d\phi_r}{dy} = 2\Gamma\frac{I_s}{I_0}\cos\Phi_g \tag{3.29}$$

$$\frac{d\phi_s}{dy} = 2\Gamma\frac{I_r}{I_0}\cos\Phi_g \tag{3.30}$$

where

$$\Gamma = \frac{1}{2}\mathrm{k}_0\mathrm{n}^3 r_{eff}|E_\omega| \tag{3.31}$$

is the coupling strength for given k_0, the wave propagation constant in free space, and $I_r=|E_r|^2$ and $I_s=|E_s|^2$ are the intensities of the two writing beams. Subject to the boundary conditions, $I_r(y=0)=I_{r0}$ and $I_s(y=0)=I_{s0}$, the Bernoulli-type equations, (3.27) and (3.28), can be solved analytically, yielding the solutions:

$$I_r(y) = \frac{I_0}{1+\mathrm{m}_0\exp(-2y\,\Gamma\sin\Phi_g)} \tag{3.32}$$

$$I_s(y) = \frac{I_0\mathrm{m}_0\exp(-2y\,\Gamma\sin\Phi_g)}{1+\mathrm{m}_0\exp(-2y\,\Gamma\sin\Phi_g)} \tag{3.23}$$

$$\Delta\phi(y) = \phi_0 + \frac{\cot\Phi_g}{2}\ln\left(\frac{(1+\mathrm{m}_0)^2\exp(-2y\,\Gamma\sin\Phi_g)}{[1+\mathrm{m}_0\exp(-2y\,\Gamma\sin\Phi_g)]^2}\right) \tag{3.34}$$

where $\mathrm{m}_0=I_{s0}/I_{r0}$ is the initial writing beam intensity ratio, $\Delta\phi(y)=\phi_r-\phi_s$ is the phase difference between the two writing beams and ϕ_0 is a constant phase difference which is usually taken as zero.

We can see from the solutions that, in general, the relative intensity and relative phase between the two writing beams change along the crystal thickness. This will result in a grating where the modulation, m, and the phase, $\Delta\phi$, are functions of the y coordinate. The grating will be bent due to the y dependence of $\Delta\phi$. In particular, when Φ_g=0 (drift dominant), the intensities of the two beams will remain constant, so there is no intensity coupling, but the phase difference varies linearly, resulting in a tilted grating. On the other hand, in the case that $\Phi_g=\pi/2$ (diffusion dominant), there is strong intensity coupling, but no phase coupling, so no tilting or bending of the grating occurs in the steady state, but the modulation varies with depth.

3.4 Diffraction Efficiency and Angular Response

So far we have discussed the grating formation in a two-wave mixing configuration. In this section we discuss the readout properties of a recorded grating. In doing so a readout beam with the same wavelength and polarization as that of the reference beam used for recording is assumed, and the intensity of this readout beam is assumed sufficiently weak that the grating should not be affected in any way. Kukhtarev et al solved the coupled wave equations for replay without considering explicitly the effect of grating bend. They gave an analytical solution for the diffraction efficiency, η_0, which occurs at a readout angle identical to the reference beam angle used for recording (they claimed as Bragg incidence). The formula for η_0 in our notation is as follows [Kuk79a]:

$$\eta_0 = \frac{2m_o}{1+m_o} \cdot \frac{\exp(-\Gamma d \sin\Phi_g)[\cosh(\Gamma d)\ \sin\Phi_g - \cos(\Gamma d)\ \cos\Phi_g]}{1+m_o \exp(-2\Gamma d \sin\Phi_g)} \tag{3.35}$$

where d is the crystal thickness. When the grating phase shift, Φ_g, equals zero, Eq. (3.35) can be reduced to

$$\eta_0 = \frac{4m_o}{(1+m_o)^2}\sin^2\frac{\Gamma d}{2} \tag{3.36}$$

Eq. (3.36) coincides with Kogelnik's result for the case when the grating is read out at the Bragg angle, i. e. the phase mismatch term ξ=0 (see Eq.(2.17) in Chapter 2). This simple formula is widely used in the estimation of diffraction efficiencies.

To find out the angular response of the gratings recorded in photorefractive crystals the same procedure as that for calculating diffraction efficiency has been carried out by Heaton et al, but the readout beam is allowed to have an incident angle differing slightly from the recording angle. The coupled-wave differential equations for the amplitudes of the directly transmitted readout beam, e_r and the diffracted readout beam, e_s, are as follows [Hea84]:

$$\frac{de_r}{dy} - j\,\kappa_r e_s e^{+j[\Delta\phi(y)+\delta y]} = 0 \qquad (3.37)$$

$$\frac{de_s}{dy} - j\,\kappa_s e_r e^{-j[\Delta\phi(y)+\delta y]} = 0 \qquad (3.38)$$

where δ is the off-Bragg term and

$$\kappa_{r,s} = \frac{\cos\theta_r}{\cos\psi_{r,s}}\Gamma\frac{\sqrt{I_r(y\ )I_s(y\ )}}{I_0} \qquad (3.39a)$$

For very thick materials, the off-Bragg term δ can be related to the recording angle, θ_r, the readout beam angles, ψ_r, and the diffracted beam angle, ψ_S, using the vector diagram shown in Fig. 3.3. In Fig. 3.3 the grating, **K**, is written by writing waves with wave vectors $\mathbf{k}_r$ and $\mathbf{k}_S$. If the readout angle, ψ_r, deviates from the recording angle, θ_r, by a small angle, $\Delta\theta$, the off-Bragg term, δ, can be expressed as

$$\delta = \mathrm{k}(\cos\psi_r - \cos\psi_S) \qquad (3.39b)$$

where

$$\psi_S = \sin^{-1}(2\sin\theta_r - \sin\psi_r) \qquad (3.39c)$$

and k is the modulus of the wave-vector.

Note that the modulation, $\frac{\sqrt{I_r(y\ )I_s(y\ )}}{I_0}$, and the phase, $\Delta\phi(y)$, of the grating given in Eqs. (3.37) - (3.39) are already determined during the recording process by Eqs. (3.32) - (3.34). In addition, the coupling constant, Γ, should be the same as that determined by Eq. (3.31).

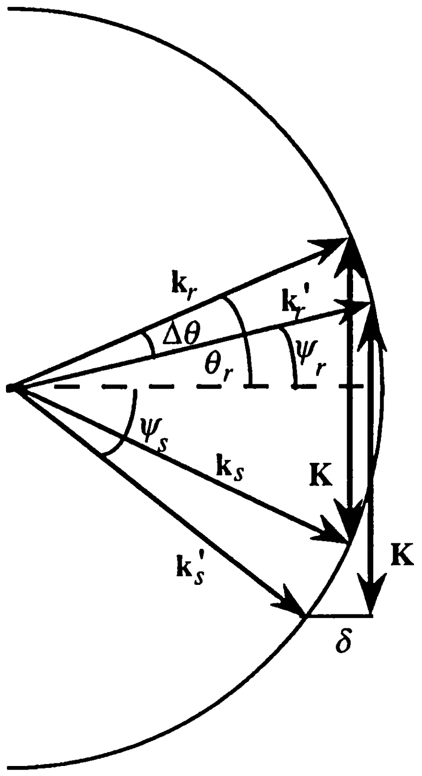

Fig. 3.3 Vector diagram showing recording and replay conditions and off-Bragg term δ for the transmission geometry. The writing wave vectors are $\mathbf{k}_r$ and $\mathbf{k}_s$.

By solving equations (3.37) and (3.38) for the boundary conditions $e_r(0)=1$ and $e_s(0)=0$, the diffraction efficiency, $\eta=|e_s(d)|^2$ (where d is the crystal thickness) can be calculated as a function of the readout angle ψ_r. Using this method, Heaton et al [Hea84] obtained the following analytical solution for η in the special case, $\Phi_g=0$:

$$\eta=\frac{\cos\psi_s}{\cos\psi_r}\cdot\frac{\kappa_s^2\sin^2\left[\kappa_r\kappa_s d^2+(\gamma d/2)^2\right]^{1/2}}{\left[\kappa_r\kappa_s+(\gamma/2)^2\right]^{1/2}} \tag{3.40a}$$

where

$$\gamma=\Gamma\frac{m_0-1}{m_0+1}+\delta \tag{3.40b}$$

These two equations predict a maximum diffraction efficiency for a readout angle equal to the recording angle (i.e. δ=0) only when the initial writing beam intensity ratio, m_0, is equal to one (m_0=1). Heaton et al also obtained an approximate formula (in this special case, Φ_g=0) for the optimum angular deviation, $\Delta\theta$ (= $\psi_r - \theta_r$, the deviation from the recording angle for maximum efficiency replay):

$$\Delta\theta = \frac{m_o - 1}{m_o + 1} \cdot \frac{\Gamma d}{4\pi(d/\lambda_m)\sin\theta_r} \qquad (3.40c)$$

where λ_m is the writing beam wavelength. In the case that $\Phi_g = \pi/2$, they solved Eqs. (3.37) and (3.38) numerically and generated angular response curves for m_0=1, 3 and 5 which showed that in these cases no obvious angular deviation of the readout beam was required for the maximum diffraction efficiency. A prediction was made by them that the maximum diffraction efficiencies will usually be obtained at readout angles different from the recording angle. This prediction has never been verified experimentally.

For an arbitrary phase shift, Φ_g, Eqs. (3.37) and (3.38) can only be solved numerically. We will present our detailed calculations together with the experimental verifications in Chapter Four.

3.5 Kinetics of Grating Recording and Erasure in Photorefractive Crystals

In this section we first discuss the response time of photorefractive materials, and then turn our attention to look at the exposure procedures required for multiple recording, when uniform diffraction efficiencies in the gratings are required.

3.5.1 Response Time

The response time constant is a useful figure of merit for applications such as holographic storage, in which the grating must be written or erased in a set time scale with a set diffraction efficiency. This is a problem of the kinetics of grating recording and erasure.

The equations 3.7-3.10 given in Section 3.2, which govern the build-up of the space charge field, are partial differential equations with respect to both spatial and temporal variables. In Sections 3.3 and 3.4 we discussed the steady-state solutions of Eqs. 3.7 - 3.10 by letting $\frac{\partial}{\partial t} = 0$ together with other approximations. Having ignored the time evolution of the space charge field, this treatment cannot provide the kinetic characteristics of the grating formation. Kukhtarev presented an analytical solution for the transient case, giving a rather complicated formula for the space charge field [Kuk76]. A clearer form of Kukhtarev's formula, showing that the transient response of the space charge field has an overdamped oscillatory behaviour, is given by Valley and Klein as [Val83] (in our notation):

$$E_\omega(t) = E_\omega(1 - e^{-\frac{t}{\tau_e}} e^{j\Omega t}) \qquad (3.41)$$

where E_ω is the steady state value given by Eq.(3.14), τ_e is the response time constant and Ω is the oscillatory frequency, and both are functions of material parameters and exposure conditions.

The oscillation at frequency Ω may be neglected if $1/\tau_e >> \Omega$. Thus, the kinetics of the formation of index gratings may be expressed as:

$$\Delta \mathrm{n}(t) = \Delta \mathrm{n}_{\mathrm{sat}}(1 - e^{-\frac{t}{\tau_e}}) \qquad (3.42)$$

where $\Delta \mathrm{n}_{\mathrm{sat}}$ is the index modulation on saturation. The change in the refractive index, Δn, can be related to the change in the relative dielectric constant, $\Delta\varepsilon_r$, by $\Delta \mathrm{n}_{\mathrm{sat}} = \Delta\varepsilon_r / 2\mathrm{n}$. Therefore, using Eq. (3.21), the index modulation at saturation can be expressed as

$$\Delta \mathrm{n}_{\mathrm{sat}} = \frac{1}{2}\mathrm{n}^3 r_{eff} E_{sc1} \qquad (3.43)$$

where E_{sc1} is the space charge field in steady state.

The response time constant , τ_e, is given by the dielectric relaxation time, τ_{di}, multiplied by a factor that takes into account variations in the conductivity due to the excitation, transport and recombination of the spatially varying electron number density [Val83]. Under some conditions this complicated factor is of order one, and the response time may reduce to the dielectric relaxation time :

$$\tau_e \approx \tau_{di} = \frac{\varepsilon_s}{\sigma_i + \sigma_d} \tag{3.44a}$$

where ε_s is the static dielectric constant and σ_i and σ_d are the photo-and dark-conductivity respectively. For grating writing and optical erasure the dark-conductivity is negligible, and the response time can be expressed as [Val83]:

$$\tau_e = \frac{\varepsilon_s \gamma_r}{\mu e s} \frac{1}{I_0} \frac{N_A}{N_D - N_A} \tag{3.44b}$$

So the response time depends on the material parameters and the average exposure intensity. The ratio $\frac{N_A}{N_D - N_A}$ is the inverse of the reduction ratio (the concentration ratio of Fe^{3+} to Fe^{2+} in $LiNbO_3$ crystals for example), and this can be controlled by nondestructive processing via reduction or oxidation during crystal preparation.

Optical erasure occurs when the crystal is illuminated by a uniform light beam with wavelengths that the crystal is sensitive to. The uniform illumination excites all electrons out of the traps, and redistributes them evenly throughout the volume, thus bringing the sample back to its original state. Theoretically the response time for erasure is the same as that for recording, if the same wavelength is used for both recording and erasure, so that the space charge field and the index change are given by

$$E_\omega(t) = E_{\omega 0} e^{-\frac{t}{\tau_e}} \tag{3.45}$$

and

$$\Delta \mathrm{n}(t) = \Delta \mathrm{n}_0 e^{-\frac{t}{\tau_e}} \tag{3.46}$$

where $E_{\omega 0}$ and Δn_0 is the initial value of E_ω and Δn respectively. This "symmetric" writing/erasure time characteristic has been quoted by many authors (see, for example, [Kuk76], [Kur77], [Pel77], [Val83] etc.), and has been confirmed experimentally for various materials such as BSO [Hui76], $LiNbO_3$ doped with iron by diffusion [Phi72], and SBN without an external field [For92]. However, it has been noted that in certain cases the erasure sensitivity (the energy density required to erase a hologram to half of its original strength) is roughly an order of magnitude lower than the writing sensitivity for a given crystal. This suggests an asymmetry in the writing/erasure time constants, which may arise from some additional complexity [Phi72]. For example, a possible cause is the oscillation term in Eq. (3.41), which causes the index modulation, Δn, to rise more quickly than in the case when $1/\tau_e >> \Omega$ during the initial stage of recording [For92]. For the purpose of multiple storage this asymmetric response is very useful for reducing erasure during recording. The writing time constant, τ_W, and the erasure time constant, τ_E, are introduced in Eq.(3.42) and (3.46) respectively to replace the "symmetric" response time constant, τ_e.

3.5.2 Exposure procedures for uniform diffraction efficiency

In angular multiplexing, multiple holograms are incoherently superimposed in the same volume of the crystal. The angular separation used for adjacent recordings is generally large enough to minimise crosstalk. Therefore, the writing beams of subsequent recordings have an insignificant reading effect on the holograms already written, but behave as erasure illumination to them. Thus, if all the holograms are recorded using an identical exposure time, the diffraction efficiencies of holograms recorded earlier will be lower than those recorded later. However, most applications of multiplexed holograms require uniform diffraction efficiencies for all holograms. In order to obtain uniform diffraction efficiencies from an angularly multiplexed memory, two exposure schemes, scheduled and incremental, have been developed. Both schemes are based on the exponential writing and erasure characteristics of the index modulation, $\Delta n(t)$. $\Delta n(t)$ is given by Eqs. 3.42 and 3.46, and these may be rewritten:

$$\Delta n(t_W) = \Delta n_{sat}(1 - e^{-\frac{t_W}{\tau_W}}) \qquad \text{(writing)} \qquad (3.47)$$

and

$$\Delta n(t_E) = \Delta n_0 e^{-\frac{t_E}{\tau_E}} \qquad \text{(erasure)} \qquad (3.48)$$

where τ_W and τ_E are the writing and erasure time constants respectively, t_W and t_E are the exposure time for writing and erasure respectively, Δn_{sat} is the index modulation at saturation, and Δn_0 is the initial index modulation of the erasure process. Typical curves of the index modulation versus time for both the writing and erasure processes are shown in Fig. 3.4.

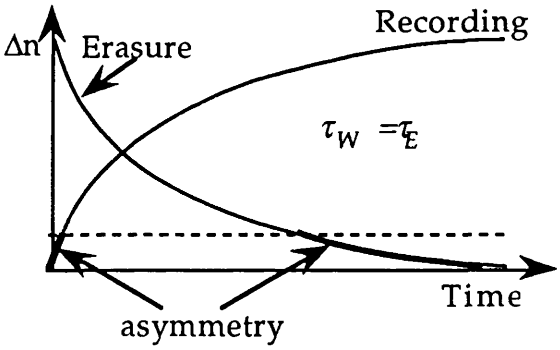

Fig. 3.4 Index modulation, Δn, versus time in the case of symmetric writing and erasure time constants. Although the time constants are symmetric, the writing and erasure sensitivity (measured by the slope of the curves) are asymmetric at low Δn.

Incremental exposure scheme

The incremental exposure scheme was developed recently [Tak91, Man92, Tak92], and is based on the fact that the writing sensitivity is greatest near the foot of the writing curve, and the erasure sensitivity is lowest in this region (see Fig. 3.4). This is despite the fact that the time constants are symmetric. In incremental recording scheme, the whole writing process is divided into a series of identical cycles, in each cycle all of the M holograms are sequentially recorded, each with an exposure time of Δt. This "incremental" exposure time is extremely short compared to the writing time constant of the crystal. The asymmetric "near foot" writing-erasure characteristic ensures that some of the index modulation of the first recorded hologram remain after incrementing the other M-1 holograms. As this process is repeated, the diffraction efficiencies of all the holograms gradually increase. After many cycles, the recording process approaches saturation, where the increase of the recording increment is exactly matched by the decrease during the (M-1) erasure increments.

The incremental recording does not require a detailed knowledge of the writing and erasure complexities, in particular, it does not require the writing and erasure time constants to be known accurately. This is convenient for experiments in materials, of which the time constants are difficult to determine. However, if incremental recording is used, the recording system must repeatedly display the object and reference pairs, reproducing the interference pattern of each writing beam pair to within much less than one fringe width. This puts a critical requirement to the equipment used for recording.

Scheduled procedure

The scheduled procedure has been widely investigated during the past two decades [Bur77, Blo78, Psa88, Str89, Man91, Mok91]. These authors used different methods to reduce the exposure time of subsequent recordings to compensate for the erasure effect during recording. All of these methods were based on the exponential writing and erasure characteristics of the index modulation. Knowing the writing and erasure time constants of the crystal, τ_W and τ_E, and the index modulation at saturation, Δn_{sat}, the refractive index modulation of the Nth hologram, Δn_N, can be obtained from:

$$\Delta n_N = \Delta n_{sat}\left(1 - e^{-\frac{t_N}{\tau_W}}\right)\cdot e^{-\frac{T_N}{\tau_E}} \qquad (3.49)$$

where t_N is the exposure time of the Nth hologram and T_N is the total erasure time suffered by the Nth hologram due to the subsequent recordings. T_N is given by:

$$T_N = \sum_{i=N+1}^{M} t_i \tag{3.50}$$

where M is the total number of holograms to be recorded. Uniform diffraction efficiency requires that the index modulation (as determined by Eq. 3.49) for all holograms is identical. The exposure time sequence $\{t_i, i=1, 2, \cdots, M\}$ can then be calculated if the exposure time of the first (or last) hologram is given. The resultant time schedule features a monotonic reduction in the exposure time. A hologram recorded earlier requires a writing time longer than those recorded later.

The calculation of the correct exposure time sequence requires precise determination of the writing and erasure time constants of the crystal. The time constants depends on the material parameters and the exposure conditions, which include the writing beam ratio and the total recording intensity. In practice the time constants are usually determined by experiment [Mok92, For92].

3.6 Material Properties for Holographic Storage

According to the discussions in section 3.2, any electrooptic material having a photo-excitation mechanism is in principle a photorefractive material, since at least one of the charge transport mechanisms, diffusion, occurs in any material. More than twenty photorefractive materials have been studied for various applications according to a literature survey [Poo91]. Materials of particular interest are those with properties meeting the requirements of particular applications. In this section we summarise the main properties of materials used for holographic storage.

3.6.1 Material requirements for holographic storage

For multiple holographic storage we are mainly concerned with the following attributes:

1. The laser wavelength required to induce refractive index changes
2. Dynamic range (maximum refractive index change)
3. Sensitivity
4. Persistence
5. Crystal size and optical quality
6. Others

In the following we discuss separately each of these requirements and the approximate range for the most important materials.

1. Laser wavelength for inducing refractive index change

The photorefractive materials considered for holographic storage should be photosensitive at a convenient laser wavelength. At present, holographic recordings are mainly performed using visible laser light such as that produced by argon ion (488/514nm) and helium neon (633nm) lasers. Materials and suitable dopants have been found which allow recording across a rather broad range of wavelengths extending from the near ultra-violet to the near infrared.

2. Dynamic range (maximum refractive index change)

The maximum refractive index change (i.e. the steady-state or saturation change in the refractive index, Δn_{sat}) is defined as the index change reached after illumination for a time that is long compared to the response time, τ_e. This figure of merit approximately determines the largest diffraction efficiency that can be recorded in a crystal of a given thickness via the theory of Kogelnik (see Eq. 2.17 and 2.19 in Chapter 2). And this determines also the number of holograms that can be recorded in a given volume. We will give a more detailed discussion about this in Chapter Five.

The maximum refractive index change depends upon the material parameters, n and r_{eff}, and the maximum space charge field, E_{scl} (see Eq. 3.43). The latter depends also on the material parameters such as the donor and trap densities. For a given crystal, E_{scl} can be optimized by selecting a suitable grating spacing. Values of Δn_{sat} up to 10^{-3} have been measured for $LiNbO_3$ [Kur77b] and $BaTiO_3$ [Kur76, Kur77b].

3. Sensitivity

The photorefractive sensitivity, S, is defined as the index change per unit of absorbed energy per unit volume at the initial stage of photorefractive recording:

$$S_n = \frac{d(\Delta n)}{dw}, w=\alpha W_0$$

where α is an absorption coefficient and W_0 is the incident optical energy) [vdL75, Gla78, Kra78, Gun83]. The sensitivity is a useful figure which indicates how well a material uses a given amount of optical energy. It has been shown that the sensitivity can be improved by decreasing the number density of empty traps in the material (Fe^{3+} in $Fe:LiNbO_3$ for example) [Val83]. It has also been shown both theoretically and experimentally that the sensitivity of $Fe:LiNbO_3$ is proportional to the number density of Fe^{2+}, whilst the maximum refractive index change is proportional to the number density of Fe^{3+} [Kra90, Som89]. So there must be some trade-off between the sensitivity and the dynamic range in the crystal preparation.

A more practical definition of the sensitivity of a holographic recording material, S_η^{-1}, is the energy density, W(1%) in mJ/cm^2, required to write a grating of 1% diffraction efficiency in a 1mm thick crystal [Hui81, Gun82]. Kratzig and Rupp used a similar definition except that they omitted the thickness specification [Kra86]. Since the diffraction efficiency depends highly on the crystal thickness, their sensitivity data should be regarded as giving the sensitivities of individual samples. Sensitivities for various crystals (using the above definition, S_η^{-1}) have been found to vary between 10^{-1} for KTN to 10^{3} for $Fe:LiNbO_3$.

4. Persistence

The persistence of a hologram is specified by the dark storage time, i.e. the time during which the original index change distribution remains recorded in the dark after recording. This is also given by the dielectric relaxation time, τ_e, in Eq.(3.44), but determined only by the dark-conductivity. Electrooptic crystals typically have large dielectric constants and they can be highly insulating. The dark storage times of the available photorefractive crystals range from seconds ($BaTiO_3$ and SBN) to years ($LiTaO_3$) according to the values of ε_s and σ_d given in Ref [Gun82].

Materials with a short persistence are suitable for real-time signal processing, coherent light amplification and optical phase conjugation. However, a long persistence is essential for read-only memories. In these cases complete fixing of the stored images can be accomplished by transforming the electronic space charge pattern into a stable ionic charge pattern. The maximum persistence of the recorded and fixed holograms is estimated to be $\sim 10^5$ years at room temperature. Holograms recorded and simultaneously fixed in $LiNbO_3$ have shown no degradation in either diffraction efficiency or image quality [Bur78]. Fixing is also possible for BSO [Her86, Ari89].

5. Crystal size and optical quality

Crystal growth is a materials science and technology problem. Crystals with a reasonably large size and excellent optical quality are always desirable for high capacity holographic storage. Unfortunately, we must compromise between size and optical quality. For example, the optical quality of the most sensitive material, KTN, is very poor [Kra86], and another attractive crystal, SBN, is usually accompanied by "growth fringes" (due to an additional inhomogeneous index change during crystal growth), so that crystals larger than a few millimetres with a good optical quality are not available in practice yet.

6. *Other properties*

Spatial frequency response (spatial resolution)

Since most of the photorefractive materials are single crystals, the spatial resolution is in principle limited by the distance between traps. A hologram can be recorded at a frequency of 1000 line pairs per millimetre even in an undoped crystal with a trap density as low as 10^{15} cm^{-3} [Gun82]. Trap densities in excess of 10^{18} cm^{-3} can be easily achieved by impurity doping, giving a distance between traps of only 10 nm. This should be sufficient for any holographic application.

Unlike the conventional static holographic recording materials (silver halide, DCG, etc.), the modulation transfer function (MTF) of photorefractive crystals is not usually flat even at frequencies lower than the "cut-off" frequency. For very large or very small grating spacings the space charge field may be limited by the values of the characteristic fields (see Eq. 3.14). Burke et al measured the spatial frequency response curve for an Fe:$LiNbO_3$ crystal, showing a nearly flat response over a spatial frequency bandwidth from 1350 lines/mm to about 1900 lines/mm [Bur78].

Scattering noise

Scattering noise is an intrinsic problem in photorefractive materials. Any defect that scatters light produces a spherical wave, which then interferes with the original beam, leading to a noise grating [Sol89b]. The noise grating, in turn, scatters more light so that a complicated scattering pattern is built up rapidly, which produces noise in the reconstructed images. Scattering noise reduces the spatial resolution of the crystal, degrades the image quality and decreases the number of holograms which can be stored in a given crystal.

3.6.2 Material properties

Table 3.1 lists the holographic storage properties of photorefractive materials, comparing their sensitivities, index change ranges and storage persistence. The most popular materials are $LiNbO_3$ and BSO. As the first material in which photorefractive effects were found, $LiNbO_3$ has received intensive investigation. The writing and erasure sensitivities of $LiNbO_3$ can be adjusted by dopant concentrations and externally applied voltages. The large dynamic range of $LiNbO_3$ allows a large number of holograms to be multiplexed in a given crystal. The persistence of holograms in $LiNbO_3$ is fairly long and can be fixed. The disadvantage of $LiNbO_3$ is a rather low sensitivity. BSO is one of the most sensitive materials with a sensitivity comparable to holographic silver halide emulsions. The short and nearly symmetrical writing/erasure time constants of BSO makes it suitable for real-time holography. However, the dynamic range of BSO is rather small, the maximum diffraction efficiency of a single hologram recorded in BSO is usually only a few percent. Both $LiNbO_3$ and BSO can easily be grown to a large size, and with excellent optical quality. This has led us to choose $LiNbO_3$ as the dense holographic storage material, and BSO as a starting material to investigate the readout properties of holographic gratings in photorefractive crystals. In the next chapter we present the results of our investigations.

Table 3.1 Holographic storage properties of photorefractive materials

	Measurement Conditions			Sensitivity				
Material	λ (nm)	E_0(kV/cm)	Λ(μm)	$S_n^{-1}(10^3 J/cm^2)$	$S_\eta^{-1}(mJ/cm^2)$	Δn_{max}	Persistence	Reference
$LiNbO_3$, undoped					10^4			[Amo72]
$LiNbO_3$, 0.1wt%:Fe								
slightly reduced	488				200			[Sta74]
$LiNbO_3$, 0.005wt%:Fe (for symmetrical write/erase behavior)								
heavily reduced	488				12 (for 0.08% efficiency)			[Sta74]
$LiNbO_3$:Fe	514			20-200	1000	10^{-5}-10^{-3}	100h-1yr	[Kur77]
$LiNbO_3$:Fe	351	50		0.06-600		10^{-4}		[Orl77]
$LiTaO_3$					50	10^{-4}	10yrs	[Kra78]
$LiTaO_3$	351	15			66	10^{-4}		[Kra78]
$KNbO_3$				6-60		5x10^{-5}	1sec-1day	[Gun78]
$KNbO_3$		7	10	0.08		10^{-5}		[Gun78]
$K(NbTa)O_3$				0.1[a]	0.24[a]		7months	[Orl80, Boa80]
$KTa_{.65}Nb_{.35}O_3$		10		0.03	0.13			[Orl80, Boa80]
$BaTiO_3$					50-1000	2.2x 10^{-5}	15h	[Kra80]
$BaTiO_3$		10			0.1-10[b]	5x10^{-5}		[Kra80]
$Bi_{12}SiO_{20}$		6	5	0.014	0.7	5x10^{-6}*	6days[d]	[Pel77]
$Bi_{12}GeO_{20}$		6	5	0.05	2.6		12h[d]	[Pel77]

Table 3.1 Holographic storage properties of photorefractive materials (contd)

	Measurement Conditions			Sensitivity				
Material	λ (nm)	E_0(kV/cm)	Λ(μm)	$S_n^{-1}(10^3 J/cm^2)$	$S_\eta^{-1}(mJ/cm^2)$	Δn_{max}	Persistence	Reference
$Ba_2NaNb_5O_{15}$		3			3^a			[Tha74]
$Ba_{.4}Sr_{.6}Nb_2O_6$::Ce					15		1h-1month	[Meg77]
$Ba_{.6}Sr_{.4}Nb_2O_6$::Ce	633			12-75	2.5-15		1h-17month	[Dor81]
$Ba_{.6}Sr_{.4}Nb_2O_6$::Ce (0.02wt%)	514	6-0	2		$17\text{-}100^c$	$3.7x10^{-4}$	12h	[For91,For92]
$Ba_{.6}Sr_{.4}Nb_2O_6$::Ce (Fibre)	514				~50			[Hes88]
$K(D_{.7}H_{.3})_2PO_4$ (T=113K)	300			5			7days	[Fri78]
$Pb_5Ge_3O_{11}$	514						1day	[Kro90]
InP:Fe	1060						10^{-4}sec	[Gla84]
$La_3Ga_5SiO_{14}$-Pr^{3+}	514						10h	[Pau90]
GaAs	1150		0.63				8sec	[Chen88]
PLZT ceramic (9/65/35)		10			$100\text{-}600^a$	10^{-3}		[Burg76]

[a]: defined as the incident energy density per unit index change, or for recording of 1% diffraction efficiency

[b]: depending on incident intensity.

[c]: calculated using the data provided by the reference(s)

[d]: calculated using the data of ε_s and σ_d from [Gun82]

*: results from our own measurement

CHAPTER FOUR

PERFORMANCE OF HOLOGRAPHIC GRATINGS FORMED IN PHOTOREFRACTIVE CRYSTALS

In the preceding chapters we have described the background and foundation of our work. This chapter presents our new experimental and numerical results, and explains these results using existing theory.

The dynamic nature of holographic recording in photorefractive crystals, discussed in Chapter Three, ensures that the performance of holograms recorded in such crystals, when replayed, is rather different from that in static materials such as photographic films. The characteristics of interest for multiple storage, particularly the angular sensitivity and the diffraction efficiency, are strongly affected by the material properties and the recording/readout conditions. In addition, all photorefractive crystals in current use are optically anisotropic, and, as a result, the polarisation state of recording and readout waves strongly affects the readout behaviour.

Angular sensitivity means the dependence of diffraction efficiency on readout angle. This dependence includes 1) the readout angle at which maximum diffraction efficiency occurs (peak position), and 2) how far the readout beam can deviate from the peak position whilst still giving a significant diffraction efficiency (selective angle). In this chapter the selective angle is chosen to be the 10dB angular width of the main lobe in the curve of diffraction efficiency versus angular deviation from recording angle (angular response curve). The angular sensitivity is essential for both the storage and retrieval of multiplexed holograms. The selective angle determines the optimum angular separation during recording to achieve a storage capacity as high as possible with given crosstalk. The peak position determines the optimum access configuration during readout that results in the highest diffraction efficiency and SNR.

In this chapter we discuss the peculiarities of the angular sensitivity and the diffraction efficiency of single transmission gratings in photorefractive crystals. In Section 4.1 we present our experiments on the angular sensitivity of gratings formed in our BSO sample. Our results show that the polarization properties agree well with the predictions of anisotropic diffraction theories. In Section 4.2 we present our new results with $LiNbO_3$ crystals. These form the first direct experimental verification of the theories that are described in Chapter Three (on curved/bent gratings formed in photorefractive materials). Our experimental measurements show clearly that the phase coupling between the two writing beams during recording can cause a "Bragg-shift" of the recorded grating during readout. In Section 4.3 the effect of a non-uniform grating caused by intensity coupling is discussed. Self-enhancement of the diffraction efficiency during readout or erasure is briefly described in Section 4.4. Finally we summarise the angular response behaviour, yielding an overall estimation of the storage capacity, which is limited by the finite angular selectivity.

4.1 The Effect of Polarisation on Angular Sensitivity

4.1.1 Theoretical considerations

In the theoretical treatment of Chapter Three we neglected any complications involving the vectorial nature of light, such as optical activity or birefringence. The beam polarization (extraordinary) was taken into account firstly in the determination of the coupling constant Γ (through the change in the dielectric constant, Eq.3.20), and secondly in its effect on the modulation depth of the interference fringe pattern through the factor $\cos 2\theta$ (Eq. 3.6). Within the small recording angle approximation we could assume that the polarizations of the two beams were parallel, and could treat the light as a scalar wave. This scalar approximation implies that the polarization vectors of the light waves undergo no change whilst propagating inside the crystal. However, due to the anisotropic nature of the electrooptic materials, only the polarisation of waves which are eigenmodes of the crystal retain their polarisation unchanged while travelling through the crystal. Furthermore, diffraction from photorefractive gratings may change the polarization states of both the readout beam and the diffracted signal beam.

Herriau et al found for the first time [Her78] that the polarisation state of the diffracted wave from a grating written in photorefractive BSO could be different from that of the directly transmitted readout wave. Therefore, by inserting into the diffracted beam an analyzer (which could be adjusted to eliminate the transmitted beam), the readout SNR could be significantly improved for a nearly on-axis recording configuration. The first experiments on the polarization properties of diffraction from $LiNbO_3$ were performed by Stepanov et al [Ste77, Pet79, Pet81, Pen82]. They noted that there were two types of diffraction in optically uniaxial ($LiNbO_3$) crystals or in cubic, optically active (BSO) crystals: "isotropic or intramodal diffraction" and "anisotropic or intermodal diffraction" [Pen82].

Intramodal diffraction (the most usual type) occurs when the diffracted beam has the same polarisation state as the incident readout beam. For symmetric recording geometry the resultant grating vector is independent of the refractive index of the material. The length of the grating vector, K, depends only on the free-space propagation constant of the light wave used for recording, and the external recording angle which is regarded as the nominal Bragg angle. If the diffraction is intramodal, only one propagation constant is involved, so the readout beams with different eigenstates of polarization require the same external Bragg angle as the nominal one. Intermodal diffraction (anisotropic diffraction) is distinct from this. A vector diagram is shown in Fig.4.1a, and illustrates intermodal diffraction, in which an incident wave with one eigenstate of polarization and propagation vector, k_1', is diffracted (by the existing grating, K) into another eigenstate of polarisation

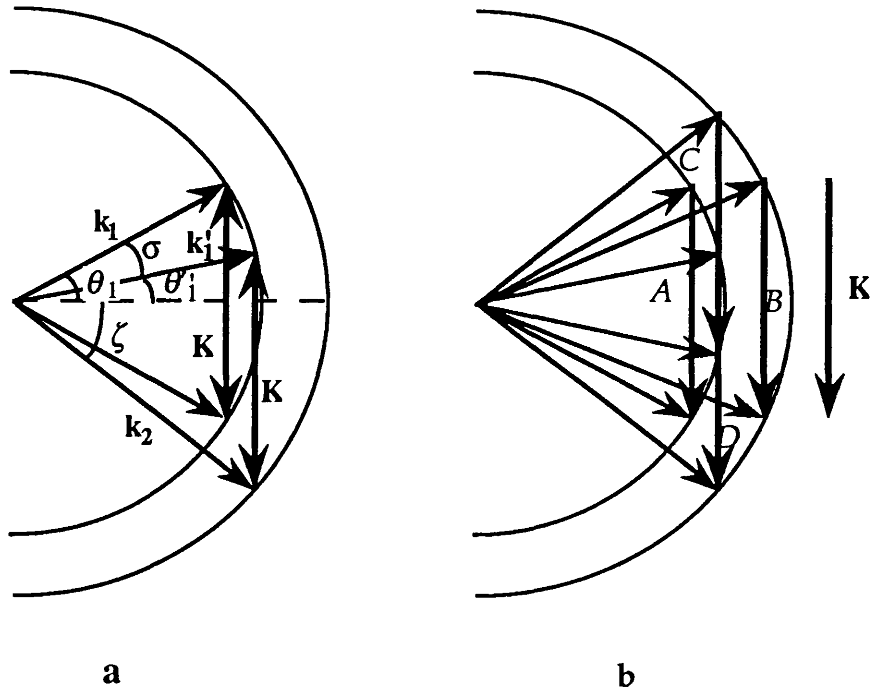

Fig.4.1 Vector diagram showing intramodal and intermodal diffraction in BSO. Two wave-surfaces correspond to left and right circularly polarized waves respectively. **a**: If intramodal diffraction occurs, the optimum incident angle is the nominal Bragg angle, θ_1. If intermodal diffraction occur, the optimum angle shifts by a small angle, σ. **b**: For an existing grating, **K**, there are four possible eigenmodes for the diffraction process in BSO: two are intramodal (*A* and *B*) and two are intermodal (*C* and *D*).

with propagation vector, $\mathbf{k}_2$. As can be seen in Fig. 4.1**a**, when intermodal diffraction occurs, the Bragg angle shifts from the nominal Bragg angle by a small amount, σ. The value of σ can be calculated in the case of BSO as follows.

If the Bragg angle for intramodal diffraction (nominal Bragg angle) is θ_1, and the Bragg angle for intermodal diffraction is θ_1', then $\sigma = \theta_1 - \theta_1'$.

From Fig. 4.1a we have

$$\begin{aligned}&2k_1\sin\theta_1=K\\&k_1\sin\theta_1'+k_2\sin\zeta=K\\&k_1\cos\theta_1'=k_2\cos\zeta\end{aligned}$$

where $k_1=|\mathbf{k}_1|, k_2=|\mathbf{k}_2|$ and ζ is the internal diffraction angle after intermodal diffraction has taken place. The change in angle is then found to be (for small σ):

$$\begin{aligned}\sigma &= (\sin\theta_1-\sin\theta_1')/\cos\theta_1\\ &= \Delta k/(K\cos\theta_1)\end{aligned}\qquad(4.1)$$

here $\Delta k=k_1-k_2=2\rho$, where ρ is the optical rotary power (rad.mm^{-1}) and K is the length of the grating vector. σ is in a different sense for left and right circular polarizations, but has the same magnitude.

Vachss and Hesselink developed a set of vector-coupled-wave equations by including the dielectric and gyratory tensors of the photorefractive material in the wave equation and by ignoring beam coupling during recording. The resulting system of equations proved to be analytically soluble in all cases, though extremely cumbersome [Vac87]. Meanwhile Marrakchi et al derived, independently, a set of coupled-wave equations which incorporated the effects of optical activity and birefringence of BSO [Mar86]. They gave the angular deviation from the nominal Bragg angle, required for intermodal diffraction, in BSO (σ) as

$$\sigma = 2\rho/K \qquad (4.2)$$

Our result (Eq. 4.1) differs from Eq. 4.2 by a factor of $\cos\theta_1$. This difference becomes significant only when θ_1 is greater than $\pi/6$ radians. A detailed description of the vector diffraction theories of Vachss & Hesselink and Marrakchi et al is beyond the scope of this thesis. In this section we simply present the results of our experiments on BSO which confirm, and can be explained by, the above theories.

Although as for all cubic crystals, BSO has no natural birefringence, it does have a significant optical activity. The optical rotation power of BSO, at a wavelength of λ=632.8nm, is 21.4°/mm, corresponding to a refractive index difference of $|n_{left}-n_{right}|=8\times10^{-5}$ [Pen82], where n_{left} and n_{right} are the refractive indices for left and right circularly polarised beams respectively. Left and right circularly polarised eigenmodes are eigenstates of propagation in BSO in the absence of applied electric fields (or internal space-charge fields). An external field, as well as an internal space charge field, induces linear birefringence in cubic crystals, like BSO, through the electro-optic effect. But this birefringence is one or two orders of magnitude lower than the optical activity due to the small electrooptic coefficient of BSO (r_{eff}=5x10^{-12}m/V [Gun82]). In this case the eigenstates of propagation in BSO crystals (with photorefractive gratings recorded in them) are approximately left and right circularly polarised eigenmodes (in fact elliptic). As can be seen in Fig. 4.1**b**, there are four possible eigenmodes of diffraction in BSO which can be modelled using the theories of Heaton et al and Kogelnik. In these, anisotropic intermodal diffraction for different circularly polarised readout beams must be taken into account.

4.1.2 Experimental results

In this subsection we present the results of our experiments to discover the effect of polarisation on the angular sensitivity of gratings recorded in BSO. The experimental technique was to measure the angular response curves with the highest accuracy possible. For recording we used a symmetric transmission geometry and a crystallographic orientation optimized for holographic storage [Mar81] (grating vectors were parallel to the external field which was applied through the pair of crystal $1\bar{1}0$ faces, see Fig. 4.2**a**). The recording wavelength was 514.5nm and the readout wavelength was 632.8nm, which eliminated erasure during readout. Details of the experimental apparatus are described in Appendix A.

The experimental arrangement is shown in Fig.4.2. A BSO crystal of 2.98mm thickness (supplied by GEC Hirst Research Centre, Wembley, UK) was mounted on a Micro-Controle motor-driven rotary stage, having an angular resolution of 0.001°. The diffraction efficiency was monitored using a Newport picowatt digital power meter. Both the rotary stage and the power meter were controlled by an IBM-PC computer through an IEEE-488 interface. Horizontally polarised light from a Spectra-Physics argon ion laser (λ=514.5nm) was split into a reference beam and an object beam. Both writing beams were expanded, collimated and apertured to give a beam size large enough to fully illuminate the crystal at angles of $\pm\theta_{ext}$ to the normal of the crystal 110 face (Fig.4.2a), with a beam intensity ratio of unity. An external field E_{so} = 6KV/cm (or -6KV/cm) was applied through the pair of crystal $1\bar{1}0$ faces. The recording intensity was about 20mW/cm^2 and the exposure time was long enough (typically 10-60 seconds) to saturate the diffraction efficiency. After recording, the argon-ion laser was turned off. The readout beam from a Melles-Griot He-Ne laser (λ=632.8nm) was expanded, collimated and apertured to give a beam diameter of 7mm. A polariser and quarter-wave-plate pair allowed the polarisation state of the readout beam to be linear or left-or-right circular. The readout beam was carefully angled to match the Bragg condition corresponding to replay at the longer wavelength (Fig. 4.2b). As soon as the readout beam was turned on, the crystal was rotated in steps of 0.002-0.005^o so as to scan the angle of readout beam about the Bragg angle. The diffracted power was measured for each step. The intensity of the readout beam was carefully adjusted to be 100μW/cm^2 in most of the measurements, so as to obtain a reasonable signal to noise ratio, with no obvious erasure of the grating during the measurement. A 100 step measurement required about 60 seconds. For some measurements the external field was maintained to make the grating last long enough for repeated measurements [Del89]. The measurements were performed for recording angles of θ_{ext}= 5^o, 8^o, 12.5^o and 15.5^o (where θ_{ext} is the angle used in recording, external to the crystal, and θ_0 is the corresponding internal angle).

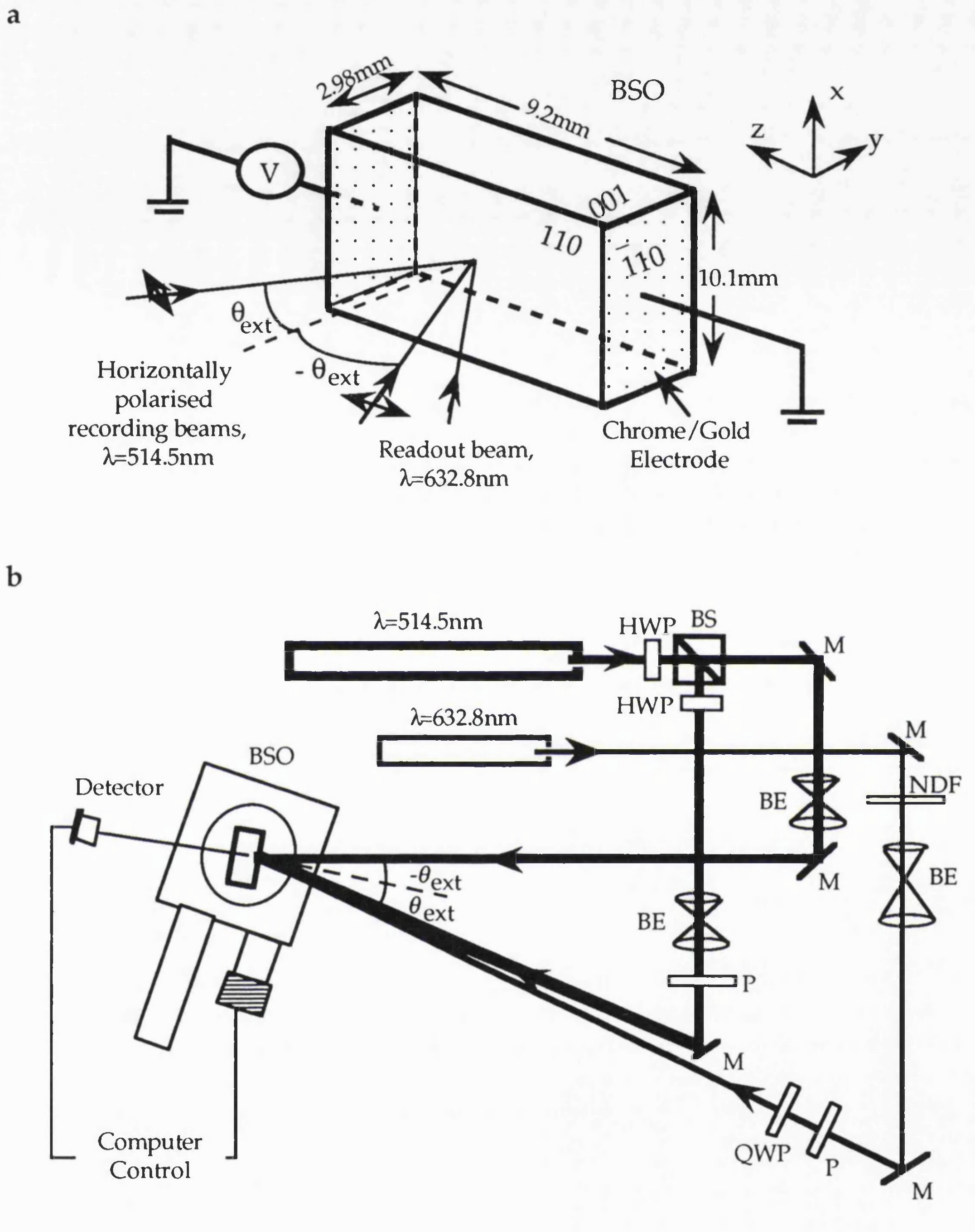

Fig. 4.2 Experimental arrangement for investigating the effect of polarisation on the angular sensitivity of gratings recorded in BSO. **a** BSO crystal orientation and size. **b** Schematic diagram showing the experimental set-up. HWP: half wave plate; QWP: quarter wave plate; BS: beam splitter; BE: beam expander; P: polariser; M: mirror; NDF: neutral density filter.

Initially we recorded gratings with an applied electric field of 6kV/cm, using recording angles of $\theta_{ext}= 8^o$ and 15.5^o. On switching off the external field, we replayed the gratings using linearly polarized readout beams. Curves of the normalised diffraction efficiency versus angular deviation from the Bragg angle were plotted, and these can be seen in Fig. 4.3a and Fig. 4.3b (for $\theta_{ext}= 8^o$ and 15.5^o respectively). We have assumed in Fig. 4.3 that the experimental maximum efficiency occurred when the grating was read at the nominal Bragg angle. This is because setting the incident angle to the Bragg angle within a few thousandths of a degree for readout at a different wavelength was impossible in practice.

For comparison, curves showing the same quantity, as calculated by the theories of Kogelnik (Eq. 2.17 in Chapter 2) and Heaton et al (Eqs. 3.37-3.38 in Chapter 3), are also drawn in Fig. 4.3 using the same axes. In the calculations the experimentally measured maximum diffraction efficiency of 2% was used to determine the coupling constant (Γ in Eq. 3.37-3.38 and v in Eq. 2.17). The same answers were given by the two different theoretical approaches, implying that the angular selectivity of BSO is more sensitive to geometric factors (such as the crystal thickness and recording geometry) than to photorefractive complexities. The form of the theoretical and experimental curves agree qualitatively but the absolute magnitudes of the selective angles do not agree very well. The measured selective angles were 50-90% greater than the calculated results. In Table 4.1 are listed the calculated and measured selective angles for different gratings and different polarisation states of the readout beams.

Now we shall consider the effects of using circularly polarised readout beams. We performed the experiments using readout beams with both left and right circular polarisation. Circularly polarised beams gave a much better agreement between experiment and theory for the selective angles (Fig. 4.4). Neither of the theories of Kogelnik nor Heaton et al assume a particular polarisation state for the readout beam, as long as the polarisation does not change during its propagation through the crystal. Since circularly polarized waves are approximate eigenmodes of BSO, and therefore, suffer a negligible polarisation change whilst propagating through the BSO, we would expect a very close agreement between experiment and theory, and this is what we observe.

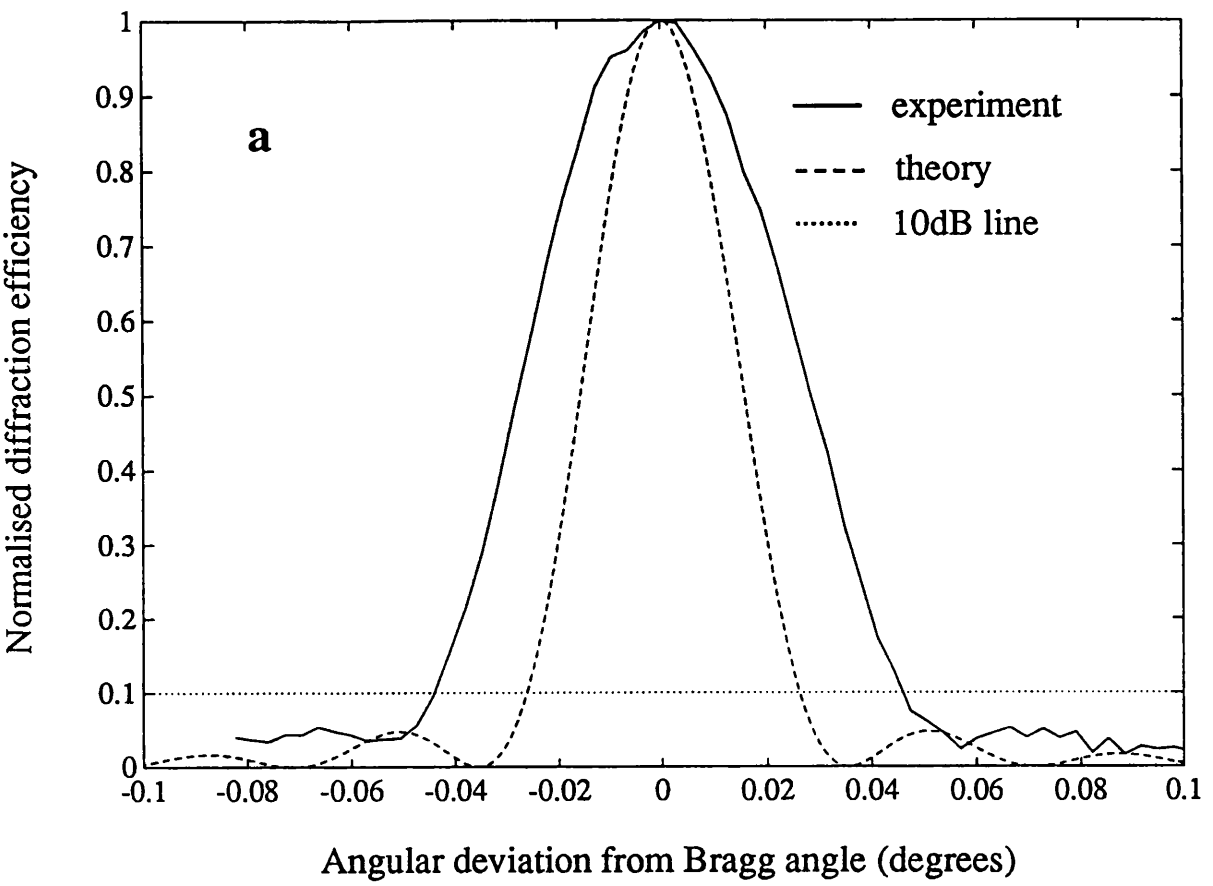

Fig. 4.3a Angular sensitivity curves for a typical grating written in a BSO crystal. Grating spacing $\Lambda=1.85\mu m$ ($\theta_{ext}=8^o$). A linearly polarized readout beam is used and no external field is applied during replay. The theoretical curves calculated from both theories, i.e. Eq.(2.17) and Eqs.(3.37-3.38) are indistinguishable from each other and so appear as one curve.

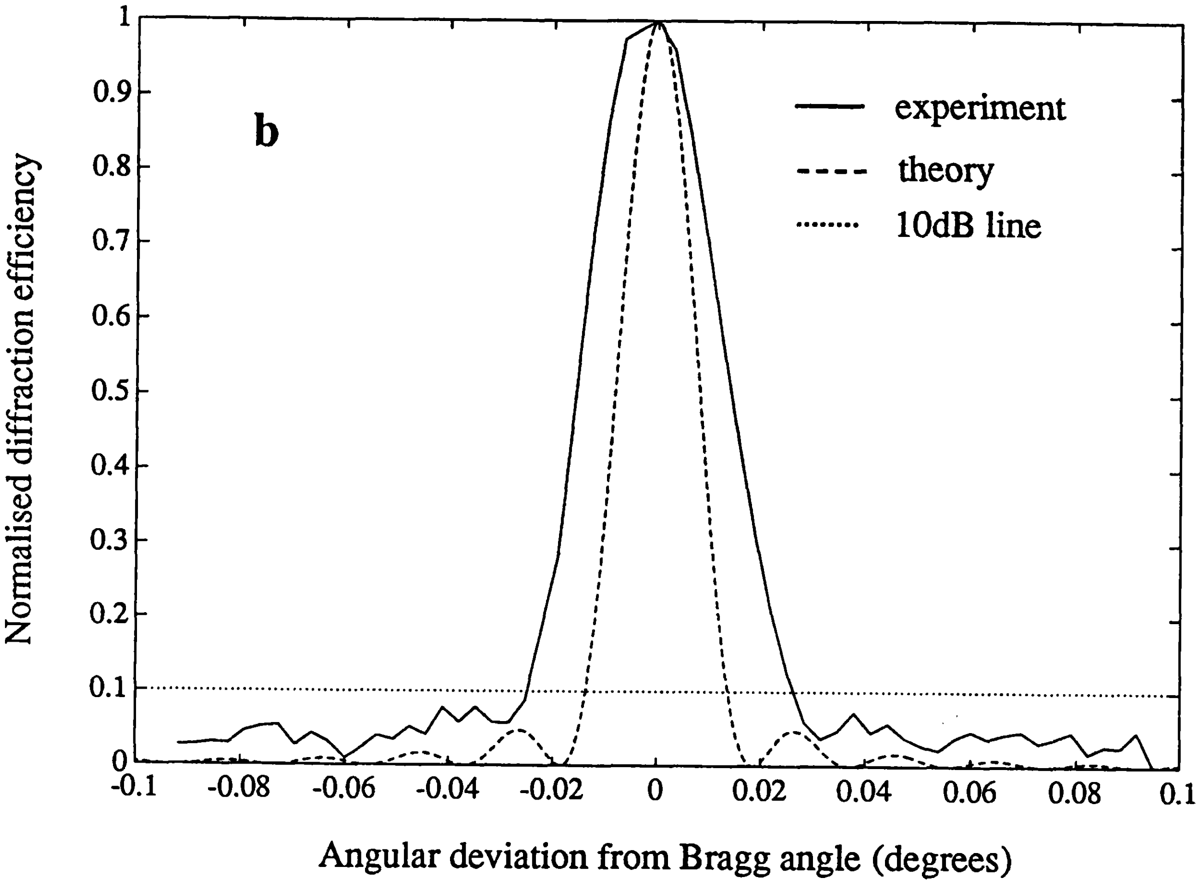

Fig. 4.3b Angular sensitivity curves for a typical grating written in a BSO crystal. Grating spacing Λ=0.96μm (θ_{ext}=15.5°). A linearly polarized readout beam is used and no external field is applied during replay. The theoretical curves calculated from both theories, i.e. Eq.(2.17) and Eqs.(3.37-3.38) are indistinguishable from each other and so appear as one curve.

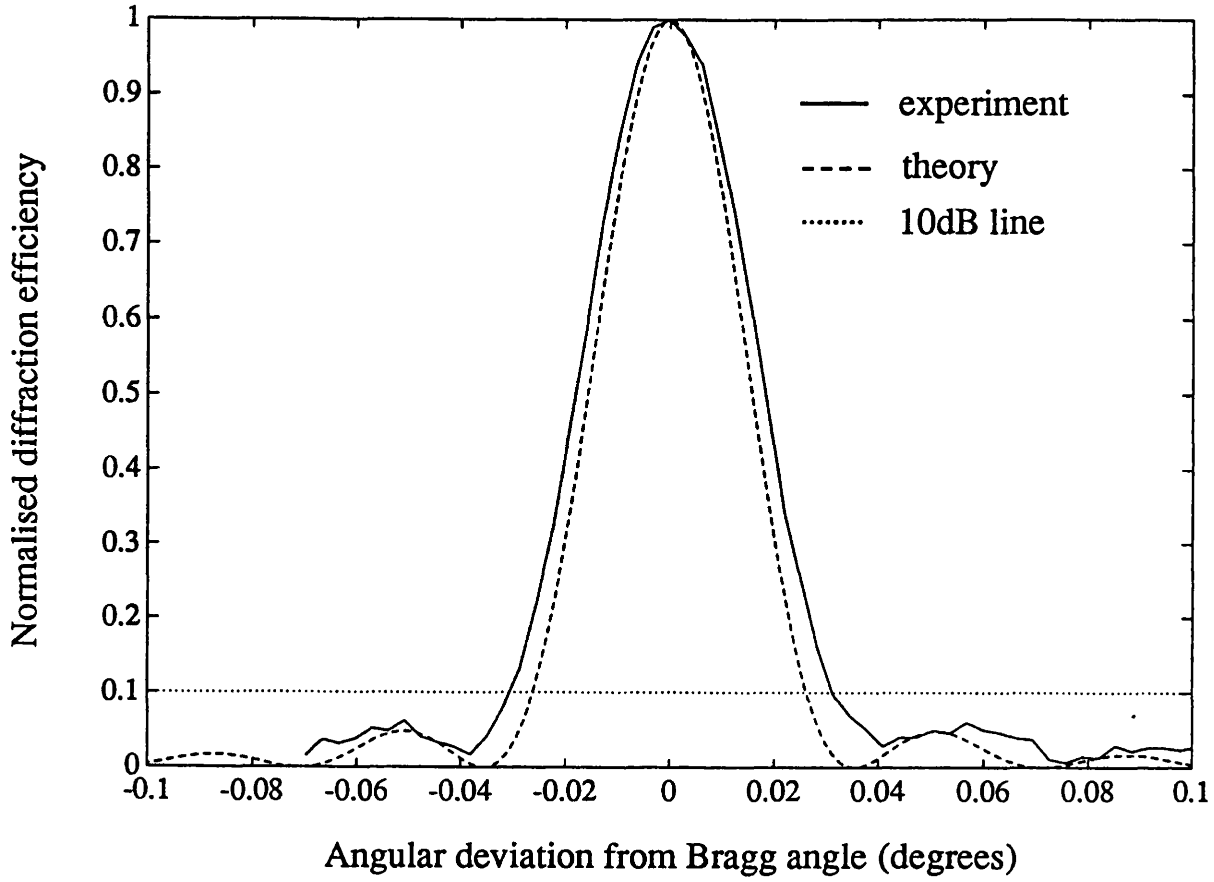

Fig. 4.4 Angular sensitivity curves for a grating written in a BSO crystal. Grating spacing $\Lambda=1.85\mu m$ ($\theta_{ext}=8^o$). A circularly polarized readout beam is used and no external field is applied during replay. The theoretical curves are the same as in Fig. 4.3a.

The intermodal diffraction of a grating recorded with $\theta_{ext}=8^o$ is shown in Fig.4.5. The polarization of the readout beam was chosen to be left circular, right circular and vertically linear respectively, and the angular response curves were measured for these three cases. The average of the two curves measured for the two circularly polarised readout beams was calculated and plotted in the same figure, so in total four curves are shown. The measured angular sensitivity curve for the linearly polarized readout beam agrees very well with the average of the two separate curves, measured using left and right circularly polarized readout beams respectively. This is to be expected since linearly polarised light is composed of equal quantities of left and right hand circularly polarised light. The angular peak positions measured for left and right circularly polarised light are each shifted in opposite senses from the nominal Bragg angle by an angle, σ, see Eq. (4.1). The angular separation of the two circular peaks, 2σ, was measured and is compared with theory in Table 4.2. Since the two different circularly polarised readout beams require different Bragg angles, we believe that we have observed intermodal diffraction in BSO for this specific crystal orientation (K perpendicular to <001>).

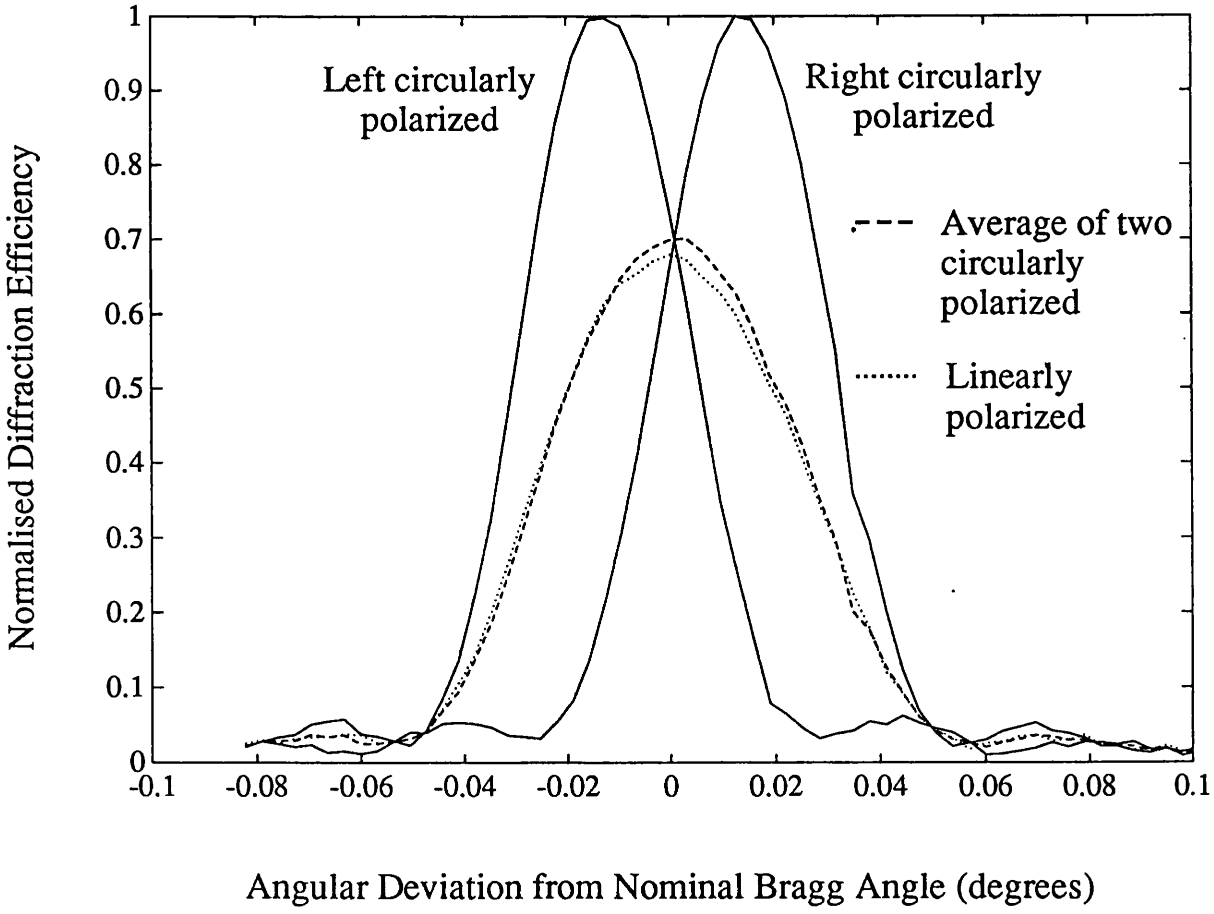

Fig. 4.5 Angular selectivity curves measured for a typical grating (Λ=1.85μm, $\theta_{ext}=8^o$) showing intermodal diffraction.

Table 4.1 lists the selective angle (external) dependence on grating spacing and polarization state of readout beam. The measured selective angles for linearly polarised readout beams were 50-90% greater than the calculated results depending on the grating spacing. In the far right hand column of Table 4.1 we present the measured selective angle for circularly polarised light as a function of grating spacing for two gratings. This is in fairly close agreement with the theoretical predictions of Kogelnik and Heaton *et al.* The measured selective angles are 0.01^0 greater than the calculated ones. This can be partly explained as being due to the diffraction limited angular spread caused by the finite crystal entrance size of 9.2x10.1 mm^2 and the finite readout beam diameter of 7mm.

Table 4.1: Selective Angle (External) Dependence on Grating Spacing and Polarization State of Readout Beam

external recording angle θ_{ext} (degrees)	internal recording angle θ_0 (degrees)	grating spacing Λ (mm)	10dB angular width (degrees)		
			calculated*	measured$^{(l)}$	measured$^{(c)}$
5.00	1.91	2.95	0.084	0.131	——
8.06	3.07	1.85	0.052	0.089	0.062
12.50	4.74	1.19	0.034	0.058	——
15.50	5.85	0.96	0.027	0.051	0.037

* Results from both theories of Kogelnik and Heaton et al are the same to this level of accuracy.

(l) Readout beam is linearly polarized.

(c) Readout beam is circularly polarized.

In Table 4.2 we present the angular separation of the diffracted left and right circular beams, 2σ. As can clearly be seen the experimental angular separations agree very well with the theoretical predictions of Eq. (4.1), to within experimental error.

Table 4.2. External Angular Separation, $\pm\sigma$, between the Peak Diffraction Efficiency Directions for Left and Right Circularly Polarized Readout Beams and that for Linearly Polarized Readout Beam.

external recording angle θ_{ext} (degrees)	grating spacing Λ (mm)	nominal Bragg angle θ_1 (degrees)	Angular Separation σ (degrees)	
			calculated*	measured
8.0	1.85	3.88	0.0126	0.013
15.5	0.96	7.46	0.0066	0.007

* Using Eq.(4.1) and converted to external angle.

By making use of the experimental angular selectivities of Table 4.1 we recorded two gratings, superimposed in the same volume with an angular separation of 0.062° (0.16° external) for $\theta_{ext}=8^{\circ}$, and addressed them first by linearly and secondly by circularly polarised beams. Fig. 4.6 shows their angular sensitivity. As can be seen the circularly polarised readout beam results in lower crosstalk, and also shows about a factor of two improvement in the diffraction efficiency.

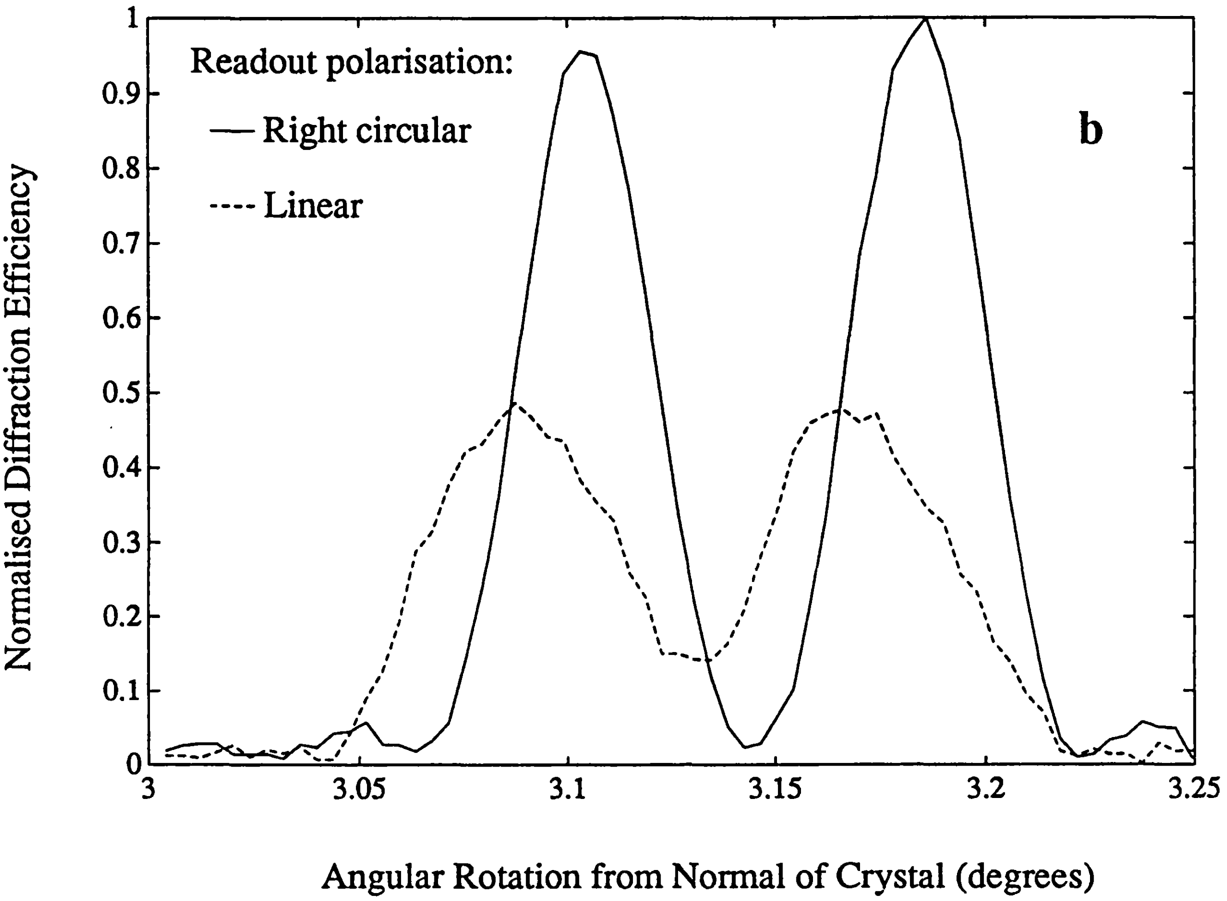

Fig. 4.6 Angular replay response of two multiplexed recordings using an external angular separation of 0.16°. Λ=1.85μm, read out by linearly and right circularly polarized beams respectively.

Finally we consider the effect that an applied electric field during replay has on the angular sensitivity. We measured the angular response curves with a positive field, a negative (reversed) field and with no field. One of the results is shown in Fig. 4.7. The presence of the applied field does not affect the selective angle, no matter whether the readout beams are linearly or circularly polarised. Also, the applied field does not affect the angle of the Bragg maximum for circularly polarised readout beams. It does, however, introduce an asymmetry when readout is performed by a linearly polarised beam. In this case the peak position shifts from that occurring without the applied field. The direction of this shift depends on the direction of the applied field.

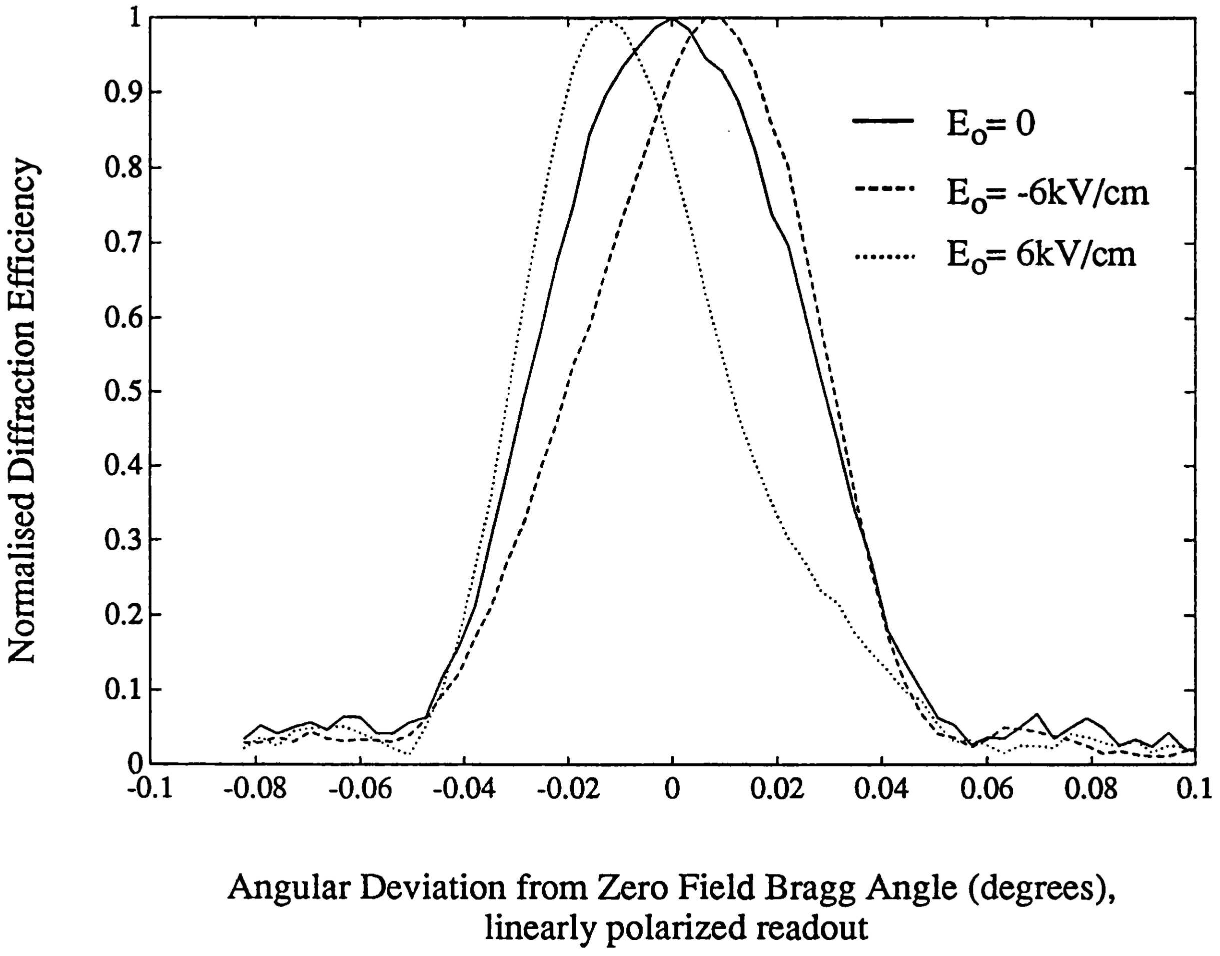

Fig. 4.7 Experimentally measured curves showing the asymmetry in the angular sensitivity of a typical grating, Λ=1.85μm, when addressed by a linearly polarized beam with and without an externally applied field, E_0, during readout.

The results of our experiments on BSO confirm the analysis of Vachss & Hesselink and the intermodal diffraction model. The results suggest that a linearly polarised readout beam usually causes a broadening of the selective angle, reduces the diffraction efficiency peaks and, in the case when an external field is applied, shifts the peak position. Therefore, we conclude that to obtain the optimum readout performance from gratings written in BSO, circularly polarised readout beams must be used.

4.2 Phase Coupling Effect: "Bragg-Shift"

Peak diffraction efficiency can, in general, be obtained for readout at a Bragg angle equal to the angle used for recording the hologram provided that the same wavelength employed in the recording stage is used in replay. This is true if static materials are used for recording. In static materials the grating fringe surfaces are parallel to the bisector of the angle between the wave vector directions of the two writing beams (interbeam angle), and these surfaces are not affected by the recording and readout processes. In photorefractive crystals, however, these fringe surfaces are predicted to be curved and will be tilted from the above mentioned bisector [Kuk79a]. Heaton et al [Hea84] concluded that, due to these curved or tilted grating surfaces, the maximum diffraction efficiencies of photorefractive gratings should, in general, occur at readout angles different from the recording angle (already discussed in Chapter Three). We refer this behaviour as to the "Bragg-shift". This theoretical prediction has never been verified experimentally. Now we are able to present detailed numerical calculations and an experimental verification of the above theory.

4.2.1 Numerical calculations

We use the theoretical model developed by Heaton et al [Hea84] (described in Chapter Three) in a detailed numerical calculation. Consider Eqs. 3.37-3.39 and Fig. 3.3. The diffraction efficiency as a function of the angular deviation from the recording angle can be calculated by solving the differential equations 3.37-3.39, in which the writing beam intensities, $I_r(y)$ and $I_s(y)$, and the phase shift, $\Delta\phi(y)$, are given by Eqs. 3.32-3.34. We calculated the curves of diffraction efficiency versus the angular deviation for a series of grating phase shifts, Φ_g (varying from $-\pi/36$ to $\pi/2$), and initial writing beam intensity ratios, m_0 (in the range 1/15 to 15). This enabled us to compare the prediction with our experimental measurements of Fe:LiNbO$_3$ samples described in the next subsection. Other parameters were set to the fixed values that were used in our experiments: d=8mm, λ=514.5nm and the external recording angle was set at $\theta_{ext}=25^0$. The refractive index for extraordinary waves, n, was taken to be 2.2 [Kir88]. A strong coupling, $\Gamma d=3$ (which corresponds to a high diffraction efficiency), was also used for the calculation. The angular deviation was converted to be that external to the crystal. From each of the above curves we found the optimum angular deviation, $\Delta\theta_{ext}$, and the corresponding maximum diffraction efficiency, η_{max}.

Figure 4.8 shows the external optimum angular deviation, $\Delta\theta_{ext}$, as a function of both the grating phase shift, Φ_g, and the recording beam intensity ratio, m_o. Zero angular deviation ($\Delta\theta_{ext}=0$) only appears along one line $\Phi_g=\pi/2$ (1.57 rad. in the figure) and one curve in the Φ_g-m_o plane. The conclusion obtained by Heaton et al (that the maximum efficiency occurs at the recording angle only for $m_o=1$), is valid only for $\Phi_g=0$. For an arbitrary grating phase shift (except for $\Phi_g=\pi/2$), there exists an initial writing beam ratio at which the maximum efficiency occurs when the grating is read out at the recording angle (for example, for $\Phi_g=3\pi/16=$ 0.59 rad, if the initial writing beam ratio, m_o, is chosen to be 5, from Fig. 4.8 we can see that the maximum efficiency occurs when the grating is read out at the recording angle).

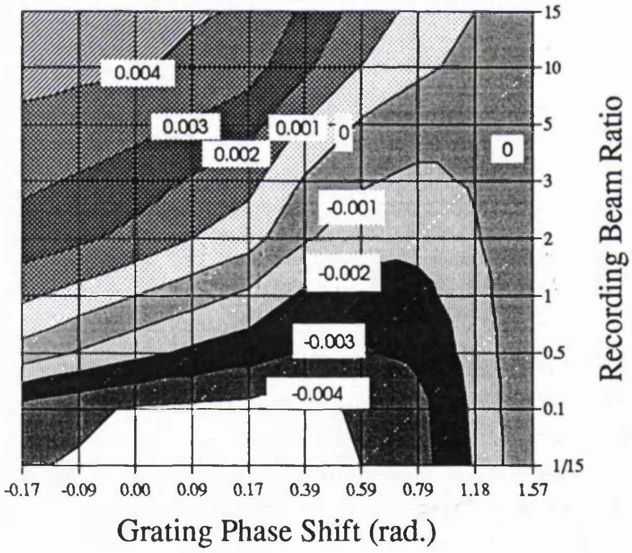

Fig. 4.8 The optimum deviation of the readout angle from the recording angle, $\Delta\theta_{ext}$, as a function of the initial writing beam intensity ratio, m_o, and the grating phase shift, Φ_g. $\Gamma d=3$, d=8mm. The labels mark the boundaries of the regions of $\Delta\theta_{ext}$.

The existence of a non-zero optimum angular deviation, $\Delta\theta_{ext}$. implies that the index grating is tilted or slanted. The readout beam is taken as (or slightly differs from) the reference beam in the calculation, so that the sense of the optimum angular deviation allows us to find the tilt direction. The tilt direction depends on both the writing beam ratio and the grating phase shift with respect to the incident light pattern. If $\Phi_g<\pi/2$ (i.e. in the non-diffusion dominant case), the optimum angular deviation, $\Delta\theta_{ext}$, in the top and bottom areas of Fig. 4.8 (corresponding to beam ratios far from unity) are in opposite senses, and are independent of the phase shift. This means that, for the extreme case when $I_r(0) << I_s(0)$, $\Delta\theta_{ext}$ is always positive, and the fringe surfaces tilts towards the reference beam, and vice versa. This is shown in Fig. 4.9.

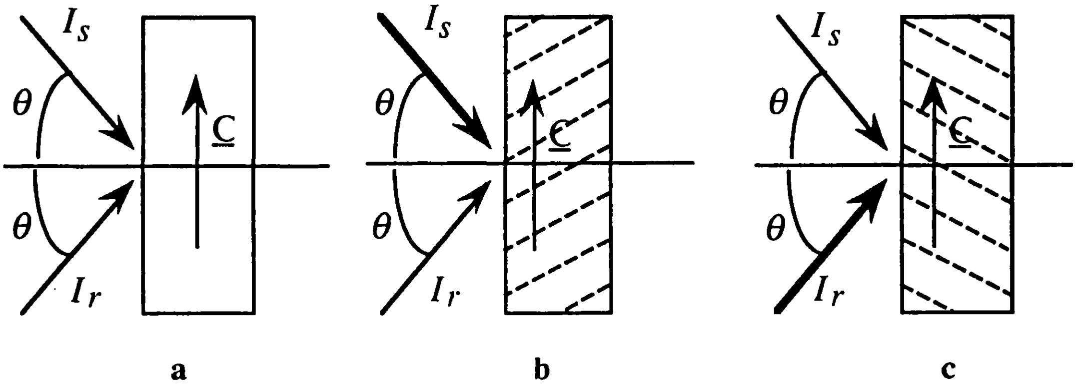

Fig. 4.9 Schematic diagram showing that the fringe surfaces of a grating written with a symmetric geometry are tilted. **a**: Writing geometry. **b**: $m_0=I_s/I_r>>1$. c: $m_0=I_s/I_r<<1$

In general, a grating written in a photorefractive crystal using a symmetrical geometry will be slanted. As a result, the original writing beams no longer satisfy the Bragg condition during replay. Kukhtarev et al claimed that their analytical formula for diffraction efficiency (given in Eq. 3.35 of Chapter Three) is valid for Bragg incidence. This is not quite true. Eq. (3.35) applies when the grating is read out at the recording angle, which, in general, differs from the new Bragg angle due to the resulting slant of the grating. Replay at the optimum readout angle should best satisfy the Bragg diffraction condition so gives the maximum efficiency.

The maximum efficiency obtained at the optimum readout angle is plotted in Fig. 4.10. For comparison, the diffraction efficiency obtained at the recording angle, η_0, can be calculated using the analytic solution, Eq. 3.35, derived by Kukhtarev et al. The calculated result (using the same parameters as the result in Fig. 4.8) is shown in Fig. 4.11. We define a diffraction efficiency enhancement factor, E_η ($E_\eta=\eta_{max}/\eta_0$), to indicate how far the diffraction efficiency can be improved by reading out at the optimum angle, rather than at the recording angle. Fig. 4.12 shows E_η as a function of Φ_g and m_0.

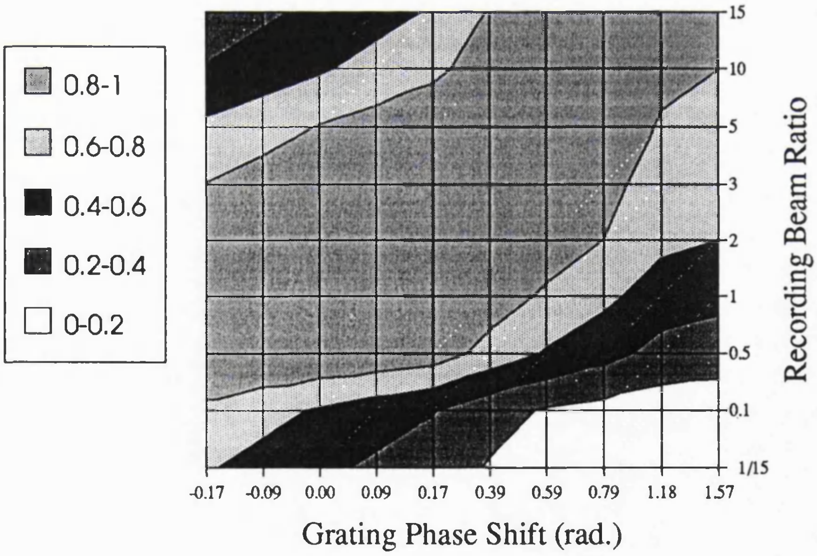

Fig. 4.10 Maximum diffraction efficiency, η_{max}, obtained at the optimum readout angle as a function of the initial writing beam intensity ratio, m_0, and the grating phase shift, Φ_g, calculated using the numerical model of Heaton et al (Eq. 3.37-3.39). $\Gamma d=3$, d=8mm.

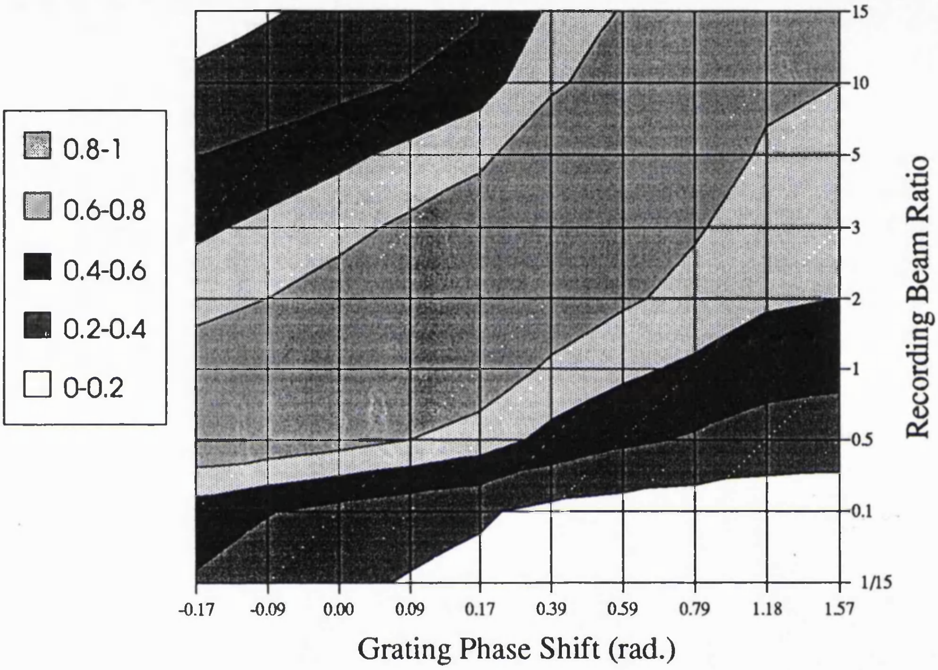

Fig. 4.11 Diffraction efficiency, η_0, obtained at the recording angle as a function of the initial writing beam intensity ratio, m_0, and the grating phase shift, Φ_g, calculated using the analytical solution of Kukhtarev et al (Eq. 3.35). $\Gamma d=3$, d=8mm.

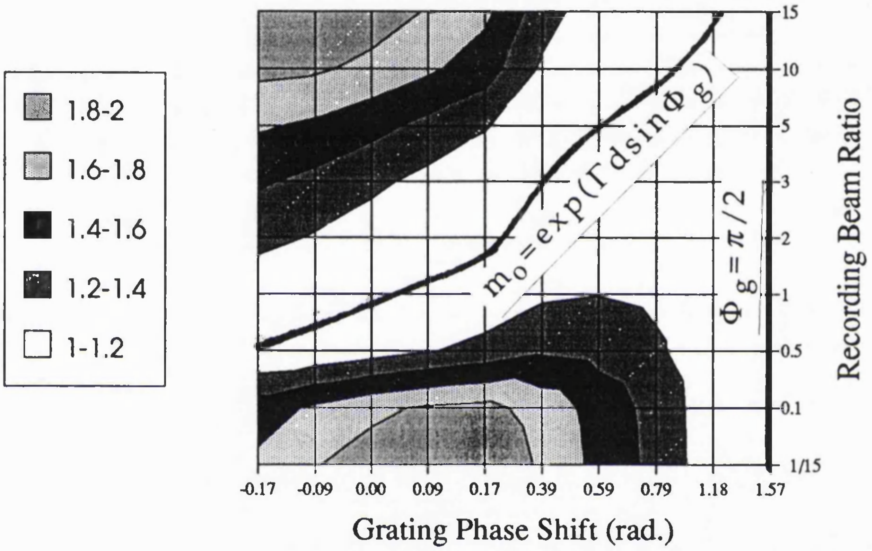

Fig. 4.12 Diffraction efficiency enhancement factor, E_η ($E_\eta=\eta_{max}/\eta_0$) as a function of the initial writing beam intensity ratio, m_o, and the grating phase shift, Φ_g. η_{max} and η_0 are taken from Fig.4.10 and Fig. 4.11 respectively. The curve $m_o=\exp(\Gamma d \sin\Phi_g)$ and the line $\Phi_g=\pi/2$ are highlighted, along which the maximum diffraction efficiency occurs at the recording angle and E_η is unity.

It can clearly be seen, by comparing Fig. 4.12 with Fig. 4.8, that E_η is proportional to the absolute value of the optimum angular deviation $|\Delta\theta_{ext}|$, and is generally greater than unity, except for the line $\Phi_g=\pi/2$

and a curve in the Φ_g - m_0 plane, for which both the numerical calculation [Hea84] and the analytic solution [Kuk79a] give the same diffraction efficiency (i.e. $E_\eta=1$), within the numerical tolerance.

We solved analytically the equation, $\frac{d\eta_0}{d\,m_o} = 0$, for a given phase shift, Φ_g, and a given coupling constant, Γ, (where η_0 is the analytical formula for the diffraction efficiency at the recording angle, derived by Kukhtarev et al, i.e. Eq. 3.35). This allowed us to find the condition, under which a maximum value for η_0 occurs. The solution was given by:

$$m_0=\exp(\Gamma d\sin\Phi_g) \qquad (4.3)$$

Equation (4.3) determines a curve in m_0-Φ_g plane (for a given Γ). This means that, for a given Φ_g (and Γ), the diffraction efficiency of a grating, recorded with an initial beam ratio satisfying $m_0=\exp(\Gamma d\sin\Phi_g)$, is greater than that for any other grating recorded with a different beam ratio (provided that the grating is read out at the recording angle). Our numerical calculation confirmed that it is this same curve, $m_0=\exp(\Gamma d\sin\Phi_g)$, along which there is no Bragg shift ($\Delta\theta_{ext}$ is zero), and therefore, along which E_η is unity (see Figs. 4.8 and 4.12). The importance of this result is that the Bragg shift introduces some complexities into the readout system for a memory stored in a photorefractive crystal, if the maximum diffraction efficiency is required. However, if Eq. (4.3) is satisfied during recording, the same recording angle can be used for readout as that used for recording, enabling the highest efficiencies to be obtained with a simple recording and readout system.

It is clear from the above discussion that, in general, the Bragg angle of a grating, formed in a photorefractive crystal, shifts slightly from the recording angle by a small angle, $\Delta\theta_{ext}$. The analytical formula for diffraction efficiency, Eq. (3.35), given by Kukhtarev et al, underestimates the maximum available diffraction efficiency, except for cases when $\Phi_g=\pi/2$ and when $m_0=\exp(\Gamma d\sin\Phi_g)$. If the readout is carried out at the new Bragg angle (the optimum readout angle) the diffraction efficiency may be significantly enhanced. In the next subsection we present experimental measurements verifying this conclusion.

4.2.2 Experimental measurements

Two iron doped lithium niobate crystal samples were used in the experiments; sample 1 had a doping concentration of 0.015mol% (which is equivalent to 0.016wt%) and a size of 20x4.7x20 mm^3 (XxYxZ), and sample 2 had a doping concentration of 0.1wt% and a size of 18x8x20 mm^3 (XxYxZ). Due to the relatively heavy doping, it was difficult to coherently erase the crystals after recording. Our experiments showed that following exposure and erasure some of the crystal parameters (write and erase time constants for example) became modified. To allow a comparison between gratings, all gratings were recorded in "fresh" spatial locations on the crystal face, i.e. well separated from each other in regions unexposed following a thorough erasure using incoherent UV light.

We used an experimental set-up similar to that used for investigating the angular sensitivity of gratings in BSO as shown in Fig. 4.2**b**. The low writing sensitivity, and even lower erasure sensitivity of these $LiNbO_3$ samples, allowed us to use a similar wavelength for both recording and replay. It also allowed the grating formation process to be monitored by blocking the signal beam at regular intervals (typically, every 10 seconds) and sampling the power diffracted from the reference beam by the grating which was being formed. Each sampling lasted about 0.8 seconds which was chosen to be short enough so that negligible erasure and self-enhancement (which we will discuss in Section 4.4) should occur to the existing grating. Immediately after recording we measured the angular response curves by monitoring the diffraction efficiency whilst scanning the readout beam (one of the two writing beams) around the recording angle.

Some typical experimental curves for sample 1 are shown in Figs. 4.13-4.15 corresponding to the initial writing beam ratios m_0=0.10, 1.00 and 10.0 respectively. In Figs. 4.13-4.15 the figures labelled **a** correspond to grating formation, showing the diffraction efficiency histories up to saturation. The last data indicates the final diffraction efficiencies when read out at the recording angle. The figures labelled **b** show the angular response curves of the resultant gratings, illustrating not only the shift of the peak efficiencies but also the fact that the maximum efficiencies were about 30% to 50% higher than the final values shown in part **a** when the writing beam intensity ratio was much different from unity. The optimum angular deviations can be easily found from these curves. For the case of $m_0=1$, the efficiency enhancement is not obvious although the peak efficiency shifts by -0.001° to -0.002° which we have confirmed by repeated measurements.

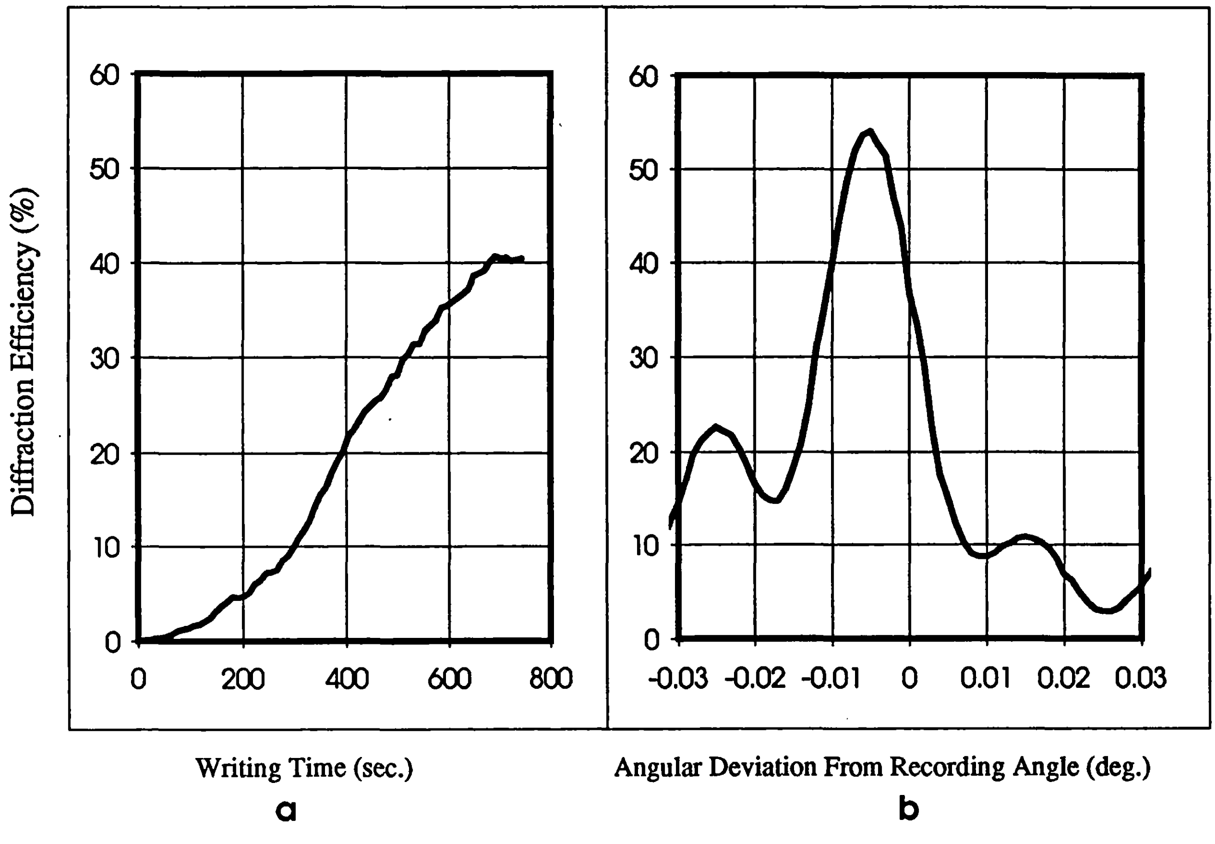

Fig. 4.13 Experimentally measured curves for $m_0=0.10$. a Grating formation, b angular response of the resultant grating. The maximum diffraction efficiency occurs when the readout angle is 0.006° less than the recording angle. It is about 35% greater than that achieved when read out at the recording angle by the end of recording .

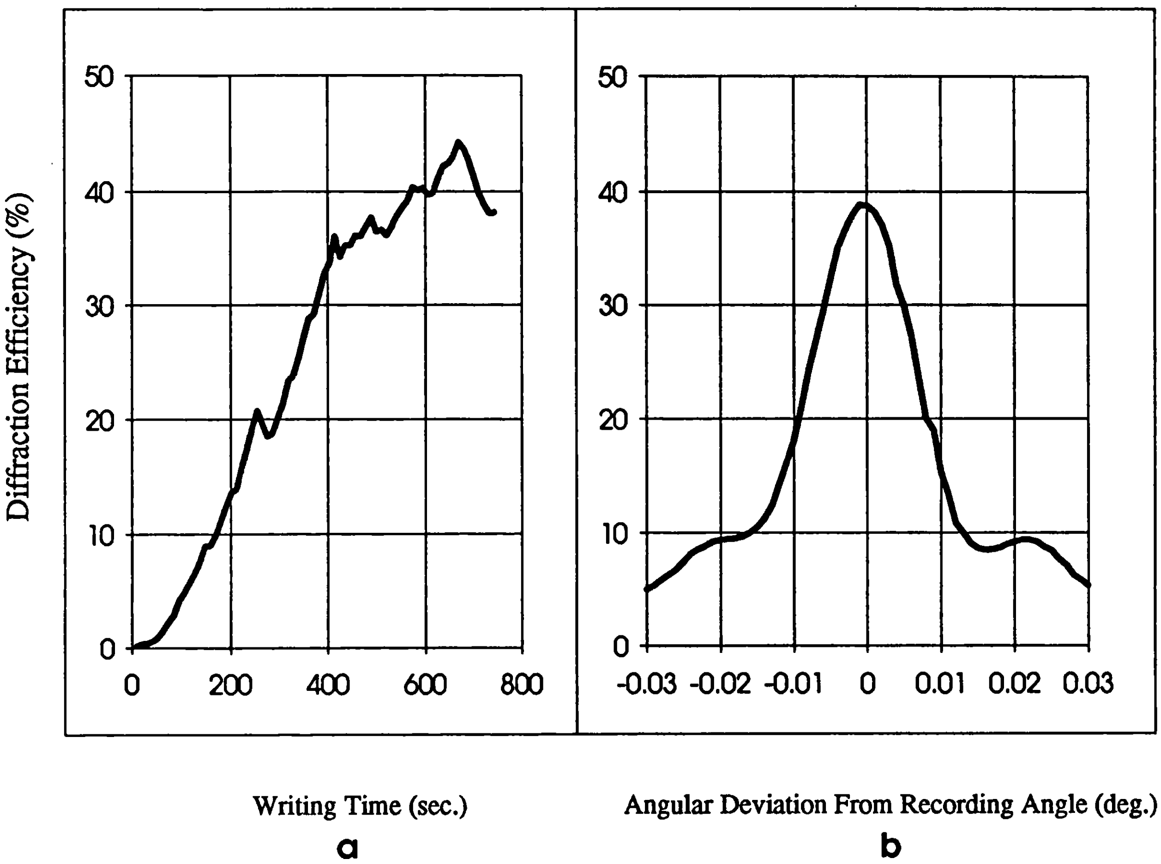

Fig. 4.14 Experimentally measured curves for m_0=1.0. a Grating formation, b angular response of the resultant grating. The maximum diffraction efficiency occurs when the readout angle is 0.001^0 less than the recording angle. It is slightly greater than that achieved when read out at the recording angle by the end of recording.

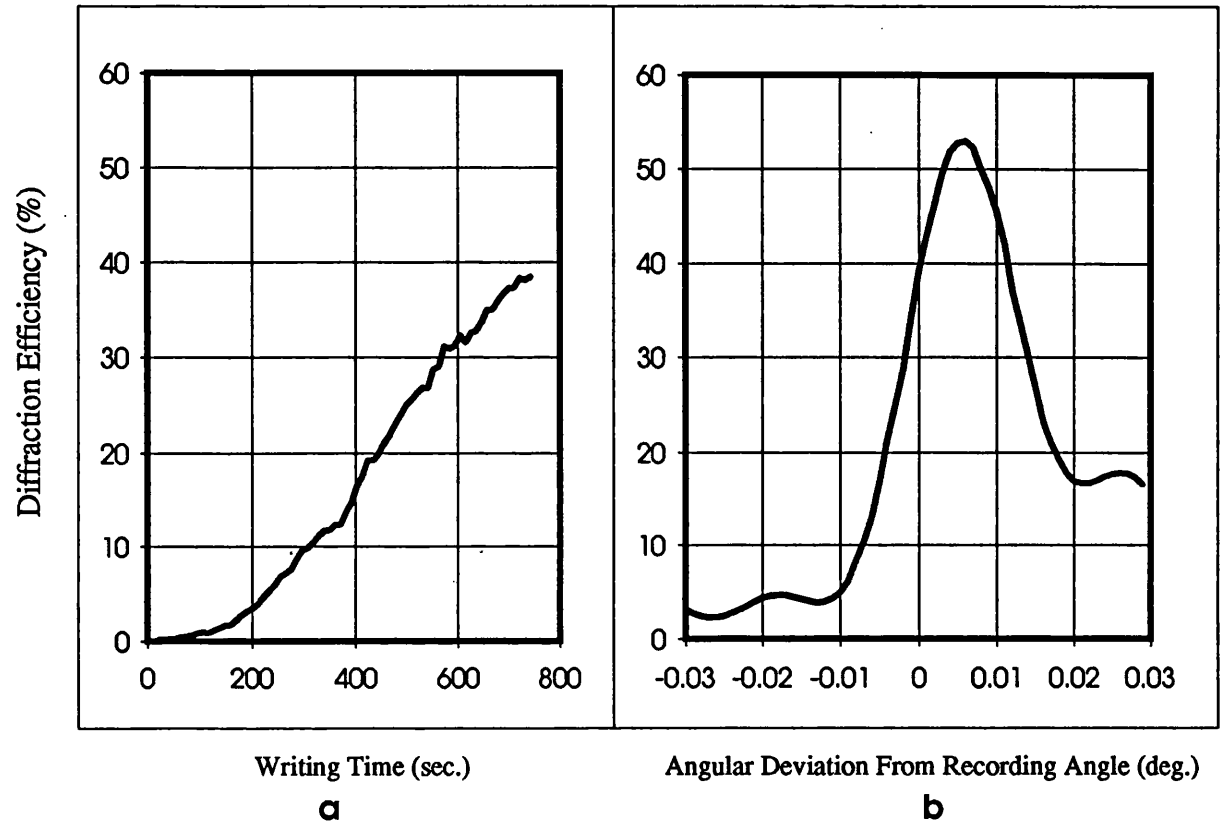

Fig. 4.15 Experimentally measured curves for $m_0=10.0$. a Grating formation, b angular response of the resultant grating. The maximum diffraction efficiency occurs when the readout angle is 0.006° greater than the recording angle. It is about 35% greater than that achieved when read out at the recording angle by the end of recording.

We also performed a series of measurements of the optimum angular deviation for both samples and the results are shown in Fig. 4.16 together with numerically calculated curves for comparison. One can see the good qualitative agreement between experiment and theory. The measured angular deviation has the same order of magnitude and the same form as that predicted by the theory for $\Phi_g \sim 0.17$rad ($\pi/18$).

From the measured diffraction efficiencies we estimated that Γd is approximately 1.6 for sample 2. However, the theoretical curves shown are for $\Gamma d=3$. The analytical solution of the optimum deviation of the readout angle from the recording angle in the special case that $\Phi_g=0$, derived by Heaton et al (Eq. 3.40c in Chapter Three), suggests that the optimum angular deviation should be proportional to Γd, so that the measured $\Delta\theta_{ext}$ are generally greater than the theoretical predictions (Fig. 4.16).

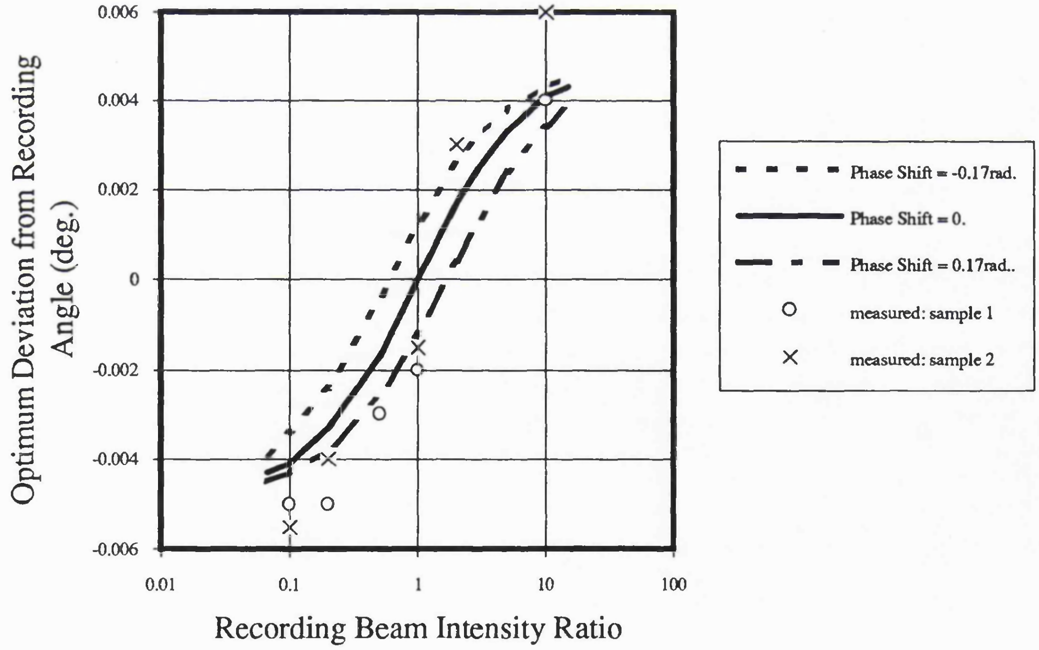

Fig. 4.16 A comparison of the measured $\Delta\theta_{ext}$ with numerically calculated results. The calculated data is taken from Fig. 4.8.

The numerical calculations and the experiments we have discussed so far are only concerned with plane gratings. The diffraction efficiency enhancement effect is particularly significant when Fourier transform holograms are recorded (a commonly used technique for multiple holographic storage). Fig. 4.17 shows an example recording in crystal sample 2, using a writing beam ratio estimated to be 0.01. The signal beam on the crystal was the Fourier transform of a binary pattern displayed on a spatial light modulator and illuminated by a plane signal beam shone through a diffuser. The diffraction enhancement factor E_η was as high as 230%.

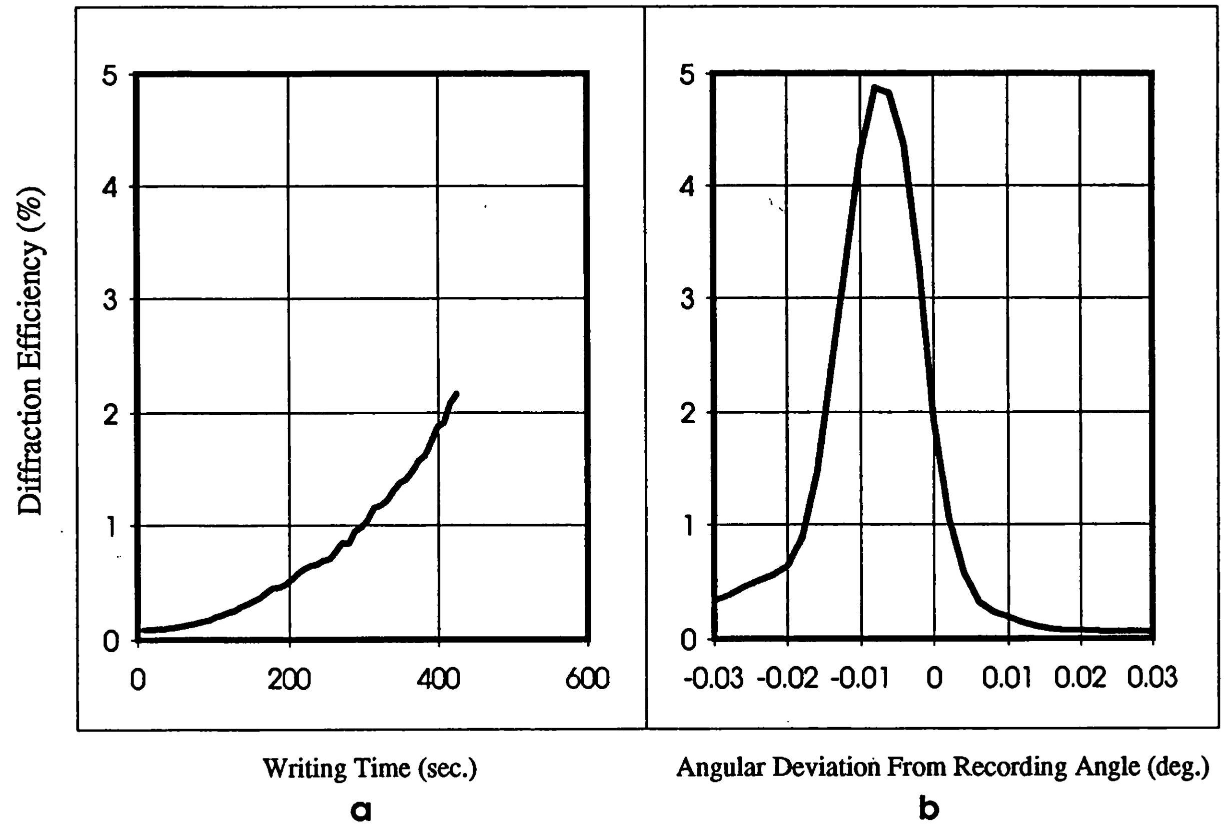

Fig. 4.17 A typical experimental result for a Fourier transform hologram with m_0~0.01. a. hologram formation, b. angular response of the resultant hologram.

In conclusion, we have found experimentally that in most practical cases the maximum diffraction efficiency of gratings formed in photorefractive Fe:$LiNbO_3$ crystals occurs at a readout angle different from the recording angle (when similar wavelengths are used in recording and replay). To our knowledge this is the first time that experimental verification has been provided for a shift in the Bragg angle, theoretically predicted more than twenty years ago. This shift can be fully explained by previously published theories on curved or tilted gratings and is due to phase coupling during grating formation. There is a good agreement between experimental measurements and numerical calculation. Although more accurate equipment is required for precise measurements when beam intensity ratios are close to unity, the measured results for most cases are repeatable and reliable. To obtain uniformly high efficiencies from holographically stored data-bases written in photorefractive materials, the effects of this diffraction efficiency enhancement must be taken into account.

4.3 Intensity Coupling Effect on Angular Sensitivity

In this section we discuss the angularly sensitivity of photorefractive crystals. This departs from the prediction of the basic Kogelnik theory, but can be explained by including intensity coupling between the writing beams during grating formation, together with absorption in the crystal.

We have measured angular response curves for BSO (Figs. 4.3-4.4), which show the same shape as that predicted by the theories of both Kogelnik and Heaton et al, but which are wider. The broadening can be well explained, using the intermodal diffraction theory discussed in Section 4.1. In fact, application of the experimental data for BSO to the theories of both Kogelnik and Heaton et al leads to very similar curves for each theoretical model (symmetric, side lobe peaks much lower than the main peak, well-defined periodic nulls, etc.). However, this does not mean that incorporation of photorefractive self-diffraction into the coupled-wave theory (Heaton et al) does not affect the shape of the angular response curves. The observed similarity of the two theories in this case arises from the very weak coupling (small Γd) in BSO, and because they are based on the same assumption, that gratings recorded in photorefractive crystals are lossless. The absorption of light in the storage material has been neglected during grating formation in these theories. If the coupling strength and the optical thickness, αd (α is the absorption coefficient and d is the thickness of the crystal), were both to increase (as in the case of $LiNbO_3$), the situation would be substantially changed.

Our measurements with several $LiNbO_3$ samples under various experimental conditions repeatedly show that the angular response curves usually have non-zero minima and higher side lobes than in theory. (Experimental curves of doped $LiNbO_3$ crystals showing non-zero minima were obtained by Arizmendi et al [Ari87] but this feature did not draw their attention.) Typical curves are shown in Fig. 4.18 which compares experimental measurements on two samples of $LiNbO_3$ to the theory of Kogelnik. Fig. 4.18a shows the angular response curve of a grating written in a 2.5mm thick 0.015mol% Fe:$LiNbO_3$ crystal, using a symmetric recording geometry, with a recording angle of $\theta_{ext}=15^o$. A theoretical curve, calculated using the theory of Kogelnik (Eq. 2.17), is also shown. The minima and side lobes of the measured curve are higher, and the measured main lobe width is wider than predicted by the theory of Kogelnik (see Fig. 4.18a). Furthermore, there always exists an asymmetry (with respect to the main peak) accompanied by the presence of a Bragg shift, discussed in the last subsection (see Figs. 4.13 and 4.15). Theoretically calculated and experimentally measured angular response curves, for a grating written in an 8mm thick 0.1wt% Fe:$LiNbO_3$ crystal, are shown in Fig. 4.18b. A symmetric recording geometry was used for recording and the recording half interbeam angle, θ_{ext} was 25^o. The theoretical curve is calculated using the theory of Kogelnik (Eq. 2.17). In this figure all of the side lobes for the measured curve vanish, and the curve of diffraction efficiency versus angular deviation magnitude becomes monotonic. This is in contrast to the prediction of Kogelnik's theory, using the lossless phase grating model.

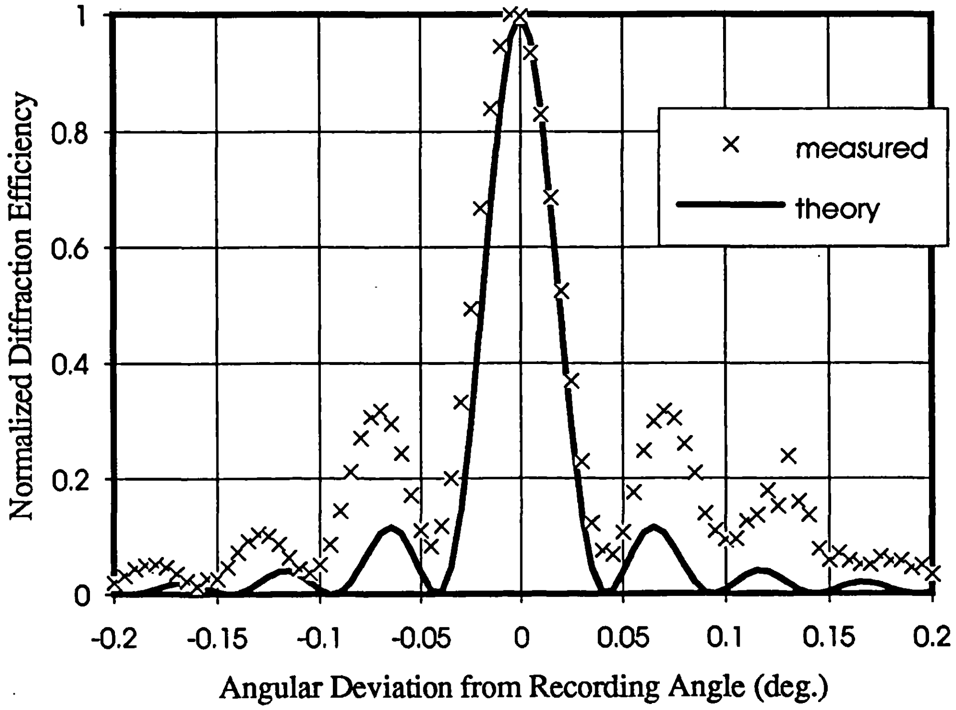

Fig. 4.18a Theoretical and experimental results for the angular response of a grating written in a 2.5mm thick 0.015mol% Fe:LiNbO$_3$ crystal. A symmetric recording geometry was used with a recording angle of $\theta_{ext}=15^o$. The theoretical curve is calculated using the theory of Kogelnik (Eq. 2.17).

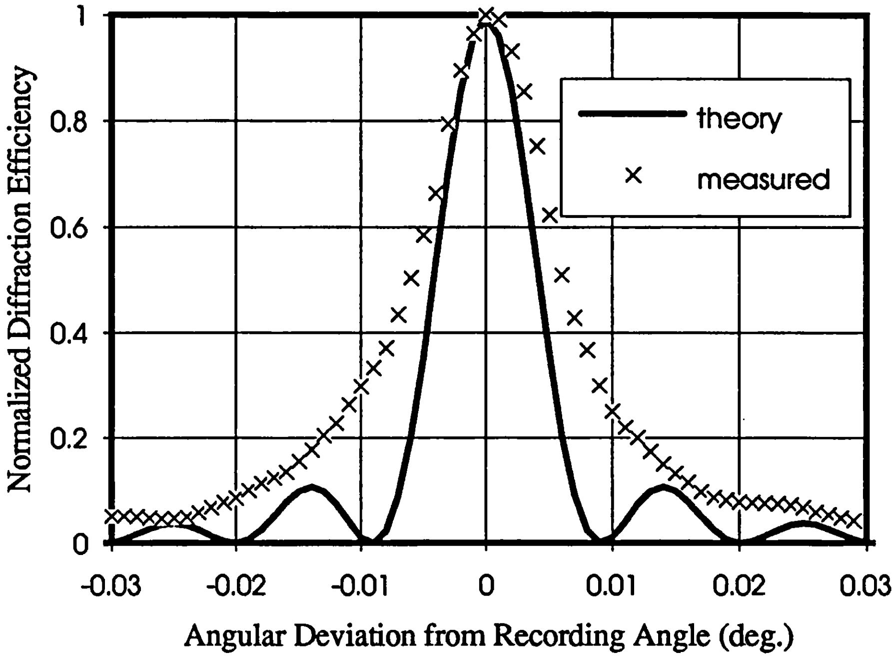

Fig. 4.18b Theoretical and experimental results for the angular response of a grating written in an 8mm thick 0.1wt% Fe:$LiNbO_3$ crystal. A symmetric recording geometry was used with a recording angle of $\theta_{ext}=25^o$. The theoretical curve is calculated using the theory of Kogelnik (Eq. 2.17).

The above mentioned phenomena are believed to arise from the non-uniformity of the grating modulation depth. This is a result of two factors: the presence of absorption during grating formation, and the intensity coupling during grating formation. The effect of absorption on the angular sensitivity which has been theoretically analysed and experimentally verified by many authors, and (if the absorption during recording is large) results in the presence of non-zero minima and monotonic "wings" in the angular response curves (see, for example, [Kub78], and also a review by Solymar and Cooke [Sol81]). The intensity coupling effect is discussed here, and can be explained by the theory of Heaton et al.

The analytic form of the efficiency vs angular deviation curve (in the case that $\Phi_g=0$, i.e. phase coupling only), given by Heaton et al (see Eq. 3.40a), is similar to that given by the theory of Kogelnik. This cannot, therefore, predict any non-zero minima. On the other hand, the curves for $\Phi_g=\pi/2$ with a large coupling strength ($\Gamma d=3.0$), presented by Heaton et al (see Fig.5 in [Hea84]), showed that the first few minima are usually non-zero. We applied the numerical model of Heaton et al to the case of a small grating phase shift (which is close to our experimental situation) and a large coupling constant. The calculated results are shown in Figs 4.19 and 4.20. Although the quantitative agreement with the experimental curves is not very good, the trend roughly agrees: In Fig. 4.19, the theoretical and experimental curves for the angular response of a grating written in a 2.5mm thick 0.015mol% Fe:$LiNbO_3$ crystal are shown. A symmetric recording geometry was used with a recording angle of $\theta_{ext}=15^o$. The theoretical curve was calculated using the numerical model of Heaton et al (Eq. 3.35-3.37) with parameters $\Gamma d=5$ and $\Phi_g=0.17$rad. Both curves show high side lobes and non-zero first minima. In Fig. 4.20, The angular response curve of a grating written in an 8mm thick Fe:$LiNbO_3$ crystal, calculated using the numerical model of Heaton et al (Eq. 3.35-3.37) with parameters $\Gamma d=12$, $d=8$mm, $m_0=1/15$ and $\Phi_g=0.17$rad is shown. A symmetric recording geometry was used with a recording angle of $\theta_{ext}=25^o$. Bragg shift, non-zero nulls, broadening and asymmetry of the angular response can be seen, which were seen in the experimental measurements of Figs. 4.13-4.15, 4.18 and 4.19.

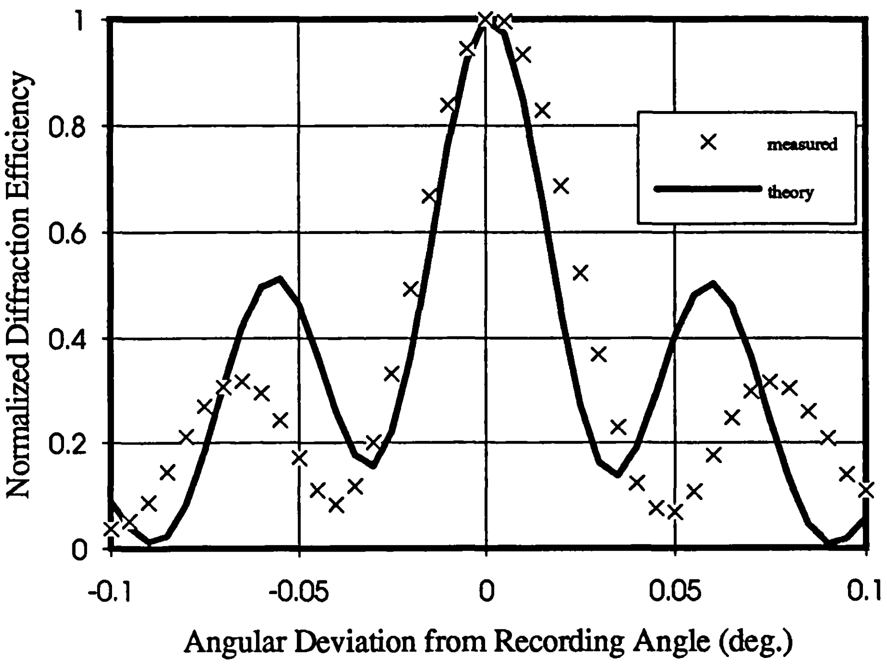

Fig. 4.19 Theoretical and experimental results for the angular response of a grating written in a 2.5mm thick 0.015mol% Fe:$LiNbO_3$ crystal. A symmetric recording geometry was used with a recording angle of $\theta_{ext}=15^o$. The theoretical curve was calculated using the numerical model of Heaton et al (Eq. 3.35-3.37) with parameters $\Gamma d=5$ and $\Phi_g=0.17$rad. Both curves feature high side lobes and non-zero first minima.

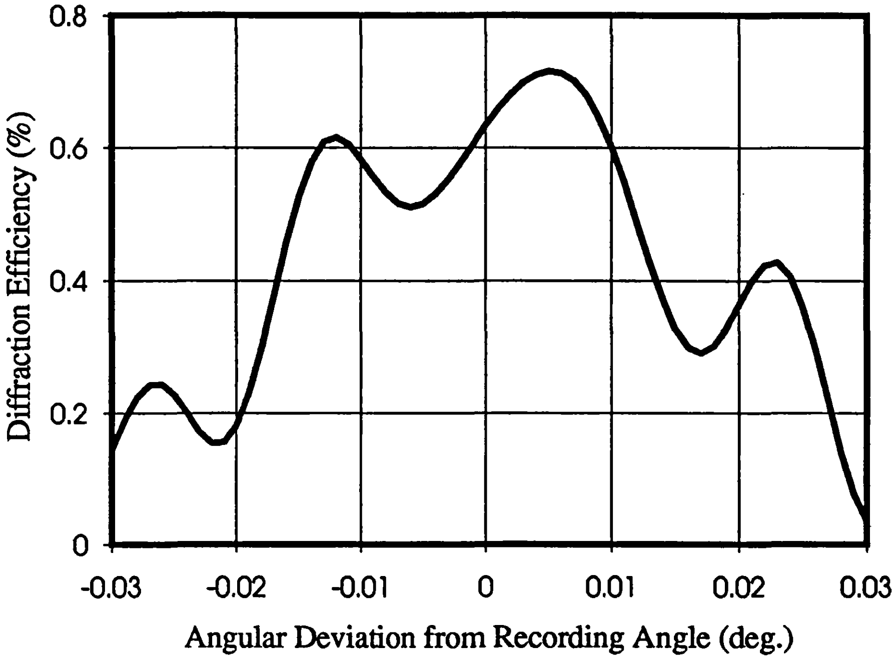

Fig. 4.20 The angular response curve of a grating written in an 8mm thick Fe:LiNbO$_3$ crystal, calculated using the numerical model of Heaton et al (Eq. 3.35-3.37) with parameters $\Gamma d=12$, d=8mm, $m_0=1/15$ and $\Phi_g=0.17$rad. A symmetric recording geometry was used with a recording angle of $\theta_{ext}=25^0$. Bragg shift, non-zero nulls, broadening and asymmetry can be seen.

It is worth mentioning that the non-zero minima of gratings made in doped $LiNbO_3$ (as shown in [Ari87]) were noted by Goltz and Tschudi. They presented an analytic solution based on the theory of Heaton et al, but with an additional undepleted approximation (whereby the amplitude of the signal beam was assumed much weaker than that of the reference beam). Their calculation showed that, with increasing coupling strength, the sharpness of the periodic variation of the angular response curves decreases. For very strong coupling almost all the minima vanish and the first few significant side lobes are predicted to merge into the main lobe [Gol88]. Although their analysis is somewhat ambiguous, the results are confirmed qualitatively by our experimental measurements.

In conclusion, we showed, in this section, the experimentally measured selective angles for Fe: $LiNbO_3$ crystals, which are usually wider than that predicted by Kogelnik's theory. It is difficult to eliminate the broadening because this is a result of the presence of absorption, and photorefractive intensity coupling, during grating formation. (For photorefractive materials, the absorption at the writing wavelength is necessary for photorefractive sensitivity, and also, for a given material such as Fe:$LiNbO_3$, it is difficult to avoid the intensity coupling effect.)

4.4 Self-enhancement of Grating Diffraction Efficiency during Readout

The readout beam will partially erase an unfixed hologram in a photorefractive crystal if the crystal is sensitive to the wavelength of the readout beam. This was briefly discussed in Chapter Three. A more complicated issue is self-enhancement [Ozo86, Shv87, Ott89, Ott92], whereby the diffraction efficiency of a hologram increases in the first stage of readout. It was first predicted by Staebler and Amodei, who found that self-enhancement should occur on illuminating the hologram with a uniform light beam at or near the Bragg angle [Sta72]. The first experimental account of this effect was reported by Gaylord et al [Gay73]. In certain $LiNbO_3$ samples, self-enhancement even occurs at an incident angle far from the Bragg angle [Bra90]. To explain the main properties of the self-enhancement effect, Shvarts et al developed a model whereby complementary holographic gratings are considered to be formed by the readout process in the photorefractive crystal, and they also presented experimental results [Shv87].

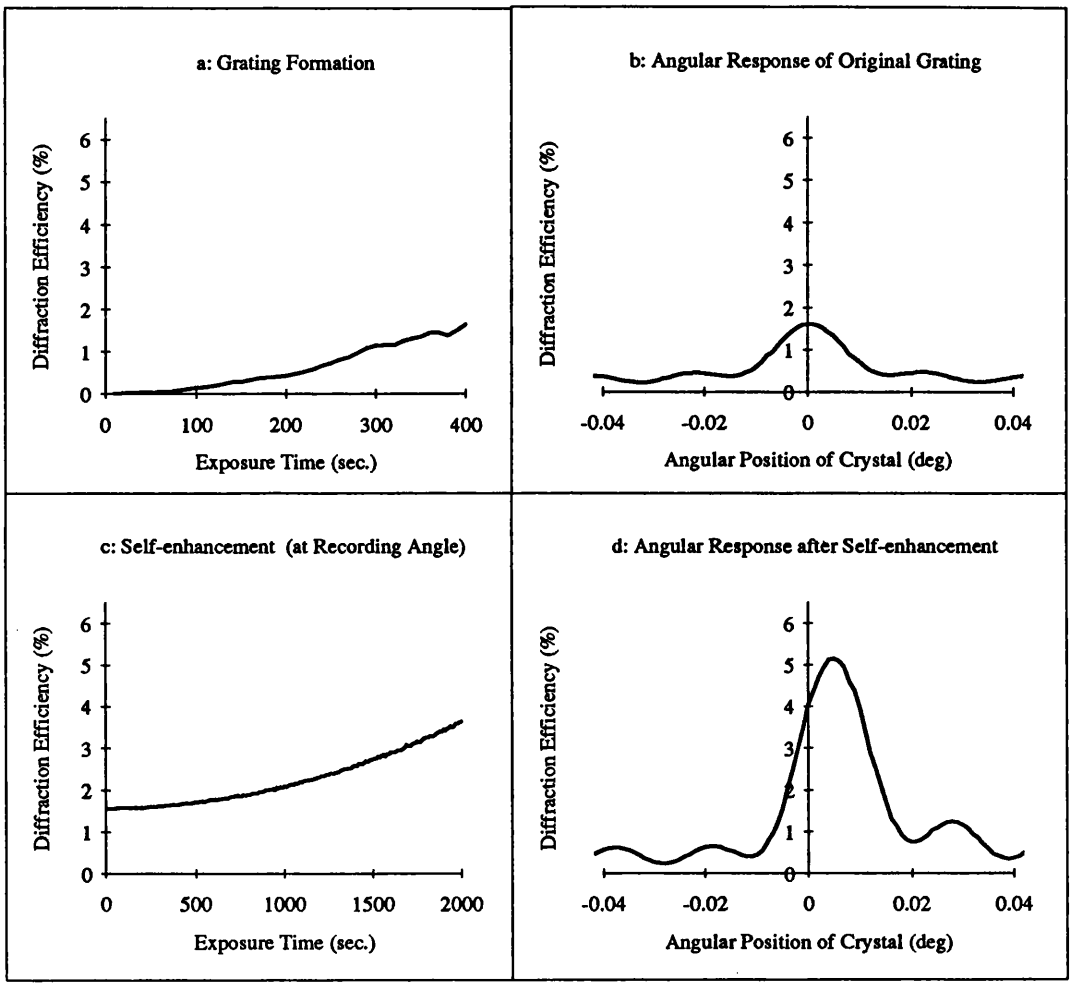

Fig. 4.21 Initial formation, self-enhancement and angular responses before and after self-enhancement of a grating written in a 4.7mm thick Fe:LiNbO$_3$ crystal. The diffraction efficiency in all the graphs (a-d) is similarly scaled. The writing beam intensity ratio m_0=1. The original grating shows low efficiency and no obvious Bragg shift. After self-enhancement at the recording angle with a total exposure of 14J/cm^2, the peak efficiency increased by a factor of 3, and the peak position shifted by 0.006^{o}.

Our experimental measurements showed that self-enhancement usually occurred for a readout angle at or near the Bragg angle for our Fe:LiNbO$_3$ crystal samples. For example, the efficiency of a grating written by beams of equal intensity, was usually increased by a factor of 2 to 3 after self-enhancement, as shown in Fig. 4.21. This agrees with the results in [Shv87]. Our new finding is that self-enhancement gives rise to a further Bragg-shift in addition to the original one. This feature is also shown in Fig. 4.21.

4.5 Summary

For dense holographic storage in photorefractive crystals, small selective angles, high diffraction efficiency, and angular position are all of importance. Readout at the correct angle can significantly enhance the diffraction efficiency. We note that, in general, the real Bragg peak deviates from the nominal Bragg angle (recording angle). The possible reasons are:

1). The grating fringes bend due to the phase coupling (the variation of the phase difference between the writing beams as they propagate inside the crystal).

2). Anisotropic diffraction due to the natural optical activity of BSO makes the Bragg peak shift from the nominal Bragg angle, the shift being proportional to the optical rotary power and the grating spacing. (This may also apply to natural birefringence in other crystal types, although we have not yet obtained experimental evidence in the case of LiNbO$_3$.)

3). The presence of an external field applied to BSO during replay shifts the Bragg peaks, for linearly polarized readout beams, away from their nominal positions.

4). Erasure (or readout) at or near the Bragg angle for sufficiently long times causes a further shift of the Bragg peak, whilst self-enhancing the diffraction efficiency.

Our numerical calculations and experimental measurements for the case of Fe:LiNbO$_3$ showed that the Bragg shift due to phase coupling is significant, and readout at the recording angle usually reduces the achievable diffraction efficiency. This introduces some complexities into the readout system for a memory stored in a photorefractive crystal, if the maximum diffraction efficiency is required. However, for a given crystal and recording geometry, if the initial writing beam ratio, m_o, is carefully chosen, such that Eq. (4.3)

$$m_o=\exp(\Gamma d\sin\Phi_g)$$

is satisfied during recording, the same recording angle can be used for readout as that used for recording, enabling the highest diffraction efficiencies to be obtained with a simple recording and readout system.

The number of gratings which can be angularly multiplexed is limited by the finite selective angle, and also the problem of erasure of earlier recorded holograms during the recording of subsequent holograms. We note also, that the theoretically predicted selective angle (based on the basic coupled-wave theory given by Kogelnik) is sometimes broadened by the polarisation effect in electrooptic materials, and by the non-uniformity of the grating modulation depth. The latter is a result of the presence of absorption, and photorefractive intensity coupling, during grating formation. For photorefractive materials, the absorption at the writing wavelength is intrinsic, as this is the necessity for the photorefractive sensitivity. Also for a given material such as Fe:$LiNbO_3$, it is difficult to avoid the intensity coupling effect. Taking into account the broadening of the selective angle, the angular separation between reference beams for angularly multiplexed holographic storage must be wider than a minimum possible value predicted by the basic Kogelnik's theory. In the next chapter the influence of these factors on the storage capacity of a photorefractive crystal will be considered, when we discuss the storage capacity limitations for angular multiplexing.

CHAPTER FIVE

HOLOGRAPHIC STORAGE CAPACITY LIMITATIONS FOR ANGULAR MULTIPLEXING

One advantage of using photorefractive crystals for both data storage [Sta75, Mok91] and optical interconnection [Psa87, Lee89, Mok92], is their high storage capacity. In this chapter we discuss in detail the storage capacity limitations of photorefractive crystals for angular multiplexing, as this multiplexing scheme is most useful for thick storage media to achieve the high storage capacity.

In Chapter Two we calculated the bit storage capacity of spatially multiplexed F. T. hologram arrays. This is of the order of A/λ^2 (A is the area of the storage medium and λ is the free-space light wavelength used), and the calculation was based on the diffraction effect of the finite hologram aperture size. We also calculated the degree of angular multiplexing using symmetric, transmission geometry, in a crystal with thickness d, which is of the order of nd/λ (n is the refractive index of the medium). This calculation was based on the selective angle given by Kogelnik's coupled wave theory. Thus, by multiplying A/λ^2 and nd/λ, the storage capacity of a crystal is of the order of nV/λ^3 (V=Ad is the volume of the crystal). This result agrees with that originally predicted by van Heerden ($V/\lambda^{3,}$ see [vHe63]), and it can be referred to as the upper (or diffraction) limit of the storage capacity, since no other limitation has been considered. It can be seen from the discussion in Chapter Four that the selective angle of a hologram recorded in a photorefractive crystal is, in general, larger than that predicted by Kogelnik's theory. This will affect the storage capacity of a photorefractive crystal. Furthermore, the capacity which can be obtained in a practical system is limited by many factors, in particular by the required signal to noise ratio (SNR).

In Section 5.1 we discuss the major sources of noise. Crosstalk, the manner in which it limits the storage capacity, and the choice of proper angular separation of reference beams between adjacent recordings to eliminate crosstalk in angularly multiplexed recordings will be discussed in Section 5.2. We also present our results of vertical angular selectivity and grating degeneracy in this section. Detection noise, which puts a lower limit on the diffraction efficiency of each hologram, thereby limiting the degree of angular multiplexing (due both to the finite dynamic range of the crystal and also to the erasure effect during readout), will be discussed in Section 5.3. In Section 5.4 we briefly discuss limitations of storage capacity imposed by practical optical components. Finally, a summary of the factors governing storage capacity will be given in Section 5.5.

5.1 Noise in Holographic Storage

In page oriented volume holographic storage, each page must be retrieved independently and with reasonable fidelity. The presence of noise in the reconstructed and detected images will deteriorate the fidelity [Blo79, Wea81]. One measure of the image quality of a reconstructed binary data page is the ratio of the average power in a "one" bit to the average power in a "zero" bit (SNR). The error probability (EP) or the bit error rate (BER), however, is a more practical parameter used to describe the quality of the reconstructed signal in a binary system [Wea81]. By analogy with digital communication theory [Yar85], the error probability in a binary data storage system can be defined as the probability that any given bit in the detected image does not agree with the corresponding bit in the input image. BER can be related to SNR through the error function [Yar85].

The three main sources of noise in holographic storage systems using photorefractive crystals as their storage media, are as follows:

1) Noise arising from imperfections in the optical components, such as speckle noise (random interference patterns generated by spatially coherent scattering from defects in the optical system used to record and replay the hologram), "cosmetic noise" (interference or diffraction patterns due almost entirely to multiple reflections between the crystal surfaces [Bur77], as can be seen in Ref. [Mok91]), and scattering noise from the crystal itself (diffraction from noise gratings [Sol89b, War89] recorded in the electrooptic crystal).

2) Crosstalk noise arising from the finite angular selectivity of angularly multiplexed volume holograms.

3) Detection noise.

In the first type of noise, the cosmetic noise can be reduced by the use of redundancy techniques [Fir72], and by using anti-reflection coated optics with a high-quality surface finish [Bur77]. Scattering and speckle noise are problems which affect all types of holographic storage, and we shall not discuss them in detail. We therefore turn our attention to the crosstalk noise and the detection noise, and see how these affect the storage capacity of angular multiplexing.

5.2 Storage Capacity Limited by Crosstalk

In angular multiplexing, Bragg selectivity ensures that the desired page associated with a particular reference beam being used for readout, is reconstructed with the highest efficiency. However, other stored pages are also reconstructed with lower efficiencies and with distortions and spatial shifts due to Bragg mismatch. The sum of such Bragg-mismatched components in the readout represents a form of crosstalk. As the number of pages and the number of pixels per page increase, the stray intensity due to this cross-readout at a given pixel of the desired image, acts as a source of random noise, and may cause a bit error. This inherent crosstalk puts a limit on the storage capacity that can be approached in angularly multiplexed holographic storage.

Crosstalk depends greatly on the arrangement of the reference beam angles. For transmission F. T. holograms each angled reference beam can be regarded as a point source in the front focal plane of a F. T. lens. The object pages are also located in the front focal plane. We split this plane into two halves, S and R, corresponding to the reference and signal planes respectively (see Fig. 5.1). The horizontal and the vertical planes are defined as follows: when the first hologram is recorded, the plane which contains the two writing beam vectors is referred to as the horizontal plane. Any plane which is perpendicular to the horizontal plane and passes through the centre of the system (the centre of the F.T. lens in the case of Fourier transform holography), is referred to as a vertical plane. Referring to our coordinate system throughout this thesis, the horizontal plane is the y-z plane; and any plane parallel to the x- axis passing though the centre of the F.T. lens, is a vertical plane (see Fig. 5.1). We shall discuss the horizontal (along the z-axis) and vertical (along the x-axis) arrangement of reference points in the following subsections.

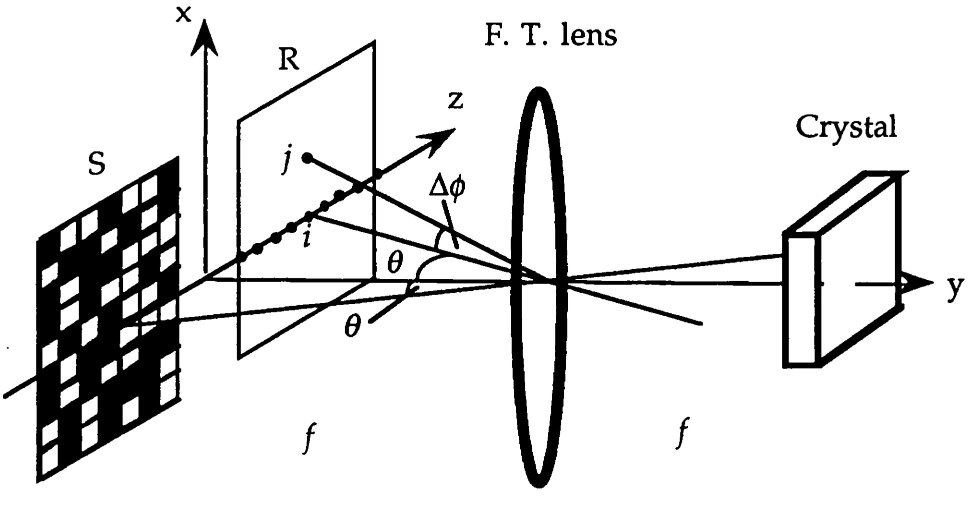

Fig. 5.1 Diagram showing the arrangement of the object plane (S) and the reference plane (R). The horizontal plane is the y-z plane. Any plane perpendicular to the horizontal plane and passing through the centre of the F.T. lens is a vertical plane.

5.2.1 Reference points arranged in the horizontal dimension

If all reference points are arranged in the horizontal dimension, all writing and readout beams will be in the same horizontal plane, so that

Kogelnik's theory (described in Chapter Two) can be used for the analysis. We first of all calculate the diffraction limits, using Kogelnik's theory, and then briefly discuss the storage limitations caused by crosstalk noise.

Diffraction limitation

In Section 2.4.3 we defined the selective angle, $\Delta\Theta$, as the full angular width (null to null) of the main lobe of the angular response (η–ξ) curve, in estimating the storage capacity. For $\nu \ll \pi$ (small diffraction efficiency approximation), $\Delta\Theta$ is given as (also see Eq. 2.28)

$$\Delta\Theta = \frac{2\,\lambda \cos\theta_s}{\mathrm{n\,d}\sin 2\Phi} \tag{5.1}$$

here θ_S is the angle of the diffracted beam, $2\Phi = \theta_r - \theta_S$ is the recording interbeam angle (θ_r is the reference beam angle), n and d are the refractive index and the thickness of the material respectively. Eq.(5.1) is simplified for unslanted gratings to be (Eq. 2.29):

$$\Delta\Theta = \frac{\lambda}{\mathrm{n\,d}\sin\theta_r}$$

where θ_r indicates the reference angle inside the material, and then we calculated in Section 2.4.3 the maximum degree of angular multiplexing, $M_{ang,u}$, for unslanted gratings as (Eq. 2.30)

$$\begin{aligned} M_{ang,u} &= \int_0^{\frac{\pi}{2}} \frac{\mathrm{n\,d}\sin\theta_r}{\lambda} d\theta_r \\ &= \frac{\mathrm{n\,d}}{\lambda} \end{aligned} \tag{5.2}$$

In the case of slanted gratings, we consider first that the object beam is a plane wave with incident angle θ_S ($\pi/2 > \theta_S \geq 0$). We can calculate the total number of slanted gratings, $M_{ang,s}$, by integrating $\frac{d\theta_r}{d\,\Theta}$ (where $d\Theta = \Delta\Theta$ is given by Eq. 5.1) over the whole range of possible reference beam angles (from -π/2 to π/2):

$$M_{ang,s} = \int_{-\pi/2}^{\pi/2} \frac{n\, d\, |\sin(\theta_r - \theta_s)|}{2\, \lambda \cos\theta_s} d\theta_r$$
$$= \frac{n\, d}{\lambda\, \cos\theta_s} \qquad (5.3)$$

The number of holograms from Eq. (5.3) appears to be greater than that from Eq. (5.2) since $\cos\theta_s \leq 1$.

In page oriented holographic storage as shown in Fig. 5.1, every reference beam with a unique wave vector, $\mathbf{k}_1$, associates with an object beam with a group of wave vectors, $\{\mathbf{k}_2\}$, resulting in a group of grating vectors, $\{\mathbf{K}\}$. The angular range of each $\{\mathbf{k}_2\}$ equals α_s (which is the angle of the object from a point on the lens plane, see Fig. 2.3a). To record two of these groups as closely as possible whilst remaining free of crosstalk, the angular separation between two reference beams must be no less than the selective angle, ΔΘ, given by Eq. (5.1). This does not mean that the storage capacity of the input bits is the product of the maximum degree of angular multiplexing, $M_{ang,s}$, given by Eq. (5.3), and the number of pixels in each page, regardless how many pixels there are in each input image. In practice, a larger dimension of the signal, D_s, which can accommodate more input bits, reduces the possible reference angle range (see Fig. 5.2).

Taking the angular range of the object beam into account, the expression for $M_{ang,s}$ in (5.3) must be modified by altering the integration range. For example, if the object pages are located in the half plane, S (see Fig. 5.1), i.e. $(\pi/2-\alpha_s/2) \geq \theta_s \geq \alpha_s/2$, then integrating Eq. (5.3) from $\theta_r=-\pi/2$ to $\theta_r=\theta_s-(\alpha_s/2)$ gives the number of pages that can be stored using angular multiplexing as:

$$M_{ang,page} = \frac{n\, d}{2\, \lambda \cos\theta_s}\left(\cos\frac{\alpha_s}{2} + \sin\theta_s \right) \qquad (5.4)$$

This is, in general, smaller than the result from Eq. (5.3). Note that the other integration range, from $\theta_r=\theta_s+(\alpha_s/2)$ to $\theta_r=-\pi/2$, is neglected because this range for θ_r is inconvenient in practice.

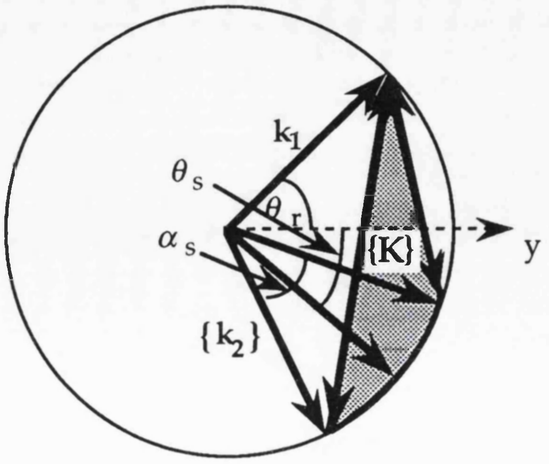

Fig. 5.2 The signal page occupies an angular range, α_S, in **k**-space, so that the possible angular range of the reference beam is reduced by α_S.

Note that the results of Eqs. (5.2)-(5.4) are based on the condition that the directions of the writing beams are within the range $-\pi/2$ to $\pi/2$ (inside the crystal). In practice, however, there is usually a limitation on the access range of the writing beams (say, $\pm\theta_{r0}$). For example, the refraction at the air-crystal interface limits the access angle range to $|\theta_{r0}| = \sin^{-1}(1/n)$, where n is the average refractive index of the crystal. Taking into account this reduction in the access range, Eqs. (5.2)-(5.4) are modified, respectively, as follows:

$$M_{ang,u} = \frac{2n\,d}{\lambda}\sin^2\theta_{r0} \tag{5.5}$$

$$M_{ang,s} = \frac{2n\,d}{\lambda\ \cos\theta_s}\sin^2(\theta_{r0} - \theta_s) \tag{5.6}$$

$$M_{ang,page} = \frac{n\,d}{2\,\lambda\,\cos\theta_s}\left[\cos\frac{\alpha_s}{2} - \cos(\theta_{r0} + \theta_s)\right] \tag{5.7}$$

Eqs. (5.5)-(5.7) also include the diffraction limitation on the maximum degree of angular multiplexing, as we have assumed that there is no crosstalk when the holograms are recorded with an angular separation, $\Delta\Theta$ (Eq. 5.1), between adjacent recordings.

Crosstalk noise consideration

If a signal page is recorded using a set of reference points *i*, the horizontal selective angle, $\Delta\Theta$, determines the minimum distance between the adjacent reference points along z axis. $\Delta\Theta$ is based on the full angular width of the main lobe of the angular response ($\eta \sim \xi$) curves. The zeros of the $\eta \sim \xi$ curves, (corresponding to $\nu^2+\xi^2=p^2\pi^2$, where p is an integer) are not equally spaced (Fig.2.6), and $\Delta\Theta$ depends upon the reference angle (Eq. 5.1). This means that there is no way to arrange the reference points such that, at a single readout angle, one page is retrieved with a maximum efficiency, whilst at the same time all other Bragg-mismatched pages have zero efficiency. In other words, crosstalk is inevitable.

Burke and Sheng have calculated (using Kogelnik's theory), and experimentally measured, the SNR as a function of the angular spacing between reference beams, in cases involving a regular arrangement of the reference points in the z-dimension only. Their results showed that the SNR is oscillatory with a period inversely proportional to to the effective grating thickness (which is smaller than the physical thickness) [Bur77]. So it should be possible to place reference beams periodically to obtain high SNR.

Gu et al [Gu92] obtained an expression for the storage capacity limited by crosstalk noise in the case that the reference points are arranged in one dimension along the z-direction, and this expression may be written, in our notation, as:

$$M_{ang,cn} = \frac{2d}{\lambda\, \alpha_I (S/N)_{re}} \tag{5.8}$$

where $M_{ang,cn}$ is the upper bound of the number of angularly multiplexed holograms (the degree of angular multiplexing), d is the thickness of the recording medium, λ is the wavelength of light , α_I is the angle of the image plane from a point in the lens plane as shown in Fig. 2.3b, and $(S/N)_{re}$ is the required signal-to-noise ratio in terms of intensity. Their numerical calculation showed that the crosstalk is minimum at the centre of the output (image) plane, and increases as the points under observation move to the edge of the output plane. This is why the angle of the image plane, α_I, also limits the storage capacity. Their conclusion is that, for a given SNR, the system can accommodate a maximum number, $M_{ang,cn}$, of angularly multiplexed pages, each consisting of A/λ^2 (strictly $F^2\alpha^2A/\lambda^2$, as in equation 2.24) resolvable pixels, even though the reference points are arranged along the horizontal axis only. In their calculation Gu et al used a regular angular separation between reference beams equivalent to the "average" half selective angle. Burr et al have recently proposed that the SNR could be improved by making the separation between adjacent holograms variable and equal to the half selective angle for any two holograms[Burr93].

We noted in Chapter Four that the angular response curves of an Fe:$LiNbO_3$ crystal are, in general, broader than the prediction by Kogelnik's theory, and, in the case of strong coupling, become monotonic (as shown in Fig. 4.18b). This is a possible cause of the reduction in the effective thickness mentioned by Burke and Sheng. In this case the arrangement of reference points chosen by Gu et al greatly increases the crosstalk noise, and an angular separation 3 to 5 times larger than the half selective angle is required.

5.2.2 Reference points arranged in two dimensions

One may ask if it is possible to significantly increase the storage capacity by expanding the arrangement of reference point sources into two dimensions. To answer this question we should look at several aspects, such as the angular selectivity in the vertical plane, degeneracy, and the peculiarities of photorefractive recording.

Vertical angular selectivity

Strict calculation of vertical angular selectivity requires 3-D coupled-wave theory. We can approximate this using the simple geometrical method illustrated in Figs. 5.1 and 5.3.

Before the discussion, let us describe the geometry of the real space and the **k**-vector space. For homogeneous and isotropic media, for simplicity, the 3-D **k**-space is a sphere, as shown in Fig. 5.3, with radius of $k=2n\pi/\lambda$, where n is the refractive index of the medium, and λ is the wavelength in free space. The centre of the sphere, o, corresponds to the centre of the F. T. lens in Fig. 5.1. The equatorial plane (the dotted plane in Fig. 5.3) corresponds to the horizontal plane (y-z plane) in Fig. 5.1 and each vertical plane in Fig. 5.1, which is perpendicular to the horizontal plane and contains the centre of the lens, corresponds to a meridian plane in Fig. 5.3, which is perpendicular to the equatorial plane and contains the centre of the sphere. A grating vector, K, in Fig. 5.3 depends on the angle, 2θ, between the wave vectors of the two writing beams (interbeam angle), which is measured from the centre of the lens. Note that once a grating vector is formed, it can be seen anywhere in the sphere, but its length and direction must remain unchanged. Also for simplicity, we assume that the refractive index outside the crystal is n as well.

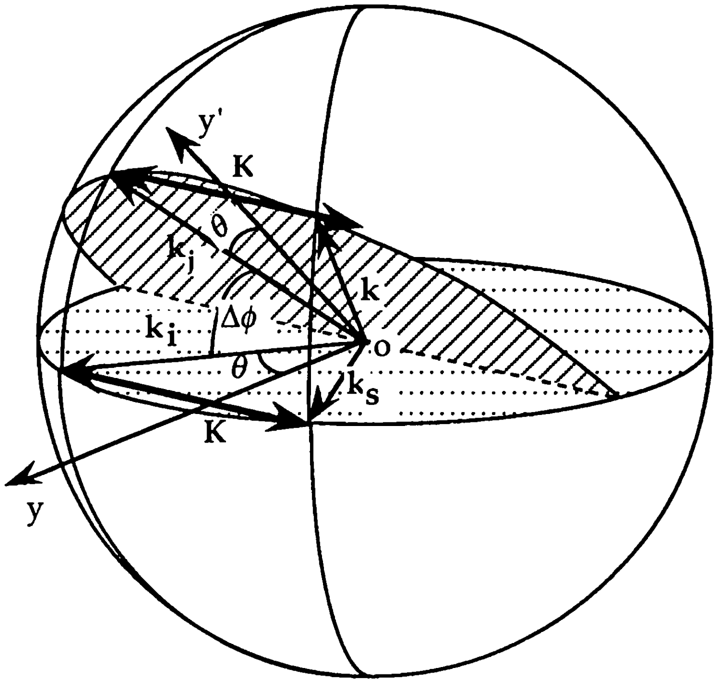

Fig. 5.3 **k**-vector sphere showing Bragg-mismatch in the vertical direction

Consider a single grating **K** which is formed with a horizontal geometry (**K** = $\mathbf{k_i} - \mathbf{k_s}$ is shown in Fig. 5.3, and Fig. 5.1 shows the reference point located at *i* in plane R, with $z_i = f\tan\theta$, x_i=0, *f* is the focal length of the lens). If this grating is read using a readout point located at *j* (in Fig. 5.1, where z_j= z_i and $x_i \neq 0$), an angular mismatch occurs due to the vertical deviation of the readout beam. Referring to Fig. 5.3, the readout beam wave vector $\mathbf{k_j}$ can be seen to make an angle, $\Delta\phi$, with the recording reference wave vector, $\mathbf{k_i}$, in the vertical plane.

Since both the direction and length of the grating vector, **K**, remain unchanged, in the plane $\mathbf{K}\sim\mathbf{k_j}$ (the shaded plane in Fig. 5.3) if the angle between $\mathbf{k_j}$ and oy′ (oy′ is the intersection between the plane $\mathbf{K}\sim\mathbf{k_j}$ and the meridian plane containing the y-axis) were still θ, the Bragg condition would not be broken. The violation of the Bragg condition can be regarded as the non-zero angular deviation of the readout angle θ' (in the plane $\mathbf{K}\sim\mathbf{k_j}$) from the recording angle θ, i.e. $\Delta\theta' = \theta-\theta' \neq 0$. Using $\theta' \approx \theta\cos\Delta\phi$, the relation between $\Delta\theta'$ and $\Delta\phi$ is given by:

$$\Delta\theta' = \theta(1-\cos\Delta\phi)=\theta\, 2\sin^2(\Delta\phi/2) \tag{5.9}$$

for small $\Delta\theta'$ and $\Delta\phi$ we have

$$\Delta\phi = \sqrt{\frac{2\Delta\theta'}{\theta}} \tag{5.10}$$

If $\Delta\theta'=\Delta\Theta$ (the horizontal selective angle given by Eq. 5.1) we say that $\Delta\phi$ in Eq.(5.10) is the vertical selective angle, $\Delta\Phi$. Using Eqs.(5.1) and assuming a symmetrical geometry with $\theta \ll 1$, the ratio of the vertical to the horizontal selective angle is given as:

$$\frac{\Delta\Phi}{\Delta\Theta} = \sqrt{\frac{2nd}{\lambda}} \tag{5.11}$$

where n is the refractive index and d is the thickness of the crystal.

As an example, Eq. (5.11) estimates the ratio $\frac{\Delta\Phi}{\Delta\Theta}$ to be about 146 for a grating written in an Fe:LiNbO$_3$ crystal with d=2.5mm, n=2.2 and

λ=514.5nm. The experimentally measured $\Delta\Theta$ and $\Delta\Phi$ for this grating (for an external half-interbeam angle θ=25^{0}) are shown in Fig. 5.4.

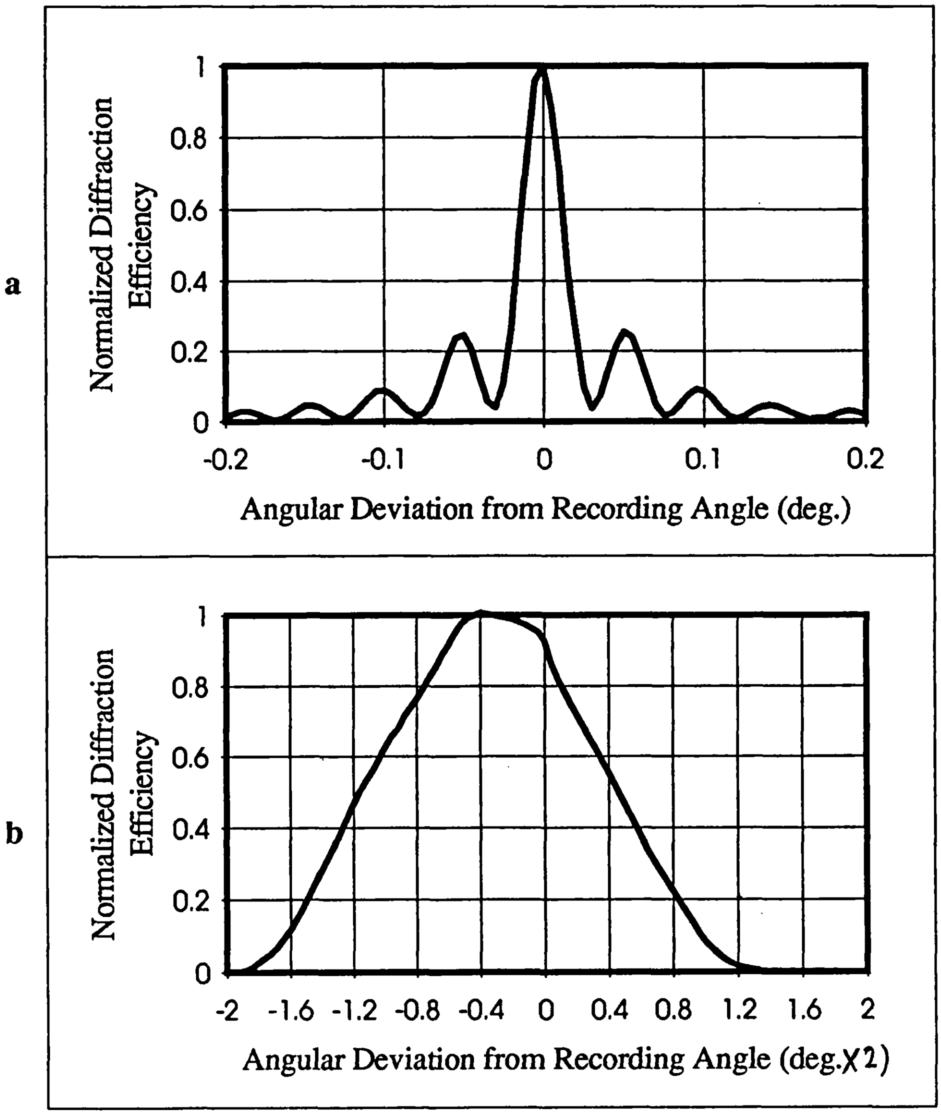

Fig. 5.4 Experimentally measured values for the selective angle of a grating written in a 2.5mm thick Fe:LiNbO$_3$ crystal, in **a** the horizontal and **b** the vertical directions using a compressed horizontal scale.

From Fig. 5.4 the measured $\Delta\Phi/\Delta\Theta$ is about 120. The measured vertical selectivity is more optimistic than the estimate of Eq. (5.11). Nevertheless, from the large vertical selective angle, it seems that the extension of the reference geometry into two-dimensions can only increase the storage capacity by a small factor, which depends on the horizontal selective angle and the vertical dimension of the reference plane. Note that grating degeneracy has not yet been considered.

Grating degeneracy

Grating degeneracy has been noted by many authors [Mid87, Lee89, Gu92]. When the reference and object points are allowed to distribute in two dimensions, there are sets of pairs of object and reference points whose corresponding wave vectors, , $\{\mathbf{k}_p , \mathbf{k}_q \}$, satisfy the condition,

$$\mathbf{k}_p - \mathbf{k}_q = \mathbf{K}$$

where **K** is a constant grating vector written by, say, one of the pairs in the horizontal plane, $(\mathbf{k}_i , \mathbf{k}_s)$. All these pairs of writing wave vectors form identical gratings. This is called grating degeneracy. The loci of the end points of these degenerate grating vectors are two rings on the **k**-vector sphere. These are generated by rotating the two writing wave vectors around a **k**-sphere diameter, this diameter being parallel to the grating vector, **K** (shown in Fig. 5.5**b**).

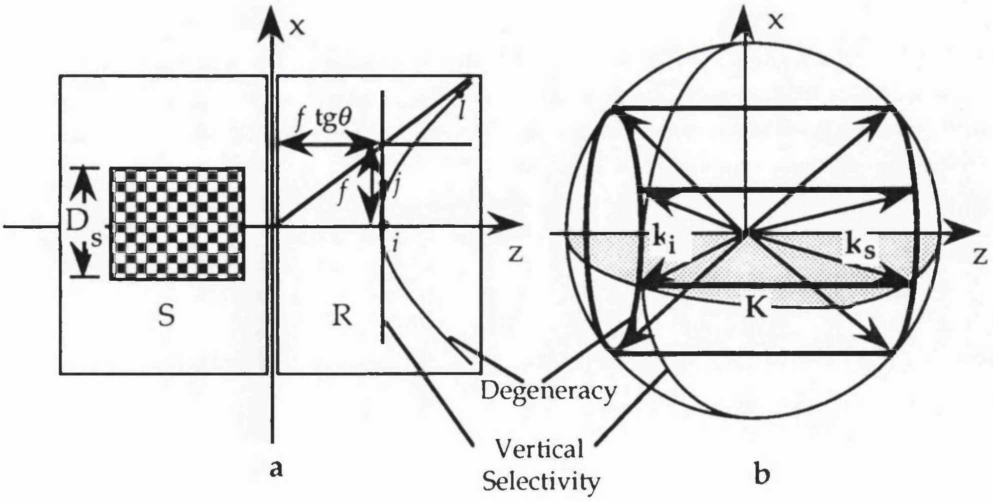

Fig. 5.5 Grating degeneracy and vertical selectivity shown in **a** object and reference planes, and **b** the **k**-vector sphere. θ is the reference beam angle in the horizontal plane and f is the focal length of the F.T. lens.

From the viewpoint of holographic storage, if several holograms are recorded in the crystal such that they have identical grating vectors, one readout beam will address all these holograms simultaneously, and tremendous crosstalk occurs. Even in page-oriented holographic storage, signal pages are located at the same position in the object plane (this means that the signal wave vectors are fixed). Once a page is recorded, it can be read out, without breaking the Bragg condition, by all readout waves whose wave vectors end on the degeneracy ring of the recording reference beam. Therefore, any other points on this ring should not be chosen for recording another page.

It should be noted that vertical angular selectivity and grating degeneracy are separate issues. Referring to Fig. 5.5a, if one page has been recorded using reference point *i* ($x_i=0$, $z_i=f\tan\theta$), the vertical angular selectivity is measured along a meridian in the **k**-vector sphere, which corresponds to the *vertical line*, $z_i=f\tan\theta$, in the reference plane. In this line a point, *j*, (such that $x_j>f\Delta\Phi$, where $\Delta\Phi$ is the vertical selective angle given by Eq. 5.11) may be selected as another reference point for storing another page. On the other hand, grating degeneracy occurs along the degeneracy ring in the **k**-vector sphere, which is the intersection between the **k**-sphere and the circular cone, whose axis is a diameter of the sphere (parallel to **K**) and which has a semi-vertex angle equal to $(\pi/2)-\theta$. This circular cone can be expressed as:

$$x^2+y^2=(z\cot\theta)^2$$

The intersection between this circular cone and the reference plane, $y=f$, results in a hyperbola:

$$\left(\frac{z}{f\ \tan\theta}\right)^2-\frac{x^2}{f^2}=1 \qquad (5.12)$$

Therefore the degeneracy ring in the **k**-vector sphere corresponds to a *hyperbola* in the reference plane, with the major semi-axes being *f* and $f\tan\theta$ respectively. No point along this hyperbola can be selected for storage of another page unless the signal pages have limited vertical dimension, D_s, and a point l may only be chosen if $x_l > D_s$. It is only when $\tan\theta << 1$ that the degeneracy hyperbola can be treated as a vertical line. In the design of a practical system both effects must be taken into account.

Our discussion is based on a situation where the signal plane has a fixed size and position, and the number of pixels in this plane is made as large as possible. The number of reference points (number of holograms) is in general smaller than the number of pixels. We shall note some similarities and differences between our considerations for storage purposes and those required for optical interconnection and neural network systems. Page oriented holographic storage (with the reference points arranged in one dimension) is useful for the implementation of N^2-->N and N-->N^2 interconnects, where N is the maximum number of the resolvable points in one dimension of the input and output planes, so that N is approximately D_s/λ (or D_r/λ, where D_s and D_r are the dimensions of the input and output planes respectively) [Psa87]. However, there is also a need for an interconnection between input and output planes having roughly equal numbers of points. In this case, if the total capacity of the storage medium is N^3 (assuming that the dimensions of the crystal cube is D_H, and that $D_H = D_s = D_r$), the maximum number of points in each plane which can be connected by the storage medium is $N^{3/2}$ out of the N^2 available sites. Several sampling grids, including a fractal grid, were proposed by Psaltis et al for the correct selection of the locations of points in each plane to avoid grating degeneracy. In the derivation of their sampling grids angular selectivity was not taken into account, and grating degeneracy was considered to occur along vertical straight lines [Psa88c, Psa90a].

It is worth noting that, while grating degeneracy is, in general, harmful for holographic storage and interconnection, it may be useful for some other tasks. Recently Gu et al proposed and demonstrated a new method, which utilised grating degeneracy in photorefractive media in conjunction with an incoherent laser array to implement parallel optical matrix-matrix multiplication [Gu93].

Crosstalk considerations

Ramberg derived the following expression for the crosstalk-limited storage capacity based on the assumption that the reference point sources are randomly arranged in two dimensions in the reference plane, and that the crosstalk noise could be averaged over all stored pages [Ram72]:

$$N_a = \frac{d}{4\lambda (S/N)_R^2} \tag{5.13}$$

here $(S/N)_R$ is the required signal-to-noise ratio (SNR). This is similar to the result of Gu et al (Eq. 5.8). Note that Ramberg's SNR is defined such that $(S/N)_R{}^2=(S/N)_{re}/2$, and $(S/N)_{re}$ is the required SNR in Eq. (5.8), in which it is assumed that the reference points are arranged in one dimension (z) only. The similarity between the two results shows that the storage capacity is not improved by expanding the reference points from one dimension into two. On the contrary, in the case of a random distribution of reference points, there is a finite probability of the occurrence of grating degeneracy for which the sharing of gratings by different object-reference pairs gives rise to crosstalk. To ensure that every reconstructed image has crosstalk noise below a prescribed level, degeneracy noise must be eliminated completely, and so regularly arranged reference points should be used [Gu92].

Crystal anisotropy consideration

The conclusions from the above discussion are not concerned with anisotropy, and so apply to isotropic volume holographic storage materials. For photorefractive crystals the relative orientations of the grating vector and the crystal C-axis are essential to the performance of the resultant grating, and especially to the diffraction efficiency. To take advantage of the largest electrooptic coefficient, r_{33}, in the electrooptic tensor, grating vectors parallel to the crystal C-axis (z direction) are desired. Thus, unslanted gratings written by quasi-symmetrical geometries are recommended.

5.3 Storage Capacity Limited by Detection Noise

Even if the reconstructed image itself were noise-free, the measured image would still be noisy because of a fundamental limit imposed by noise in the detector. This noise comes from several sources, including shot (quantum) noise, Johnson (thermal) noise, and laser noise (random fluctuations in laser power due to spontaneous emission in the laser oscillator and amplifier) [Yar85]. We will not discuss detection noise in detail, but only look at how it affects the storage capacity of a photorefractive crystal.

According to Kogelnik's theory, the maximum diffraction efficiency of a single volume phase grating is

$$\eta_0 = \sin^2 \nu \tag{5.14}$$

where

$$\nu = \pi \, \Delta n \, d / \lambda \cos\theta \tag{5.15}$$

where Δn is the change in the refractive index, and θ is the recording angle for a symmetric geometry). If ν is an integral multiple of $\pi/2$, the diffraction efficiency can reach 100%. As the number, M_{ang}, of holograms multiplexed in the same volume increases, the refractive index change for each hologram becomes $\Delta n_{sat}/M_{ang}$ (if each hologram has the same diffraction efficiency). Thus the diffraction efficiency of each hologram is reduced to:

$$\eta_o = \left(\frac{\pi \, \Delta \, n_{sat} \, d}{M_{ang} \lambda \cos\theta} \right)^2 \text{ (valid for large enough } M_{ang}\text{)} \tag{5.16}$$

This reduction in diffraction efficiency decreases the number of photons diffracted to the desired detector. However, the presence of detection noise requires a minimum number of photons for the detector to detect each bit of information with a sufficiently low probability of error. If a detector requires a minimum diffraction efficiency, η_{min}, the maximum number of holograms that can be stored is given by:

$$M_{ang} = \frac{\pi \Delta n_{sat} d}{\lambda \cos\theta \sqrt{\eta_{min}}} \tag{5.17}$$

Therefore, detector noise limits the maximum number of holograms which can be stored in a given volume using angular multiplexing.

For photorefractive crystals, Δn_{sat} can be very large (10^{-3} for Fe:LiNbO$_3$ [Kur77]), and the ratio of d/λ can be of the order of 10^4. Therefore, 3000 holograms could be angularly multiplexed in such crystals if the minimum diffraction efficiency is required to be of the order of 10^{-4}. The storage capacity, in terms of number of holograms, can be further enhanced by an asymmetric writing/erasure time characteristic (i.e. writing and erasure time constants, τ_W and τ_E, are not equal, see Section 3.6). In this case, Eqs. (5.16) and (5.17) can be modified to [Man91]:

$$\eta_o = \left(\frac{\tau_E \pi \Delta n_{sat} d}{\tau_W M_{ang} \lambda \cos\theta} \right)^2 \tag{5.18}$$

and

$$M_{ang} = \frac{\tau_E \pi \Delta n_{sat} d}{\tau_W \lambda \cos\theta \sqrt{\eta_{min}}} \tag{5.19}$$

The asymmetric time constants cause the erasure process to be slower than the recording process. Therefore, if the first exposure is made to saturation, an increase in the sum of the index modulation results on subsequent exposures, since each exposure rises more rapidly than the previous one decays [Man91]. Crystals with a large erasure to writing time constant ratio, a large dynamic range and a large thickness make possible a large degree of angular multiplexing.

Erasure during readout also affects the storage capacity and this effect is not included in Eq.(5.19). This erasure is serious when the data pages stored in unfixed crystals are read out serially, as the readout of one hologram will partially erase all of the other holograms. Every readout needs a finite duration so that the necessary number of photons can be diffracted to the detector. The condition that the entire database must be read out at least once before it is erased puts another limit on the number of stored pages. Blotekjaer performed a detailed study of the storage capacity limitation of photorefractive (and photochromic) media, taking into account the effects of the required reading speed and the partial erasure during readout. In the model that Blotekjaer used, the crystal surface was divided into N_s locations, in each location N_a data pages (each with N_b bits) were superimposed by angular multiplexing. The resulting storage capacity, in bits, was therefore $N_{max}=N_sN_aN_b$. The calculations of Blotekjaer showed that erasure put a limit on all kinds of multiplexing (i.e. limits all of the numbers, N_s, N_a, and N_b), but the situation for angular multiplexing was the most unfavourable [Blo79]. According to this calculation, the larger the product of N_sN_b, the larger was the total storage capacity in bits, although a smaller degree of angular multiplexing resulted. This suggests that, by decreasing the degree of angular multiplexing whilst increasing the degree of spatial multiplexing, a higher storage capacity may be obtained.

5.4 Storage Capacity Limited by Optical System Components

We discussed spatial multiplexing in Chapter Two, and the effect that the numerical aperture of a practical optical system has on the storage capacity. This is because the numerical aperture limits the solid angle that the signal (or image) plane can make with the F. T. lens (Eq. 2.25). Similarly for angular multiplexing there is always a limit on the angular range within which a reference beam angle can be chosen for the recording of a page (see Fig. 5.6). Theoretically, any point at the front focal plane of the F. T. lens can be chosen as a reference point provided that it is outside the signal plane. In practice, however, the size of the reference plane is limited by the numerical aperture of the lens.

Usually the reference and signal planes use separate lenses. In this case the reference angle range, Φ, is (see Fig. 5.6)

$$\Phi = 2\tan^{-1}[(D_L-d_H)/2f] \qquad (5.20)$$

where D_L and d_H are the dimensions of the collimation lens and of the hologram respectively, and f is the focal length of the lens. If $f>>D_L>>d_H$, Eq.(5.20) can be simplified to:

$$\Phi = D_L/f \tag{5.21}$$

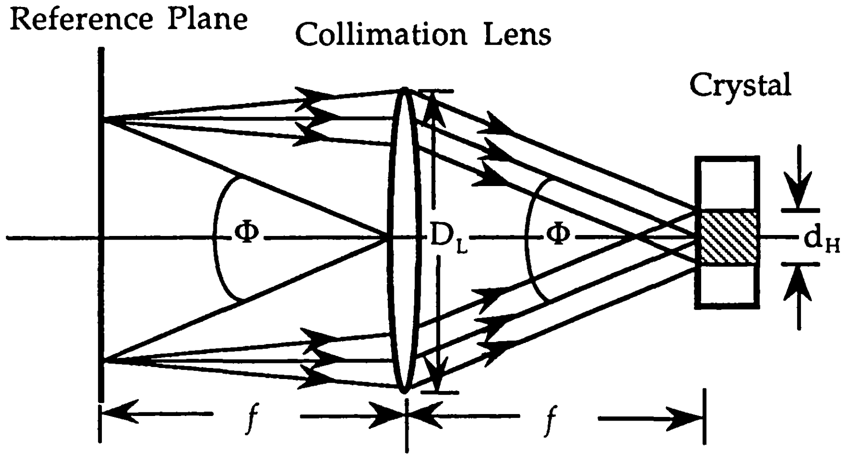

Fig. 5.6 Reference angle range, Φ, limited by the numerical aperture of the lens.

The number of available reference angles, M_0, when the reference points are arranged in the horizontal dimension only, is given by

$$M_0 = \Phi/a\Delta\Theta \tag{5.22}$$

where $\Delta\Theta$ is the horizontal selective angle, and a is a factor chosen according to the broadening of the selective angle for the photorefractive crystal used.

In considering the optical system as a whole, other factors, such as the range and resolution of the beam deflector, (this provides the angled reference beams), should also be taken into account. This range must be larger than the numerical aperture of the collimation lens, and the resolution must be better than the required angular separation.

5.5 Summary

We have discussed several practical factors limiting the maximum number of holograms which can be stored using angular multiplexing. These factors are: required crosstalk noise ($M_{ang,cn}$ in Eq. 5.8), the detection noise (M_{ang} in Eq. 5.19), and the finite numerical aperture of the system components (M_0 in Eq.5.22). The ultimate limit is given by the smallest of these three numbers, unless M_0 is the smallest, and the signal plane is much smaller than the reference plane. This is because, in this case, a 2-D arrangement of reference points is possible to increase the storage capacity without added crosstalk due to grating degeneracy [Mok92].

At the time our work began, the largest number of holograms stored using angular multiplexing was 500, and was achieved by two groups, both using 1cm^3 Fe:LiNbO$_3$ crystals [Sta75, Mok91]. In one of these experiments, 500 holograms were stored and fixed, giving diffraction efficiencies in the range 2.5% to 25% [Sta75]; in the other experiment 500 high resolution holographic images were stored with more uniform, although weaker, diffraction efficiencies of $0.01 \pm 0.001\%$ [Mok91]. This latter work followed sixteen years of development in exposure schemes, which were designed to achieve more uniform diffraction efficiencies [Bur77, Blo79, Str89, Tak91]. The result was that a larger number of holograms could be recorded, but only at the cost of a lower diffraction efficiency. Recently, it has been reported that 5000 pages (each with a resolution of 320 by 220 pixels) have been recorded in a single 3cm^3 Fe:LiNbO$_3$ crystal (using angular multiplexing), to give a total capacity of 3.5×10^8 bits [Mok92, Mok93]. The diffraction efficiency of each of the 5000 holograms was reported to be 4×10^{-6} [Mok93], however, there is no report of the details about the crystal used. In the work of [Mok92], $a\Delta\Theta$ in Eq. (5.22) was chosen to be 0.01°, and the angular range of the reference beam was 12°, putting a limit on M_0 of 1200, which was far less than the 5000 reference angles required. Therefore, the reference points were arranged in five rows [Mok92], separated from each other by a distance not less than the vertical dimension of the object plane, as this was the only way to provide the 5000 reference beams required.

Our aim is to store as many high resolution patterns in a crystal as possible, so that all the pages can be recalled in parallel. This would allow the memory to be incorporated in a high order feedback neural network (HOFNET). Both a high storage capacity and a reasonably high (and uniform) diffraction efficiency are required. According to Blotekjaer's research (mentioned in Section 5.3), higher memory capacities, in terms of bits, might be achieved by using a larger number of pixels in each page and/or by storing the pages in spatially separate parts of the crystal instead of relying on angular multiplexing alone [Blo79]. The need for high capacity, high diffraction efficiency, and the possibility of parallel recall has motivated us to seek a new method for the multiplexing of holograms in photorefractive crystals. In the next chapter we will discuss our invention: spatio-angular multiplexing (SAM).

CHAPTER SIX

SPATIO-ANGULAR MULTIPLEXING (SAM) SCHEME

In this chapter we discuss our new hologram multiplexing scheme for dense holographic storage in photorefractive crystals, Spatio-Angular Multiplexing or SAM. SAM is a novel combination of both angular multiplexing of volume holograms and spatial multiplexing of Fourier transform holograms. Crystals recorded using SAM can be incorporated into a content addressable memory (CAM) system (such as a high order feedback neural network, HOFNET) for parallel correlation and pattern recognition. In Section 6.1. we introduce the background to this work (i.e. the motivation for investigation of spatio-angular multiplexing), and start with a discussion of the memory requirements for a HOFNET. In section 6.2 we propose our novel SAM scheme, and discuss its storage capacity and diffraction efficiency as compared to purely spatial and purely angular multiplexed schemes. In Section 6.3 we describe possible configurations for SAM memory recording, and for parallel correlation using a HOFNET in which a SAM memory is incorporated.

6.1 Motivation for the investigation of Spatio-Angular Multiplexing

In Chapter One we introduced optical neural networks in which the interconnects between neurons can be constructed in three dimensions by means of a volume hologram. Interconnection in three dimensions allows the possibility of very high memory densities, and neural network connection weights can be modified by using photorefractive crystals as storage media [Psa88a]. The memory capacity (the number of patterns that can be stored in and distinguished by the network) of higher order neural networks is much larger than that of linear neural networks having the same number of neurons [Psa88b]. The high order of non-linearity could be implemented by using non-linear devices such as phase conjugate mirrors [Owe87]. Due to the limited dynamic range of the non-linear devices used, only second order neural network systems had been demonstrated optically. To overcome this problem, a novel high order feedback neural network, abbreviated to HOFNET, was proposed by Mao et al [Sel90, Mao91, Sel91, Mao92a, Mao92b]. In this model a high order of non-linearity, or high order of correlation, is implemented by a feedback loop, instead of using the non-linear devices. A schematic diagram of an optical HOFNET is shown in Fig. 6.1.

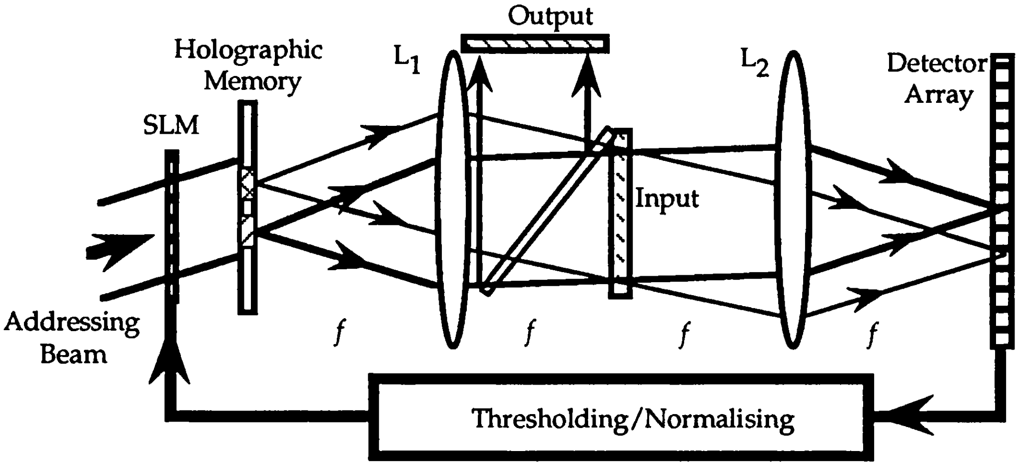

Fig. 6.1 Schematic diagram showing an optical HOFNET system. L_1 and L_2: Fourier transform lenses; SLM: electrically addressable spatial light modulator.

In the system shown in Fig. 6.1, the holographic memory is a Fourier transform hologram array, recorded using spatial multiplexing (as shown in Fig. 2.7 of Chapter Two). All patterns reconstructed from the memory are superimposed at the input plane (corresponding to both the rear focal plane of lens L_1 and also the front focal plane of lens L_2). An input pattern (which may be a partial or distorted version of one of the patterns stored in the memory) is placed in exactly the same position as the reconstructed patterns. A multiplication of the input and the stored patterns is performed in this plane, and the spectrum correlations between the input and each of the stored patterns can be obtained in the detector array. These correlation values are well separated from each other in space, and the separation is determined by the separation of adjacent holograms in the memory. These correlation peaks are measured by separate detector elements which provide control signals for thresholding and normalising via a feedback loop. In subsequent iterations the readout beam amplitude of each hologram is individually controlled in an analogue manner (actually, multiple level digital) after each feedback (via the spatial light modulator), and all the patterns, reconstructed by these weighted readout beams, multiply the input pattern once again. The correlation order of the HOFNET system increases by one after each iteration, so that the order can easily become greater than two. As a result of the high order, a HOFNET is noise-tolerant and can achieve a high memory capacity [Mao92b].

From the above description, one can see that a HOFNET requires essentially a spatially multiplexed hologram array for the memory element. Holograms in the array are recorded in different locations, which ensures that the spatially separated correlation peaks are distinguished by the detector array. In particular, for the system of Fig. 6.1, all object beams are Fourier transforms of the patterns to be stored, and they travel along similar directions during recording (see Fig. 2.7), so that all the reconstructed patterns appear at exactly the same location as that of the input. The spatially multiplexed Fourier transform hologram array is most suitable for the HOFNET.

Although it can be shown that the memory capacity of HOFNET systems depends mainly upon the storage capacity of the memory device used, only a HOFNET system with 16 patterns has been demonstrated in a preliminary experiment [Mao92b]. The disadvantage of the current design of HOFNET is that the interconnections between neurons have not yet been constructed in three dimensions, because only spatially multiplexed hologram arrays have been used. The storage capacity of spatial multiplexing in thin materials is limited (Eqs. 2.23 and 2.25 in Chapter 2). Also, in the demonstration of the first optical HOFNET system, the hologram array was stored in a bleached silver halide photographic plate, and so the efficiency and SNR were rather poor, due to scattering noise. To fully take advantage of the large capacity of optical neural networks, we intend to expand the holographic storage of HOFNET memories into three dimensions, and to use photorefractive crystals as storage media to give a higher memory performance.

A direct way of extending a two dimensional holographic array into three dimensions is to use a conventional 3-D multiplexing scheme, i.e. block oriented holographic storage (BOHS). In this scheme the material would be divided into spatially separated block locations, and each block could accommodate a number of patterns superimposed using angular or wavelength multiplexing (as discussed in Chapter Two, see Fig. 2.10). However, it is very difficult for all the patterns recorded in such a way to implement a full parallel correlation with an input using a HOFNET. The major problem is that the correlations between the input and the reconstructed patterns from the same block will appear at the same pixels of the detector array. This means that individual control of the readout beam for each hologram becomes difficult, and usually requires two separate channels of detection signals for the control. An example of such a HOFNET system is shown in Fig. 6.2.

In the memory of this system (Fig. 6.2), all patterns in each block are stored using wavelength multiplexing with a geometry similar to that shown in Fig. 2.10a in Chapter Two. For correlation, each block is replayed using the same multiple wavelengths as those used for recording. This ensures that all reconstructed beams from all blocks travel in the same direction, and so that after Fourier transformation by an achromatic lens, L_1, all reconstructed images superimpose exactly at the same location, in the rear focal plane of L_1, as that of the input pattern (see Fig. 6.2).

The above system requires a polychromatic light source (PLS), where the intensity of every discrete wavelength component can be individually controlled by the signal from the thresholding/normalising loop. After correlation, this system requires a dispersive element (a diffraction grating for example) to separate correlation peaks of different colours. Although a single detector array can be used to detect all of the peaks, there must be two detection channels so as to discriminate both spatial blocks and different wavelengths in each block. A complicated electronic signal processing unit is needed in the thresholding and normalising loop to control the SLM (for the selection of spatial blocks) and the PLS (for the wavelength selection). The complexity is not only due to the hardware required, but also due to the method used: the two-channel detection system is based on the the average of the signals from all of the detector pixels corresponding to each channel, and one control will effect many weights. This may make the wrong decision unless a good learning/feedback control algorithm can be designed. Therefore it would be difficult to design such a system with optical control and feedback.

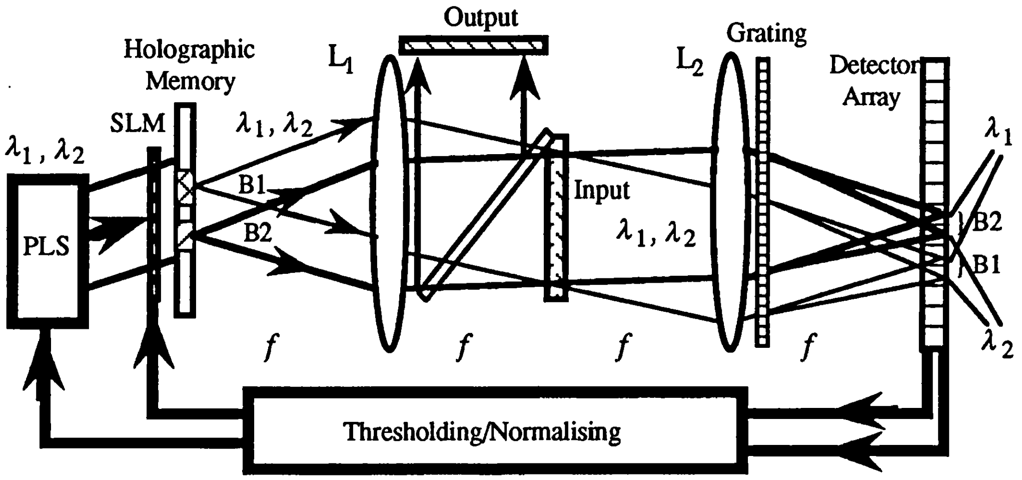

Fig. 6.2 Parallel correlation using a HOFNET which incorporates a memory recorded using conventional BOHS techniques. PLS: polychromatic light source; L_1 and L_2: achromatic Fourier transform lenses; SLM: electrically addressable spatial light modulator. B1 and B2 indicate different blocks, and λ_1 and λ_2 indicate different wavelengths used for wavelength multiplexing in each block.

We can now see that, for practical use in a HOFNET, each stored pattern in the memory must have its own unique "spatial address", so that only one detection channel is needed. Spatio-Angular Multiplexing (SAM) is a possible method of extending 2-D spatial multiplexing into the third dimension, whilst providing a unique spatial address for each hologram, and so such a recorded memory could be used in a HOFNET. In the next section we discuss SAM in detail.

6.2 Spatio-Angular Multiplexing (SAM)

6.2.1 Description of SAM

In traditional 2-D spatial multiplexed holographic storage using *thin* recording materials, all holographic spots of diameter d_H are separated by distances of Δ_x and Δ_z, and these spots do not overlap because $\Delta_x, \Delta_z \geq d_H$ (Fig. 6.3a). This allows an identical reference beam angle to be used for the recording of all holograms, and during readout, individual holograms can be addressed without crosstalk. However, this limits the number of holograms, M_S, that can be recorded ($M_S \leq (D_H/d_H)^2$, where D_H is the dimension of the square crystal, see Fig. 6.3a). If the separation, Δ_x and Δ_z, decreases, the holograms overlap (Fig. 6.3b) so that, when one hologram is replayed, the readout beam replays several holograms at once, and this results in crosstalk. Using different angled reference beams would not improve this situation, as thin materials have a poor angular selectivity.

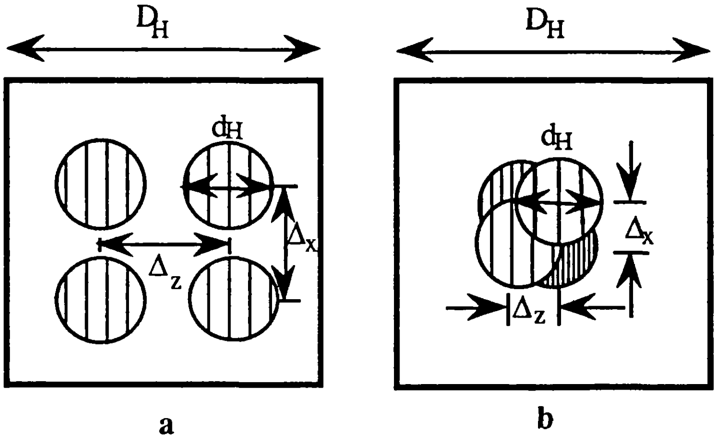

Fig. 6.3 **a** Spatial multiplexing and **b** spatio-angular multiplexing (SAM)

However, if the material is *thick*, (a photorefractive crystal for instance), the angular selectivity of the volume hologram would allow the holographic spots to overlap, and to be distinguished from one another by using different angled reference beams. Complete overlapping is referred to as purely angular multiplexing, whilst partial overlapping leads to spatio-angular multiplexing (SAM).

In the SAM recording scheme Fourier transform holograms are formed in spatially overlapping regions of the crystal and are distinguished from one another by using variously angled reference beams. The SAM recording introduces a slight spatial separation $\Delta_x, \Delta_z << d_H$ (between adjacent recordings), together with a slight change in the reference beam angle, $\delta\theta$ (where $\delta\theta$ is greater than the selective angle of the holograms so as to avoid crosstalk).

It is convenient to choose $\Delta_x = \Delta_z = \Delta$, and we can further define a spatial overlap factor, μ, as:

$$\mu = d_H / \Delta \qquad (6.1)$$

Obviously, μ is an important parameter in specifying a volume holographic memory. If $\mu \leq 1$, all holograms are spatially well separated, and this corresponds to spatial multiplexing. As $\mu \rightarrow \infty$, the case reverts to that of angular multiplexing. When μ is a finite number greater than unity, it results in SAM.

The other significance of the overlap factor, μ, is that it is related to the local (or differential) degree of angular multiplexing in SAM. It is hard to determine how many holograms overlap another, because different parts of one hologram are overlapped by different parts of several others. However, if we look at a small area of one hologram, the answer can be found. Let us refer to Fig. 6.4, and consider only square holograms. The small area mentioned above is marked by *P*, and we draw a square around it with a dimension of d_H (the hologram size), centred at *P*. Since all holograms have the same size (d_H), only holograms centred within this square (such as H_2 in Fig. 6.4) will overlap *P*, and others centred outside this square (such as H_1 in Fig. 6.4) will not. All holograms are separated by Δ in both the x- and the z- directions, so that the total number of holograms which overlap *P* is $(d_H/\Delta)^2=\mu^2$. We can then say that μ^2 is the local degree of angular multiplexing in SAM.

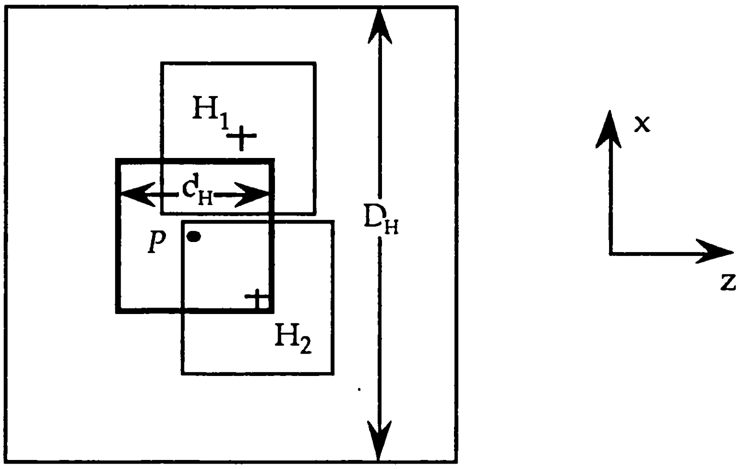

Fig. 6.4 Diagram for calculating the local degree of angular multiplexing in SAM. d_H: dimension of each hologram; D_H: dimension of the recording material.

There will be an upper limit on the value of μ, depending upon the particular use required of SAM. The separation between holograms in the memory plane, Δ, is equal to the separation between the correlation peaks in the detector plane (if a unity magnification system is used, as shown in Fig. 6.1). Therefore, Δ must not be smaller than the pixel pitch, d_I, in the detector array, and the maximum value of μ for a HOFNET will be d_H/d_I, assuming that each correlation peak occupies one detector pixel. The other limit on μ is the required diffraction efficiency, which we will discuss in the next subsection.

It is worth noting that the local degree of angular multiplexing for SAM is not uniform throughout the whole array. This quantity is smaller at the edges of the array (in the margin of width d_H) than elsewhere. If the material size is much larger than the hologram size, this quantity in most of the array area is equal to μ^2. All discussions in the next subsection assume that this is the case, and that μ^2 can be taken as the local degree of angular multiplexing.

6.2.2 The storage capacity and diffraction efficiency of a SAM memory

SAM aims at increasing storage capacity whilst still meeting the requirement of a HOFNET system. Let us look at the storage capacity and the diffraction efficiency of a SAM memory in this subsection.

First we shall compare the storage capacity of SAM with that of pure spatial multiplexing. The memory plane filling factor, F_S, for pure spatial multiplexing is defined as (also see Chapter Two):

$$F_s = \sqrt{M_s} d_H / D_H \tag{6.2}$$

where M_S is the number of holograms that are stored using spatial multiplexing. Purely spatial multiplexing has a maximum M_S which is not greater than $(D_H/d_H)^2$ (assuming square holograms), implying a maximum filling factor $F_S=1$. If SAM is used, for the same size of the individual holograms, d_H, and the same crystal dimension, D_H, the total number of holograms that can be stored is given by (see Fig. 6.5):

$$\begin{aligned} M_{SAM} &= \left(\frac{D_H - d_H}{\Delta} + 1 \right)^2 = \mu^2 \left(\frac{D_H}{d_H} - 1 + \frac{1}{\mu} \right)^2 \\ &= \mu^2 N_{SAM} \end{aligned} \tag{6.3}$$

where

$$N_{SAM} = \left(\frac{D_H}{d_H} - 1 + \frac{1}{\mu} \right)^2 \tag{6.4}$$

Since μ^2 is the local degree of angular multiplexing for SAM, we can define an "equivalent degree of spatial multiplexing" for SAM, by analogy with the conventional BOHS scheme. This equivalent degree of spatial multiplexing (N_{SAM}) is given by Eq. (6.4). In the case when $D_H \gg d_H \gg \Delta$ and $N_{SAM} \approx M_{s,max}$ (where $M_{s,max}=(D_H/d_H)^2$, and is the maximum number of holograms that can be stored using pure spatial multiplexing), then for $D_H \gg d_H \gg \Delta$, the storage capacity of SAM, in terms of the number of holograms, is given by:

$$M_{SAM} \approx \mu^2 M_{s,max} \tag{6.5}$$

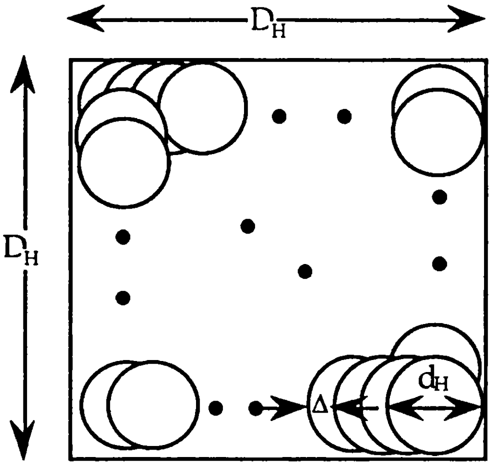

$$\sqrt{M_{SAM}} = \frac{D_H - d_H}{\Delta} + 1$$

Fig 6.5 Storage capacity of SAM

Accordingly, the filling factor for SAM, F_{SAM}, can be defined, by analogy with pure spatial multiplexing, as:

$$F_{SAM} = \sqrt{M_{SAM}} d_H / D_H \qquad (6.6)$$

Substituting Eq. (6.5) into Eq. (6.6), we have:

$$F_{SAM} = \mu F_s \quad \text{(valid for } D_H >> d_H >> \Delta) \qquad (6.7)$$

Therefore, F_{SAM} is increased by a factor of μ compared to pure spatial multiplexing, and can be much greater than unity. The storage density of SAM, in terms of bits, can be calculated using Eq. 2.25

$$S_{D,SAM} = F_{SAM}^2 \frac{\alpha_s{}^2}{\lambda^2} \approx \mu^2 S_{D,s} \qquad (6.8)$$

where $S_{D,s}$ is the storage density of pure spatial multiplexing if the same recording system is used for both schemes. From Eq. (6.8) one can see that, compared to purely spatial multiplexing, SAM increases the storage capacity by a factor of approximately μ^2. Obviously, the larger the overlapping factor μ, the larger the storage capacity that can be achieved. This increase in the storage capacity is gained at the price of losing the ability to individually erase local memories, and also of a decrease in the diffraction efficiency. For pure spatial multiplexing, each hologram could reach the diffraction efficiency that a single hologram would have; however, when holograms overlap and share the same volume (even partially), the diffraction efficiency decreases.

We calculate now the diffraction efficiency and storage capacity of SAM compared to pure angular multiplexing. First of all, we assume that the efficiency of each hologram using SAM (with a spatial overlapping factor equal to μ) is equal to that of each hologram using pure angular multiplexing, with a degree of angular multiplexing equal to μ^2. This is a reasonable assumption because SAM has a local degree of angular multiplexing equal to μ^2. We will further justify this approximation in the next chapter. Using this assumption we can carry out the calculations below.

We start with a comparison of the diffraction efficiencies of SAM and pure angular multiplexing. For pure angular multiplexing, the maximum number of holograms that can be stored is limited by the required minimum diffraction efficiency, as discussed in Chapter Five. The diffraction efficiency of one hologram (assuming that all of the holograms have identical efficiencies), η_{ang}, was given by Eq. 5.18, which can be shortened to:

$$\eta_{ang} = A/M_{ang}^2 \tag{6.9}$$

where A is a constant specifying the crystal parameters and recording conditions, and M_{ang} is the degree of angular multiplexing (the number of holograms superimposed in the same volume). If, however, SAM is used to record the same number of holograms as that recorded using purely angular multiplexing (i.e. $M_{SAM}=M_{ang}$), the number of holograms overlapping a given hologram (i.e. actually angularly multiplexed) is reduced. According to the discussion in the last subsection, the local degree of angular multiplexing of SAM is μ^2, and by the assumption made in the paragraph above, we may write the diffraction efficiency for SAM as:

$$\eta_{SAM} = A/(\mu^2)^2 \tag{6.10}$$

Since we require $M_{SAM}=M_{ang}$, substituting Eq. (6.3) into Eq. (6.9) gives:

$$\eta_{ang} = A/M_{SAM}^2 = A/(\mu^2 N_{SAM})^2 = \eta_{SAM}/N_{SAM}^2$$

Alternatively, we obtain:

$$\eta_{SAM} = N_{SAM}^2 \eta_{ang} \tag{6.11}$$

It can be seen from Eq. (6.11) that, compared with pure angular multiplexing, SAM increases the diffraction efficiency by the square of the degree of spatial multiplexing.

We turn our attention to the storage capacity of SAM in comparison with pure angular multiplexing. If the same target diffraction efficiency, say η_{target}, must be obtained by both SAM and pure angular multiplexing, it is expected that more holograms can be stored by using SAM than that by using purely angular multiplexing. If SAM is used with an overlapping factor of μ, the local degree of angular multiplexing for SAM is then μ^2, which is given by:

$$\mu^2 = \sqrt{\frac{A}{\eta_{target}}} \tag{6.12}$$

And the number of holograms to be stored using pure angular multiplexing, M_{ang}, is also determined by the target efficiency:

$$M_{ang} = \sqrt{\frac{A}{\eta_{target}}} = \mu^2 \tag{6.13}$$

Substituting Eq. (6.13) into Eq. (6.3), we obtain the total number of holograms that can be stored using SAM is

$$M_{SAM} = N_{SAM} \cdot M_{ang} \tag{6.14}$$

Therefore, compared with pure angular multiplexing, SAM increases the storage capacity by a factor equal to the equivalent degree of spatial multiplexing if the same target diffraction efficiency is required.

Equations (6.11) and (6.14) are our main results, showing how the SAM can increase the diffraction efficiency and storage capacity as compared to pure angular multiplexing. A common factor in these two equations is the equivalent degree of spatial multiplexing, N_{SAM}, which is defined by Eq. (6.4). In the case of $D_H >> d_H >> \Delta$, (i.e. the crystal size is much greater than the hologram size, and the spatial separation between adjacent holograms is small compared to the hologram size) N_{SAM} is approximately $(D_H/d_H)^2$, and Eqs. (6.11) and (6.14) can be rewritten:

$$\eta_{SAM} = \left(\frac{D_H}{d_H}\right)^4 \eta_{ang} \tag{6.15}$$

for the enhancement of diffraction efficiency (in the case of the same target storage capacity, in terms of the number of holograms, stored), and

$$M_{SAM} = \left(\frac{D_H}{d_H}\right)^2 \cdot M_{ang} \tag{6.16}$$

for the same hologram efficiencies in both cases.

From Eqs. (6.15) and (6.16) one can see that the enhancement of efficiency and storage capacity due to SAM is of a high order of the magnitude of the ratio of the material size to the hologram size. If the hologram size is fixed (this is common in practice), SAM obtains more benefit from an increase in material size than would a purely angularly multiplexed scheme.

Finally we can compare the storage capacity of SAM with a BOHS configuration, where, for both SAM and BOHS, the holograms and media have the same sizes (d_H and D_H), and the same target diffraction efficiency (η_{target}) is to be obtained. According to our basic assumption, the local degree of angular multiplexing for SAM (μ^2), and the true degree of angular multiplexing for BOHS (N_{BOHS}), are determined by Eqs. (6.12) and (6.13). The capacity of BOHS, in terms of the number of holograms, is given by:

$$M_{BOHS} = M_{s,max} \cdot N_{BOHS} \tag{6.17}$$

where $M_{s,max}=(D_H/d_H)^2$ is the true degree of spatial multiplexing for BOHS storage. Comparing Eq. (6.17) with Eq. (6.14), the storage capacity for BOHS is larger than that for SAM, since N_{SAM} is smaller than $M_{s,max}$. However, in the common case when $D_H >> d_H >> \Delta$, $N_{SAM} \approx M_{s,max}$, the difference is negligible.

In summary, we have proposed a novel hologram multiplexing scheme, SAM. SAM is specified by a local degree of angular multiplexing, μ^2, and an equivalent degree of spatial multiplexing, N_{SAM}. Compared to pure angular multiplexing, SAM increases the diffraction efficiency and the storage capacity by a factor of $(N_{SAM})^2$ and N_{SAM} respectively, and the most benefit is gained if N_{SAM} is large, i.e. the material size is much larger than the hologram size.

The discussions in this subsection are based on the condition when $D_H >> d_H$, so that μ^2 can be taken as the local degree of angular multiplexing for the whole array. In the case when this condition is not satisfied (if D_H were slightly larger than d_H, for instance), pure spatial multiplexing and BOHS schemes are impossible. SAM, however, is still applicable, and increases both the diffraction efficiency and storage capacity, since all of the recording material is utilised by SAM. However, in this case, the local degree of angular multiplexing is rather non-uniform, and is definitely not equal to μ^2 for most of the array. The analyses in this subsection (in particular, Eqs. (6.15) and (6.16)) are not valid.

6.3 Design of a HOFNET System Using a SAM Memory

6.3.1 Memory recording

Each hologram in a SAM memory has two linear addresses (x and z) and two angular addresses (θ and ϕ, in the horizontal and vertical planes respectively). If the reference beams are arranged in the horizontal dimension only, the number of addresses can be reduced to three (x-z-θ). The recording of a SAM memory requires suitable equipment to provide a distinct x-z-θ address for each hologram.

The x-z-θ address of individual holograms can be provided by non-mechanical positioning such as shown in Fig. 6.6 (a system proposed by d'Auria et al [d'Au74] and [Gla79]).

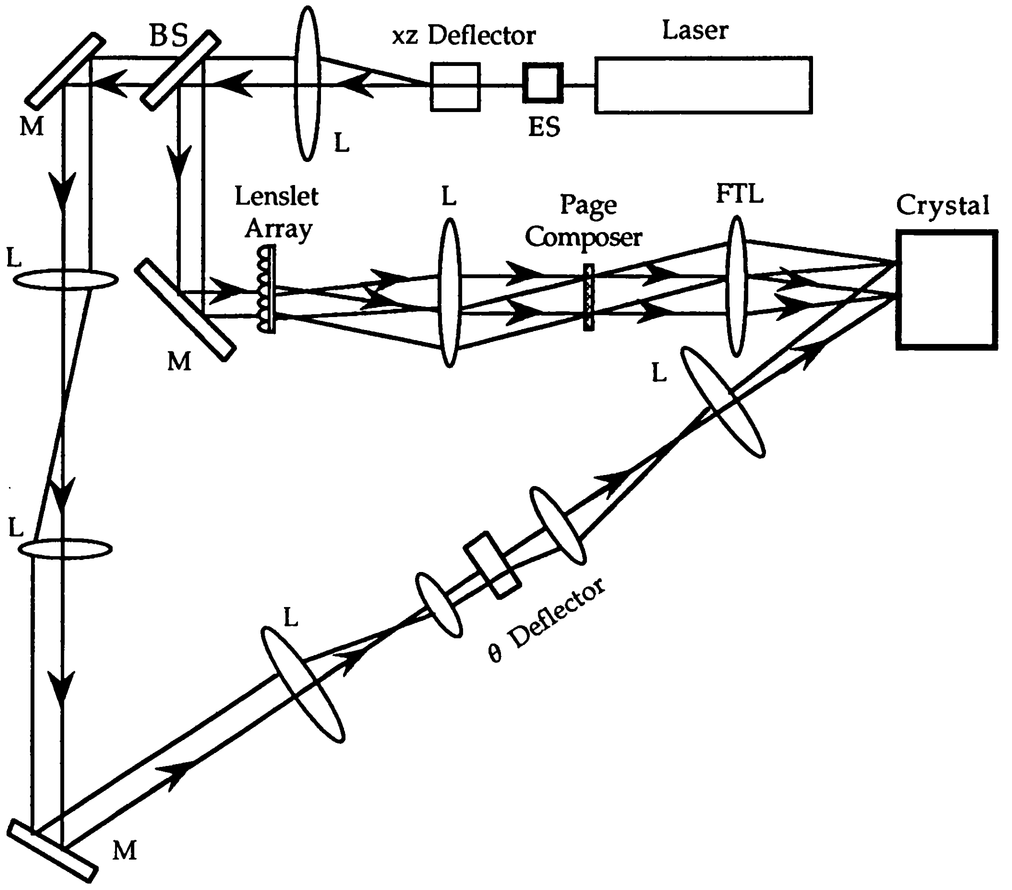

Fig. 6.6 A conventional 3-D storage recording system. ES: electrical shutter; BS: beam splitter; FTL: Fourier transform lens; L: lens; and M: mirror.

In this configuration the x-z-θ address is determined by two beam deflectors, an xz deflector and a θ deflector. The xz deflector is a combination of x- and z- deflectors, so actually three deflectors are required. A rather complicated optical system keeps the reference beam intersecting the object beam at any x-z-θ address. Since there is no need to move the recording medium, the beam deflectors in this system can be non-mechanical. Acoustooptic and electrooptic deflectors are suitable for this system. The former should only be used before the beam splitter, because an acoustooptic defector introduces a Doppler shift into the light frequency. This will reduce the coherence of the writing beams if only one optical path includes the acoustooptic deflector. The advantage of this system is the potentially high access speed offered by the non-mechanical beam defectors. The main drawbacks of this system are high price due to expensive devices, and the high loss when the light propagates through so many optical surfaces.

Another proposed configuration for SAM memory recording is shown in Fig. 6.7. In this configuration, the x-z address of each hologram is achieved by 2-D translation of the recording media which is mounted on an x-z linear stage pair, and the θ address (the angle of the reference beam) is achieved by a mirror mounted on a rotary stage. Data pages are input into the page composer by means of either a transparency, a spatial light modulator (either electrically or optically addressed), or a liquid crystal TV. The aperture restricts the size of each hologram. A unity magnification telescope can be used to change the reference angles and to ensure that the relative position of the object beam on the crystal surface remains unchanged.

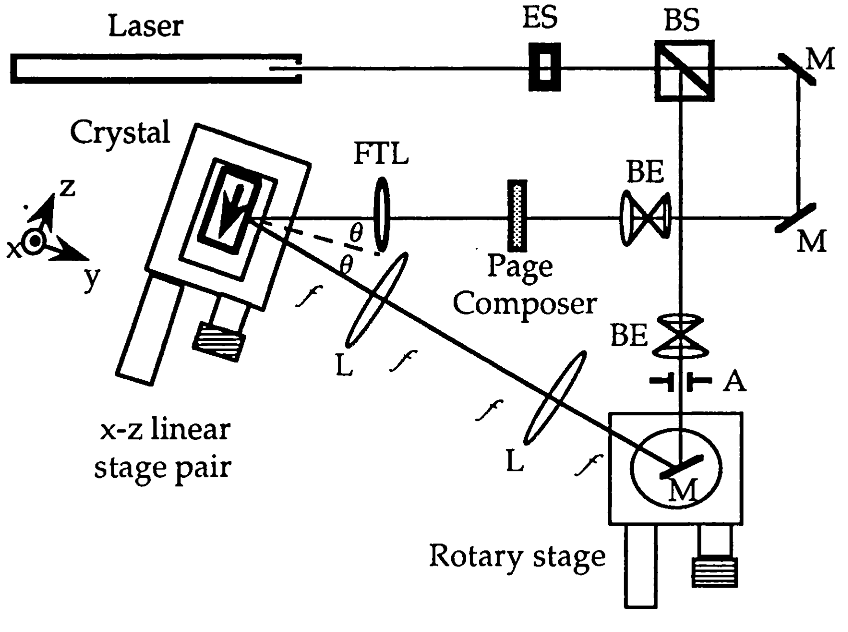

Fig. 6.7 Configuration for SAM memory recording. ES: electrical shutter; BS: beam splitter; BE: beam expander; FTL: Fourier transform lens; L: lens; M: mirror, and A: aperture.

The advantage of this system is its simplicity compared to the system of Fig. 6.6. The small number of optical components avoids the loss of light power through reflection and absorption and makes the alignment of optical components easier. In this system, mechanical positioning equipment (linear and rotary stages) are used, and these provide a large range of motion (for example, the rotary stage may be turned through 360^{o}). The main disadvantage of this system is in the mechanical control of the hologram position and of the incident angle of the reference beam. This requires high resolution and reliability from the positioning equipment, and adjustment is inevitably slow. Also, the mechanical motion causes vibration of the optical table, and this may affect the stability of the optical set-up, which is critical for successful holographic recordings.

6.3.2 Parallel replay system

The reference paths in both systems described in the last subsection can be used to provide readout beams for serial replay of the recorded SAM memory, although the second system (Fig. 6.7) requires x-z motion of the memory medium. However, neither system (Figs 6.6 and 6.7) is suitable for the parallel recall and parallel correlation required by HOFNET. This is because there is only one reference beam provided by these systems at any time. Parallel recall in a HOFNET memory using spatio-angular multiplexing needs a multiple angled weighted beam generator (MAWBG) to provide all the readout beams in parallel. A possible design of such an MAWBG is schematically shown in Fig. 6.8.

In Fig. 6.8 the combination of a lens and a grating can also be replaced by a lenslet array, a holographic optical element (HOE), or a computer generated hologram (CGH) (A surface emitting microlaser diode array can also be used in this system [Pae90]). This combination creates the readout point sources in the rear focal plane of the lens. A spatial light modulator is put in this plane, and it receives a control signal from the feedback and thresholding loop. In this way it can weight the readout beams in each iteration. A schematic diagram of the whole correlation system is shown in Fig. 6.9.

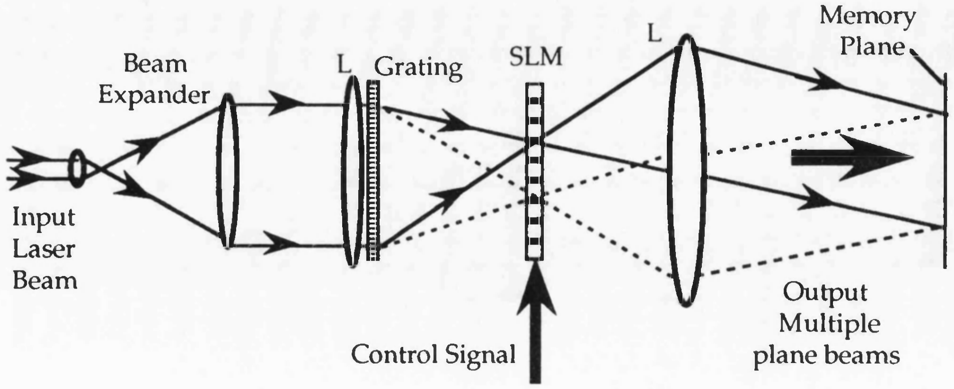

Fig. 6.8 Multiple angled weighted beam generator (MAWBG)

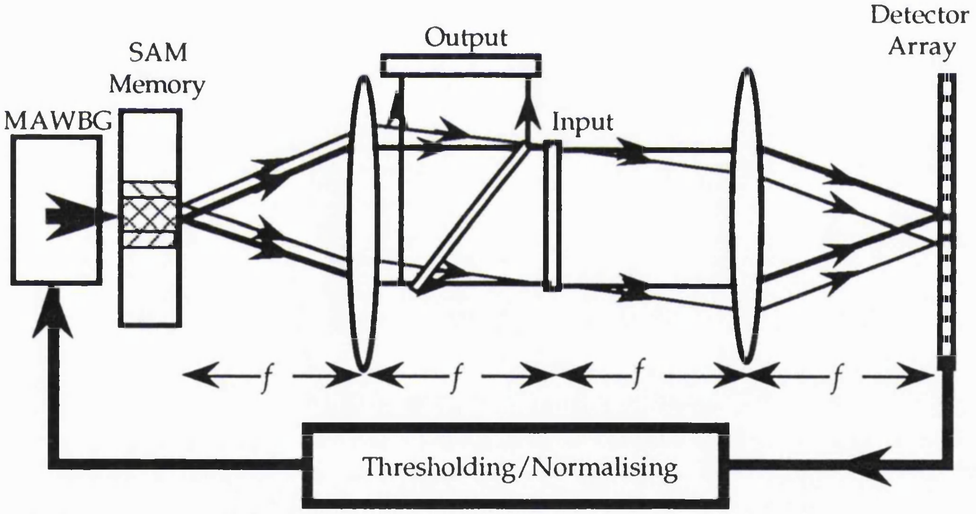

Fig. 6.9 Parallel correlation by a HOFNET which includes a SAM memory. MAWBG: multiple angled weighted beam generator.

In Fig. 6.9 when the SAM memory is read out by an MAWBG (Fig.6.8), all reconstructed patterns from all holograms are brought to the same location on the correlation plane, and these multiply the input pattern.

All correlation peaks in the detector array are well separated. The separation between correlation peaks is determined by the separation between holograms, Δ (in Fig. 6.5), and the system magnification. These peaks can be distinguished by a high resolution detector array (such as a CCD camera) which can provide a control signal to the MAWBG using electronic and/or optical feedback and thresholding. Only one channel of detection is required if each hologram is recorded using a distinct reference beam angle. Compared to the system described in Section 6.1 (which uses BOHS scheme, see Fig. 6.2), the use of SAM memory reduces the complexity (number of channels of detection) required for parallel correlation, whilst allowing three dimensional optical interconnections to be implemented in a high order feedback neural network. However, there are still some complicated issues left to resolve. For example, each of the readout beams generated by the MAWBG must match precisely the corresponding holograms for Bragg readout. We will discuss this briefly in the future work section.

In summary, we have discussed the type of memory required by a HOFNET, and have considered the incorporation of a 3-D memory element into a HOFNET. To improve the memory capacity of current HOFNET designs, we have proposed a novel multiplexing scheme for memory recording, SAM. SAM memories have a larger capacity than that offered by either purely spatial or purely angular multiplexed schemes. The diffraction efficiency of SAM memory will be higher than that recorded using pure angular multiplexing, by a factor of $(N_{SAM})^2$, if both schemes multiplex the same number of holograms. SAM provides the possibility of parallel recall and a high order of nonlinearity of the original HOFNET, in addition to a high storage capacity. In the next chapter we describe in detail our preliminary experiment for SAM memory recording.

CHAPTER SEVEN

EXPERIMENTAL STORAGE OF 756 HOLOGRAMS IN AN Fe:LiNbO$_3$ CRYSTAL USING SPATIO-ANGULAR MULTIPLEXING

In the previous chapter we have described the principles behind spatio-angular multiplexing (SAM), and have predicted that the storage capacity, and the diffraction efficiency, of a SAM memory will be larger than that obtained by pure angular multiplexing. In this chapter we describe in detail our preliminary calibration experiment on the storage of 756 holograms in an Fe:LiNbO$_3$ crystal using SAM. In section 7.1 we consider the design details of the experimental arrangement, with special regard to the peculiarities of SAM recording in photorefractive crystals. The test patterns used as the stored signal pages are described in section 7.2. Section 7.3 deals with the determination of exposure conditions. The process of determining the optimum writing beam ratio and the total writing intensity is discussed in subsection 7.3.1. The measurement of the writing and erasure time constants under the experimental exposure conditions is described in subsection 7.3.2. The measured time constants were used for calculating the exposure time sequence which is discussed in subsection 7.3.3. In section 7.4 the experimental storage and the performance of the recorded memory are described. Finally, in section 7.5, we analyse the results and draw conclusions from the experiment.

7.1 Experimental Arrangement

7.1.1 The selection of a recording material

From Table 3.1 in Chapter Three, we know that iron doped lithium niobate (Fe:LiNbO$_3$) and cerium doped strontium barium niobate (Ce:SBN) are most suitable for holographic storage owing to the large dynamic range it is possible to attain in the modulation of their refractive indices [Kur77, For92]. In addition, SBN is rather sensitive, and LiNbO$_3$ has a long persistence (long dark decay time). The disadvantages of SBN are its short dark decay time, and its high cost (due to the difficulties of growing large bulk SBN crystals which also have a good optical quality [Red88]). LiNbO$_3$ has been investigated quite extensively [Amo72, Kur77a, Kur77b, Kra86, Rin89]. It can be grown easily and to a large size with excellent optical quality. This has led us to choose LiNbO$_3$ in our experiments on dense holographic storage using SAM.

It has been reported [Bur78] that, to be used for multiple storage applications, LiNbO$_3$ crystals should meet the following criteria:

(1) Crystals should be of the order of 1cm thick, as this allows the angular separation between holograms to be sufficiently small;

(2) The optical density, D, defined as D=log(1/T) where T is the transmittance, should be approximately 0.3 at the recording wavelength (i.e. transmittance approximately equal to 50%), as this maximises the overall record-readout efficiency. This optical density should be uniform throughout the crystal;

(3) The Fe^{2+} concentration must be much less than the Fe^{3+} concentration, so as to minimise erasure during storage.

The crystal used for SAM recording was prepared by the Shanghai Institute of Ceramics, at the Chinese Academy of Sciences, and was provided by Photox Optical Systems, U. K. The growth of the crystal was aimed at meeting the above criteria. The crystal was grown in an air atmosphere, using the Czochralski method, from a congruent melt with a dopant Fe concentration of 0.1wt%. An annealing treatment in an oxygen atmosphere was carried out after growth. This ensured a high concentration ratio of Fe^{3+} to Fe^{2+}. A sample measuring 18mm x 8mm x 20mm was used for this work. The uniformity of the overall transmittance is critical for SAM recording, as it ensures a uniform diffraction efficiency. We measured the transmittance, T, over a major part of the crystal before the SAM recording, using an extraordinary plane beam at a wavelength of 514.5nm, with beam size of 7mm. The results are shown in Fig. 7.1. The average transmittance was $T=(32.4\pm0.5)\%$, corresponding to an optical density of 0.490 ± 0.006. The uniformity is fairly good although the optical density is higher than the recommended value (0.3).

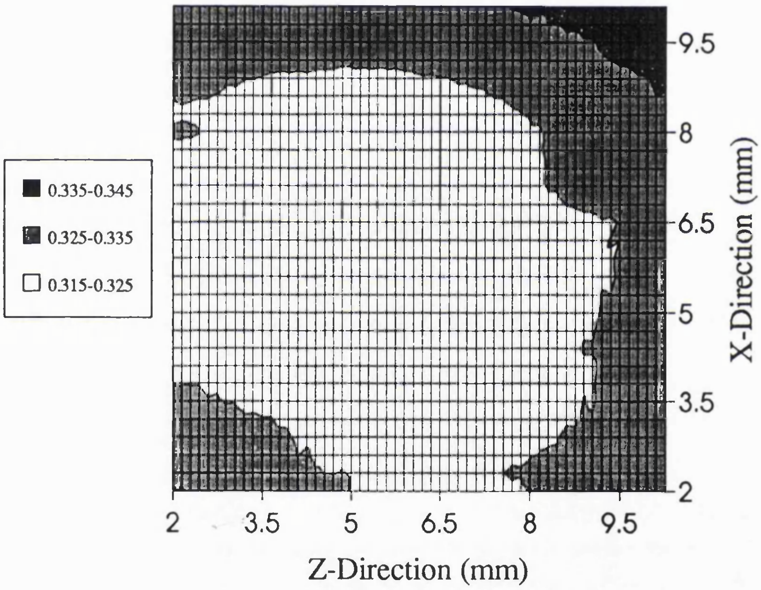

Fig. 7.1 A contour plot showing the uniformity of the crystal transmittance, measured using extraordinarily polarised light, at wavelength of 514.5 nm.

7.1.2 Information page generation

A spatial light modulator (SLM), provided by STC Technology Ltd (now Thorn-EMI, CRL, Smectic Technology, U. K.), was chosen to form the information pages to be stored. This SLM uses a 1.7μm thick layer of ferroelectric chiral smectic C liquid crystal. The 16,384 pixels (128x128) are formed at the intersections of identical row and column electrodes. They are on a 165μm pitch with a gap between the pixels of 15μm. The pixels can be thought of as halfwave plates whose optic axis can be switched through 45^o. This change is made visible by viewing the device between crossed polarisers [Stc89]. Test binary patterns, generated by computer, were sequentially down-loaded onto the SLM, and these patterns modulated the incident plane laser beam so as to create test signal beams. The contrast ratio between the "on" and "off" states of pixel array depended upon the alignment of the crossed polariser pair, and was also limited by the gaps between the pixels (which may be regarded as always being "on"). We measured the best contrast ratio to be 16:1 over an array of pixels.

7.1.3 Hologram size and spatial overlap factor

The size of each hologram depended on the finest pattern structure (generated by the SLM) which was to be resolved. We shall calculate here the minimum hologram size required for a given resolution. The spatial structure, P(x), for a typical pattern is shown in Fig. 7.2a., and is the sum of many rectangular functions of various widths. The minimum width of "on" pixels, d_p, is equal to twice the SLM pitch (330μm) in our test patterns, and the minimum separation between rectangular functions, d_s, is equal to the SLM pitch, i.e. 165μm (this is the width of the "off" margins around the identification number of each pattern, described later in section 7.2).

When this pattern is applied to the SLM (remembering that the gaps between pixels are always in the "on" state), the light distribution through the SLM, s(x), can be expressed as (in one dimension):

$$s(x) = P(x)\cdot\left[\mathrm{rect}\left(\frac{x}{b}\right)\otimes\mathrm{comb}\left(\frac{x}{d_s}\right)\right]+\mathrm{rect}\left(\frac{x}{D_s}\right)\cdot\left[\mathrm{rect}\left(\frac{x}{d_g}\right)\otimes\mathrm{comb}\left(\frac{x-d_s/2}{d_s}\right)\right] \tag{7.1}$$

where b is the width of each pixel, D_s is the dimension of the SLM, d_s is the SLM pitch, d_g is the width of the gap, comb specifies comb function [Goo68], and ⊗ indicates convolution. Equation (7.1) indicates that the light distribution consists of two items: the first is the input pattern that has been pixellated, and the second is the light coming from all gaps. This distribution is shown in Fig. 7.2**b**.

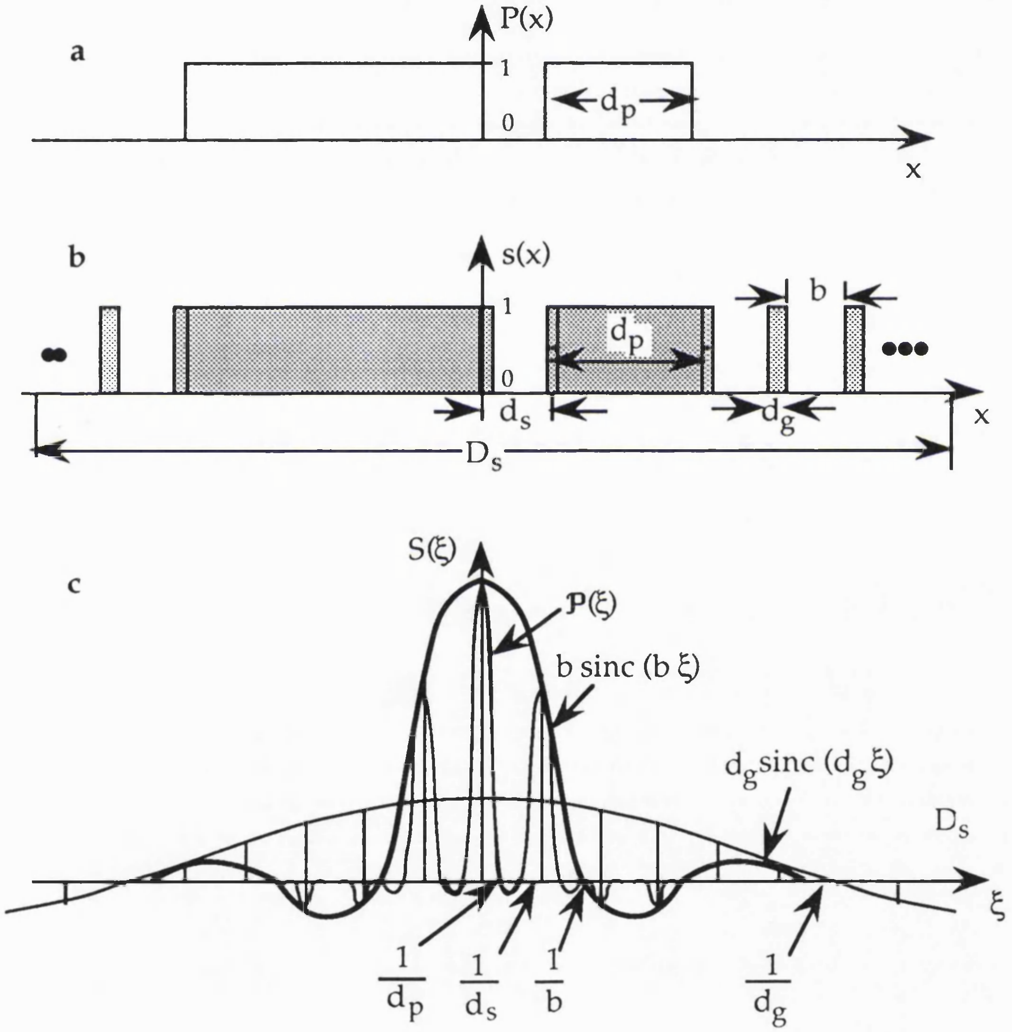

Fig. 7.2 Diagram of **a** the spatial structure of a typical pattern to be stored, **b** the light distribution after transmission through the SLM, and **c** the light distribution in the F. T. hologram recording plane. The distributions are shown in one dimension only.

The light distribution in the hologram plane, S(ξ), is the Fourier transform of Eq. (7.1) [Goo68], and is given by:

$$S(\xi) = P(\xi) \otimes \left[b\, d_s\, \mathrm{sinc}(b\xi)\, \mathrm{comb}(d_s\xi) \right] + \\ + D_s\, \mathrm{sinc}(D_s\xi) \otimes \left[d_g\, d_s\, \mathrm{sinc}(d_g\xi)\, \mathrm{comb}(d_s\xi) \cdot e^{-j\pi d_s \xi} \right] \tag{7.2}$$

where $P(\xi)$ is the Fourier transform of the pattern function, P(x). The spectrum expressed by Eq. (7.2) is schematically shown in Fig. 7.2c. The widths of the spectrum functions are inversely proportional to the widths of the corresponding spatial structures. Since d_g (the gap width) <b (the pixel width) <d_S (the pitch) <d_p (the width of the finest structure in the pattern) <D_S (the dimension of the SLM), the relation between the widths of the spectra is:

$$\frac{1}{d_g} > \frac{1}{b} > \frac{1}{d_s} > \frac{1}{d_p} > \frac{1}{D_s} \tag{7.3}$$

The very narrow linewidth due to the SLM frame (width $1/D_S$) is not shown in the figure.

In the hologram plane, the spatial coordinate, x_H, may be obtained from the spatial frequency coordinate, ξ, by (Eq. 2.8):

$$x_H = \lambda f \xi \tag{7.4}$$

where λ is the light wavelength used for recording and f is the focal length of the F.T. lens. Therefore, the minimum hologram size, d_H, is determined by the minimum spatial frequency component, ξ_{min}. If we decided to resolve at least the pixel pitch ($\pm\xi_{min}=1/d_S$, $d_S=165\mu m$), then, for $\lambda=514.5nm$ and $f=125mm$ we have:

$$d_H \geq 2\, \lambda f / d_S = 0.8\ \mathrm{mm} \tag{7.5}$$

Another limit to the minimum hologram size is the interaction depth of the two writing beams, which should not be less than the crystal thickness, d (so as to take advantage of the high angular sensitivity provided by a thick crystal). Referring to Fig. 7.3, and assuming that the diameters of the two writing beams are equal, and that they are also collimated (this corresponds to the case of simple grating recording), the hologram size should satisfy:

$$d_H \geq d \cdot \tan\theta \tag{7.6}$$

where θ is the internal half interbeam angle , and d is the crystal thickness. For d=8mm and $\theta=11^0$ (corresponding to an external half interbeam angle of $\theta_{ext}=25^0$ as used in the experiment), we have $d_H \geq$ 1.6mm. We chose d_H to be 2.4mm; this was large enough to satisfy both the condition of Eq.(7.5) and that of Eq. (7.6), and included a margin of safety.

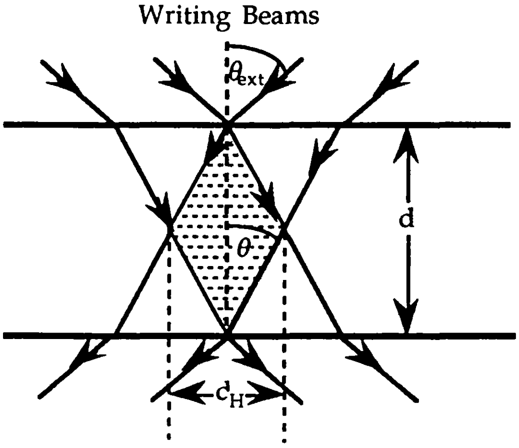

Fig. 7.3 Hologram size limited by the desired interaction depth

The overlap factor, μ, (defined in Chapter Six as the ratio of the hologram size to the one-dimensional spatial separation between adjacent holograms), is very important for the performance of SAM memories. A large μ is needed for a large storage capacity, but it is limited by the size of correlation peaks, by the pitch of the detector array and by the minimum target diffraction efficiency, as discussed in the previous chapter. Assuming that a CCD camera with a sensor element pitch of 1.2μm[1] will

---

[1] See *Largest Image Sensor*, Electro Optics Products, March 1993

be used to detect the correlation peaks (see Fig. 6.8), and assuming the very extreme case that a correlation peak occupies only one pixel of the detector, then the value of μ could be as large as 2000. However, the local degree of angular multiplexing will be $M_{ang}=\mu^2$, and the diffraction efficiency will be too low to be detected (of the order of A/μ^4, see Eq. 6.8). In fact, the overlapping factor was determined by the required diffraction efficiency.

We shall assume that the ratio of the erasure to writing time constants (τ_E/τ_W) is 9, and that $\nu=\pi\Delta n_{sat}d/(\lambda\cos\theta)=0.52$ (corresponding to a maximum efficiency for a single grating of 25%, see Eq. 5.14). These values were obtained from experimental measurements which will be discussed later in this chapter. By substituting these values, and the target efficiency for each hologram, η_{min}, into Eq. 5.19 , the local degree of angular multiplexing, M_{ang}, and the corresponding overlap factor, μ, are calculated to have the following values:

η_{min}	$M_{ang}(=\mu 2)$	μ
0.01%	520	22.8
0.1%	164	12.8
0.5%	73	8.6

μ was chosen to have a value of 8. This allowed us to record 784 holograms (forming a 28 X 28 array) in approximately 1cm^3 of a crystal of LiNbO$_3$, and led us to expect an average diffraction efficiency of 0.5%.

These 784 holograms occupied an area of about 10.5 x 12.1 mm^2, which was much less than the 20 x 18 mm^2 entrance size available. This allowed us to perform characterisation experiments on the crystal using the remaining areas. Fig. 7.4 shows the crystal size, its orientation, and the areas of it used both for characterization and for the final recording.

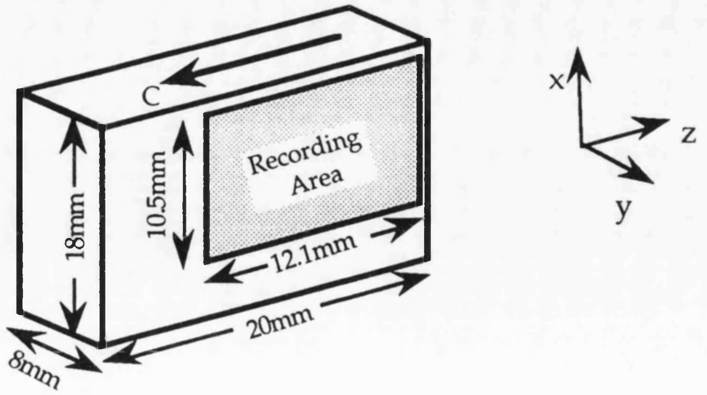

Fig. 7.4 The crystal size and orientation. The plain area was used for exposure characterisation experiments.

7.1.4 Recording geometry and angular separation between holograms

A symmetric geometry was chosen for the recording, so as to make the grating vectors and the C-axis parallel. This ensured a large coupling strength and, hence, a high efficiency. In practice, a quasi-symmetrical geometry was used, so that multiple reflections between the optics and the crystal could be avoided.

The interbeam angle (which determines the spatial carrier frequency) was governed by the desired angular selectivity and the spatial frequency response of $LiNbO_3$. We calculated the variation of the *external* selective angle with the external half-interbeam angle (using the Kogelnik's theory), and this is shown in Fig. 7.5. Note the non-monotonic nature of this curve, in contrast to the monotonic function of the *internal* selective angle vs the internal half interbeam angle as specified by Eq. 2.29. From Fig. 7.5 it can be seen that, whilst the external half-interbeam angle stays between 20^{o} and 70^{o}, the external selective angle is fairly small and varies only slowly.

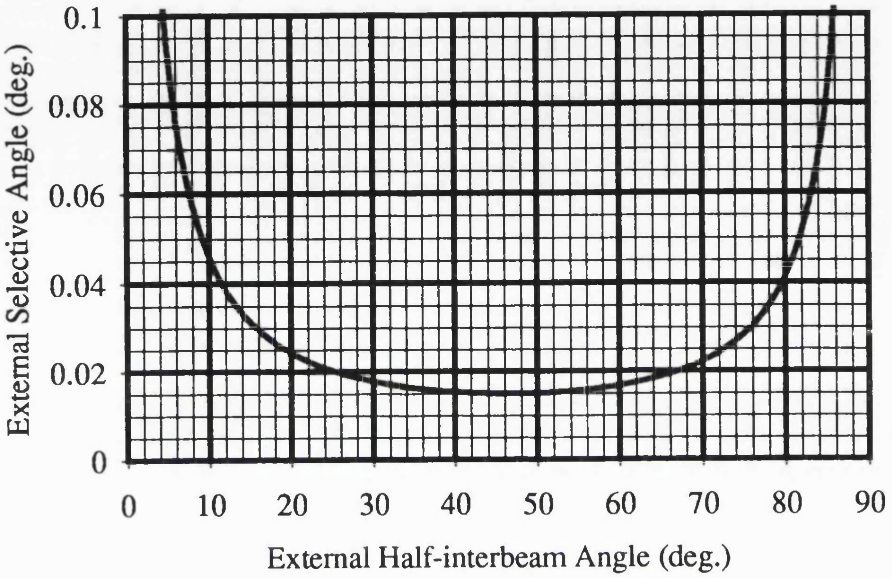

Fig. 7.5 the external selective angle as a function of the external half interbeam angle for an 8mm thick LiNbO$_3$ crystal, calculated using Kogelnik's theory.

Another factor which must be taken into account is the spatial frequency response (or modulation transfer function, MTF, which means the variation of diffraction efficiency with spatial frequency) of Fe:LiNbO$_3$. Burke et al measured the curve of the spatial frequency response of Fe:LiNbO$_3$, and showed that the full width half maximum response lies between 1350 lines/mm and about 1900 lines/mm, and peaks at 1600 lines/mm (see Fig. 7.6). This corresponds to an external half-interbeam angle range extending from 20^{o} to 29^{o}, and centred at 24.3^{o}. We decided to adopt this result, and so chose the external half interbeam angle, θ, to be 25^{o}.

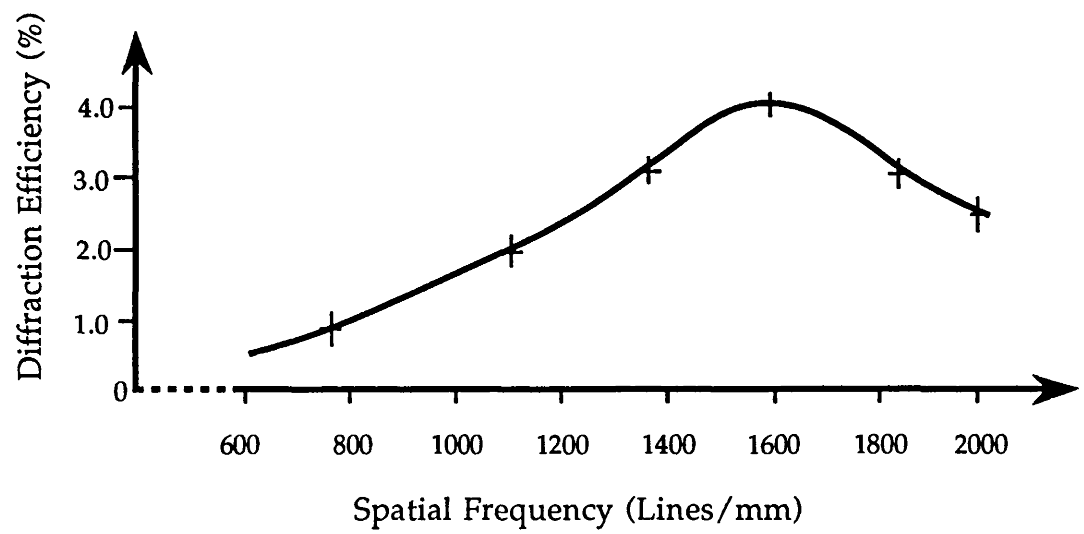

Fig. 7.6 Spatial frequency response of Fe: LiNbO$_3$ (from [Bur78])

The angular separation of the reference beams between recordings was determined by the selective angle, $\Delta\Theta$. The theoretically calculated selective angle corresponding to a half-interbeam angle of 25^o can be found from Fig. 7.5, and is equal to 0.02^o external. However, the selective angle of gratings recorded in photorefractive crystals is usually greater than the theoretical prediction, using Kogelnik's theory, as discussed in Chapter Four. A typical measurement of the selective angle for this crystal and geometry is shown in Fig. 4.18b where no efficiency nulls and side lobes are seen. The 10dB angular width of the main diffraction lobe is approximately 0.03^o. Since we would superimpose a large number of holograms in a given volume, the 10db angular width, taken as the angular separation between recordings, might not be large enough to minimise crosstalk. We chose the external angular separation to be 0.1^o, as this was large enough to ensure low cross-talk with an adequate safety margin.

7.1.5 Use of diffuser

An important requirement for the memory is that it should produce reconstructed images of good quality. We used a 4*f* imaging system to investigate the image quality: A resolution target was located in the front focal plane of the first F. T. lens, and the image was formed in the rear focal plane of the second F. T. lens. The crystal was located in the F.T. plane (the rear focal plane of the first F. T. lens, which was also the front focal plane of the second F. T. lens). Fig. 7.7**a** shows a direct image of the resolution target, formed by this system. The quality is fairly good, and confirms that the crystal did not introduce significant distortions into the image. Fig. 7.7**b** shows the reconstructed image of the same object from a hologram. The quality of the holographic image is rather poor, and seems to be better vertically than horizontally. Although different writing beam ratios were tried for the holographic recording of this object, no evident improvement was obtained.

In order to improve the reconstruction we decided to use a ground glass diffuser to introduce random phase shifts into the light illuminating the SLM. This technique had proved useful in obtaining high storage densities and quality in holograms of diffraction limited size containing digital information [Kur79, Tsu73, Tsu76]. After Fourier transformation by the F.T. lens, the intensity distribution on the crystal was much more uniform than in the case without a diffuser. Fig. 7.7**d** shows the image reconstructed from a hologram which was recorded with a diffuser inserted into the object path. The replay beam was the reference beam for recording. The image quality is significantly improved, so that there was no evident difference between the holographic image and the direct image which is shown in Fig. 7.7**c** (with the same diffuser).

7.1.6 Experimental set-up

Fig. 7.8 is a photograph showing the experimental set-up. A schematic diagram of this set-up is shown in Fig. 7.9. A description of the major equipment used in the experiment is given in Appendix A.

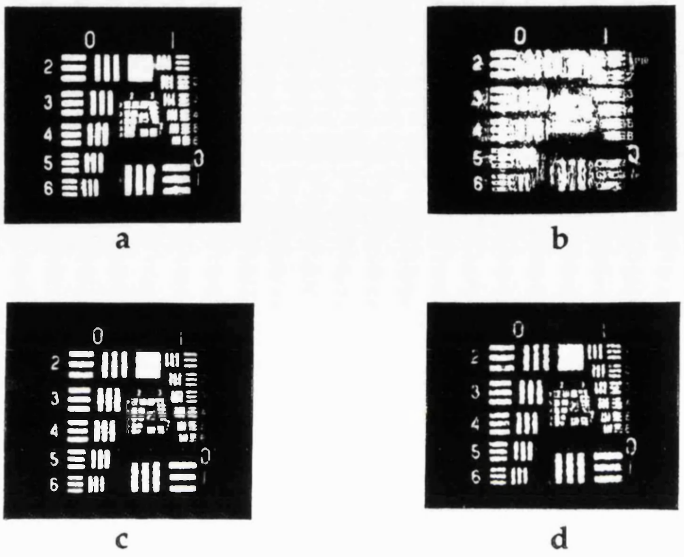

Fig. 7.7 Images of a resolution target through a Fe:LiNbO$_3$ crystal. **a**: Direct image without a diffuser. **b**: Reconstructed image from a hologram, without a diffuser. **c**: Direct image with a diffuser. **d**: Reconstructed image from a hologram, with a diffuser.

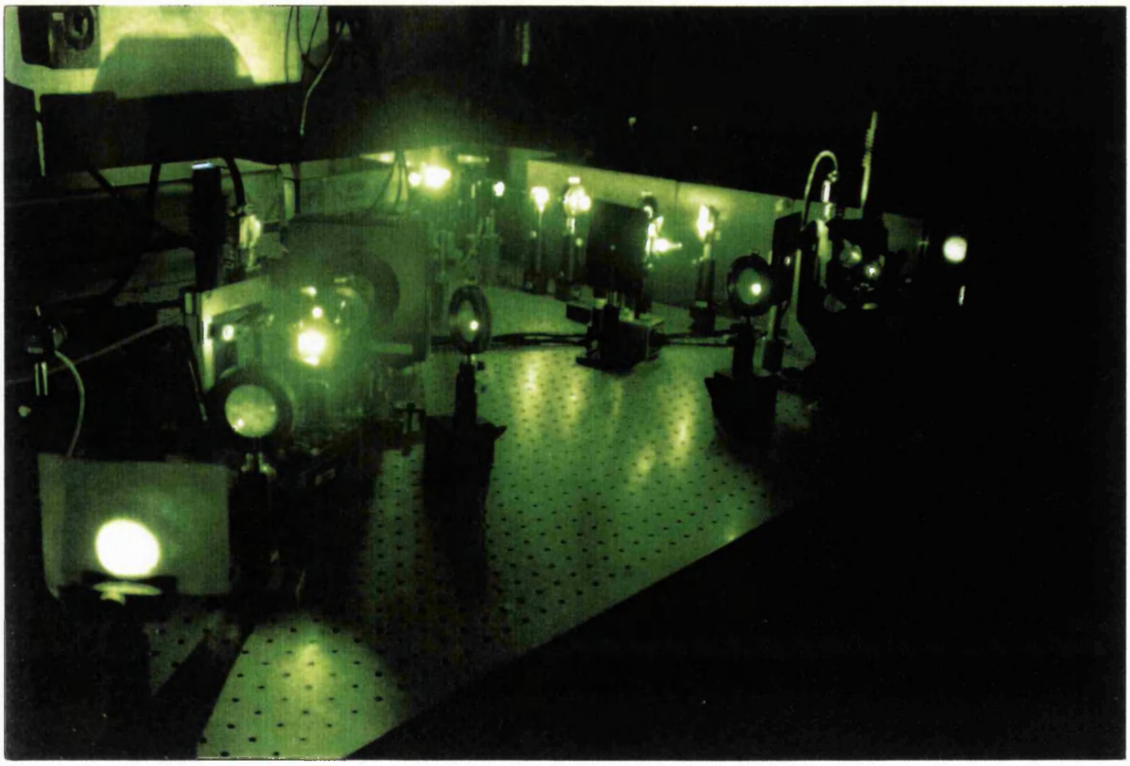

Fig. 7.8 Photograph of the experimental set-up.

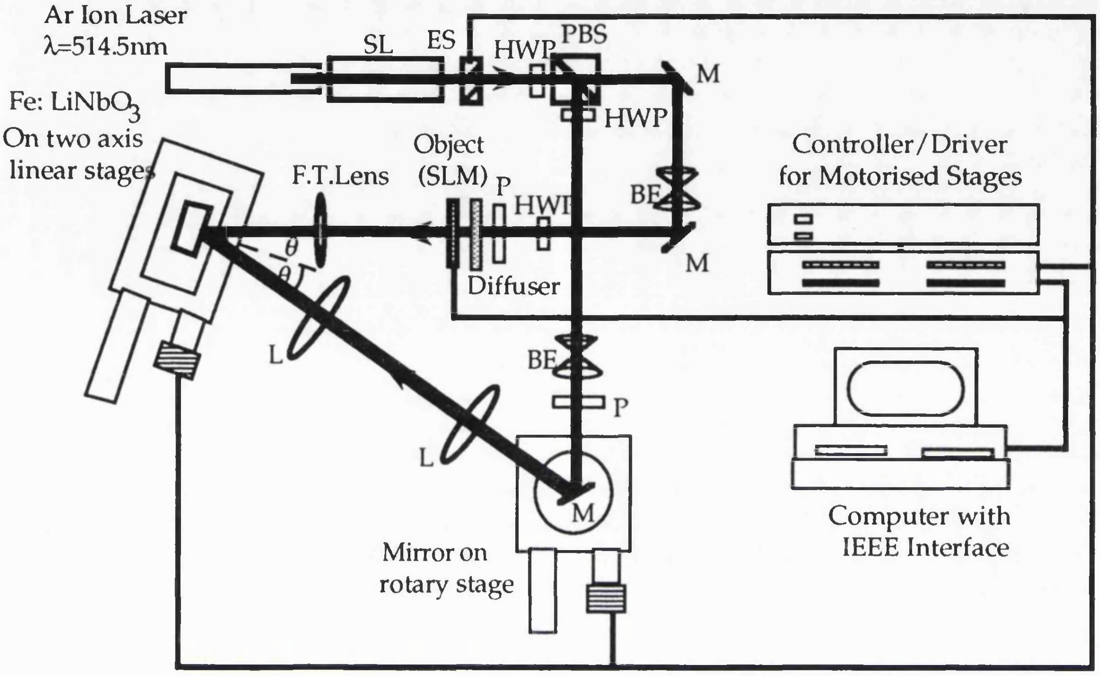

Fig. 7.9 Schematic diagram of the experimental set-up. SL: laser stabiliser; ES: electronic shutter; HWP: half wave plate; PBS: polarising beam splitter; BE: beam expander; P: polariser; L: lens; M: mirror.

A Spectra Physics Argon-ion laser with intracavity etalon (λ=514.5nm) was used as the coherent light source, and was power-stabilised by a laser stabiliser to within 0.5%. An assembly of one polarising beam splitter and two half wave plates was used to adjust the desired writing beam ratio, and to maintain the extraordinary (horizontal) polarisation state of the two writing beams. A pair of polarisers enabled the beam polarisation state to be finely adjusted. The crystal was mounted on a two axis (x-z) motor-driven linear stage pair which had a resolution and unidirectional motion repeatability of 1μm. A F.T. lens, which performed Fourier transformation of the pattern displayed on the SLM, had a diameter of 38mm and a focal length 125mm. A mirror (mounted on a Micro-Controle motor-driven rotary stage with a resolution and repeatability of 0.001^{o}) and a unity magnification telescope system (consisting of two identical lenses with an effective diameter 40mm and focal length 200mm) were used to change the reference angles and to keep the position of the reference beam on the crystal surface constant. A computer-controllable electronic shutter (with time resolution of 10ms) was used to switch the writing beams on and off. The stages, the shutter and the SLM were controlled by a PC386 computer through an IEEE parallel interface. All of the equipment was firmly mounted on a Newport, heavy duty optical table (model Research Series Plus), which was floated on airsacs during the experiment to isolate the optical set-up from any floor vibrations.

Ideally, we needed 784 distinct reference angles to record the 784 holograms. However, this optical system could only provide a reference angle range of approximately 10^{0}, and so only about 100 distinct angles could be realised. This was due to the limited numerical apertures of the lenses (L in Fig. 7.9), and was governed by Eq. (5.12). The size of the object plane (SLM) was of the same order as that of the reference plane which was equal to the aperture size of the lens pair, L. This means that we could not increase the number of distinct reference angles by arranging the reference points in two dimensions, because of hologram degeneracy (discussed in section 5.2). Since SAM was used, and an overlapping factor of $\mu=8$ was chosen, when two holograms have 7 (i.e. μ-1) others in between them in the same row (or in the same column), the distance between these two will be $\mu\Delta$ (equal to the hologram size, d_H), and so they will not overlap each other. Therefore, SAM enables the same reference angles to be reused for recording holograms which are not located in the same $\mu \times \mu$ sub-array. We modified the ideal spatio-angular multiplexing scheme so as to accommodate the optical component limitation, and to demonstrate the principle. We chose to use only 64 of these 100 angles, and to use them as follows: each regular 8 x 8 square sub-array of holograms within the main array was arranged so that all of the 64 reference beam angles in it were different. This ensured that any two overlapping holograms had different reference beam angles, and crosstalk could be minimised.

After the optical set-up was ready, there were still two essential tasks to be fulfilled before the final recording. We discuss these in the following two sections.

7.2 Test Patterns

The memory we stored using SAM was designed for use in a neural network such as a HOFNET, as discussed in section 6.1. It has been shown [Sel89] that if all the stored patterns are orthogonal to each other and carefully selected, the memory capacity of some networks can be equal to half the number of neurons in one pattern. This is much higher than the memory capacity would be if all patterns are chosen randomly (in this case the memory capacity would be 0.15 times the number of neurons in one pattern). We decided to use orthogonal binary pattern sets for our calibration experiment. The theory of, and the computation method for, the orthogonal projections can be found in references, for example, [Koh88], and we shall not discuss this any further, since it is beyond the topic of this thesis. The procedure we used to generate binary orthogonal pattern sets is similar to that in [Mao92], and is described in Appendix B.

We needed 784 patterns so that a set of 1024 patterns, each with 1024 elements (32 X 32) were generated. Since our SLM had 128 X 128 pixels, each element in the pattern contained 4 X 4 pixels, and measured 660μm square. We also included an identification number at the centre of each pattern to aid in evaluation. Each digit of the number consisted of 6 x 10 pixels, with a border, one pixel wide, around the digits to separate them from the binary pattern. Photographs of 4 such sample patterns from the set of 1024 (as displayed on the screen of the computer monitor) is shown in Fig. 7.10.

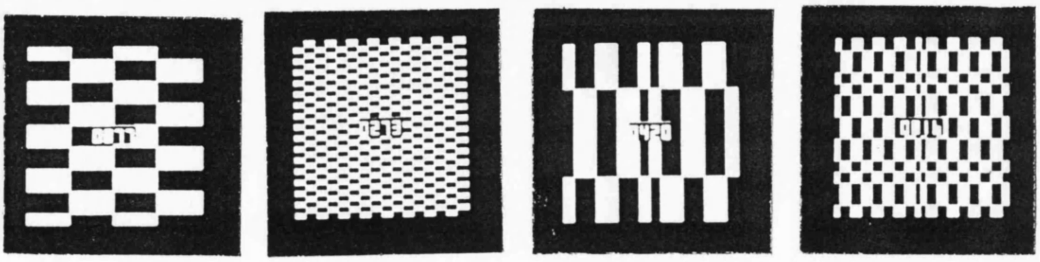

Fig. 7.10 Photographs of 4 sample patterns from the set of 1024 orthogonal patterns. 784 such patterns were stored in the memory using the SAM scheme.

All patterns in an orthogonal pattern set generated in the manner described in Appendix B (except for the first pattern) have the property that the number of "on" elements is equal to the number of "off" elements. This is important for holographic storage because, to achieve a uniform diffraction efficiency for all of the holograms, the writing beams must all have a similar intensity ratio. When the pattern is down-loaded onto the SLM, the "on" area allows the incident light to pass through (with some attenuation), whilst the "off" area blocks the light. The equal "on" and "off" areas ensure that all patterns have the same total bright and dark surface areas, so that the recording beam ratio does not vary from one recording to another.

7.3 Experimental Determination of Exposure Time Sequence

In this section we discuss the determination of the exposure time sequence we used for SAM recording.

There are two exposure schemes for obtaining a uniform diffraction efficiency from a purely angularly multiplexed memory: scheduled and incremental. Both of these methods are based on the exponential writing and erasure characteristics of a photorefractive crystal (as discussed in section 3.5.2, Chapter 3). For SAM the erasure process during recording is much more complicated than that for pure angular multiplexing. The erasure depends not only on the erasure time but also on the area of overlap between two holograms. Furthermore, there is no erasure at all if the two holograms are fully separated. Theoretically, the incremental exposure method should be most suitable for SAM recording, because incremental recording does not require detailed knowledge of writing and erasure complexities. However, if incremental recording is used, the recording system must repeatedly display the object and reference pairs, reproducing the interference pattern of each writing beam pair to within much less than one fringe width (the fringe spacing $\Lambda=0.6\mu m$ in our experiment). Our mechanical positioning system does not satisfy this requirement, and so we have to choose scheduled recording.

The calculation of the correct exposure time sequence requires precise determination of the writing and erasure time constants of the crystal. The time constants depends on the material parameters and the exposure conditions, which include the writing beam ratio and the total recording intensity. In practice the time constants are usually determined by experiment. Also the exposure conditions must be optimised to achieve a high efficiency and a high erasure/writing asymmetry. This process of crystal characterisation is discussed in subsection 7.3.1. The measurement of the writing and erasure time constants under the exposure conditions determined experimentally is described in subsection 7.3.2. The measured time constants were used to calculate the exposure time sequence which is discussed in subsection 7.3.3.

7.3.1 Determination of the optimum beam intensity ratio and total exposure intensity

From a series of experiments characterising the LiNbO$_3$ crystal, we knew that there were differences between single recordings and superimposed recordings. Furthermore, erasing the crystal by illuminating it for about 30 hours with incoherent UV light (two 8W fluorescent tubes), changed the crystal time constants (which, to our knowledge, has not been reported before). We decided that the characterisation experiments must be performed only after a thorough erasure by UV light, and must use only a part of the crystal (as indicated in Fig. 7.4). Also the same conditions as the actual recording, were to be used for the characterisation. This meant that we used the same geometry used for the SAM recording, and had object beams emerging from SLM patterns which were illuminated by a diffuse plane light beam.

The measured diffraction efficiencies are shown in Fig. 7.11 as functions of the exposure time, for various ratios of reference to signal beam intensities (I_r/I_s). In all these measurements the total writing intensity was fixed to I_0=45mW/cm^2.

It can be seen from Fig. 7.11 that, for a beam ratio larger than 10, the diffraction efficiency grew more smoothly and could reach higher saturation values. We chose the writing beam ratio to be 15. At this beam ratio the diffraction efficiency versus exposure dosage for various total writing intensities were measured, and these are shown in Fig. 7.12. From these measurements we chose a total intensity of 60mW/cm^2, as this allows a good compromise between high efficiencies and short writing time constants for small or medium exposures.

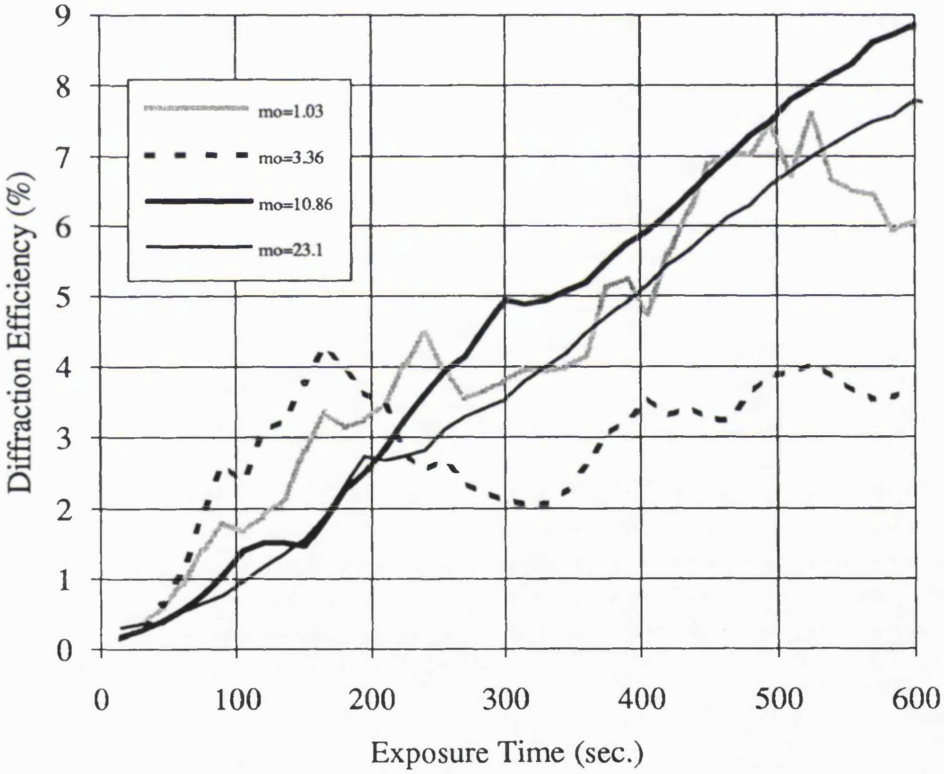

Fig. 7.11 Diffraction efficiency versus exposure time for writing beam ratios (mo in the figure) of 1, 3.5, 11, and 23. The total writing intensity was fixed at 45mW/cm^2.

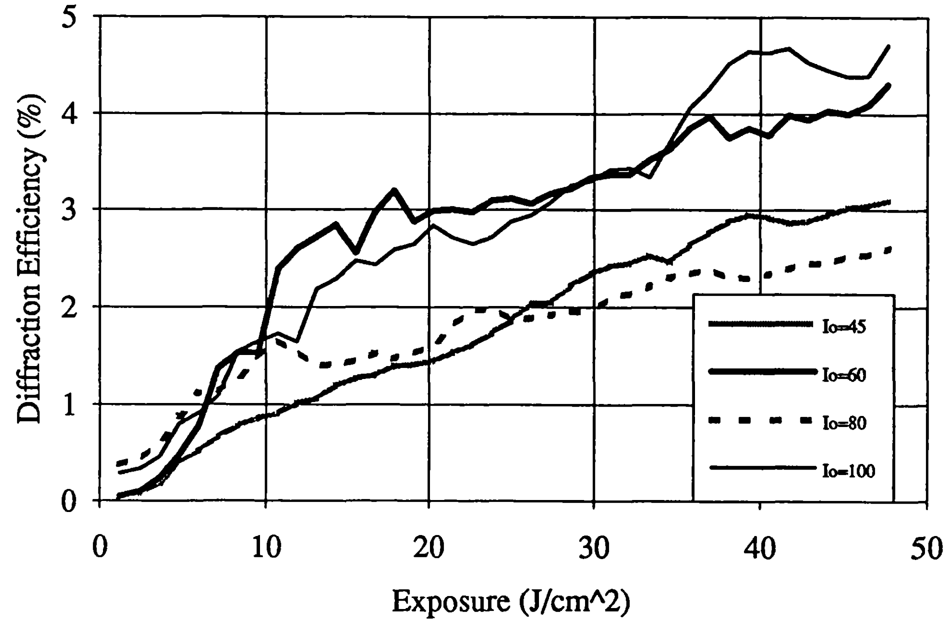

Fig. 7.12 Diffraction efficiency versus exposure dosage for a total writing intensity (Io) of 45mW/cm^2, 60mW/cm^2, 80mW/cm^2, and 100mW/cm^2. The writing beam ratio was fixed at 15.

7.3.2 Measurement of writing and erasure time constants

Under the exposure conditions determined above (beam ratio 15 and total writing intensity 60mW/cm^2) we carried out a series of experiments to measure the crystal time constants.

Writing time constant

We recorded two saturated holograms and measured the curves of diffraction efficiency versus exposure time. After recording we measured their angular response curves and found the efficiency enhancement factors, E_η (see section 4.2), for each writing curve . We multiplied each writing curve with its E_η, and the average of the two modified curves is shown in Fig. 7.13 (labelled as "measured").

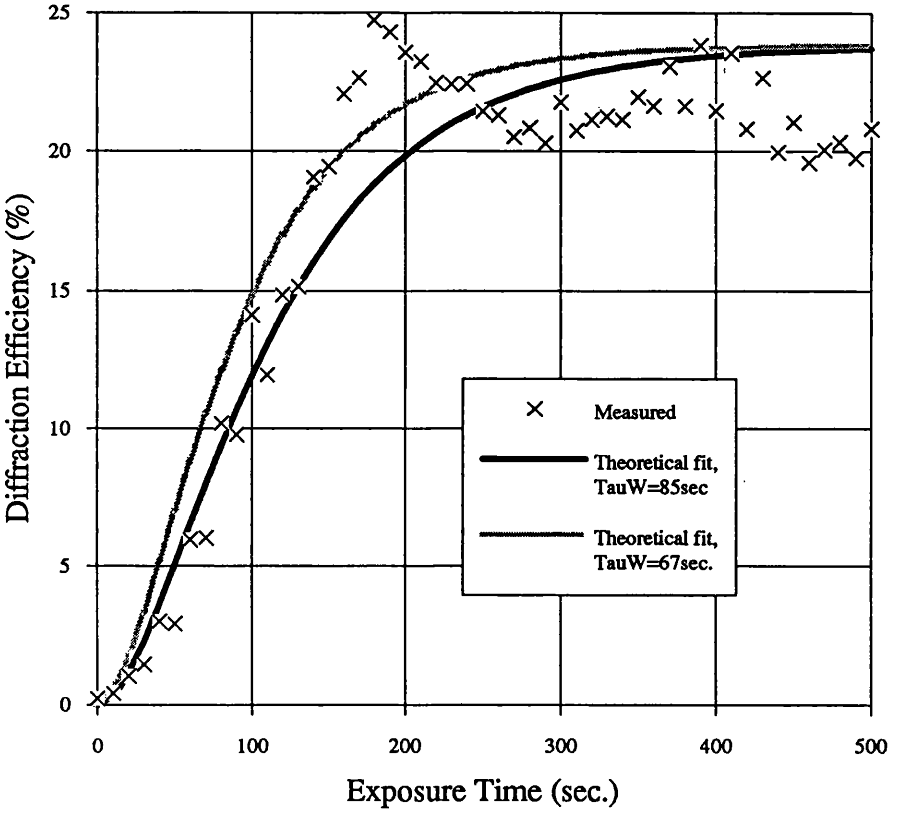

Fig. 7.13 Determination of the writing time constant, τ_W. The experimental data is the average of two measurements. The theoretical curves shown used different values for τ_W (as described in the text), and this is labelled as TauW in the figure.

From the experimental data the maximum efficiency was measured to be 25%. Using this value for the maximum efficiency, the hologram amplitude, ν ($\nu = \sin^{-1}\sqrt{\eta_{\max}}$, see Eq. 5.7), was calculated to be 0.52, corresponding to an index modulation depth of $\Delta n_{sat}=10^{-5}$. This is two order of magnitude less than the reported maximum value (see Table 3.1).

Using a "least squares" method to fit the measured average efficiencies to the theoretical expression below we obtained τ_W=67 sec (see Eqs.2.19, 2.20, and 3.42):

$$\eta(t) = \sin^2\left[\frac{\pi d}{\lambda \cos\theta}\Delta n_{sat}\left(1-e^{-\frac{t}{\tau_W}}\right)\right] \tag{7.7}$$

We could also determine a value for τ_W directly from the measured data. We found that, when t = 85 seconds, $\eta(t)$=10%, corresponding to an index modulation of $(1-e^{-1})\Delta n_{sat}$. This implied a value for τ_W of 85 sec. Two efficiency vs exposure time curves were calculated using writing time constants τ_W=67 sec. and τ_W=85 sec., and these are also shown in Fig. 7.13. Having compared the two theoretical curves with the measured data we decided to choose τ_W=85 sec. as this fitted the experimental data well in the small and medium exposure time regions at a room temperature of 24°C. (Most of the holograms in the memory were recorded with an exposure time, less than 50 sec. - see the next section).

Erasure time constant

Erasure time constants are usually obtained by observing the diffraction efficiencies of a number of holograms written sequentially, using an equal recording time for each [Mok91]. Experience tells us that the initial diffraction efficiencies of equally exposed holograms can be very different from each other, and so an accurate measurement usually requires a large number of equally exposed holograms (100 or more) to be observed. We designed a procedure to measure the degree of erasure for each hologram of 10 with reasonable accuracy:

1) Record 10 holograms using purely angular multiplexing, each with an equal writing time of t_W=50sec, and monitor the build up of the diffraction efficiency of each hologram.

2) After each recording, measure the angular response curve of this hologram to find its peak efficiency, $\eta_{0,N}$, and efficiency enhancement factor, $E_{\eta,N}$ (N=1, 2, ···,10).

3) After the 10 recordings, measure the diffraction efficiencies of all 10 holograms once again to find the efficiency of each hologram after erasure, $\eta_{e,N}$.

The erasure time constant was determined with the following data manipulations:

1) Each writing curve was multiplied by its $E_{\eta,N}$, and the average of the 10 modified writing curves was calculated along with the average peak efficiency $\overline{\eta_0}$ ($\overline{\eta_0}$=2.5%). This is shown in Fig. 7.14 which reflects the time history of the diffraction efficiency, with better accuracy, for the first 50 seconds of exposure.

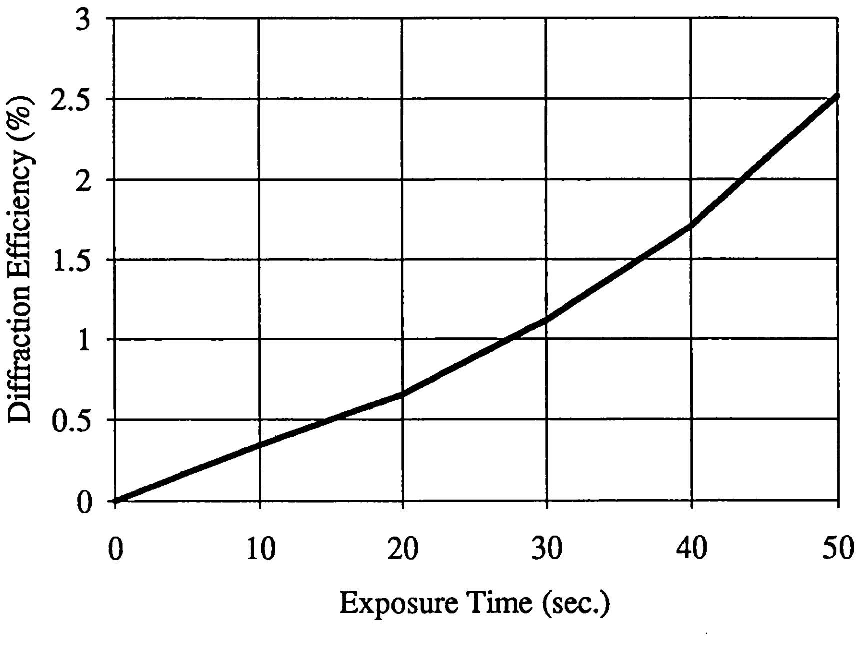

Fig. 7.14 The average writing curve of 10 holograms, the data is modified by the efficiency enhancement factor.

From Fig. 7.14, the holographic sensitivity of our Fe:LiNbO$_3$ sample, in terms of the energy density required to write a grating of 1% diffraction efficiency (using the definition similar to [Kra86]), was found to be S_η^{-1} =1620mJ/cm^2. This sensitivity is lower than reported value for iron doped lithium niobate, listed in Table 3.1.

2) A modified diffraction efficiency of each hologram after erasure, $\eta_{e,N}^*$, was calculated, and this is given by:

$$\eta_{e,N}^* = \overline{\eta_0} \cdot (\eta_{e,N} / \eta_{0,N}) \tag{7.8}$$

The modified $\eta_{e,N}^*$ are shown in Fig. 7.15.

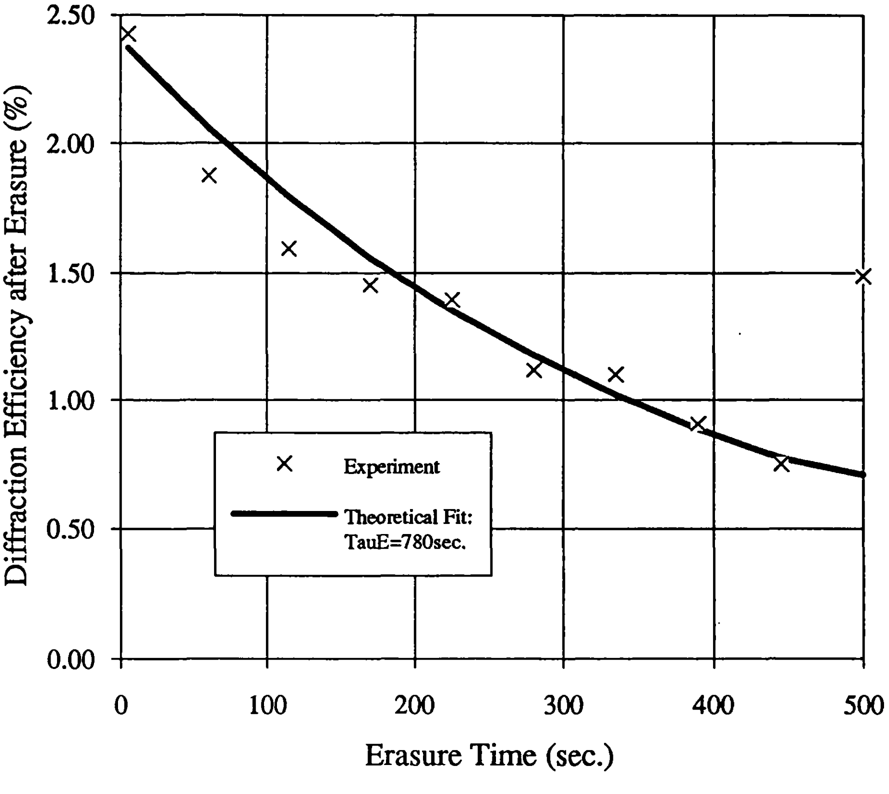

Fig. 7.15 Determination of the erasure time constant. The data points marked by crosses represent the modified efficiency after erasure ($\eta_{e,N}^*$ see the text). The theoretical curve using an erasure time constant of τ_E=780 sec (labelled by TauE in the figure) is also shown.

3) The erasure time of each hologram, $t_{E,N}$, is the sum of the writing time of subsequent recordings plus the total time spent during all of the readout operations performed after the recording.

4) The $\eta_{e,N}{}^*$ and $t_{E,N}$ were fitted to following theoretical expression:

$$\eta_{e,N}{}^* = \sin^2\left[\frac{\pi d}{\lambda\cos\theta}\overline{\Delta n_0}\cdot e^{-\frac{t_{E,N}}{\tau_E}}\right] \tag{7.9}$$

where

$$\frac{\pi d}{\lambda\cos\theta}\overline{\Delta n_0} = \sin^{-1}\sqrt{\eta_0} \tag{7.10}$$

A least squares method was used for the fit, using Eq. (7.9), we found the erasure time constant to be τ_E=780 sec. The calculated erasure curve using this erasure time constant is also shown in Fig. 7.15. So $\tau_E/\tau_W = 9.176$.

7.3.3 Calculation of the exposure time sequence

Model for calculating the exposure time sequence

We modified a mathematical model, described by Eq.(3.49) and (3.50) in Chapter Three, to calculate the exposure time sequence. First, we shall describe how the exposure time sequence of purely angularly multiplexed holograms can be calculated using this model, as this is the basis for developing our exposure sequence. For pure angular multiplexing, Eq.(3.49) and (3.50) can be normalised to give:

$$\nu = \left(1-e^{-t_N}\right)\cdot e^{-T_N} \tag{7.11}$$

and

$$T_N = \psi\sum_{i=N+1}^{M} t_i \tag{7.12}$$

where $\nu = \Delta n_N/\Delta n_{sat}$ is the normalised index modulation of the Nth hologram, $t_N = t_N / \tau_W$ is the normalised writing time of the Nth hologram, T_N is the normalised erasure time suffered by the Nth hologram and $\psi = \tau_W / \tau_E$ is the ratio of the writing to erasure time constants of the crystal (writing-erasure asymmetry). We proceed with the calculation in a reverse order, starting with a prescribed "last recording time", t_M (M is the total number of holograms to be stored). This gives us a value for the target normalised index modulation, $\mathbf{v} = \left(1 - e^{-t_M}\right)$. For purely angular multiplexing, the erasure time for the (M-1)th hologram is the recording time for the last (Mth) hologram. The condition that $\mathbf{v}$ is the same for each hologram means that ([Blo78, Mok91]):

$$\left(1 - e^{-t_M}\right) = \left(1 - e^{-t_{M-1}}\right) \cdot e^{-\psi t_M} \tag{7.13}$$

so that the normalised writing time of the (M-1)th hologram, t_{M-1}, can be found by solving equation (7.13). Continuing in this manner, the writing time of all the remaining holograms can be obtained [Mok91].

For SAM recording, however, the erasure effect of one recording on a previously recorded hologram depends not only on the writing time of the one recorded later, but also on the overlapping volume of these two holograms. The dependance of erasure on the overlapping volume may appear rather complicated. This is because different parts of one hologram may be erased by several other holograms, and the overlapping volume of two holograms may be rather irregular. Our first step is to reduce the complexity of the erasure effect by making the following two simplifying assumptions:

1) The erasure rate of one SAM hologram by another is proportional to the fraction of the volumes of the two holograms which are overlapped. Therefore, the remaining index modulation of a hologram, Δn (after erasure due to the recording of another hologram for a recording time, *t*) can be expressed as:

$$\Delta n = \Delta n_0 \cdot e^{-W \frac{t}{\tau_E}} \tag{7.14}$$

where Δn_0 is the initial index modulation before erasure, and W is the volume overlapping fraction of these two holograms which is defined as:

$$W=(\text{overlapping volume})/(\text{volume of each hologram}) \quad (7.15)$$

This assumption is rather arbitrary. W=0 and W=1 indicate cases of pure spatial and pure angular multiplexing respectively, and Eq. (7.14) is valid for these two special cases. However, the validity of Eq.(7.14) for SAM (0<W<1) needs to be verified by experiment, and we shall discuss this in detail in section 7.5.

2) The second assumption is that the overlapping volume of two partially separated holograms is proportional to their overlapping area on the entrance of the crystal.

This assumption is valid if the volume of each hologram is proportional to its area on the crystal entrance. In our experimental design, the object beam size is rather larger than that of the reference beam due to the insertion of a diffuser into the object path. Therefore the hologram approximately forms a cylinder inside the crystal, as shown in Fig. 7.16, and so our second assumption is valid. The intensity ratio of the reference to the object beams is fixed at 15, and so the object beam has only a small contribution to successive erasures. In this case the volume overlapping fraction of two holograms can be calculated as the fractional area overlapping of two partially separated circles.

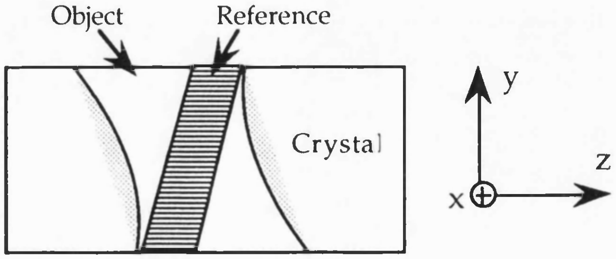

Fig. 7.16 A sectional diagram of a recorded crystal, showing that the hologram forms a cylinder determined by the reference beam (shaded area).

The SAM memory is designed to be a $\sqrt{M}\times\sqrt{M}$ array, with a total number of M holograms. Each hologram is labeled by its row, R, and column, C, numbers. The recording takes place by first recording every element in the first row, and then proceeding, row by row in raster manner. Under the above assumptions, the mathematical model for calculating the exposure time sequence of a SAM memory is given by:

$$\mathbf{v}=\left(1-e^{-t_{R,C}}\right)\cdot e^{-T_{R,C}^{SAM}} \tag{7.16}$$

where the equivalent erasure time, $T_{R,C}^{SAM}$, is given by:

$$T_{R,C}^{SAM}=\psi\sum_{i,j}\mathrm{W}(i,j)\,t_{R+i,C+j} \tag{7.17}$$

where $\mathrm{W}(i,j)$ is the area overlapping fraction of the (R, C)th hologram and the (R+i, C+j)th hologram. The summation is performed over a range restricted by:

$$|i|,\ |j|\leq\mu-1 \tag{7.18a}$$

$$1\leq R+i\leq\sqrt{M},\ 1\leq C+j\leq\sqrt{M} \tag{7.18b}$$

and

$$(R+i-1)\cdot\sqrt{M}+(C+j)\geq(R-1)\cdot\sqrt{M}+C \tag{7.18c}$$

where μ is the hologram overlapping factor, defined by Eq.(6.1) in Section 6.2, which is usually taken as an integer for convenience, and is determined to be 8 in our experiment. Eq. (7.18a) reflects the fact that if $i, j \geq \mu$ or $i, j \leq -\mu$, the two holograms will not overlap each other. Eq. (7.18b) specifies the array size, and Eq. (7.18c) represents the fact that only those holograms which are recorded *after* the one labelled by (R, C) have any erasure effect on it.

The erasure effect is now represented in a form analogous to the case of pure angular multiplexing, with an "effective" erasure time determined by Eq. (7.17). Knowing all of the values for W(i, j), we can form an "erasure weight matrix", and the exposure time sequence of a SAM memory can be calculated in the same way as for pure angular multiplexing. The next stage is to calculate the erasure weight matrix.

Calculation of the erasure weight matrix

We shall refer to Fig 7.19, which shows two holograms, labelled by (R, C) and ($R+i$, $C+j$) respectively, which are spatially separated by $i\Delta$ in the x- (vertical) direction and by $j\Delta$ in the z- (horizontal) direction respectively, where Δ is the spatial shift between adjacent recordings, and is equal to d_H/μ (d_H is the hologram diameter, see Eq. 6.1). The distance between the centres of these two holograms is:

$$\sqrt{i^2+j^2}\,\Delta \tag{7.19}$$

and the overlapping area, $S(i, j)$, can be calculated as:

$$S(i,j)=\frac{1}{2}d_H^2\left(\alpha-\sqrt{\frac{i^2+j^2}{\mu^2}}\cdot\sin\alpha\right) \tag{7.20}$$

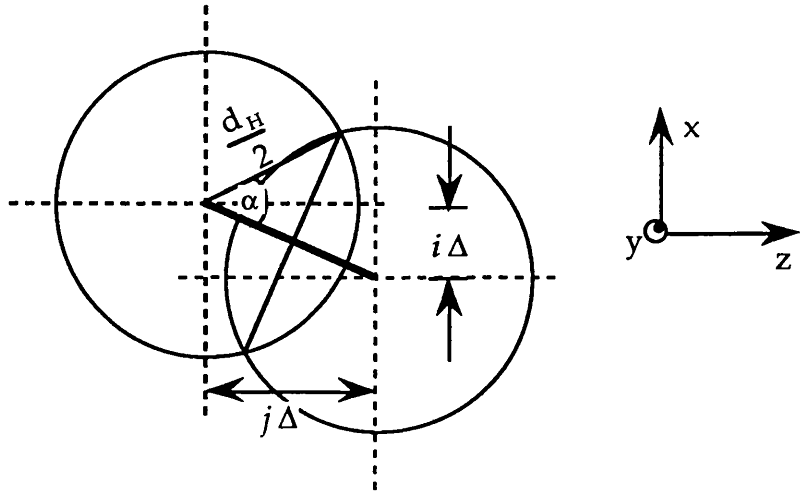

Fig. 7.17 The overlapping area of two partially separated holograms

where the angle α in Fig. 7.17 is:

$$\alpha = \tan^{-1}\sqrt{\frac{\mu^2}{i^2+j^2}-1} \qquad (i^2+j^2>0) \tag{7.21}$$

The hologram area is:

$$S_H = \frac{\pi}{4}d_H^2 \tag{7.22}$$

Therefore, the erasure weight matrix, W(*i*, *j*) is given by:

$$W(i,j) = \frac{2}{\pi}\left(\alpha - \sqrt{\frac{i^2+j^2}{\mu^2}}\cdot\sin\alpha\right), \quad (i^2+j^2>0) \tag{7.23}$$

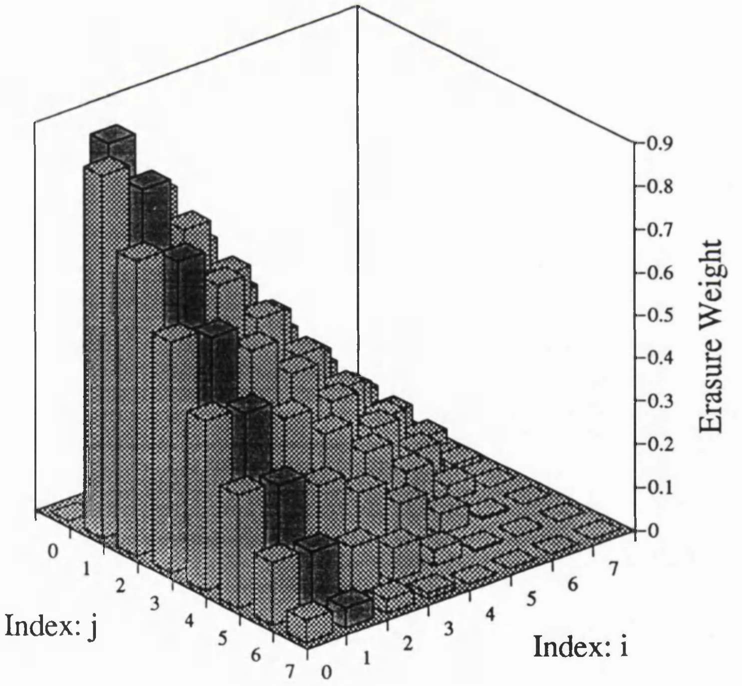

Fig. 7.18 A quarter of the erasure weight matrix, with a hologram overlapping factor μ=8

$W(i, j)$ is circularly symmetric in the indices i and j. A quarter of such a matrix for $\mu=8$ has been calculated and is shown in Fig. 7.18. Note that $i=j=0$ represents the hologram (R, C) itself. This cannot erase itself, and so $W(0,0)=0$.

Resultant time sequence

Knowing the writing and erasure time constants (τ_W=85sec. and τ_E=780sec.), the erasure weight matrix, $W(i, j)$, and the memory array size ($\sqrt{M} \times \sqrt{M} = 28 \times 28$), we could calculate the time sequence by running a computer program based on the mathematical model discussed above. The maximum number of holograms which can be stored using SAM is restricted by:

$$T_{R,C}^{SAM} < \ln\left(\frac{1}{\nu}\right) \tag{7.24}$$

$1/\nu$ can be regarded as the normalised dynamic range of the crystal due to the prescribed target efficiency. Equation.(7.24) ensures that a finite, real writing time, $t_{R,C}$, is obtained from equation (7.16).

We started with a last recording time, $t_{28,28}$ = 15 sec (normalised recording time $t_{28,28}$ = 0.176, see Eqs. 7.11-7.13). This corresponds to a target diffraction efficiency of 0.5% (according to the experimental curve in Fig. 7.14), and also to a target normalised index modulation, ν = 0.162 (according to Eq. 7.16). The program stopped when the calculated normalised erasure time broke the condition (7.24). With a last recording time of 15sec., only 239 holograms could be recorded. Actually, the calculated time sequence is very sensitive to the selection of the last recording time, and after running the program several times (with fine adjustment of the last recording time), a figure of 784 holograms was attained, with a last recording time of $t_{28,28}$ = 11.39 sec. The total exposure time for all the 784 holograms was calculated to be 20,713 sec. with a longest exposure of 151 sec. Two plots illustrating the exposure time as a function of both the row number and the element number are shown in Figs. 7.19 and 7.20.

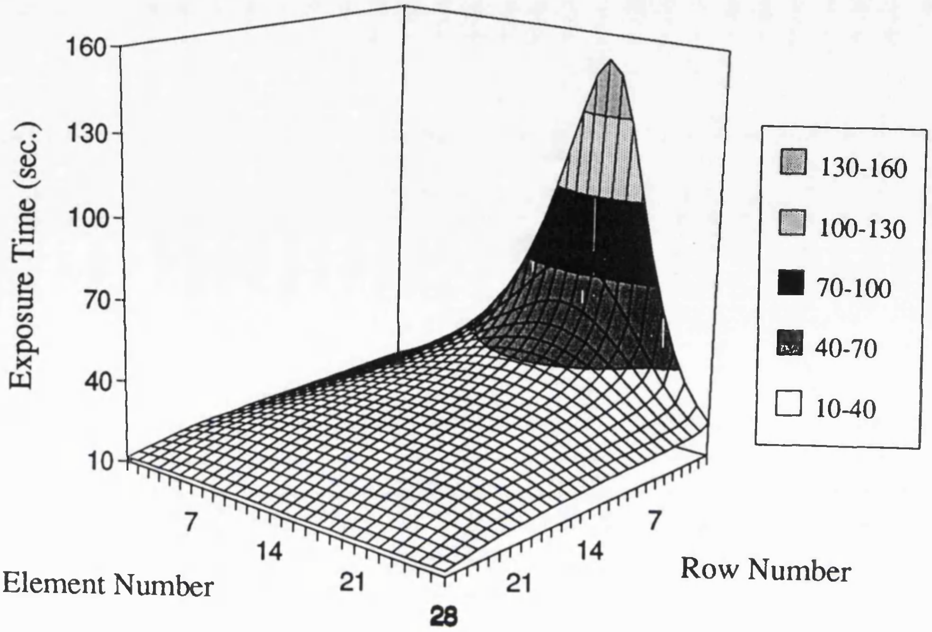

Fig. 7.19 A 3-D plot showing the exposure time as a function of the row number and the element number of the hologram to be recorded.

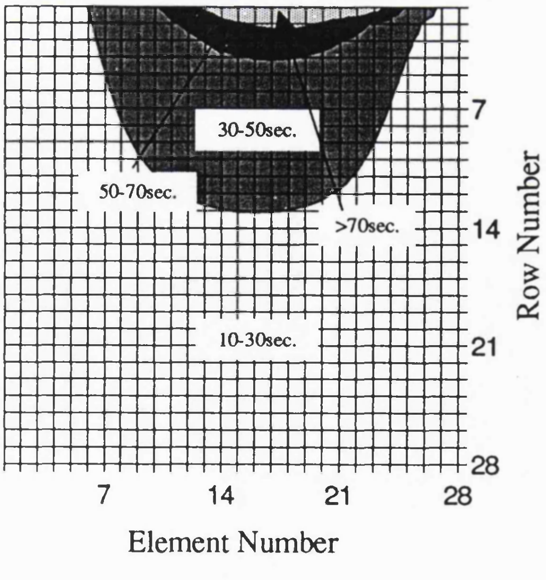

Fig. 7.20 A contour plot showing the exposure time as a function of the row number and the element number of the hologram to be recorded.

It can be seen clearly from Figs. 7.19 and 7.20 that the time sequence required for sequential exposure varies non-monotonically, as opposed to the monotonic reduction in exposure time characteristic of purely angular multiplexing [Mok91]. A hologram (in a SAM hologram array) recorded earlier may require a writing time shorter than some others recorded later. A longer exposure time is required by holograms located in the upper central area as these would be subject to erasure from more of the subsequent recordings than those located on the edge and/or lower area.

The time sequence shown in Figs. 7.19 and 7.20 was used for our SAM recording.

7.4 Storage and Performance of a SAM Memory

In this section we describe the successful storage and performance of 756 holograms, using the Spatio-Angular Multiplexing technique.

7.4.1 Recording and readout

The experimental set-up for the SAM memory recording, was described in Section 7.1.6 and is shown in Figs. 7.8 and 7.9. The experiment was designed to be performed under the automatic control of a PC-386 computer via an IEEE interface. No operator intervention should have been required, and the recording of the 784 holograms would have taken 8 hours. However, due to problems with the laser cooling system, the laser tripped out several times during the recording of the first horizontal row. The program was restarted at the second row, and the multiple sequential recording of the remaining 756 holograms took 7 hours without any further problems. During this period the room temperature was 24 ± 1^{o}C.

We achieved a successful readout of the recorded memory, and this enabled us to evaluate the performance of the SAM memory. The experimental set-up for readout is shown in Fig. 7.21.

After the recording was complete, the object beam was blocked, and the reference beam intensity was attenuated by a neutral density filter, to 7% of that used for recording. This weak beam was used to read the whole array, by using the following procedure: the crystal was moved to a position corresponding to a hologram, then the readout beam was scanned near the recording angle over a range equal to the angular separation between adjacent holograms (0.1^o external), whilst the diffracted power was monitored by a Newport Picowatt digital power meter. The data from the power meter was stored in the PC computer via the IEEE bus. After the diffraction efficiencies[2] of all the 756 holograms were measured, the power meter and the neutral density filter were removed, and the memory was read out again. A video camera was used to make a film of all the reconstructed images, which were projected onto an image screen by a second F. T. lens. Several sample photographs of the images were taken by a still camera.

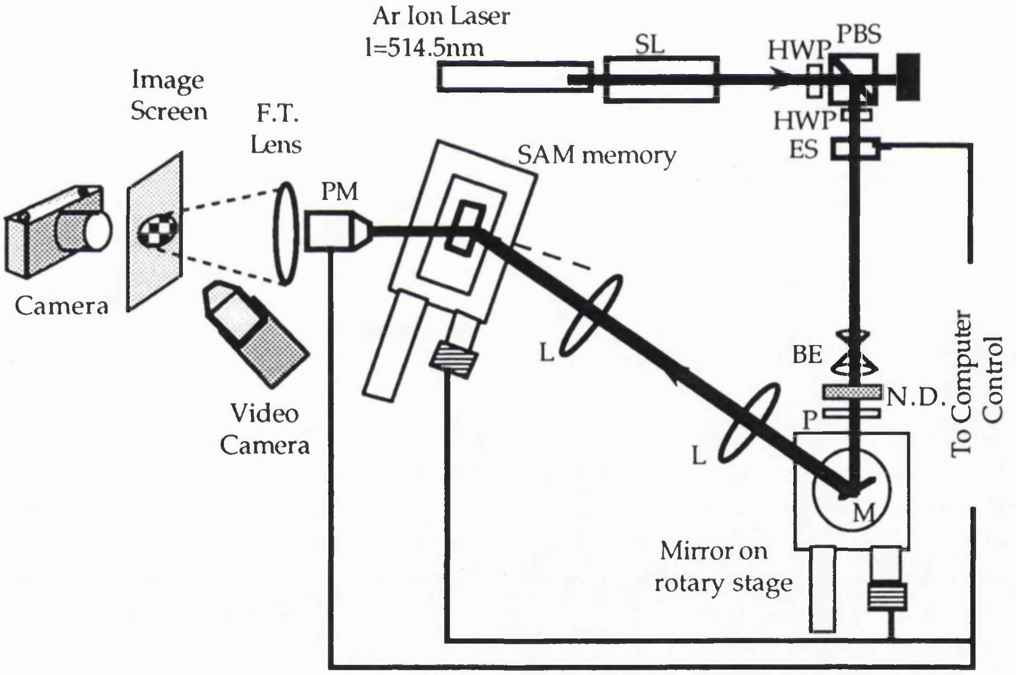

Fig. 7.21 Schematic diagram of the experimental set-up for a SAM memory readout. SL: laser stabiliser; ES: electronic shutter; HWP: half wave plate; PBS: polarising beam splitter; BE: beam expander; L: lens P: polariser;; M: mirror; PM: power meter; N.D.: neutral density filter.

---

[2] The diffraction efficiency was defined as the ratio of diffracted power to the power directly transmitted through an area where there was no hologram recorded.

7.4.2 Performance of the recorded SAM memory

We investigated the performance (in particular, the diffraction efficiency and angular sensitivity) of single gratings recorded in Fe:LiNbO$_3$ crystals in Chapter Four. Now we are able to experimentally investigate the performance of a SAM holographic memory based on the readout results from all 756 holograms. The statistic results mentioned below were obtained by using the PC software package "Excel".

Diffraction efficiency

The diffraction peaks of all 756 holograms were obtained from the data files. Figs. 7.24**a** and **b** show the peak diffraction efficiency of the whole array as a function of the hologram position (row number and element number).

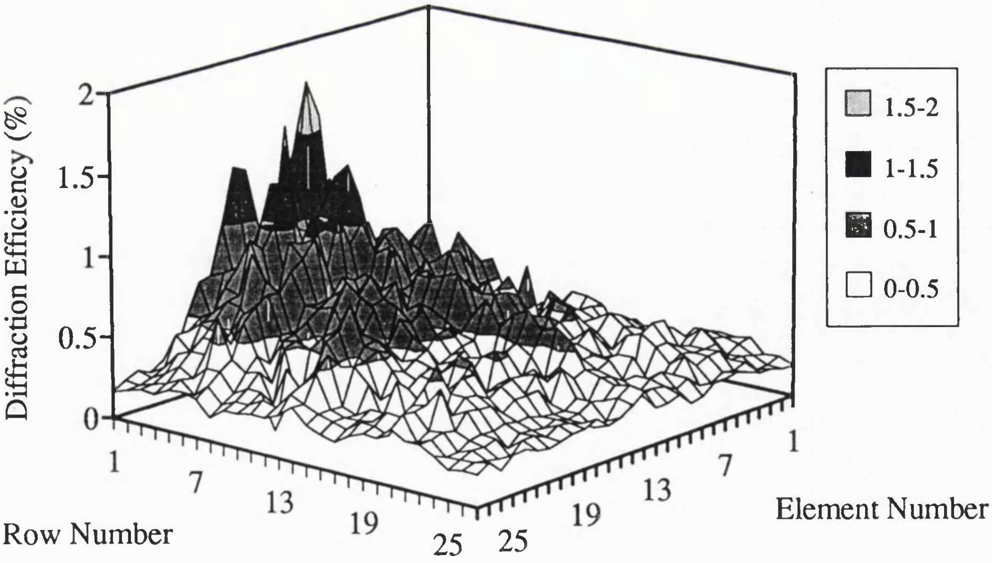

Fig. 7.22**a** A 3-D plot showing the diffraction efficiency of the array as a function of hologram position.

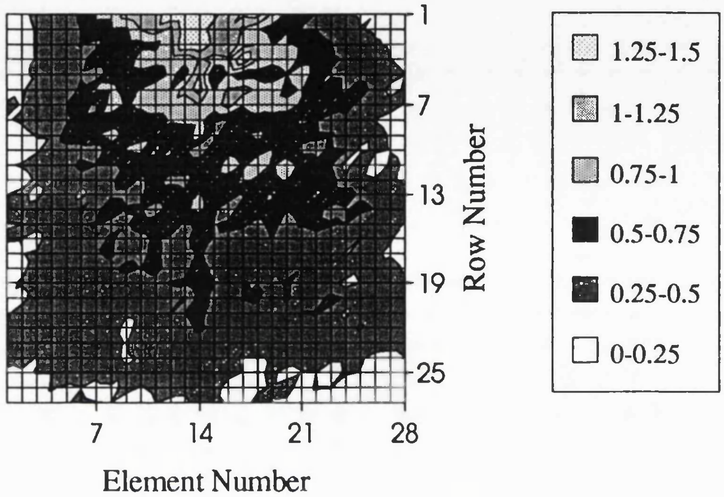

Fig. 7.22**b** A 2-D contour showing the diffraction efficiency of the whole array as a function of hologram position.

Each diffraction peak corresponded on a maximum diffraction efficiency of a hologram in the array, readout at the optimum angle (with an accuracy of 0.002^{o}), as discussed in Chapter Four. The average peak diffraction efficiency was 0.5±0.2%. This is as expected in the design (see section 7.1.3). This expectation was based on a definition of the "local degree of angular multiplexing" for SAM memories, i. e. if the hologram overlap factor was μ, then the "local degree of angular multiplexing" for SAM was μ^2. This leads to an expected diffraction efficiency for SAM equal to that for μ^2 holograms recorded using pure angular multiplexing. The results of our preliminary experiment show that this definition is reasonable and can be used in SAM memory design.

Although the average diffraction efficiency is as expected, the overall diffraction efficiency is not very uniform. The efficiencies of the rows recorded earlier in the process are higher than those recorded later, and the efficiency drops towards the edges in each row. If we consider the exposure time sequence (Figs. 7.21 and 7.22), we can see that the holograms which were exposed for longer gave higher efficiencies. This suggests that the erasure effect was overestimated while calculating the time sequence, resulting an over-long writing time. We shall discuss this later in section 7.5.

Peak position shift

The position of the peak diffraction efficiencies for holograms in the first 8 columns of the array, were also extracted from the readout data, and a contour diagram can be seen in Fig. 7.23. The accuracy of this measurement is ±0.002°, because a resolution of 0.001° in the positioning of the mirror corresponds to a resolution of 0.002° in the readout beam angle.

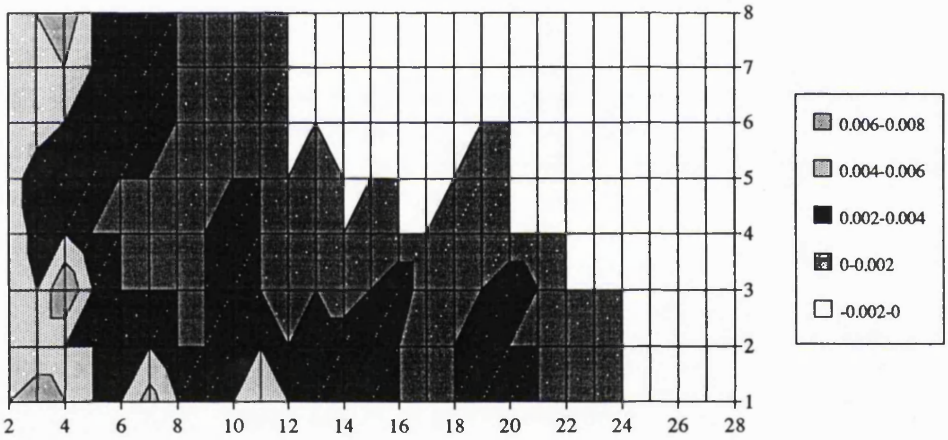

Fig. 7.23 The shift in the position of the peak diffraction efficiency, as a function of hologram position, for the first eight columns in the SAM memory array.

Although this accuracy is lower than that described in Chapter Four, the trend is shown clearly. The peak positions of most of the holograms, which had a small or medium exposure time, shifted insignificantly (except for those at the edges of the array). However, the peak positions for holograms written with a longer exposure time had an evident shift. For those holograms with a larger peak shift, the diffraction efficiency obtained at the optimum angle was up to 25% greater than that obtained at the recording angle. Note that the peak position shift in this SAM holographic memory cannot be compared easily with the results discussed in Chapter Four, where all the gratings were recorded in a "fresh" area of the crystal with no other holograms overlapping them.

Image quality and crosstalk

Photographs of several reconstructed images are shown in Fig. 7.24. The top 4 in Fig. 7.24 are photographs reprinted from a video tape, and the bottom 4 are photographs made by a still camera. We have chosen to present images from near the beginning, middle and end of the recording, and one image that had a high spatial frequency. There is no crosstalk apparent, nor are there additional fringes caused by multiple reflections between the crystal faces (which were not anti-reflection coated). All these photos, especially the video reprints, show good image quality, and the identification numbers are easily recognisable as well as the 165μm wide margin around them (see section 7.2), and this implies that the resolution attained was at least this good.

The crosstalk effect was best observed when the SAM memory was read out. As the reference beam was scanned about the angle required for peak diffraction, one could see crosstalk from other, overlapping holograms, recorded with different reference angles. However, when the angle was such that peak diffraction occurred, no crosstalk was apparent and a good signal to noise ratio allowed the patterns to be easily identified, and the identification numbers to be clearly read (in most images).

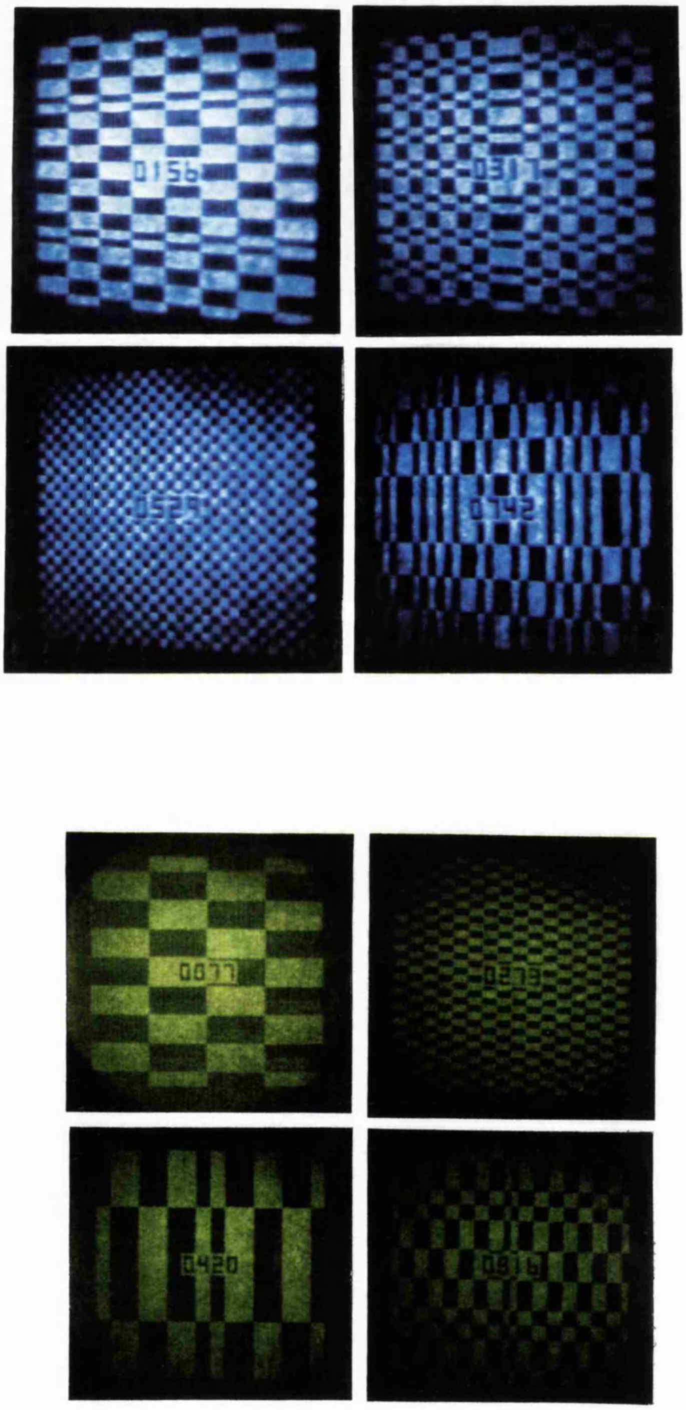

Fig. 7.24 Photographs of sample reconstructed images. Top: video reprints. Bottom: photos made by a still camera.

signal to noise ratio (SNR)

The signal to noise ratio can be obtained by observing the angular response curves of several rows of holograms. Four typical curves are shown in Fig. 7.25. The rows were chosen from near the start, middle and end of the recording. Note that the scale for each of these curves is different, as this allows the detail to be shown for rows that were recorded later (with lower diffraction efficiency). The figure shows well-defined and narrow diffraction peaks, well above the noise floor and also well separated in angle to avoid crosstalk. The noise level in a row appears to fluctuate less than the diffraction efficiency, and so the local SNR varies.

In addition we calculated the SNR (defined as the intensity ratio of the peak diffraction efficiency to the adjacent minimum) for a single column (the 8th column). The SNR for this column is 7.6±0.8 dB, which is low, compared to other reported work (37dB for 1000 holograms, see [Mok93]).

Persistence

We did not measure the persistence (dark storage time) of this SAM memory. However, we measured a single hologram, recorded using the same experimental arrangement, in the same crystal. Having been stored in the dark for 19 days after recording, the diffraction efficiency of this unfixed hologram decreased to 80% of its original value, yielding a dark storage time constant of 172 days.

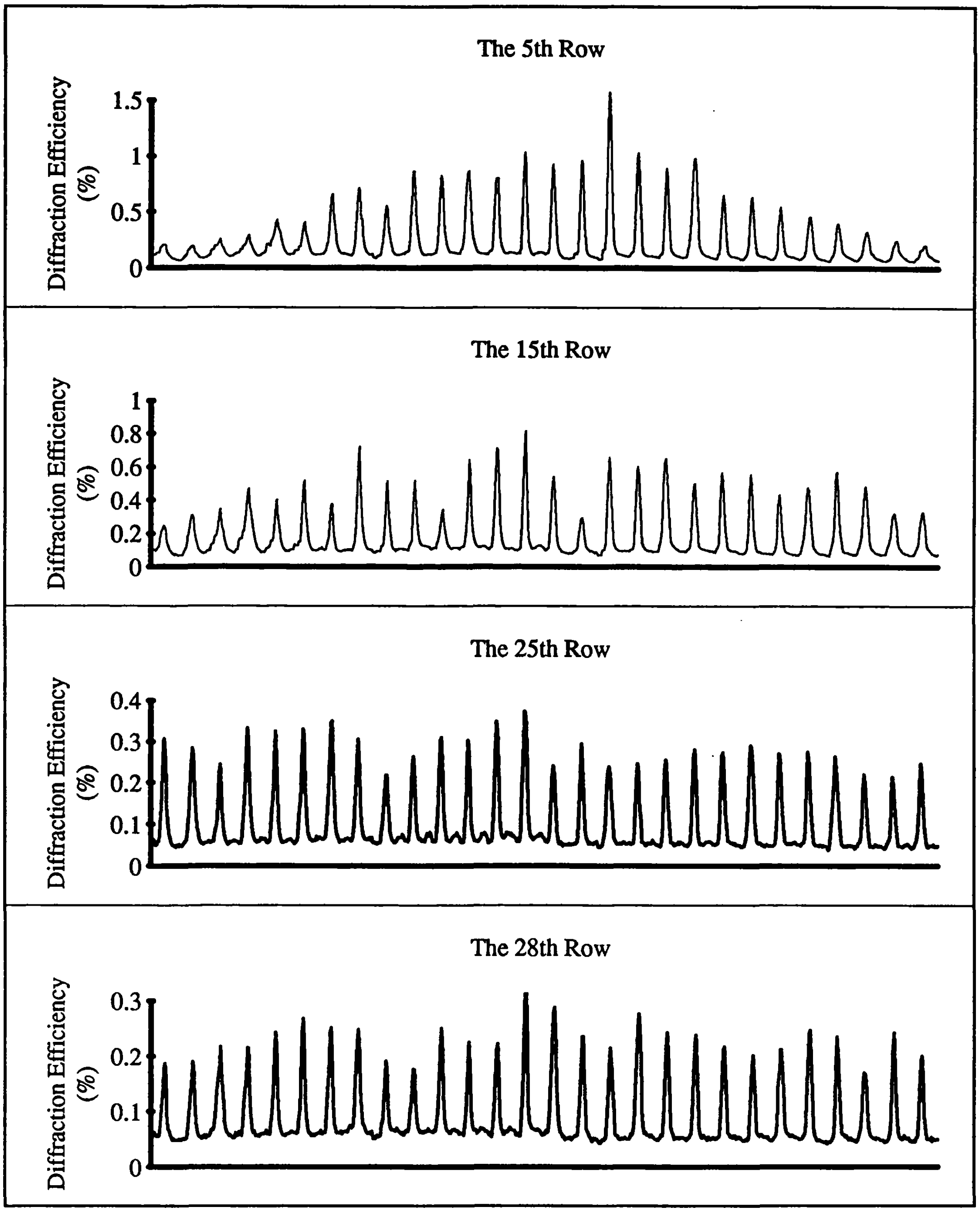

The 5th Row

The 15th Row

The 25th Row

The 28th Row

Fig. 7.25 Diffraction efficiency as a function of hologram position and readout beam angle for four sample row.

7.5 Analysis of the measured results

From the previous section, one can see that the image quality and SNR of this SAM memory are fairly good. The average diffraction efficiency (0.5%) is much higher than that of previous work (0.01% in [Mok91]). However, the uniformity of the diffraction efficiency is not so good as can be seen in Fig. 7.22a. The average diffraction efficiency was 0.5±0.2%, implying a relative standard deviation of 40%. The diffraction efficiency of [Mok91] was 0.01±0.001%, a standard deviation of 10%. In this section we discuss the possible sources of this non-uniformity, starting with an assessment of the errors in the measurement.

7.5.1 Accuracy of the experimental measurement

The measured diffraction efficiency was based on a measurement of diffracted power as a function of the crystal position and the angle of the readout beam. We analyse the sources of measurement errors as follows:

1) Detection error. The picowatt power meter, when operating at 200μW range (for most of the measurements), has a resolution of 0.01μW, and the fluctuation in measured power caused by detection noise is no more than 0.3μW. The readout laser power (after being transmitted from the crystal) was 61μW. The error caused by detection noise is less than 1%. The power meter had an autoranging function which ensured the same order of error for measurement of small power, so the detection error can be ignored.

2) Laser power fluctuation. The laser was operating in a light control mode which ensured that the fluctuation in the output power was less than 1%. A laser stabiliser was used to reduce the ripple even further to below 0.5% (0.1% in most cases), so this error can also be ignored.

3) The non-uniformity in the transmittance of the crystal. The transmittance was measured to be (32.4±0.5)% (see section 7.1.1), implying that a relative error of ±0.15% could be introduced into the measurement of diffraction efficiency, since an identical transmittance (32.4%) was used to normalise the diffracted power from each of the holograms. However,

this is also too small to explain the relative deviation of 40% in the average diffraction efficiency.

4) Positioning error of the crystal. If the crystal is not positioned precisely, the measured diffraction efficiency will deviate from its correct value. The linear stages which position the crystal have a resolution and unidirectional repeatability of 0.8μm, and the motion of the stages was carefully programmed to avoid any backlash. This positioning error would cause a measurement error of less than 1/2400 (the hologram size was 2.4mm), so can be ignored.

5) Alignment error of the readout beam angle. If the step size when scanning the readout beam scanning is too large, the diffraction peak may be missed, and so a measurement error will occur. In our experiment, the mirror which provides the readout beam was rotated by 0.001^o at each step, using a rotary stage that had a resolution and unidirectional repeatability of 0.001^o. This means the scanning step of the readout beam angle was 0.002^o, i.e. one fifteenth of the full selective angle (a selective angle of 0.03^o was measured for our crystal, see section 7.1.4). Using a standard sinc function we calculated the measurement error for a missed diffraction peak to be 3%.

In summary, the total error in the measurement could not be more than 5%, mainly caused by the alignment error of the readout beam angle. This error should be random and should not have caused such a large non-uniformity in the diffraction efficiency of the whole array. We examine the possible reasons for the non-uniform diffraction efficiency in the next subsection.

7.5.2 Possible reasons for non-uniform diffraction efficiency

The diffraction efficiencies of the array can be seen in Figs. 7.24a, **b** and 7.27, and these figures show that i) the diffraction efficiencies appear to roll off towards the edges of the rows, and ii) the efficiencies of the rows recorded and read out earlier are higher than those recorded and readout later. Partial erasure during readout could have caused the second observation, although this has yet to be tested by performing an experiment where the holograms are readout in reverse order. However, partial erasure during readout cannot explain the first observation, because erasure during readout has a smaller effect on holograms located at the left edge than for those elsewhere (the readout started on the left for each row). Comparing the efficiency distribution (Fig. 7.22**a**) to the time sequence for the recording (Fig. 7.19), it seems that observations (i) and (ii) could result from an overestimation of the erasure of one hologram by another during recording. The possible sources of the overestimation are examined below.

The model used to calculate the time sequence

We made two simplifying assumptions to account for erasure during SAM memory recording. Firstly, we assumed that the erasure rate of one hologram by another is proportional to the volume overlapping fraction, W, for these two holograms. Therefore, we have from Eq (7.14):

$$\Delta n = \Delta n_0 \cdot e^{-W\frac{t}{\tau_E}} \qquad (7.25)$$

To examine the validity of this equation, let us look at the simplest case, whereby one newly recorded hologram (say H1) is partially erased by the next recording. We assume that the index modulation of H1 is Δn_0, and that it is uniform throughout the volume of H1 before erasure. The initial diffraction efficiency, η_0, can be expressed as:

$$\eta_0=(A\cdot\Delta n_0)^2 \qquad \text{(valid when } A\Delta n_0<<1) \qquad (7.26)$$

where A is a constant. A fraction, W (W<1), of the volume of H1 is overlapped by the next hologram (say H2) whose recording time equals t. After H2 is recorded, the efficiency of H1 reduced to η_1, which can be expressed as:

$$\eta_1 = (1\text{-W})\cdot\eta_0+\text{W}\cdot\eta' \qquad (7.27)$$

where η' is the efficiency that the overlapped part contributes, and is given by:

$$\eta' = (A\Delta n_0 \cdot e^{-t/\tau_E})^2 \tag{7.28}$$

Substituting Eqs. (7.26) and (7.28) into Eq. (7.27), we have:

$$\eta_1 = (A\ \Delta n_0)^2 \cdot [1-W(1-e^{-2t/\tau_E})] \tag{7.29}$$

If $t/\tau_E \ll 1$, the following approximations:

$$e^{-2t/\tau_E} = (1-2t/\tau_E) \tag{7.30}$$

and

$$1-2W \cdot t/\tau_E = e^{-2Wt/\tau_E} \tag{7.31}$$

are valid. Therefore, we have from Eq. (7.29):

$$\eta_1 = (A\Delta n_0 e^{-Wt/\tau_E})^2 \tag{7.32}$$

We can now introduce an equivalent index modulation after erasure, $\Delta n'$, which is given by:

$$\Delta n' = \Delta n_0 e^{-Wt/\tau_E} \tag{7.33}$$

so that the efficiency of H1 after partial erasure can be expressed as:

$$\eta_1 = (A\Delta n')^2 \tag{7.34}$$

Eq. (7.33) is identical to Eq.(7.14). From the above derivation it can be seen that, in replacing Eq. (7.29) with Eq. (7.32), we underestimated the remaining diffraction efficiency, η_1, because $[1-W(1-e^{-2t/\tau_E})]$ is always greater than e^{-2Wt/τ_E}. In other words, we overestimated the erasure effect of SAM recording. It is only when i) the initial hologram amplitude, $A\Delta n_0$, is small enough, and ii) the erasure time is much smaller than the erasure time constant (i.e. $t/\tau_E \ll 1$), that the first assumption for our erasure model of SAM (Eq. 7.14) is valid. Both of these two conditions require that the writing time of every hologram must be short enough compared to the erasure time constant.

Our second simplifying assumption is that the overlapping volume of two partially separated holograms is proportional to the overlapping area on the entrance of the crystal. Under the conditions described in section 7.3.3, this is true. In practice, however, both the object and reference beams have a Gaussian profile, and the index modulation is not uniform. Even though the erasure is performed by the reference beam only, different points on the reference beam profile have a different effect on the erasure, due to the non-uniform intensity distribution. We treated the edges of the beam profile with the same weight as the centre when we calculated the erasure weight matrix. This also results in an overestimation of the erasure of the SAM recording. A reference beam with a more uniform intensity profile could overcome this problem to some degree.

The determination of the time constants

If the erasure time constant used is shorter than the true value, or alternatively, if the writing time constant used is longer than the true value, the erasure effect could be overestimated. The method we used to determine the erasure time constant should be accurate enough. However, if more test recordings had been made (we recorded only ten), the result would have been more accurate. As for the writing time constant, there were two possible values which we arrived at. One (67 sec.) was obtained from a lest squares fit of measured data to theory, whilst the other (85 sec.) was obtained by direct measurement of the $1/e^2$ point of the diffraction efficiency (see section 7.3.3 and Fig. 7.15). We chose the greater value (85 sec.), as it gave better agreement to the diffraction efficiency obtained at small and medium exposures. This is a possible source of overestimation of erasure (underestimation of the writing rate).

By investigating the writing curves in Fig. 7.13, one can see that it is difficult to find a writing time constant which fits over a large exposure range. At the beginning of the recording diffraction efficiency grows more slowly than predicted by the theoretical model (Eq. 3.47), and vice versa. This suggests again that an exposure time long compared to the writing time constant should not be chosen, for this would give an efficiency much higher than that predicted by the model used. It also suggests that a better theory is required.

The determination of the target (last) exposure time

In the recording of a SAM memory, the exposure time of each hologram is associated with all others through many intermediate holograms, even though one hologram is overlapped by only some of the others in the array. A small difference in the last recording time (which causes only a slight difference in the target diffraction efficiency), causes a huge difference in the writing time of the first few holograms. Therefore, the last recording time has a critical effect on the resultant time sequence. Fig. 7.26 shows another time sequence, calculated using the same time constants as those of the time sequence in Fig. 7.19, but with a last recording time of 11.35 sec. as opposed to 11.39 sec. This figure has the same vertical scale as that of Fig. 7.19. If this time sequence had been used for the recording, no hologram in the array would have been exposed for a time anywhere near the writing time constant. Perhaps this is the simplest way to improve the diffraction efficiency uniformity, without the need to change the theoretical model used.

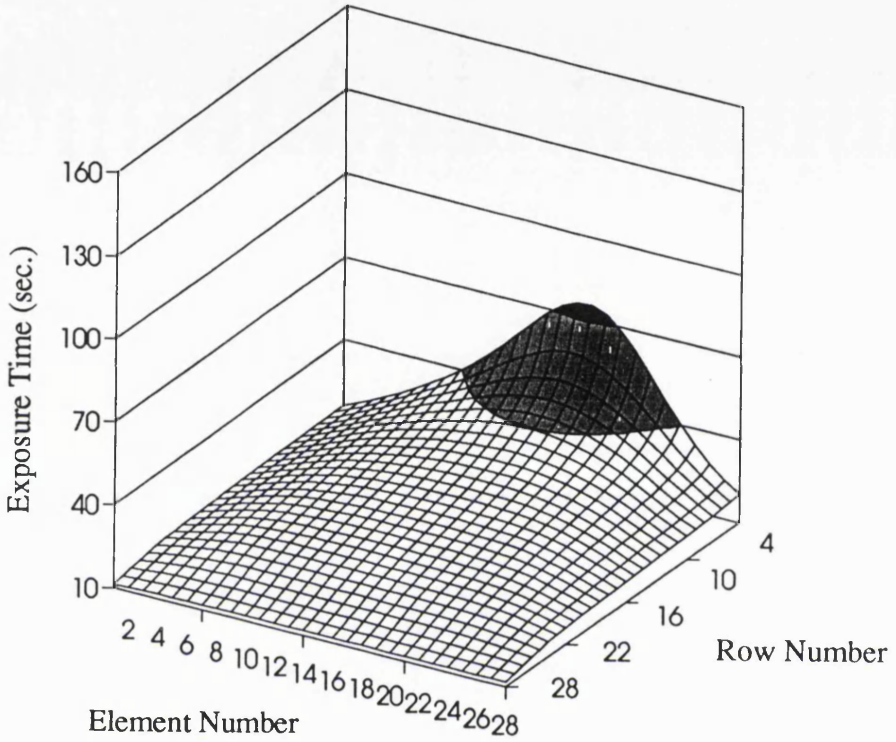

Fig. 7.26 Exposure time sequence calculated using τ_W=85 sec, τ_E=780 sec. and a last recording time 11.35 sec.

In summary, we have successfully recorded a dense holographic memory of 756 holograms in a single Fe: LiNbO$_3$ crystal of 1cm^3 effective volume, using the spatio-angular multiplexing technique. A high average diffraction efficiency was obtained, which verified the theoretical prediction that SAM could improve the efficiency, and, hence, the capacity compared to pure angular multiplexing. A special exposure model has been developed, and its validity has been examined experimentally and analytically.

CHAPTER EIGHT

CONCLUSIONS AND FUTURE WORK

8.1 Conclusions

In this thesis we have discussed in detail the principles and peculiarities of our new hologram multiplexing scheme, SAM. We have also presented the results of a preliminary experiment on the storage of 756 holograms in a single photorefractive Fe:LiNbO$_3$ crystal, and this has verified the following new ideas that were discovered during the research:

1) By partially overlapping holograms, a crystal can accommodate more holograms than is possible with pure spatial multiplexing. Therefore, SAM increases the storage capacity for holographic storage, as compared to pure spatial multiplexing, by fully using the volume of the storage medium. Readout of different holograms can be achieved with differently angled reference beams (Chapters 6 and 7).

2) The use of partially overlapped holograms also minimises the erasure effect that sequential recordings have on a previously recorded hologram. This is an intrinsic problem with angularly multiplexed holograms in unfixed photorefractive materials, and is the main limit

on the storage capacity for such materials using this technique. SAM can increase the storage capacity and the diffraction efficiency over that available with pure angular multiplexing (Chapters 6 and 7).

3) SAM memory has a local (differential) degree of angular multiplexing, which is proportional to the square of the one-dimensional overlap factor, μ (the ratio of the hologram size to the spatial distance between adjacent holograms). The diffraction efficiency of a SAM memory, with an overlap factor equal to μ, is equivalent to that obtained from μ^2 holograms recorded using pure angular multiplexing (Chapter 6). This is confirmed by our preliminary experiment (Chapter 7).

4) The SAM scheme is suitable for all types of holographic recording materials, as long as the material entrance size is larger than the required hologram size. A specific exposure procedure is needed for extending SAM to other materials, so that a good uniformity in the diffraction efficiency may be obtained (Chapters 6 and 7).

5) We discovered that the Bragg shift (the amount that the optimum readout angle differs from the recording angle), affects the readout angle settings (if the highest diffraction efficiency is required) for addressing dense data bases in photorefractive materials. This was investigated thoroughly for single gratings recorded in $LiNbO_3$ crystals, (Chapters 4 and 7). In addition, we found analytically that a proper writing beam ratio, $m_0=\exp(\Gamma d \sin\Phi_g)$, can be chosen to minimise the Bragg shift for an arbitrary phase shift between a writing intensity pattern and the resultant grating fringes, Φ_g. This enables the highest efficiencies to be obtained with a simple recording and readout system (Chapter 4).

6) We found, theoretically and experimentally, that the angular selectivity of a volume grating in the vertical dimension is finite, and is much worse than that in the horizontal dimension. (The definitions of the vertical and horizontal dimensions can be found in Section 5.2, Chapter Five). Also, the grating degeneracy occurs along a hyperbola in

the reference plane, instead of on a straight vertical line (Chapter 5). To minimise crosstalk, a random two-dimensional arrangement of reference points should be avoided.

Theoretical research and experimental results showed up the following advantages of SAM over pure spatial, pure angular and conventional block oriented (BOHS) hologram multiplexing schemes:

1) As a memory element of a neural network, a SAM memory in a photorefractive crystal can introduce a large number of 3-D optical interconnections into a high order feedback neural network (HOFNET), while still allowing full parallel correlation of all the stored images.

2) As a holographic storage technology, SAM promises a storage capacity much higher than that for pure spatial or pure angular multiplexing, and comparable to that offered by conventional BOHS. Compared to purely spatial multiplexing, SAM increases the storage capacity by a factor of approximately μ^2. Compared to pure angular multiplexing, in the case of $D_H >> d_H >> \Delta$, (i.e. the crystal size, D_H, is much greater than the hologram size, d_H, and the spatial separation between adjacent holograms, Δ, is small compared to the hologram size), the storage capacity for SAM (for the same hologram efficiencies in both cases) will be enhanced by a factor of $\left(\frac{D_H}{d_H}\right)^2$. The storage capacity for SAM is smaller than that for BOHS. However, when $D_H >> d_H >> \Delta$, the difference is negligible. In the case that the dimension of the storage material is slightly larger than the required hologram size (in this region pure spatial or BOHS multiplexing becomes impossible), SAM is still able to effectively increase the storage capacity, although a different theoretical model is needed for the analysis in this case.
The storage density that we have achieved is 1.3×10^7 bits in a single crystal of $1 cm^3$ volume. It would be feasible to increase this to 3.6×10^8 bits in the same crystal, by storing 5500 holograms (with a hologram overlapping factor $\mu=22$, and an equivalent degree of spatial multiplexing $N_{SAM}=11.45$), and by increasing the number of SLM pixels

to 256 x 256 (we believe that this is resolvable with the current size of hologram). This storage capacity would be comparable to the most recent achievement (3.52×10^8 bits [Mok92]), but the storage density would be three times higher than that in [Mok92], in which a larger crystal ($3cm^3$) was used.

3) In the case of $D_H >> d_H >> \Delta$, the diffraction efficiency of SAM will be enhanced by a factor of $\left(\frac{D_H}{d_H}\right)^4$, (as compared to pure angular multiplexing), if the same number of holograms are multiplexed using these two schemes. The diffraction efficiency we have achieved is 0.5%, fifty times higher than that reported by Mok et al (0.01% for 500 holograms in [Mok91]). Taking 0.01% as a lower limit of the diffraction efficiency, we calculated the potential capacity described in the last paragraph, that was 3.6×10^8 bits/cm^3 (by storing 5500 holograms using SAM), and the diffraction efficiency would be at least one order higher than that reported by Mok (4×10^{-6} for 5000 holograms in [Mok93]).

4) If the hologram size is fixed (this is common in practice), SAM can gain much more benefit (in terms of the storage capacity and diffraction efficiency) from an increase in the crystal size, than can a purely angularly multiplexed scheme.

Although SAM has the advantages described above, there are some limitations and disadvantages in SAM. Compared to pure spatial multiplexing, SAM loses the ability to independently erase and update individual holograms, and its diffraction efficiency decreases. Compared to pure angular multiplexing, a more complicated exposure model is required to realise uniform diffraction efficiency. The differential (local) degree of angular multiplexing in SAM is not uniform, being smaller at the edges of the array than elsewhere. This may also cause non-uniformity in the diffraction efficiency, which will need to be compensated by an improved exposure scheme.

8.2 Future Work

Although our preliminary experiment succeeded, the achievement is not not sufficient for use in a practical system. In the near future the following work directions could be considered:

1) Improved diffraction efficiency uniformity.
   The relative standard deviation of the diffraction efficiency we obtained was 40%. Reducing this to 10% should be possible. For this purpose a better erasure model must be used to calculate the exposure time sequence, and a more accurate measurement of the crystal writing and erasure time constants is essential.

2) Increased capacity
   Using the existing crystal we may obtain 5500 holograms with a 0.01% efficiency, each containing 256x256 pixels (providing an SLM with a higher resolution is available), giving a total capacity of 3.6 x 10^8 bits/cm^3, as pointed out in the last section.

3) Implementation of an ideal SAM so that it can be incorporated into a realistic HOFNET.
   The ideal SAM requires a distinct reference angle for each hologram recording. Due to geometrical limitations we could only provide about 100 distinct reference angles. as a result we used only 64 reference angles for each sub-array in our preliminary experiment. The resulting memory array was not suitable for use in a HOFNET. The approaches for improving this include: (i) reducing the horizontal selective angle, $\Delta\Theta$, by using thicker crystals and larger interbeam angles; (ii) using optics with larger numerical apertures; (iii) arranging reference points in two dimensions (being careful to eliminate reference points in the degeneracy hyperbola).

4) Investigation of fixing techniques for SAM memory.
   The memory recorded in our crystal sample could have a persistence of about 172 days if stored in the dark, and we managed to read the

memory at least 5 times before thoroughly erasing it. This may be useful for the demonstration of parallel correlation in a HOFNET, but is not good enough for practical write-once-read-many applications. So fixing techniques need to be used.

5) The design of a suitable MAWBG (multiple angled weighted beam generator) for parallel readout of all holograms in a HOFNET memory recorded using SAM.
   This is another key point in the realization of a fully parallel correlation using a HOFNET with a SAM memory. All readout beams generated by the MAWBG must match exactly the Bragg angles of the corresponding holograms. Current designs involving microlens arrays, computer-generated holograms, holographic lenslet arrays, or surface-emitting microlaser diode arrays can satisfy this condition, provided that the same design is used for recording. Unfortunately, the optimum readout angle for photorefractive materials is different from the recording angle, and if the maximum diffraction efficiency is essential, a more complicated design (which should allow individual adjustment of each angled beam) is required.

6) Last but not least, we note that there is a lot of work on the theoretical and material aspects of photorefractives still to do. For example, the writing and erasure kinetics are still not clearly understood, despite the investigations of many authors who have achieved good agreement between experiment and theory for some models (see, for example, [Kuk76, Car86 and Jar90]). The complexities appearing in our experiments, such as the change of the crystal characteristics after erasure by UV light, do not fit the existing models well. Commercially available crystals with a large size, an excellent optical quality, and grown with precisely controlled parameters, will bring SAM memory from the research laboratory into a commercially competitive system.

As in all other multiplexing schemes discussed in this thesis, SAM uses page oriented information storage. This allows a high data transfer rate as a result of the high parallelism of optical information. However, this also puts a common limitation on all the multiplexing schemes, including SAM, whereby independent erasure of individual bits is impossible. This means that, SAM memory is not suitable as a random access memory in serial computers, but it is suitable for use as a WORM (write once, read many) memory or for archival storage. Moreover, SAM is most suitable for pattern recognition in a parallel optical information processing system (for which it was designed). In such a system, compact memories recorded in photorefractive crystals using SAM technology would occupy a particular position in the memory hierarchy (which cannot be properly placed in the memory pyramid shown in Fig. 1.1). This type of memory would feature huge storage capacity, extremely high data transfer speeds, and the unique ability to correlate in parallel all stored patterns with an input pattern.

REFERENCES

[Amo72] Amodei, J. J., Phillips, W., and Staebler, D. L. (1972), "Improved electrooptic materials and fixing techniques for holographic recording", Appl. Opt. **11** (2), 390-396

[And87] Anderson, D. Z. and Lininger, D. M. (1987), "Dynamic optical interconnects: volume holograms as two-port operators", Appl. Opt. **26**, 5031-5038

[Ari87] Arizmendi, L., Kliewer, M. J., and Powell, R. C. (1987), "Laser-induced grating characteristics in doped lithium niobate crystals", J. Appl. Phys. **61** (5), 1682-1687

[Ari89] Arizmendi, L. (1989), "Thermal fixing of holographic gratings in $Bi_{12}SiO_{20}$", J. Appl. Phys. **65** (2), 423-427

[Ash66] Ashkin, A., Boyd, G. D., Dziedzik, J. M., Smith, R. G., Ballman, A. A., Levinstein, J. J., and Nassau, K. (1966), "Optically-induced refractive index inhomogeneities in $LiNbO_3$ and $LITaO_3$", Appl. Phys. Lett. **9**, 72-74

[Au88] Au, L. B., and Solymar, L. (1988), "Space-charge field in photorefractive materials at large modulation", Opt. Lett. **13** (8), 660-662

[Au89] Au, L. B., and Solymar, L. (1989), "Grating formation in photorefractive materials at large illumination", Opt. Commun. **72** (3,4), 261-264

[Ble91] Bledowski, A., Otten, J., and Ringhofer, K. H. (1991), "Photorefractive hologram writing with modulation 1", Opt. Lett. **16** (9), 672-674

[Blo79] Blotekjaer, K. (1979), "Limitations on holographic storage capacity of photochromic and photorefractive media", Appl. Opt. **18** (1), 57-67

[Boa80] Boatner, L. A., Kratzig, and E. Orlowski, R. (1980), "KTN as a holographic storage material", Ferroelectrics **27**, 247

[Bra90] Brady, D., Kagan, D., Raguin, D., and Psaltis, D. (1990), "Photorefractive holograms in $LiNbO_3$ with multiple trapping species", Topical Meeting on Photorefractive Materials, Effects, and Devices, Jan 17-19, 1990, Aussois, France, 101-104

[Burg76] Burgess, J. W., Hurditchi, R. J., Kirkby, C. J., and Scrivener, G. E. (1976), "Holographic storage and photoconductivity in PLZT ceramic materials", Appl. Opt. **15**, 1550

[Bur77] Burke, W. J. and Sheng, P. (1977), "Crosstalk noise from multiple thick-phase holograms", J. Appl. Phys. **48** (2), 681-685

[Bur78] Burke, W. J., Staebler, D. L., Phillips, W. and Alphonse, G. A. (1978), "Volume phase holographic storage in ferroelectric crystals", Opt. Eng. **17** (4), 308-316

[Burr93] Burr, G. W., Psaltis, D., and Curtis, K. (1993), "Comparison of wavelength and angle multiplexed holographic memories", Optical Computing, March 16-19, 1993 Palm Springs, California, 1993 Technical Digest Series Volume **7**, 87-90

[Car86] Carrascosa, M. and Agullo-Lopez F. (1986), "Kinetics for optical erasure of sinusoidal holographic gratings in photorefractive materials", IEEE Journal of Quantum Electronics **QE-22** (8), 1369-1375

[Che68] Chen, F. S., La Macchia, J. T., and Frazer, D. B. (1968), "Holographic storage in lithium niobate", Appl. Phys. Lett. **13**, 223-224

[Chen88] Cheng, L-J., and Partovi A. (1988), "Index grating lifetime in photorefractive GaAs", Appl. Opt. **27** (9), 1760-1763

[d'Au74] d'Auria, L., Huignard J. P., Slezak C., and Spitz E. (1974), "Experimental holographic read-write memory using 3-D storage", Appl. Opt. **13** (4), 808

[Del89] Delboulbe, A., Fromont, C., Herriau, J. P., Mallick, S., and Huignard, J. P. (1989), "Quasi-nondestructive readout of holographically stored information in photorefractive $Bi_{12}SiO_{20}$ crystals", Appl. Phys. Lett. **55** (8), 713-715

[Den92] Denz C., Pauliat G., and Tschudi T. (1992), "Potentialities and limitations of hologram multiplexing by using the phase-encoding technique", Appl. Opt., **31**, 5700-5705

[DeV79] DeVelis, J. B. and Reynolds G. O. (1979), "Fresnel holography", in *Handbook of Optical Holography*, (H. J. Caulfield, ed.) Academic Press. New York, Section 4.1

[Dor81] Dorosh, I. R., Kuzminov, Yu. S., Polozkov, N. M., Prokhorov, A. M., Osiko, V. V., Thachenko, N. V., Voronov, V. V., and Nurligareev, D. Kh. (1981), "Barium-strontium niobate crystals for optical information recording", Phys. Stat. Sol. (a) **65**, 513

[Erb88] Erbschloe, D. R. (1988), "Two-wave mixing in photorefrractive crystals", D. Phil Thesis, Chapter 2, Oxford University

[Erb89] Erbschloe, D. R. and Wilson, T. (1989), "A simple analytic solution for transient two-wave mixing in photorefractive materials", Opt. Commun. **72**, 135

[Fei80] Feiberg, J., Heiman, D., Tanguay, Jr., A. R., and Hellwarth, R. W. (1980), "Photorefractive effects and light-induced charge migration in barium titanate", J. Appl. Phys. **51** (3), 1297-1305

[Fes82] Festl, H. G., Hertel, P., Kratzig, E., and von Baitz, R. (1982), "Investigations of the photovoltaic tensor in doped $LiNbO_3$", Phys. Status Solidi B **113** (1), 157-164

[Fir72]: Firester A. H., Fox E. C., Gayeski T., Hannan W. J., and Lurie M. (1972), "Redundant holograms", RCA Review **33**, 131

[For91] Ford, J. E., Taketomi, Y., Lee, S. H., Bize, D., Neurgaonkar, R. R., and Fainman, S. (1991), "Effects of applied voltage on holographic storage in SBN:60", Conference paper

[For92] Ford, J. E., Ma, J., Lee, S. H., Taketomi, Y., Bize, D., and Neurgaonkar, R. R. (1992), "Multiple holography in strontium barium niobate with applied field", J. Opt. Soc. Am. A **9** (7), 1183-1192

[Fri78] Fridkin, V. M., Popov, B. N., and Verkhovskaya, K. A. (1978), "The photovoltaic and photorefractive effects in KDP-type ferroelectrics", Appl. Phys. **16**, 313

[Gab48] Gabor, J. D. (1948), "A new microscope principle", Nature **161**, 777-778

[Gab49] Gabor, J. D. (1949), "Microscopy by reconstructed wavefronts", Proc. Roy. Soc. **A197**, 454-487

[Gab51] Gabor, J. D. (1951), "Microscopy by reconstructed wavefronts: II", Proc. Phys. Soc. **B64**, 449

[Gay73] Gaylord, T. K., Rabson, T. A., Tittel, F. K., and Quick, C. R. (1973), "Self-enhancement of $LiNbO_3$ holograms", J. Appl. Phys., **44** (2), 896-897

[Gay79] Gaylord, T. K (1979), "Digital Data Storage", in *Handbook of Optical Holography* (H. J. Caulfield, ed.) Academic Press. New York, 379

[Gla78] Glass, A. M. (1978), "The photorefractive effect", Opt. Eng. **17**(5), 470-479

[Gla84] Glass, A. M., Johnson, A. M., Olson, D. H., Simpson, W., and Ballman, A. A. (1984), "Four-wave mixing in semi-insulating InP and GaAs using photorefractive effects", Appl. Phys. Lett. **44** (10), 948-950

[Gol88] Goltz, J. and Tschudi, T. (1988), "Angular selectivity of volume holograms recorded in photorefractive crystals: an analytical treatment", Opt. Commun., **67** (3), 164-166

[Goo68] Goodman, J. W. (1968), *Introduction to Fourier Optics*, McGraw-Hill, New York

[Goo90] Goodman, J. W. (1990), "Optical interconnections in the '80s ", Optics & Photonics News, December 1990, 21-23

[Gu92] Gu C., Hong J. McMichael I., Saxena R., and Mok F. (1992), "Cross-talk-limited storage capacity of volume holographic memory", J. Opt. Soc. Am. A **9** (11), 1978

[Gu93] Gu, C., Campbell, S., and Yeh, P. (1993), "Optical matrix amplification using grating degeneracy in photorefractive media", Optical Computing, March 16-19, 1993 Palm Springs, California, 1993 Technical Digest Series Volume **7**, 119-122

[Gun78] Gunter, P. and Micheron, F. (1978), "Photorefractive effects and photocurrents in $KNbO_3$:Fe", Ferroelectrics **18**, 27

[Gun82] Gunter, P. (1982), "Holography, coherent light amplification and optical phase conjugation with photorefractive materials", Phys. Reports **93**(4), 199-299

[Hea84] Heaton, J. M., Mills, P. A., Paige, E. G. S., Solymar, L. and Wilson, T. (1984), "Diffraction efficiency and angular selectivity of volume phase holograms recorded in photorefractive materials", Optica Acta, **31** (8), 885-901

[Her78] Herriau, J. P., Huignard, J. P., and Aubourg, P. (1978), "Some polarization properties of volume holograms in $Bi_{12}SiO_{20}$ crystals and applications", Appl. Opt. **17** (12) 1851-1852

[Her86] Herriau, J. P. and Huignard, J. P. (1986), "Holographic fixing process at room temperature in photorefractive $Bi_{12}SiO_{20}$", Appl. Phys. Lett. **49** (18), 1140-1142

[Hes88] Hesselink, L. and Redfield, S. (1988), "Photorefractive holographic recording in strontium barium niobate fibers", Opt. Lett. **13** (10), 877-879

[Hes91] Hesselink, L. and Wilde, J. (1991), "Recent advances in holographic data storage in SBN", Soviet-Chinese Joint Seminar on Holography and Optical Information Processing, 21-26 September, 1991, Bishkek, Kirghizstan, SPIE **1731**, 74-79

[Hui76] Huignard, J. P. and Micheron, F. (1976), "High-sensitivity read-write volume holographic storage in $Bi_{12}SiO_{20}$ and $Bi_{12}GeO_{20}$ crystals", Appl. Phys. Lett. **29** (9), 591-593

[Hui81] Huignard, J. P. and Marrakchi, A. (1981), "Coherent signal beam amplification in two-wave mixing experiments with photorefractive $Bi_{12}SiO_{20}$ crystals", Opt. Commun. **38** (4), 249-254

[Hun90] Hunter, S., Kiamilev, F., Esener, S., Parthenopoulos, D. A., and Rentzepis, M. (1991), "Potentials of two-photon based 3-D optical memories for high performance computing", Appl. Opt. **29** (14), 2058-2066

[Jar90] Jariego, F. and Agullo-Lopez, F. (1990), "Monotonic versus oscillatory behaviour during holographic writing in photorefractive photovoltaic materials", Opt. Commun. **76** (2), 169-172

[Jon61] Jones R. C. (1961), "Information capacity of photographic films", J. Opt. Soc. Amer. **51**, 1159

[Kan87] Kanaev, I. F., Mailinovsk, V. K., and Pugachev, A. M. (1987), "Changes in photogalvanic and photorefractive characteristics of lithium-niobate under the light", Ferroelectrics **75** (1-2), 209-230

[Kir88] Kirkby, C. J. G. (1988), "Refractive index of lithium niobate, wavelength dependence: Tables", in Chapter 5 of *Properties of Lithium Niobate*, EMIS Data Reviews Series No.5 as Inspect Publication INSPECT IEE 1989

[Koh88] Kohonen, T. (1988), *Self-organization and associative memory*, 2nd Edition, Springer-Verlag, Berlin

[Kra78] Kratzig, E. and Orlowski, R. (1978), "$LiTaO_3$ as holographic storage material", Appl. Phys. **15**, 133

[Kra80] Kratzig, E., Welz, F., Orlowski, R., Doormann, V., and Rosenkranz, M. (1980), "Holographic storage properties of $BaTiO_3$", Sol. State Commun. **34**, 817

[Kra86] Kratzig, E., and Rupp, R. A. (1986), "Holographic storage properties of electrooptical crystals", SPIE **673** International Conference on Holography Applications (1989), 483-488

[Kra90] Kratzig, E. and Sommerfeldt, R. (1990), "Influence of dopants on photorefractive properties of $LiNbO_3$ crystals", SPIE **1273** Nonlinear Optical Materials III, 2-11

[Kro90] Krolikowski, W., Cronin-Golomb, M., and Chen, B. S. (1990), "Photorefractive effect in ferroelectric lead germinate", Appl. Phys. Lett. **57** (1), 7-7

[Kub78] Kubota, T. (1978), "Characteristics of thick hologram grating recorded in absoptive medium", Optica Acta **25**, 1035-1053

[Kuk76] Kukhtarev, N. V. (1976), "Kinetics of hologram recording and erasure in electrooptic crystals", Sov. Tech. Phys. Lett., **2** (12), 438-440

[Kuk77] Kukhtarev, N. V., Markov, V. B., Odulov, S. G. (1977), "Transient energy transfer during hologram formation in $LiNbO_3$ in external electric field", Opt. Commun. **23** (3), 338-343

[Kuk79a] Kukhtarev, N. V., Markov, V. B., Odulov, S. G., Soskin, M. S. and Vinetskii, V. L. (1979), " Holographic storage in electrooptic crystals. I. Steady state", Ferroelectrics, **22**, 949-960

[Kuk79b] Kukhtarev, N. V., Markov, V. B., Odulov, S. G., Soskin, M. S. and Vinetskii, V. L. (1979), " Holographic storage in electrooptic crystals. II. Beam coupling--light amplification", Ferroelectrics, **22**, 961-964

[Kur76] Kurz, H., Doormann, V., and Kobs, R. (1976), "Photorefractive recording of volume holograms in doped $LiNbO_3$", in *Applications of Optical Data Processing,* Ed. by Marom, E., Friesem, A. A., and Wiener-Avnear, E. E., (Pergamon), 361-370

[Kur77a] Kurz, H. (1977), "Photorefractive recording dynamics and multiple storage of volume holograms in photorefractive $LiNbO_3$", Optica Acta, **24** (4) 463-473

[Kur77b] Kurz, H. (1977), "Lithium Niobate as a material for holographic information storage", Philips Tech. Rev., **37** (5/6), 109-120

[Kur79] Kurtz, R. L., Liu, H-K., and Owen, R. B. (1979), "Holographic Systems" in *Handbook of Optical Holography* (H. J. Caulfield, ed.) Academic Press. New York, Section 8.4

[Lee89] Lee, H., Gu, X., and Psaltis, D. (1989), "Volume holographic interconnections with maximal capacity and minimal cross talk", Appl. Opt. **65**, 2191-2194

[Lei62] Leith, E. N. and Upatnieks, J. (1962), "Reconstructed wavefront and communication theory", J. Opt. Soc. Amer. **52**, 1123

[Lei63] Leith, E. N. and Upatnieks, J. (1963), "Wavefront reconstruction with continuous-tone objects", J. Opt. Soc. Amer. **53**, 1377

[Lei64] Leith, E. N. and Upatnieks, J. (1964), "Wavefront reconstruction with diffused illumination and three-dimensional objects", J. Opt. Soc. Amer. **54**, 1295

[Lo92] Lo, W. K. B. (1992), "Optical implementation of neural interconnections using photorefractive volume holograms", Final Year Undergraduate Project Report, Dept. of Electronic & Electrical Eng., University College London (U. K.)

[Loh56] Lohmann, A. (1956), "Optische Einseitenbandubertragung angewandt auf das Gabor-Mikroskop", Opt. Acta **3**, 97

[Ma91] Ma, J.,Taketomi, Y., Fainman. Y., Ford, J. E., and Lee. S. H. (1991), "Moving grating and dc external field in photorefractive GaP at 633nm", Opt. Lett. **16** (14), 1080-1082

[Man90]: Maniloff, E. C. and Johnson, K. M. (1990), "Dynamic holographic interconnects using static holograms", Opt. Eng. **29** (3), 225

[Man91]: Maniloff, E. C. and Johnson, K. M. (1991) "Maximized photorefractive holographic storage", J. Appl. Phys. **70** (9), 4702-4707

[Man92] Maniloff, E. C. and Johnson, K. M. (1992), "Incremental recording for photorefractive hologram multiplexing: comment", Opt. Lett. **17**, 961

[Mao91]: Mao, Z. Q., Selviah, D. R., Tao, S., and Midwinter, J. E. (1991), "Holographic high order associative memory system", 3rd International Conference on Holographic Systems, Components & Applications, Edinburgh, U.K., Sept. 1991, IEE Proc. **342**, pp132-136

[Mao92a]: Mao, Z. Q., Selviah, D. R., and Midwinter, J. E. (1992), "Design of optical HOFNET by using image subtraction system for normalization", The IOP Conference on Optoelectronic Neural Networks, Oxford, U. K., June 1992

[Mao92b]: Mao, Z. Q. (1992), "Optoelectronic high order feedback neural network (HOFNET)", PhD Thesis, University of London, 1992

[Mar81] Marrakchi, A., Huignard, J. P., and Gunter, P. (1981), "Diffraction efficiency and energy transfer in two-wave mixing experiments with $Bi_{12}SiO_{20}$ crystals", Appl. Phys. **24**, 131-138

[Mar86] Marrakchi, A., Johnson, R. V., and Tanguay, Jr., A. R. (1986), "Polarization properties of photorefractive diffraction in electrooptic and optically active sillenite crystals (Bragg regime)," J. Opt. Soc. Amer. B, **3** (2), 321-336

[Meg77] Megumi, K., Kozuka, H., Kobayashi, M., and Furukata, Y. (1977), "High-sensitive holographic storage in Ce-doped SBN", Appl. Phys. Lett. **30**, 631

[Mid87] Midwinter, J. E. and Selviah, D. R. (1987), "Digital neural networks, matched filters and optical implementations", in *Neural Computing Architecture*, ed. by I. Aleksander (North Oxford Academic), Chapter 13

[Mok91] Mok, F. H., Tackitt, M. C., and Stoll, H. M. (1991), "Storage of 500 high-resolution holograms in a $LiNbO_3$ crystal", Opt. Lett. **16**(8), 605-607

[Mok92] Mok, F. H. and Stoll, H. M. (1992), "Holographic inner-product processor for pattern recognition", SPIE **1701**, Optical Pattern Recognition III, Orlando'92, Apr. 1992, Orland, Florida, USA, 312-322

[Mok93] Mok, F. H. (1993), "Angle-multiplexed storage of 5000 holograms in lithium niobate", Opt. Lett. **18** (11), 915-917

[Oll93] Ollikainen, O. (1993), "Optical implementation of quadratic associative memory by use of persistent spectral hole-burning media", Appl. Opt. **32** (11), 1943-1947

[Orl77] Orlowski, R., Kratzig, E., and Kurz, H. (1977), "Photorefractive effects in $LiNbO_3$:Fe under external electric fields", Opt. Commum. **20**, 171-174

[Orl80] Orlowski, R., Boatner, L. A., and Kratzig, E. (1980), "Photorefractive effects in the cubic phase of potassium tantalate-niobate", Opt. Commun. **35**, 45

[Ott89] Otten, J., Ozols, A., Reinfelde, and Ringhofer, K. H. (1989), "Self-enhancement in lithium niobate", Opt. Commun. **72** (3,4), 175-179

[Ott92] Otten, J., Ozols, A., Reinfelde, M., Bledowksi, A. and Ringhofer, K. H. (1992), "Threshold of self-enhancement in lithium niobate", Opt. Commun. **87** (4), 157-160

[Owe87] Owechko, Y., Dunning, G. J., Marom, E., and Soffer, B. H. (1987), "Holographic associative memory with nonlinearities in the correlation domain", Appl. Opt. **26**, 1900-1910

[Ozo86] Ozols, A. O. (1986), "The self-enhancement effect of dynamic amplitude-phase holograms and its applications", SPIE **673** International Conference on Holography Applications, 41-42, (1986)

[Pae90] Paek, E. G., Wullert II, J. R., Jain, M., Von Lehmen, A., Scherer, A., Harbison, J., Florez, L. T., Yoo, H. J., Martin, R., Jewell, J. L., and Lee, Y. H. (1990), "Compact and ultrafast holographic memory using a surface-emitting microlaser diode array", Opt. Lett. **15** (6), 341-343

[Pau90] Pauliat, G., Slensky, A., Fridkin, V., and Roosen, G. (1990), "Photovoltaic gratings recorded in Praeseodymium doped $La_3Ga_5SiO_{14}$ crystals", Photorefractive Materials, Effects, and Devices II, 247-250

[Pel77] Peltier, M. and Micheron, F. (1977), "Volume hologram recording and charge transfer process in $Bi_{12}SiO_{20}$ and BGO", J. Appl. Phys. **48** (9), 3683-3690

[Pen82] Pencheva, T. G., Petrov, M. P., and Stepanov, S. I. (1982), "Selective properties of volume phase holograms in photorefractive crystals", Opt. Commun. **40** (3), 175-178

[Pet79] Petrov, M. P., , and Kamshilin, A. A. (1979), "Light diffraction from the volume holograms in electrooptic birefringent crystals", Opt. Commun. **29** (1), 44-48

[Pet81] Petrov, M. P., Pencheva, T. G., and Stepanov, S. I. (1981), "Light diffraction from volume phase holograms in electrooptic photorefractive crystals", J. Optics (Paris), **12** (5), 287-292

[Phi72] Phillips, W., Amodei, J. J., and Staebler, D. L. (1972), "Optical and holographic storage properties of transition metal doped lithium niobate", RCA Review **33**, 94-105

[Poo91] Poon, P. C. H. (1991), "A compilation of holographic properties of photorefractive materials", Final Year Undergraduate Project, Department of Electronic and Electrical Engineering, University College London (1991)

[Psa87] Psaltis, D., Yu, J., Gu, X. G., and Lee, H. (1987), "Optical neural nets implemented with volume holograms", Optical Computing Conference Proceedings 1987, Nevada, 129-132

[Psa88a] Psaltis, D., Brady, D., and Wagner, K. (1988), "Adaptive optical networks using photorefractive crystals", Appl. Opt. **27**, 1752-1759

[Psa88b] Psaltis, D., Park, D. C., and Hong, J. (1988), "High order associative memories and their optical implementations", Neural Networks **1**, 149-163

[Psa88c] Psaltis, D., Gu, X. G., and Brady, D. (1988), "Fractal sampling grids for holographic interconnections", SPIE **963**, Optical Computing, 468-474

[Psa90a] Psaltis, D., Brady, D., Gu, X-G., and Lin, S. (1990), "Holography in artificial neural networks", Nature **343**, 325-330

[Psa90b] Psaltis, D. and Quio, Y. (1990), "Optical neural networks", Optics & Photonics News, December 1990, 17-20

[Rak92] Rakuljik G. A., Leyva V., and Yariv A. (1992), " Optical data storage by using orthogonal wavelength-multiplexed volume holograms", Opt. Lett. **17** (20) 1471

[Ram72] Ramberg E. G. (1972), "Holographic information storage", RCA Rev. **33**, 5

[Red88] Redfield, S. and Hesselink. L. (1988), "Data storage in photorefractives revised", SPIE **963** Optical Computing 88, 35-45

[Rin89] Ringhofer, K. H. (1989), "Holograms in lithium niobate: basic material properties", in Chapter 10 of *Properties of Lithium Niobate*, EMIS Data Reviews Series No.5 as Inspect Publication INSPECT IEE 1989

[Rin91] Ringhofer, K. H., Tao, S., Takacs, J., and Solymar, L. (1991), "The role of the longitudinal component of the electric field vector in two-wave mixing in photorefractive $BaTiO_3$", Appl. Phys. B **52**, 259-261

[Rog52] Rogers, G. L. (1952), "Experiments in diffraction microscopy", Proc. Roy. Soc. Edinburgh **63A**, 193

[Rye92] Ryan, B. (1992), "Scaling the memory pyramid", BYTE, March 1992, 161-170

[Sel89] Selviah, D. R. and Midwinter, J. E. (1989), "Memory capacity of a novel optical neural net architecture", Optical Computing Conference, Toulouse, France, 195-201

[Sel90] Selviah, D. R., Mao, Z. Q., and Midwinter, J. E. (1990), "Optoelectronic high order feedback neural net", Electronics Letters, **26** (11), 1954-1955

[Sel91] Selviah, D. R., Mao, Z. Q., and Midwinter, J. E. (1991), "An optoelectronic high order feedback net (HOFNET) with variable non-linearity", 2nd International Conference on Artificial neural Networks, Bournemouth, U. K., Nov. 1991, IEE Proc. **349**, 59-63

[Shv87] Shvarts, K., Ozols, A., Augustov, P. and Reinfelde, M. (1987), "Photorefraction and self-enhancement of holograms in $LiNbO_3$ and $LiTiO_3$ crystals", Ferroelectrics, **75**, 231-249

[Smi69] Smith H. M. (1969), *Principles of Holography,* Wiley (Interscience), New York

[Sol81] Solymar L. and Cooke D. J. (1981), *Volume Holography and Volume Gratings,* Academic Press, London

[Sol84] Solymar L., Wilson, T., and Heaton, J. M. (1984), "Space charge field in photorefractive materials", Ist. J. Electronics **57** (1), 125-127

[Sol89a] Solymar, L. (1989), "Reconfigurable optical interconnections in photorefractives", private communication

[Sol89b] Solymar, L. and Newell, J. (1989), "Silver-halide noise grating recorded in dicrhromated gelatin", Opt. Commun. **73** (4), 273-276

[Som89] Sommerfeldt, R., Grabmaier, B. C., Holtmann, L., and Kratzig, E. (1989), "The light-induced charge transport in $LiNbO_3$: Mg, Fe crystals", Ferroelectrics **92**, 219-225

[Sta74] Staebler, D. L. and Phillips, W. (1974), "Fe-doped $LiNbO_3$ for read-write applications", Appl. Opt. **13** (4), 788-794

[Sta75] Staebler, D. L., Burke, W. J., Phillips, W., and Amodei, J. J. (1975), "Multiple storage and erasure of fixed holograms in Fe-doped $LiNbO_3$", Appl. Phys. Lett. **26** (4), 182-184

[Stc89] STC Technology Ltd, "128 x 128 Ferroelectric liquid crystal spatial light modulator 2DX128", Instruction Manual, 1989

[Ste77] Stepanov, S. J., Petrov, M. P., and Kamshilin, A. A. (1977), "Optical diffraction with polarisation plane rotation in a volume hologram in an electrooptic crystal", Sov. Tech. Phys. Lett. **3**, 345-346

[Str89] Strasser, A. G., Maniloff, E. S., Johnson, K. M., and Goggin, S. D. D. (1989), "Procedure for recording multiple-exposure holograms with equal diffraction efficiency in photorefractive media", Opt. Lett. **14**, 6

[Str91] Strickler, J. H. and Webb, W. W. (1991), "Three dimensional optical data storage in refractive media by two-photon point excitation", Opt. Lett. **16** (22), 1780-1782

[Tak91] Taketomi, Y., Ford, J. E., Sasaki, H., Ma. J., Fainman. Y., and Lee. S. H. (1991), "Incremental recording for photorefractive hologram multiplexing", Opt. Lett. **16**, 1174-1176

[Tak92] Taketomi, Y., Ford, J. E., Sasaki, H., Ma. J., Fainman. Y., and Lee. S. H. (1992), "Incremental recording for photorefractive hologram multiplexing: reply to comment", Opt. Lett. **17**, 962

[Tao91] Tao, S., Selviah, D. R., Mobasher, B., Poon, P., and Midwinter, J. E. (1991), "Angular selectivity of holographic gratings in BSO", Topical Meeting on Photorefractive Materials, Effects, and Devices, July 29-31, 1991, 1991 Technical Digest Series Vol. **14**, Paper MD5

[Tha74] Thaxter, J. B. and Kestigan, M. (1974), "Unique properties of SBN and their use in a layered optical memory", Appl. Opt. **13**, 913

[Tsu74] Tsunoda, Y., and Takeda, Y. (1974), "High density image-storage holograms by a random phase sampling method", Appl. Opt. **13**, 2046-2051

[Tsu76] Tsunoda, Y., Tatsuno, K., Kataoka, K., and Takeda, Y. (1976), "Holographic video disk: an alternative approach to optical video disks", Appl. Opt. **15**, 1398-1403

[Vac87] Vachss, F. and Hesselink, L. (1987), "Holographic beam coupling in anisotropic photorefractive media", J. Opt. Soc. Am. A, **4** (2), 325-339

[Val83] Vally, G. C. and Klein, M. B. (1983), "Optimal properties of photorefractive materials for optical data processing", Opt. Eng. **22** (6), 704-711

[vdL75] von der Linde, D. and Glass, A. M. (1975), "Photorefractive effects for reversible holographic storage of information", Appl. Phys. **8**, 85-100

[vHe63] van Heerden P. J. (1963), "Theory of optical information storage in solids",Appl. Opt. **2**, 393

[War89] Ward, A. and Solymar, L. (1989), "Diffraction efficiency limitations of holograms recorded in silver-halide emulsions", Appl. Opt. **28** (10), 1850-1855

[Wea81] Weaver, J. E. and Gaylord, T. K. (1981), "Evaluation experiments on holographic storage of binary data in electro-optic crystals", Opt. Eng. **20** (3), 404-411

[Wev91] Weverka, R. T. and Wagner, K. (1991), "Fully interconnected, two-dimensional neural arrays using wavelength-multiplexed volume holograms", Opt. Lett. **16** (11), 826-826

[Wil93] Wild, U. P., Bernet, S., Altner, S., Maniloff, E. S., and Renn, A. (1993), "Spectral hole-burning, holographic storage and processing", Optical Computing, March 16-19, 1993 Palm Springs, California, 1993 Technical Digest Series Volume **7**, 60-63

[Wu90] Wu, S., Song, Q., Mayers, A., Gregory, Don A., and Yu, F. T. S. (1990), "Reconfigurable interconnections using photorefractive holograms", Appl. Opt. **29** (8), 1118-1125

[Yar84] Yariv, A. and Yeh, P. (1984), *Optical Waves in Crystals: propagation and control of laser radiation*, Wiley, 1984

[Yar85] Yariv, A. (1985), *Optical Electronics*, 3rd Edition, Saunders College Publishing

[Yu73] Yu, F. T. S. (1973), *Introduction to Diffraction, Information Processing and Holography*, MIT Press, Cambridge, Massachusetts

[Yua91] Yuan, W. (1991), "Development of the library in form of holography", Soviet-Chinese Joint Seminar on Holography and Optical Information Processing, 21-26 September, 1991, Bishkek, Kirghizstan, SPIE **1731**, 13-17

[Zec92] Zech, R. G. (1992), "Volume hologram optical memories, mass storage future perfect?", Opt. & Photonics News, August 1992, 16-25

APPENDIX

A: DETAILS OF MAJOR EQUIPMENT USED IN EXPERIMENTAL WORK

This appendix describes the details of the general equipment used for the experimental work presented in Chapters 4, 5, and 7.

The optical table: All of the experiments were conducted on a Newport Research Series Plus optical table. The top of the table was 1.2m long, 2.4m wide and 30cm thick, and was mounted on a set of 4 Newport pneumatic isolation mounts (type XL-A).

The light sources: Holograms in both BSO and $LiNbO_3$ crystals were recorded using a Spectra Physics model 164 argon ion laser. The output of the laser at a wavelength of 514.5nm was approximately 1.5W, with a beam diameter of 1.25mm and a beam divergence of 0.69 mrad. The polarisation of the output laser beam was vertical. By inserting an intracavity etalon (Spectra-Physics model 583 oven-controlled etalon) and an aperture, the laser was operated at a wavelength of 514.5nm, on a TEM00 mode and a single longitudinal mode. The output power dropped to about 800mW due to the insertion of the etalon. The coherence length of the laser beam was measured to be 400mm, using a Michelson interferometer. Throughout this work the optical paths of the object and reference beams were carefully adjusted, so that their path difference was no more than 20mm, and so high coherence between the writing beams. was ensured. The nominal output power stability was quoted as $\underline{+}0.5\%$

after a 2 hour warm-up (using the built-in output power stabiliser), but the stability was actually worse than this.

Holograms recorded in $LiNbO_3$ crystals were readout using the same laser source as that used for recording, whilst holograms in BSO were readout using a longer wavelength (632.8nm) from a Melles Griot 5mW He-Ne laser. The beam diameter of the laser output was 0.8mm, the beam divergence was 1.0 mrad and the beam polarisation was horizontal.

The laser stabiliser: The output power of the argon ion laser was further stabilised by a commercial device (model Stabilaser 2 from Electro Optic Development Ltd), which featured a nominal long term stability of 0.1%, and a transmission (without input polariser) of about 70%. This stabiliser used a Pockels cell electrooptic modulator, and so did not induce a Doppler shift into the light frequency (as would have been the case if an acoustooptic device had been used).

The power meter: A Newport laser picowatt digital power meter (model 835) with a silicon photodetector (model 818-SL, silicon PIN photodiode), and with a model 883 OD3 optical density attenuator, was used for all the measurements of optical power. The risetime of the detector was 2μs, and the dark current of the detector at 850nm (when operated with the power meter) was less than 5pA. This is a very small current compared to the detector response of 0.295A/W (without an attenuator). The electronics of this power meter provided 7 ranges, from 2nW to 2mW (without an attenuator) or from 2mW to 2W (with an attenuator), and the range can be selected manually or by autoranging. The resolution of the power meter was 0.005% of the full scale of each range, and the accuracy was (0.1-0.4)% times the reading plus (0.05-0.2)% times the full scale of the range, depending on the range selected. For example, when the power was measured to be 100 μW using a range of 200μW (this was the most frequently used range and value), then the resolution was 10nW, and the accuracy was $\pm(0.2\% \times 100 + 0.05\% \times 200) = 0.3\mu W$, giving a relative accuracy of 0.3%. The power meter had an autoranging function which ensured the same order of percentage error for measurement of low power.

The active area of the detector was $1cm^2$. There was a few percent of non-uniformity in the detector response over this active area. To avoid a eresulting measurement error, a variable aperture (1-10mm in diameter) was attached to the detector. This ensured the beam illuminated the full aperture and hit the same location on the detector.

The conversion unit of the power meter, which converts the analog input signal (produced by the detector) into a digital signal useable by the built-in microcomputer, was relatively slow (the conversion period was 170ms). This is one of the reasons that the measurement of the angular response curves was slow, typically 0.5 sec. for each measured point.

The motion system: The motorised motion system (from Micro-Controle) consists of two main parts: translation/rotary stages (each including a DC motor driver and an optical encoder) and controller/driver units. The translation (linear) stages we used were UT100.25 models with travelling ranges of 25 mm, resolutions of 1μm, repeatabilities of 1μm, hystereses of 2.5μm, and straightnesses in trajectory of 5×10^{-5} rad. The rotary stages were UR100 models with full 360^o rotary ranges, 0.001^o resolutions, 0.002^o repeatabilities (nominal), 0.006^o hystereses (nominal), and 3×10^{-5} rad ball race wobbles. We measured the unidirectional repeatability to be less than 0.001^o, but hysteresis was worse than 0.01^o. To ensure the accuracy of the measurement, the direction of motion was carefully adjusted to avoid hysteresis. With a high resolution encoder, the recommended maximum speed of the stages was 0.8^o/sec. for rotary stages or 0.8mm/sec. for linear stages.

The controller for the motion system was an MC4/MD4 model, which was capable of controlling and driving 4 motorised stages. The control could be performed manually through the front panel of the MC4, or through a built-in program, or by a host computer via an IEEE interface.

The shutters: Two Newport 845HP digital shutter systems (with model 846HP electronic shutters) were used for the experiments. The shutter response time was about 10ms. The electronics unit provides various exposure times, from 10ms to 990sec. We made the shutters computer-controllable, so that the exposure duration could be varied from 10ms up to an arbitrarily long time.

The Computer control: The power meter, the motion system and the shutter all were controlled by a 386-DX33 personal computer through an

IEEE interface (or general purpose interface board, GPIB).

B: GENERATION OF BINARY ORTHOGONAL PATTERN SETS

Orthogonal patterns are completely independent of each other. If each pattern from an orthogonal pattern set has N elements, the maximum number of patterns in this complete set is limited to N. If N is chosen to be an integer power of 2, one way to generate N orthogonal binary patterns is described below.

To generate 2^b patterns, each with 2^b elements, we start with a line of 2^b elements, which are all in the "on" state (see Fig. A.1**a**, which shows the generating pattern for b=4). This is the "zeroth" stage of the generation process (i=0). The next stage (i=1, Fig. A.1**b**) is obtained from the first stage by dividing the pattern for i=0 into two halves, and reversing the state of the bits in the second half.

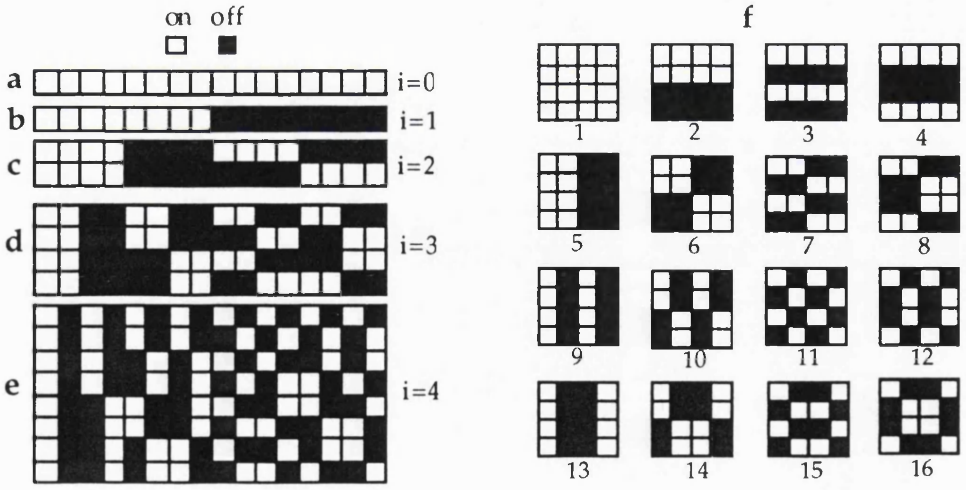

Fig. A.1 Orthogonal binary pattern set with 16 elements. **a-e**: Generation procedure for the patterns, each row corresponds to a pattern. **f**: The resulting 16 patterns.

Each subsequent stage of the generation process (labelled by i) results in 2^{i-1} patterns (Fig. A.1c, **d**, **e**), and is generated from all of the previous stages. This is done by dividing the previous stages into blocks of 2^{b-i} elements, and then reversing the elements of every other block. For instance, stage i=2 in our example (Fig. A.1c) is obtained from stages i=0 and i=1 (Fig. A.1**a** and **b**), by dividing the patterns for these stages into blocks of four ($2^{4-2}=4$), and then reversing the state of the second, fourth, sixth and eighth of these blocks, to achieve the patterns seen in Fig. A.1c.

In general, this process is continued until i=b, and all of the patterns required to form an orthogonal pattern set (as defined by [Sel89]) have been generated. The final 2-D, $2^{b/2} \times 2^{b/2}$ pattern (for even b there are 2^b, see Fig. A.1f for b=4), are obtained by filling the rows one by one, taking elements in sequence (left to right, top to bottom), from the patterns generated in all of the previous stages (i=0 to i=b)

We needed 784 patterns so b was chosen to be 10, and 1024 patterns, each with 1024 elements (32 X 32) were generated. Photographs of 4 such sample patterns from the set of 1024 (as displayed on the screen of the computer monitor) are shown in Fig. 7.10.

PUBLICATIONS

1 Z. Q. Mao, D. R. Selviah, S. Tao, and J. E. Midwinter, "Optical implementation of high order neural network (HOFNET)", presented by D. R. Selviah at the FOCUS-ESPRIT Conference, London, U. K., Jan. 1991;

2 S. Tao, D. R. Selviah, B. Mobasher, P. Poon, and J. E. Midwinter, "Angular selectivity of holographic gratings in BSO", Topical Meeting on Photorefractive Materials, Effects, and Devices, July 29-31, 1991, 1991 Technical Digest Series Vol. **14**, Paper MD5;

3 K. H. Ringhofer, S. Tao, J. Takacs, and L. Solymar, "The role of the longitudinal component of the electric field vector in two-wave mixing in photorefractive $BaTiO_3$", Appl. Phys. B **52**, 259-261, 1991;

4 Z. Q. Mao, D. R. Selviah, S. Tao, and J. E. Midwinter, "Holographic high order associative memory system", 3rd International Conference on Holographic Systems, Components & Applications, Edinburgh, U.K., Sept. 1991, IEE Proc. **342**, pp132-136, 1991;

5 S. Tao, D. R. Selviah, Z. Q. Mao, and J. E. Midwinter, "Multiple holographic recording in photorefractive crystals for associative memories", presented by D. R. Selviah to 3rd ORC Internal Colloquium, Southampton, 4 June 1992;

6 S. Tao, D. R. Selviah, Z. Q. Mao, and J. E. Midwinter, "Multiple holographic recording in photorefractive crystals for associative memories", presented by S. Tao to the European ESPRIT COSTY Meeting, Athens, Greece, 6 June 1992;

7 S. Tao, D. R. Selviah, and J. E. Midwinter, "Spatio-angular multiplexed storage of 750 holograms in an Fe:LiNbO$_3$ crystal", Opt. Lett. **18** (11), June 1993, 912-914

8 D. R. Selviah, S. Tao, and J. E. Midwinter, "Holographic storage of 750 images in a photorefractive crystal memory", Optical Computing Conference, March 16-19, 1993, Palm Springs, California, 1993 Technical Digest Series Volume 7, Paper PD2;

9 S. Tao, D. R. Selviah, and J. E. Midwinter, "High capacity, compact holographic storage in a photorefractive crystal", accepted by Topical Meeting on Photorefractive Materials, Effects, and Devices, Aug. 10-14, 1993, Kiev, Ukraine;

10 S. Tao, D. R. Selviah, and J. E. Midwinter, "Optimum replay angle for maximum diffraction efficiency of holographic gratings in Fe: LiNbO$_3$ crystals", accepted by Topical Meeting on Photorefractive Materials, Effects, and Devices, Aug. 10-14, 1993, Kiev, Ukraine.